UNIVERSITY OF CALIFORNIA, SAN DIEGO

Molecular Scale Biocomputing: An Enzyme Logic Approach

A dissertation submitted in partial satisfaction of the
requirements for the degree
Doctor of Philosophy

in

Electrical Engineering (Photonics)

by

Joshua Ray Windmiller

Committee in charge:

Professor Joseph Wang, Chair
Professor Sadik Esener, Co-Chair
Professor Yu Hwa Lo
Professor Deli Wang
Professor Liangfang Zhang

2012

The dissertation of Joshua Ray Windmiller is approved, and it is acceptable in quality and form for publication on microfilm and electronically:

_____

_____

_____

_____
Co-Chair

_____
Chair

University of California, San Diego

2012

DEDICATION

To my parents.

EPIGRAPH

Il semble que la perfection soit atteinte non quand il n'y a plus rien à ajouter,
mais quand il n'y a plus rien à retrancher.

Translation - Perfection is attained, not when there is nothing left to add,
but when there is nothing left to take away.
—Antoine de Saint Exupéry, Terre des Hommes (1939)

TABLE OF CONTENTS

LIST OF FIGURES

LIST OF TABLES

ACKNOWLEDGEMENTS

There are only two mistakes one
can make along the road to truth;
not going all the way, and not starting.

—Siddhārtha Gautama Buddha

A work of this magnitude is not the product of the trials and tribulations of a single individual. First and foremost, I would like to extend my deep gratitude to my advisor, Prof. Dr. Joseph Wang, who enthusiastically empowered me to define my own lines of research inquiry under the auspices of our funding agency's aims. Dr. Wang graciously allowed me to pursue research endeavors of broad scope and interdisciplinary nature as well as ensured that I was equipped with the support framework necessary to foster my leadership and entrepreneurial ambitions within his group. His willingness to support my professional interests as well as his proactive involvement during the course of my scientific development has been pivotal in defining me as a young scientist, engineer, innovator, and leader. Indeed, his devotion to the success of his students and associates is unparalleled.

I would also like to extend my thanks to my committee, all of whom have been extremely supportive of the interdisciplinary research effort delineated in this thesis. Thanks are also due to Prof. Dr. Evgeny Katz and his team at Clarkson University – their fruitful collaboration with our team at UCSD has resulted in the publication of a plethora of research manuscripts pertaining to biosensors that exploit biomolecular information processing principles. Prof. Dr. R. Narayan and his colleagues at the University of North Carolina / North Carolina State University are also acknowledged for kindly providing us with microneedle samples for our minimally-invasive transducers work. Dr. R. Polsky at Sandia National Laboratories is recognized for his creative suggestions. I would also like to acknowledge UCSD's Technology Transfer Office and Victoria Cajipe, in particular, who diligently ensured that our intellectual property was secured prior to the publication of our manuscripts, even at the proverbial eleventh hour. My thanks are also directed to the staff and technology business advisors at the William J. von Liebig

Center for Entrepreneurism and Technology Advancement, who fervently provided a framework to translate our innovations from the laboratory to the commercial domain. As a Gordon Scholar, the Bernard and Sophia Gordon Engineering Leadership Center has been essential to my growth as an engineering leader, and I would like to extend my gratitude to the center for its recognition of my leadership talents and potential with the Gordon Fellow Award. The NanoEngineering departmental staff is also to thank for facilitating our expeditious procurement requirements and tirelessly ensuring that our administrative needs were fulfilled so that we could concentrate our efforts on research.

Over these past three-and-a-half years, I have enjoyed the distinct opportunity and pleasure to study and work (and sometimes play) alongside some of the brightest young minds in the biosensors and electrochemistry domains. A substantive contributing factor to my success is the result of the willing support from my colleagues at the Laboratory for NanoBioElectronics, past and present, who are too numerous to list here. My heartfelt thanks is extended to all these individuals. The 'Enzyme Logic' team, in particular, is due much of the credit to my success. This includes Padmanabhan Santhosh, Min-Chieh 'Eric' Chuang, Gabriela Valdés-Ramírez, Ming Zhou, and Nandi Zhou. I'd also like to thank a few special friends that I made along the way – Daniel Kagan, Wei Gao, Amay Bandodkar, Filiz Kuralay, Sirilak Sattayasamitsathit, Aoife O'Mahony, Jahir Orozco-Holguín, Jonathan Claussen, Susana Campuzano-Ruiz, Shankar Balasubramanian, Kalayil Manian Manesh, Michal Galik, María Lobo-Castañón, Jie Wu, Chad Prior, Martin Bartošík, Sujittra Poorahong, Kerstin Malzahn, María Guix-Noguera, Miguel García-García, Serguey Parkhomovsky, Alexandra Martinez, Jimmy Chou, Juan Oviedo-Sotomayor, Cawas Engineer, and Jorge 'Jordi' Garvin-Martinez.

Upon completion of the main text of this thesis, I decided to reward myself by embarking on a gentle stroll around campus. It was a beautiful, warm, sunny day, after all. Although UCSD certainly has grown, the University still has the same feeling of vitality and vibrance as it did when I entered its doors nearly a decade ago. Upon my stroll, I came to an epiphany and realized two of the most important lessons that I can glean from my postgraduate experience. (1) *Embrace*

the unfamiliar and be highly adaptable to change. This affords us the versatility to recognize rather inconspicuous opportunities, synthesize new information, and pivot at a moment's notice when hurdles are thrown our way. I have found that dealing with the unknown empowers us with the unique ability to respond to diverse scenarios in a cool and collected manner. Science is, after all, concerned with intrepidly pushing the envelope from the known into the unknown. Along these lines, one should not be afraid to make mistakes in the process – these are *deductive* learning opportunities and just as productive as inductive forms of inquiry. (2) *Never cease to confront new challenges.* By leaving our 'comfort zone', we are introduced to ulterior methods of thought and concomitantly bring our alternative perspectives and unique approaches to developing clever solutions to problems that simply are insurmountable without such insight. I have been extremely fortunate to be exposed to projects that spanned the chemical engineering, electrical engineering, mechanical engineering, bio-engineering, nano-engineering, and software engineering domains. Confronting challenges that pervade the confines of compartmentalized disciplines of study are remarkable opportunities for personal growth and greater appreciation for science and engineering. Challenge = opportunity.

The work presented in this thesis has been, in large part, supported by the Office of Naval Research under grant number N00014-08-1202 'Integrated Enzyme-Logic Systems for "Sense and Treat" Injured Soldiers'. The Charles Lee Powell Foundation is also gratefuly acknowledged for their generous support during the critical first year of my graduate study.

Finally, but certainly no less important, this work is dedicated to my parents, who have inspired me to persevere to achieve my ambitions, no matter how lofty those endeavors may be. The sacrifices that they (and my grandparents) had to endure so that I would have the privilege of a good upbringing, education, and opportunity to pursue my dreams are nothing less than magnanimous and altruistic. They are owed more of the credit for the work presented than anyone else. I owe them a debt of gratitude that words cannot even begin to describe.

Joshua Ray Windmiller

La Jolla, CA

Portions of Chapter 5, section 2 were taken from J.R. Windmiller, A.J. Bandodkar, S. Parkhomovsky, and J. Wang. Stamp transfer electrodes for electrochemical sensing on non-planar and oversized surfaces. *Analyst*, 137(7):1570–1575, 2012. The dissertation author was the primary investigator and author of this manuscript.

Portions of Chapter 5, section 3 were taken from J.R. Windmiller, S. Chinnapareddy, P. Santhosh, J. Halámek, M.C. Chuang, V. Bocharova, T.F. Tseng, T.Y. Chou, E. Katz, and J. Wang. Strip-based amperometric detection of myeloperoxidase. *Biosensors and Bioelectronics*, 26(2):886–889, 2010. The dissertation author was the primary investigator and author of this manuscript.

Portions of Chapter 6, section 1 were taken from J.R. Windmiller, G. Strack, M.C. Chuang, J. Halámek, P. Santhosh, V. Bocharova, J. Zhou, E. Katz, and J. Wang. Boolean-format biocatalytic processing of enzyme biomarkers for the diagnosis of soft tissue injury. *Sensors and Actuators B*, 150(1):285–290, 2010. The dissertation author was the primary investigator and author of this manuscript.

Portions of Chapter 6, section 2 were taken from N. Zhou, J.R. Windmiller, G.V. Ramírez, M. Zhou, J. Halámek, E. Katz, and J. Wang. Enzyme-based NAND gate for rapid electrochemical screening of traumatic brain injury in serum. *Analytica Chimica Acta*, 703(1):94–100, 2011. The dissertation author was a co-author of the manuscript and had substantial original contributions to this work.

Portions of Chapter 6, section 3 were taken from M.C. Chuang, J.R. Windmiller, P. Santhosh, G.V. Ramírez, E. Katz, and J. Wang. High-fidelity determination of security threats via a Boolean biocatalytic cascade. *Chemical Communications*, 47(11):3087–3089, 2011. The dissertation author was a co-author of the manuscript and had substantial original contributions to this work.

Portions of Chapter 7, section 1 were taken from J. Halámek, J.R. Wind-

miller, J.A. Zhou, M.C. Chuang, P. Santhosh, G. Strack, M.A. Arugula, S. Chinnapareddy, V. Bocharova, J. Wang, and E. Katz. Multiplexing of injury codes for the parallel operation of enzyme logic gates. *Analyst*, 135(9):2249–2259, 2010. The dissertation author was a co-author of the manuscript and had substantial original contributions to this work.

Portions of Chapter 7, section 2 were taken from J. Halámek, V. Bocharova, S. Chinnapareddy, J.R. Windmiller, G. Strack, M.C. Chuang, J.A. Zhou, P. Santhosh, G.V. Ramírez, M.A. Arugula, J. Wang, and E. Katz. Multi-enzyme logic network architectures for assessing injuries: Digital processing of bio-markers. *Molecular Biosystems*, 6(12):2554–2560, 2010. The dissertation author was a co-author of the manuscript and had substantial original contributions to this work.

Portions of Chapter 7, section 3 were taken from D. Melnikov, G. Strack, J.A. Zhou, J.R. Windmiller, J. Halámek, V. Bocharova, M.C. Chuang, P. Santhosh, V. Privman, J. Wang, and E. Katz. Enzymatic AND logic gates operated under conditions characteristic of biomedical applications. *Journal of Physical Chemistry B*, 114(37):12166–12174, 2010. The dissertation author was a co-author of the manuscript and had substantial original contributions to this work.

Portions of Chapter 8 were taken from J.R. Windmiller, P. Santhosh, E. Katz, and J. Wang. Bioelectronic system for the control and readout of enzyme logic gates. *Sensors and Actuators B*, 155(1):206–213, 2011. The dissertation author was the primary investigator and author of this manuscript.

Portions of Chapter 9, section 1 were taken from M.C. Chuang, J.R. Windmiller, P. Santhosh, G.V. Ramírez, M. Galik, T.Y. Chou, and J. Wang. Textile-based electrochemical sensing: Effect of fabric substrate and detection of nitroaromatic explosives. *Electroanalysis*, 22(21):2511–2518, 2010. The dissertation author was a co-author of the manuscript and had substantial original contributions to this work.

Portions of Chapter 9, section 2 were taken from K. Malzahn, J.R. Windmiller, G.V. Ramírez, M.J. Schöning, and J. Wang. Wearable electrochemical sensors for *in situ* analysis in marine environments. *Analyst*, 136(14):2912–2917, 2011. The dissertation author was a co-author of the manuscript and had substantial original contributions to this work.

Portions of Chapter 10, section 1 were taken from J.R. Windmiller, N. Zhou, M.C. Chuang, G.V. Ramírez, P. Santhosh, P.R. Miller, R. Narayan, and J. Wang. Microneedle array-based carbon paste amperometric sensors and biosensors. *Analyst*, 136(9):1846–1851, 2011. The dissertation author was the primary investigator and author of this manuscript.

Portions of Chapter 10, section 2 were taken from J.R. Windmiller, G.V. Ramírez, N. Zhou, M. Zhou, P.R. Miller, C. Jin, S.M. Brozik, R. Polsky, E. Katz, R. Narayan, and J. Wang. Bicomponent microneedle array biosensor for minimally-invasive glutamate monitoring. *Electroanalysis*, 23(10):2302–2309, 2011. The dissertation author was the primary investigator and author of this manuscript.

Portions of Chapter 11 were taken from G.V. Ramírez*, J.R. Windmiller*, J.C. Claussen*, A.G. Martinez, F. Kuralay, M. Zhou, P.R. Miller, N. Zhou, R. Polsky, R. Narayan, and J. Wang. Multiplexed and switchable release of distinct fluids from microneedle platforms via conducting polymer nanoactuators for potential drug delivery. *Sensors and Actuators B*, 161(1):1018–1024, 2012. The dissertation author was the co-primary investigator and author of this manuscript.

Portions of Chapter 12, section 1 were taken from M. Zhou, N. Zhou, F. Kuralay, J.R. Windmiller, S. Parkhomovsky, G.V. Ramírez, E. Katz, and J. Wang. A self-powered 'Sense-Act-Treat' system that is based on a biofuel cell and controlled by Boolean logic. *Angewandte Chemie International Edition*, 124(11):2686–2689, 2012. The dissertation author was a co-author of the manuscript and had substan-

tial original contributions to this work.

Portions of Chapter 12, section 2 were taken from M. Zhou, F. Kuralay, J.R. Windmiller, and J. Wang. DNAzyme logic-controlled biofuel cell for self-powered biosensors. *Chemical Communications*, 48(32):3815–3817, 2012. The dissertation author was a co-author of the manuscript and had substantial original contributions to this work.

VITA

2004	Systems and Applications Engineering Intern, Entropic Communications, Inc.
2005 - 2006	RF and Communications Systems Engineering Intern, RF Micro Devices WPAN, Inc.
2006 - 2007	Undergraduate Research Assistant, University of California, San Diego
2007	B. Sc. in Electrical Engineering (Photonics), University of California, San Diego
2009	M. Sc. in Electrical Engineering (Photonics), University of California, San Diego
2011	C. Phil. in Electrical Engineering (Photonics), University of California, San Diego
2007 - 2012	Graduate Research Assistant, University of California, San Diego
2012	Ph. D. in Electrical Engineering (Photonics), University of California, San Diego

PUBLICATIONS

J.R. Windmiller, A.J. Bandodkar, S. Parkhomovsky, and J. Wang. Stamp transfer electrodes for electrochemical sensing on non-planar and oversized surfaces. *Analyst*, 137(7):1570–1575, 2012.

M. Zhou, F. Kuralay, J.R. Windmiller, and J. Wang. DNAzyme logic-controlled biofuel cell for self-powered biosensors. *Chemical Communications*, 48(32):3815–3817, 2012.

M. Zhou, N. Zhou, F. Kuralay, J.R. Windmiller, S. Parkhomovsky, G.V. Ramírez, E. Katz, and J. Wang. A self-powered 'Sense-Act-Treat' system that is based on a biofuel cell and controlled by Boolean logic. *Angewandte Chemie International Edition*, 124(11):2686–2689, 2012.

G.V. Ramírez*, J.R. Windmiller*, J.C. Claussen*, A.G. Martinez, F. Kuralay, M. Zhou, P.R. Miller, N. Zhou, R. Polsky, R. Narayan, and J. Wang. Multiplexed and switchable release of distinct fluids from microneedle platforms via conducting polymer nanoactuators for potential drug delivery. *Sensors and Actuators B*, 161(1):1018–1024, 2012.

J.R. Windmiller, G.V. Ramírez, N. Zhou, M. Zhou, P.R. Miller, C. Jin, S.M. Brozik, R. Polsky, E. Katz, R. Narayan, and J. Wang. Bicomponent microneedle array biosensor for minimally-invasive glutamate monitoring. *Electroanalysis*, 23(10):2302–2309, 2011.

N. Zhou, J.R. Windmiller, G.V. Ramírez, M. Zhou, J. Halámek, E. Katz, and J. Wang. Enzyme-based NAND gate for rapid electrochemical screening of traumatic brain injury in serum. *Analytica Chimica Acta*, 703(1):94–100, 2011.

K. Malzahn, J.R. Windmiller, G.V. Ramírez, M.J. Schöning, and J. Wang. Wearable electrochemical sensors for *in situ* analysis in marine environments. *Analyst*, 136(14):2912–2917, 2011.

J.R. Windmiller, N. Zhou, M.C. Chuang, G.V. Ramírez, P. Santhosh, P.R. Miller, R. Narayan, and J. Wang. Microneedle array-based carbon paste amperometric sensors and biosensors. *Analyst*, 136(9):1846–1851, 2011.

M.C. Chuang, J.R. Windmiller, P. Santhosh, G.V. Ramírez, E. Katz, and J. Wang. High-fidelity determination of security threats via a Boolean biocatalytic cascade. *Chemical Communications*, 47(11):3087–3089, 2011.

J.R. Windmiller, P. Santhosh, E. Katz, and J. Wang. Bioelectronic system for the control and readout of enzyme logic gates. *Sensors and Actuators B*, 155(1):206–213, 2011.

J. Halámek, V. Bocharova, S. Chinnapareddy, J.R. Windmiller, G. Strack, M.C. Chuang, J.A. Zhou, P. Santhosh, G.V. Ramírez, M.A. Arugula, J. Wang, and E. Katz. Multi-enzyme logic network architectures for assessing injuries: Digital processing of biomarkers. *Molecular Biosystems*, 6(12):2554–2560, 2010.

M.C. Chuang, J.R. Windmiller, P. Santhosh, G.V. Ramírez, M. Galik, T.Y. Chou, and J. Wang. Textile-based electrochemical sensing: Effect of fabric substrate and detection of nitroaromatic explosives. *Electroanalysis*, 22(21):2511–2518, 2010.

J.R. Windmiller, S. Chinnapareddy, P. Santhosh, J. Halámek, M.C. Chuang, V. Bocharova, T.F. Tseng, T.Y. Chou, E. Katz, and J. Wang. Strip-based amperometric detection of myeloperoxidase. *Biosensors and Bioelectronics*, 26(2):886–889, 2010.

J.R. Windmiller, G. Strack, M.C. Chuang, J. Halámek, P. Santhosh, V. Bocharova, J. Zhou, E. Katz, and J. Wang. Boolean-format biocatalytic processing of enzyme biomarkers for the diagnosis of soft tissue injury. *Sensors and Actuators B*, 150(1):285–290, 2010.

D. Melnikov, G. Strack, J.A. Zhou, J.R. Windmiller, J. Halámek, V. Bocharova, M.C. Chuang, P. Santhosh, V. Privman, J. Wang, and E. Katz. Enzymatic AND

logic gates operated under conditions characteristic of biomedical applications. *Journal of Physical Chemistry B*, 114(37):12166–12174, 2010.

J. Halámek, J.R. Windmiller, J.A. Zhou, M.C. Chuang, P. Santhosh, G. Strack, M.A. Arugula, S. Chinnapareddy, V. Bocharova, J. Wang, and E. Katz. Multiplexing of injury codes for the parallel operation of enzyme logic gates. *Analyst*, 135(9):2249–2259, 2010.

P. Calvo-Marzal, S. Sattayasamitsathit, S. Balasubramanian, J.R. Windmiller, C. Dao, and J. Wang. Propulsion of nanowire diodes. *Chemical Communications*, 46(10):1623–1624, 2010.

K.M. Manesh, J. Halámek, M. Pita, J. Zhou, T.K. Tam, P. Santhosh, M.C. Chuang, J.R. Windmiller, D. Abidin, E. Katz, and J. Wang. Enzyme logic gates for the digital analysis of physiological level upon injury. *Biosensors and Bioelectronics*, 24(12):3569–3574, 2009.

J.M.C. Boggio, S. Moro, E. Myslivets, J.R. Windmiller, N. Alic, and S. Radic. 155-nm continuous-wave two-pump parametric amplification. *IEEE Photonics Technology Letters*, 21(10):612–614, 2009.

E. Myslivets, N. Alic, J.R. Windmiller, and S. Radic. A new class of high-resolution measurements of arbitrary-dispersion fibers: Localization of four-photon mixing process. *IEEE Journal of Lightwave Technology*, 27(3):364–375, 2009.

E. Myslivets, N. Alic, J.R. Windmiller, R.M. Jopson, and S. Radic. 400-ns continuously tunable delay of a 10Gb/s intensity modulated optical signal. *IEEE Photonics Technology Letters*, 21(4):251–253, 2009.

S. Moro, E. Myslivets, J.R. Windmiller, N. Alic, J.M.C. Boggio, and S. Radic. Synthesis of equalized broadband parametric gain by localized dispersion mapping. *IEEE Photonics Technology Letters*, 20(23):1971–1973, 2008.

N. Alic, J.R. Windmiller, J.B. Coles, S. Moro, E. Myslivets, R.E. Saperstein, J.M.C. Boggio, C.S. Bres, and S. Radic. 105-ns continuously tunable delay of 10-Gb/s optical signal. *IEEE Photonics Technology Letters*, 20(13):1187–1189, 2008.

N. Alic, J.R. Windmiller, J.B. Coles, and S. Radic. Two-Pump Parametric optical delays. *IEEE Journal of Selected Topics in Quantum Electronics*, 14(3):681–690, 2008.

J.M.C. Boggio, J.R. Windmiller, M. Knutzen, R. Jiang, C.S. Bres, N. Alic, B. Stossel, K. Rottwitt, and S. Radic. 730-nm optical parametric conversion from near- to short-wave infrared band. *Optics Express*, 16(8):5435–5443, 2008.

CONFERENCE PROCEEDINGS

J.R. Windmiller. Wearable printed sensors for situational awareness. *IDTechEx Printed Electronics & Photovoltaics USA 2011*, Santa Clara, CA. Dec. 2011. (Invited)

J.R. Windmiller. Textile-based printed bioelectronic sensors. *IDTechEx Printed Electronics & Photovoltaics USA 2010*, Santa Clara, CA. Dec. 2010. (Invited)

J. Halámek, J.R. Windmiller, J. Zhou, M.C. Chuang, P. Santhosh, G. Strack, M.A. Arugula, S. Chinnapareddy, V. Bocharova, J. Wang, and E. Katz. Development of enzyme logic-based architectures for "Sense and Treat" of multiple battlefield injuries – Field hospital on a chip. *Chem and Bio Defense Science and Technology*, Orlando, FL. Nov. 2010.

E. Katz, J. Wang, J. Halámek, J.R. Windmiller, J. Zhou, M.C. Chuang, P. Santhosh, G. Strack, M.A. Arugula, S. Chinnapareddy, and V. Bocharova. Biocomputing coding concept approach based on parallel and multiplexed enzyme logic gates for multi-injury diagnosis. *37^{th} Northeast Regional Meeting of the American Chemical Society*, Potsdam, NY. Jun. 2010.

J.M. Chavez Boggio, S. Moro, J.R. Windmiller, S. Zlatanovic, E. Myslivtes, N. Alic, and S. Radic. Optical frequency comb generated by four-wave mixing in highly nonlinear fibers. *Conference on Lasers and Electro-Optics 2009*, Baltimore, MD. May 2009.

C.S. Bres, A.O.J. Wiberg, J.R. Windmiller, N. Alic, and S. Radic. Self-seeded multicasting of 320 Gb/s data in a 2-pump parametric amplifier. *2009 Optical Fiber Communications Conference*, San Diego, CA. Mar. 2009.

J.M. Chavez Boggio, S. Moro, E. Myslivets, J.R. Windmiller, N. Alic, and S. Radic. Raman-induced gain distortions in double-pumped parametric amplifiers. *2009 Optical Fiber Communications Conference*, San Diego, CA. Mar. 2009.

S. Moro, E. Myslivets, N. Alic, J.M. Chavez Boggio, J.R. Windmiller, J.X. Zhao, A.J. Anderson, and S. Radic. Synthesis of equalized broadband gain in one-pump fiber-optic parametric amplifiers. *2009 Optical Fiber Communications Conference*, San Diego, CA. Mar. 2009.

C.S. Bres, A.O.J. Wiberg, J.R. Windmiller, N. Alic, and S. Radic. Parametric multicasting of 320 Gb/s OTDM data. *IEEE/LEOS Winter Topicals Meeting Series 2009*, Innsbruck, Austria. Jan. 2009.

J.M. Chavez Boggio, S. Moro, J.R. Windmiller, A.J. Anderson, J.X. Zhao, N. Alic, and S. Radic. Tunable 2.5 W continuous-wave optical source based on efficient parametric conversion in highly nonlinear fiber. *IEEE/LEOS Winter Topicals Meeting Series 2009*, Innsbruck, Austria. Jan. 2009.

A.O.J. Wiberg, C.S. Bres, J.R. Windmiller, N. Alic, and S. Radic. RZ pulse source for optical time division multiplexing based on self-phase modulation and four wave mixing. *IEEE/LEOS Winter Topicals Meeting Series 2009*, Innsbruck, Austria. Jan. 2009.

J.M. Chavez Boggio, M. Knutzen, C.S. Bres, N. Alic, J.R. Windmiller, B. Stossel, K. Rottwitt, and S. Radic. All fiber parametric conversion from near to short wave infrared band. *33rd European Conference and Exhibition of Optical Communications*, Berlin, Germany. Sep. 2007.

N. Alic, E. Myslivets, J.B. Coles, R.E. Saperstein, J.R. Windmiller, S. Radic, R. Jiang, P. Firth, and C. Clarke. Equalized 42.8Gb/s transmission based on A 10Gb/s EML transmitter. *33rd European Conference and Exhibition of Optical Communications*, Berlin, Germany. Sep. 2007.

PATENTS

US/61/645,576 – *Flexible electrochemical biosensors for direct epidermal integration*, Provisional filing (2012).

US/61/625,655 – *Printed biofuel cells*, Provisional filing (2012).

US/61/565,457 – *Printed biofuel cells*, Provisional filing (2011).

WO/2011/156,095 – *Textile-based printable electrodes for electrochemical sensing*, PCT filing (2011).

US/61/530,927 – *Microneedle arrays for transdermal biosensing and drug delivery*, Provisional filing (2011).

US/8,022,292 – *Photovoltaic device employing a resonator cavity*, Issued patent (2011).

WO/2011/116,151 – *Enzyme-logic biosensing*, PCT filing (2011).

US/61/354,157 – *Textile-based printable electrodes for electrochemical sensing*, Pending patent (2010).

US/61/353,581 – *Textile-based printable electrodes for electrochemical sensing*, Pending patent (2010).

US/61/329,512 – *Multiplexing of Situational Codes for the Parallel Operation of Enzyme Logic Gates*, Provisional filing (2010).

US/61/314,494 – *Enzyme-logic biosensing*, Provisional filing (2010).

CERTIFICATES

Technology Business Creation – The von Liebig Center, June 2012

Engineering Leadership – The Gordon Center, May 2012

Springboard Program in New Business Creation – CONNECT, August 2008

Leadership Reaction Course – United States Air Force Academy, July 2001

MAJOR AWARDS

William J. von Liebig Center Fellowship

Gordon Fellow Award

Printed Electronics USA 2010 Academic R&D Award

Charles Lee Powell Foundation Fellowship

Powell Bonus Award

Governor's Scholar Award

California Academic Excellence Award in Physics, 2002

The San Diego Water Authority Award, 2002

The San Diego County Environmental Services Award, 2002

The Society of American Military Engineers Award in Engineering, 2001, 2002

The Scripps Institution of Oceanography Century Award, 2001, 2002

California Academic Excellence Award in Chemistry, 2001

The American Society of Materials International Engineering Award, 2001

The General Atomics Sciences Education Foundation Award, 2001

The Rensselaer Polytechnic Institute Award for Engineering Excellence, 2001

The Society for the Advancement of Materials Process Engineering Award, 2001

The University of San Diego Award for Excellence in Electrical Engineering, 2001

The Marine Technology Society Award for Marine Engineering, 2001

HONORS AND RECOGNITION

Gordon Scholar, 2009 – 2012

Recognition, California State Assembly for achievements in engineering, 2011

SPIE Scholarship, 2007

CP Kelco Scholarship, 2006

Provost Honors, 2003 – 2007

AP Scholar, 2003

Principal's Honor Court, 2003

Recognition, California State Assembly for dedication to academics, 2002

Recognition, United States Senate for dedication to academics, 2002

CHALLENGES AND COMPETITIONS

Winner, So. California Clean Energy Technology Acceleration Program, 2012

Finalist, UCSD Entrepreneur Challenges, Executive Summary Phase, 2012

Finalist, UCSD Entrepreneur Challenges, Business Concept Phase, 2012

Finalist, First Look West National Energy Challenge Competition, 2012

2^{nd} Place, Triton Greenovation Network Challenge, 2011

Audience's Choice Award, Triton Greenovation Network Challenge, 2011

Finalist, So. California Healthcare Technology Acceleration Program, 2011

Finalist, TATRC-Qualcomm Wireless Health Innovation Challenge, 2010

Finalist, UCSD Entrepreneur Challenges, Business Plan Phase, 2008

Winner, UCSD Entrepreneur Challenges, Executive Summary Phase, 2007

Winner, UCSD Entrepreneur Challenges, Business Concept Phase, 2007

Finalist, John D. Isaacs Memorial Scholarship in Marine Science, 2002

1^{st} Place, Greater San Diego Science & Engineering Fair, 2002

2^{nd} Place, Greater San Diego Science & Engineering Fair, 2001

PROFESSIONAL MEMBERSHIPS

Member, IEEE Computer Society, 2009 –

Member, IEEE Communications Society, 2008 –

Member, IEEE Photonics Society, 2007 –

Member, IEEE, 2007 –

Member, the Optical Society of America, 2007 –

Member, SPIE, 2006 –

Invited Member, Eta Kappa Nu, 2006 –

Invited Member, National Society of Collegiate Scholars, 2004 –

Lifetime Member, National Honor Society, 2001 –

Lifetime Member, California Scholarship Federation, 2001 –

PROFESSIONAL SERVICE

Judge,
- Printed Electronics USA 2011 Awards

Reviewer,
- IEEE Sensors Journal
- IEEE Journal of Lightwave Technology
- IEEE Photonics Technology Letters
- Electroanalysis

Educational Advisor,
- UCSD Office of Research Affairs
- UCSD Department of Electrical & Computer Engineering
- Boys & Girls Club of San Diego

FIELDS OF STUDY

Major Field: Electrical Engineering (Photonics)

Studies in Bioelectronics and Electrochemical Engineering
Dr. Joseph Wang, Distinguished Professor of NanoEngineering
University of California, San Diego

Studies in Nonlinear Fiber Optic Communications
Dr. Stojan Radic, Professor of Electrical and Computer Engineering
University of California, San Diego

ABSTRACT OF THE DISSERTATION

Molecular Scale Biocomputing: An Enzyme Logic Approach

by

Joshua Ray Windmiller

Doctor of Philosophy in Electrical Engineering (Photonics)

University of California, San Diego, 2012

Professor Joseph Wang, Chair
Professor Sadik Esener, Co-Chair

The rapid and reliable detection of injury, particularly in battlefield conditions, remains a fundamental challenge in emergency medicine. Furthermore, injuries that cause internal bleeding, especially in circumstances when the affected individual fails to exhibit outward signs of this life-threatening condition, are particularly difficult to identify. These situations have illustrated the need for advanced diagnostic measures to assess injuries to the soft tissues with a high degree of accuracy. Commonplace approaches have been directed at sophisticated diagnostic equipment for the detection of these conditions such as magnetic resonance imaging and electromyography. However, these tools are costly, time-consuming, and a challenge to operate in the field during which the delivery of an immediate

therapeutic intervention is crucial. In situations where such imaging equipment or laboratory tests are not available or cannot deliver results in a timely fashion, the diagnosis is typically administered by a medical professional upon thorough physical examination. Unfortunately, owing to the complex pathophysiology of many injuries, this approach has frequently resulted in misdiagnoses that have resulted in unnecessary treatments, thereby encumbering the healthcare provider and placing an additional burden upon the patient. Effective diagnostic tools that enable the rapid administration of a targeted treatment would offer great promise for improving the prognosis of injury, particularly in battlefield conditions. Recent research endeavors in the biochemical computing arena have resulted in the demonstration of sophisticated enzyme-based cascades that leverage Boolean principles to emulate electronic logic gates in the biochemical domain. Such enzyme-based logic gates possess the unique ability to integrate complex patterns of bio-/chemical inputs and tender a diagnosis in a straightforward binary '0'/'1' or 'NO'/'YES' format. This dissertation explores the manner in which such advanced diagnostic systems can be engineered and leveraged to achieve useful aims in the diagnosis (and eventual treatment) of injury in an autonomous fashion, thereby leading towards the development of an integrated 'Sense-Act-Treat' field 'hospital-on-a-chip' system. The systems presented in this work are evaluated at their physical limits under utilitarian embodiments and are hence shown to be of practical importance in the healthcare, fitness, security, and environmental monitoring domains.

Chapter 1

Introduction

I am always doing that which I cannot do,
in order that I may learn how to do it.

—Pablo Picasso

Since the age of classical antiquity, man has looked to the natural world to provide the inspiration necessary to enable advancements in science, medicine, architecture, and engineering [1]. Research efforts have long sought to leverage bio-inspired principles to emulate biological systems in artificially-engineered 'organic' embodiments [2, 3]. Indeed, artificial systems that exploit the anatomical 'hardware' of the biological entity would serve to overcome some intransigent obstacles that limit the deployment of such systems for utilitarian applications, thereby drammatically augmenting the capabilities of man-made devices and providing countless avenues for further technological development. Not surprisingly, the human body represents a compelling, yet formidable paradigm to emulate, marked by its ability to execute thousands of known metabolic reactions continuously [4] in an astonishingly well-orchestrated and remarkably efficient cascade that is duplicated in a massively parallel fashion in the roughly 100 trillion cells that comprise the human anatomy [5].

Owing to the vastly dissimilar principles that govern the operation of artificially engineered inorganic and naturally-occurring organic information processing systems, challenges materialize when integrating these two unique entities into a

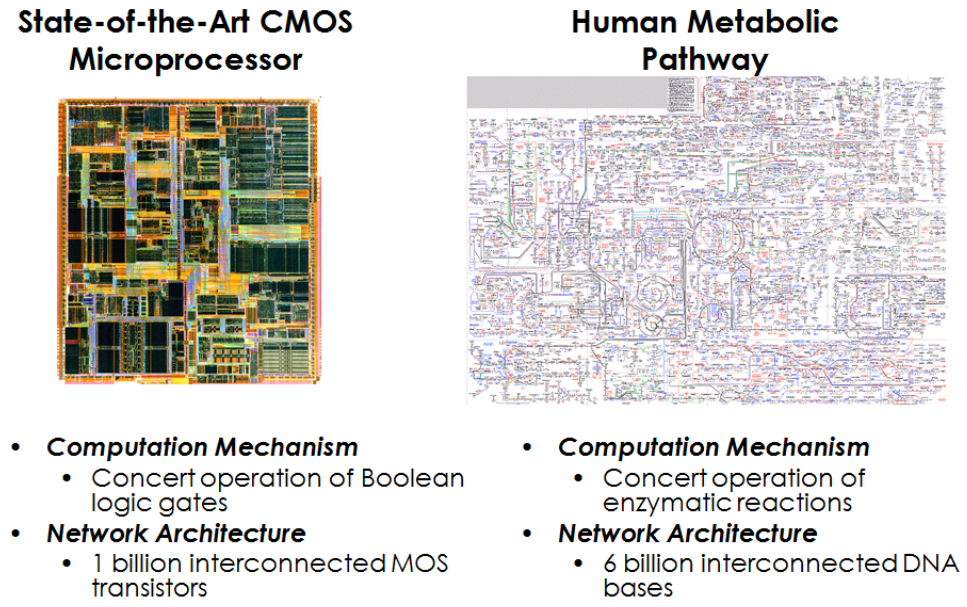

Figure 1.1: *High-level comparison between engineered and organic computing systems.*

cohesive, fully-functional 'biocomputing' system. To the detriment of those individuals conducting lines of inquiry in this domain, the biocomputing aim has been frustratingly elusive. Much effort has thus been directed at the design of the interface between these two systems to exploit the unique strengths afforded by each platform, albeit progress in this arena has been severely hampered by limitations in the exchange of information between the two mutually-exclusive embodiments with any appreciable degree of fidelity and robustness. Accordingly, practical implementations of this interfacial approach have not witnessed any utilitarian applications and have, as such, remained much of a scientific curiosity and discourse in juxtaposition.

Rather than insisting on hybrid approaches whereby two incompatible systems (inorganic and organic) are merged into a complex aggregate encompassing trivial functionality, chemical reactions may be engineered to process chemical information *exclusively in the chemical domain* prior to the transduction of the result of the information processing operation into the electrical domain for further manipulation. In this vein, certain physical effects intrinsic to bio-/chemical reactions

may be harnessed, such as catalysis, which, in turn, can be leveraged as a computational tool. By mitigating the need for multiple electronic transducers and reducing the complexity of the associated chemical-to-electrical conversion, power, geometrical, resiliency, and cost constraints can be alleviated. This novel approach would overcome the obstacles that have traditionally impeded the promulgation of bio-/chemical devices as information processing systems.

As a pragmatic examination, this dissertation explores the avenues in which biocomputing principles can be exploited to achieve useful aims. Biosensor devices and systems are taken as proof-of-principle examples and represent a compelling paradigm where the infrastructure has already been established to facilitate the interface between bio-/chemical systems and simple electronic devices. More crucially, a demonstrated need has been identified in this domain for further advancement in the state-of-the-art leading towards advanced diagnostic measures aimed at mitigating chronic diseases and acute forms of injury / trauma, thereby improving survival rates from a host of life-threatening pathophysiological conditions.

1.1 Utility of electrochemical biosensors

Broadly speaking, a chemical sensor is a device that can be employed for the detection of a specific analyte in a sample matrix [6]. In that vein, chemical sensors measure a physical quantity, converting it into a signal which can be readily interpreted by an observer or instrument. Ideally, such a device is capable of responding continuously and reversibly to the target analyte in the matrix and does not otherwise perturb the sample. Key considerations in the design of chemical sensors include elevated sensitivity to the target analyte, hence improving detection limits, high selectivity to the target and the ability to mitigate sources of interference, stability of the response over extended sensing durations, and response time to enable the rapid presentation of readings to the operator or acquisition unit [7]. Through the combination of the sample collection and measurement routines, chemical sensors obviate the need for sample preparation and handling, hence increasing reliability, mitigating the risk of sample contami-

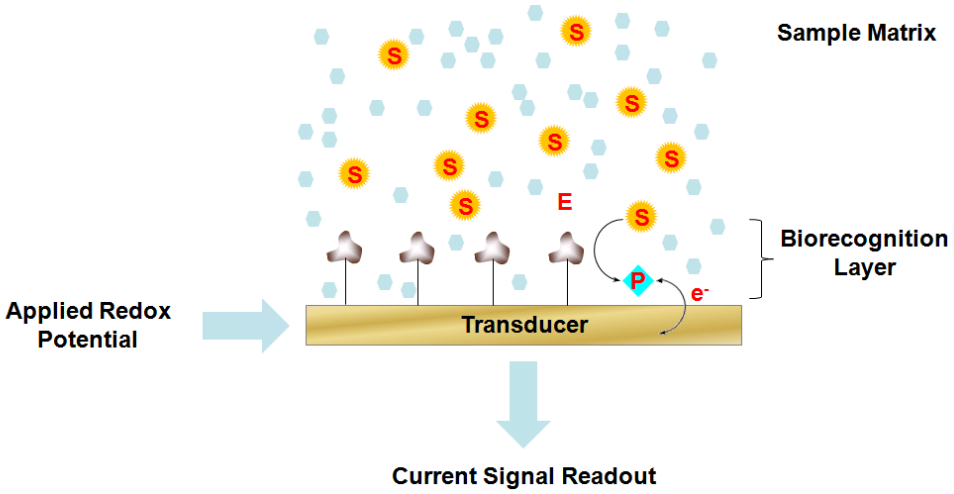

Figure 1.2: *Block-level diagram of the basic components comprising enzymatic electrochemical biosensors.* S – *Substrate,* P – *Product,* E – *Enzyme.*

nation, and substantially lowering the likelihood of user error, thereby providing the operator with an automated method for complex chemical analysis [8].

Gleaning further into specifics, a biosensor represents a subclass of chemical sensors that is designed to detect the presence of a biochemical entity in a biological environment [9]. Electrochemical biosensors represent a pervasive (and perhaps the most widely researched and clinically-implemented) segment of this domain and exploit the fact that certain chemical species can undergo reduction / oxidation reactions, thereby giving rise to a redox current that can easily be detected via the application of a suitable potential at an electrode transducer.

In order to impart selectivity towards the desired analyte, a biosensor monopolizes on a functionalized biorecognition layer at the electrode transducer surface. The biorecognition layer interacts with the target analyte in a specific manner and the physio-chemical changes that originate from this interaction are translated by the transduction element to electrical signals, as illustrated in Fig. 1.2. The biorecognition layer typically harnesses either immuno-recognition / affinity (via antibodies or nucleic acids) or biocatalytic (via enzymes or cells) principles [7]. This work is concerned, almost exclusively, with the latter – enzymatic electrochemical biosensors that are transduced in an amperometric fashion (to be discussed in

following sections).

1.2 Techniques for conventional electrochemical biosensing

Conventional electrochemical biosensors facilitate the detection of a biochemical analyte via the electrochemical reduction or oxidation of an analyte directly or by means of the reduction / oxidation of the product generated by a chemical reaction instigated by the presence of the analyte. An electroactive mediator may be employed in either scenario. Amperometric biosensors have enjoyed widespread commercial adoption due to their intrinsic sensitivity, stability / robust nature, ease of manufacture, cost-effectiveness, and compatibility with industrial thick-film fabrication processes [7, 9]. Owing to their numerous advantages, amperometric enzymatic biosensors are the current mainstay of the glucose monitoring industry and have enabled body-worn, real-time quantification of glucose due to the advantages of the technology enumerated above [10].

Typically, a three-electrode configuration is employed and consists of a working electrode (where the redox reaction of interest occurs), a counter electrode (where the current is sourced or sinked), and a reference electrode (employed to establish a stable potential from which reactions can be 'referenced' to a well-known standard electrode potential). Depending on the applied potential at the working electrode (and the nature of the reaction occurring at its surface, whether it be oxidation or reduction), it may either be considered as the anode (where oxidation reactions occur) or cathode (reduction) of the electrolytic system with the complementary redox process occurring at the counter electrode. Carbon, carbon-composite, or metallic-based materials are typically employed in working and counter electrode biosensor embodiments owing to their superior stability and electrocatalytic abilities. The surface of these electrodes can be 'roughened' (micro- or nano-structured) to impart augmented surface area to further enhance the current response and provide for 'pockets' in which biorecognition or catalytic agents may be entrapped. An Ag/AgCl-based reference electrode is widely considered the

norm in the biosensor arena due to its facile electron kinetics and thermal stability. These electrodes may either consist of bulk materials or fabricated using thick-film technology (screen printing), as will be the object of discussion in Chapter 5.

To enable percutaneous applications, an enzyme is generally immobilized on the surface of the working electrode utilizing any one of the following techniques: polymer / membrane entrapment, surface adsorption, covalent binding, electrostatic binding, or biospecific interactions [7]. The utilization of the techniques mentioned satisfies several operational requirements including enzyme stabilization and preservation of catalytic activity and hence facilitates reversible, long-term performance, which is of substantial value in implantable and subcutaneous monitoring applications. To promote the sensitive electrochemical detection of the product produced from the enzymatic interaction with the substrate, the product of the biocatalytic reaction may either be permitted to diffuse unabated to the electrode surface [11] or the detection process can be arbitrated indirectly through the implementation of a freely-diffusing redox mediator [12]. Direct electron transfer may also be achieved from the active site of the enzyme to the electrode via a number of 'wiring' techniques in order to yield further enhanced electrochemical detection [13].

From a systems-level perspective, the resultant signal generated by the biosensor is tendered to the wearer, in quasi-real-time, in order to enable them to make informed decisions regarding their physiological status. A notable exception is the ongoing development thrust leading towards the demonstration of an artificial pancreas [10], where a glucose biosensor is employed in conjunction with a tightly-regulated insulin-delivery device in order to respond to the insulin needs of the patient in an autonomous and dynamic fashion. In an attempt to further augment the specificity and diagnostic capabilities of such devices, electrode arrays may be functionalized with unique enzymes and interrogated electrochemically. The resultant signals generated by the transduction step are channeled to an embedded microcontroller, which subsequently renders a readout regarding the levels of the target biomarkers. However, owing to the size of such systems, practical embodiments of this approach have solely consisted of semi-automated

benchtop analyzers for use in the hospital laboratory. Furthermore, as a result of the complexity of this approach, the information generated by the system is left to be interpreted by experienced operators rather than the patient.

1.3 Limitation of current biosensor technologies

Conventional biomedical, industrial, security and environmental sensing techniques are limited in their capacity to process inputs in the chemical domain in a highly parallel fashion that enables the concurrent realization of high specificity / fidelity and reduced dependence on electronic signal processing. This fundamental limitation presents a challenge when utilizing such chemical sensors for a multitude of diverse applications. Although methods do exist to integrate and process a wide variety of sensor inputs, their operational merits are limited. A concept that seeks to differentiate among various scenarios must be able to address the multitude of possible situational phenomena, only some of which may be of concern. Accordingly, the development of high-fidelity biosensors necessitates the minimization of the electronic backbone and the co-location of the information processing operations within the chemical domain itself, even if multiple situations are assessed simultaneously.

The reliable and rapid detection of a multitude of common battlefield injuries is a paramount challenge in emergency medicine [14] and represents an excellent example of the need to differentiate between various pathophysiological scenarios. Accordingly, there are urgent needs for a novel sensing contingent enabling a comprehensive high-fidelity diagnosis of multiple injury conditions [14]. Battlefield injuries can vary greatly in nature, extent, and severity, and thus these injuries manifest a wide array of pathophysiological scenarios [15]. This, in turn, presents a fundamental challenge to the identification of different forms of injury in occurrences such as polytrauma, especially in cases arising from blast injury [16], where a rapid determination of the injury / injuries is essential [17]. A concept that seeks to differentiate various forms of relevant injuries must be able to mitigate the large number of combinations and permutations of physiological and pathological

states in a rapid and reliable manner, only some of which may correspond to bona fide injury. In cases involving polytrauma, the diagnosis for such injury is typically tendered by a medical professional following close physical examination and a comprehensive regimen of conventional laboratory tests [18]. Despite the advanced state of diagnostic technologies that assist the physician in assessing individual injuries, very few solutions exist in the hospital setting that can address multiple injuries in a comprehensive, rapid, and high-fidelity manner. Even fewer solutions exist that can yield such results in field settings [19]. The realization of advanced, field-based diagnostic devices for reliable injury screening thus represents a crucial challenge in healthcare today. The simultaneous evaluation of multiple injuries is a required core competency of such diagnostic system.

When mechanical damage to specific organs or tissues occurs, chemical species (proteins and / or low molecular-weight compounds, normally present only in intravascular compartments) are released into various body fluids (blood, urine, etc.). Rapid and sensitive detection of these biomarkers is essential for a proper diagnosis of injury, many of which are already present at relatively high concentrations in blood under normal physiological conditions. Additionally, increased levels of certain freely circulating chemical species following an injury are associated with the metabolic response due to the pathological processes (oxidative stress, metabolic acidosis, etc.) and are not necessarily associated with damage to specific organs or tissues. Biochemical screening of injury / disease biomarkers nowadays relies on optical immunoassays [20] performed by well-trained personnel using sophisticated semi-automated hospital analyzers [21]. As can be inferred, such analyzers are not compatible with the requirements of rapid injury diagnostics in field settings.

Several approaches have been proposed for the comprehensive decentralized assessment of multiple injuries in a convenient, single-test format [22]. These include parallel biosensors / biosensor arrays [23, 24] and lab-on-a-chip devices [25], as these devices can leverage electronics for further information processing. Although these technologies enable the integration of a number of specific biochemical functionalities for the determination of a multitude of pathophysiological

states, they suffer from several limitations [26]. Most notably, each sensing element must be read-out and processed by dedicated electronic circuitry, thereby placing an additional burden on the corresponding microelectronic devices and accompanying power sources. Consequently, such schemes are not amenable to ultra-low power decentralized operation and integration into disposable biosensors that is an essential prerequisite of field-based biosensing devices. Moreover, to handle the relatively large amount of information acquired by these systems, the above techniques must rely on multiplexing or encoding operations to be performed in the electronic domain.

1.4 Need for an alternative biosensing paradigm

The limited specificity of assays of single enzyme biomarkers can be rectified by the simultaneous analysis of several biomarkers. Although each biomarker may not allude to a specific injury when evaluated on an individual basis, the integration of multiple biomarkers would enable distinction among various injury conditions and thereby provide more comprehensive insight into the nature and extent of the injury. This analysis could be performed with the implementation of Boolean logic in biocatalytic systems [27, 28, 29, 30, 31], whereby the biochemical input and output signals are considered in the binary format: 0 / 1 (False / True, No / Yes). In this regard, a threshold separating the normal and pathological concentrations of the biomarkers can be implemented and operation can be ascribed to a pre-defined truth table. Logic-based systems with multiple-input markers can be designed in such a manner that a positive diagnosis is tendered only in scenarios when pathological levels of all biomarkers are presented.

Bearing in mind the future potential use of bio-/chemical computing systems for molecular computers [32, 33] based on novel concepts analogous to artificial intelligence [34, 35], there still remains a need to identify immediate applications for these systems based on the present level of technology. One of the stimuli for the development of biocomputing systems is their potential application in novel multi-signal responsive biosensors [36, 37] and actuators [38, 39] able to tender a

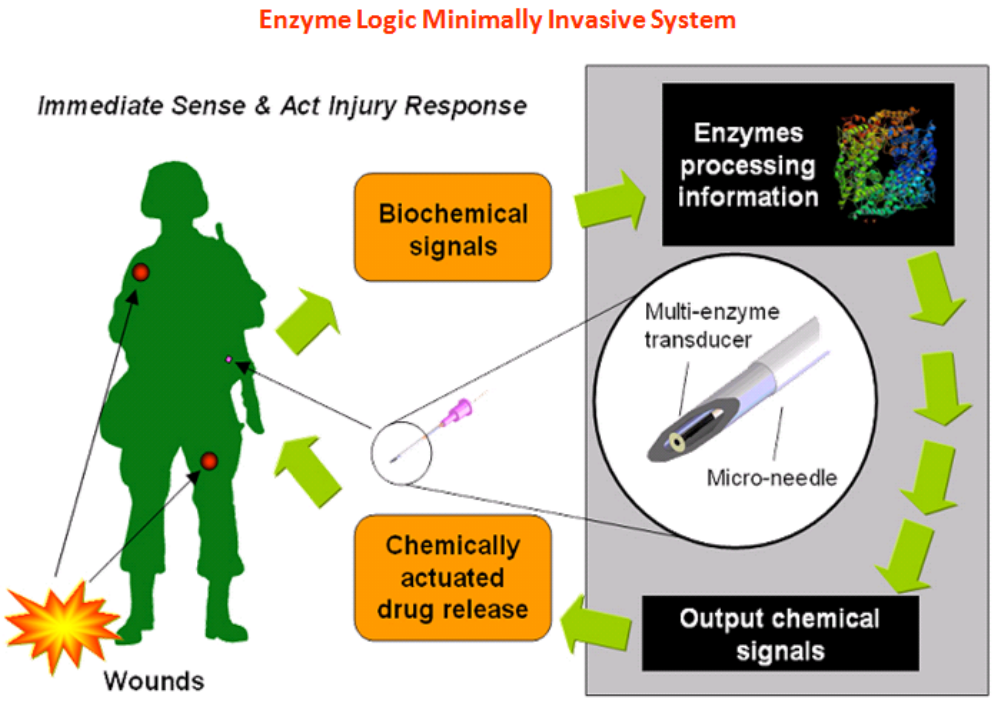

Figure 1.3: *Enzyme logic minimally invasive concept illustrating the components involved in a 'Sense-Act-Treat' system.*

logic-based assessment of complex patterns of biochemical signals (e.g. for biomedical applications) [40, 41, 42, 43]. Extending this concept one step further, such biosensors and actuators can be interconnected in order to form autonomous reactive biomedical devices in connection to a 'Sense-Act-Treat' concept to identify, act upon, and ameliorate a pathological condition or injury that has been detected. Indeed, most biosensors of the current day are capable of analyzing concentrations of only a single analyte (e.g. glucose) [44, 45]. In order to perform simultaneous analysis of several analytes, complex sensor arrays must be employed [46]. Signals generated by such multi-sensor arrays require additional back-end processing in the electronic domain in order to present the results in the final format. Since the data is usually manifested by various concentrations presented in 'analog' form, an expert evaluation should be involved in the decision-making process. Still, separate analysis of multiple analytes could be justified if they represent unrelated chemical parameters. However, in most common applications (particularly in biomedical applications), the measured parameters (analyte concentrations) are related and can be processed in a Boolean logic-based fashion all together. This novel approach to biosensing can, in fact, leverage biocomputing systems [47]. Implemented in the correct manner, these systems can logically process several related analytes ('inputs') by considering their physiological concentrations in the binary format (**0**,**1**) and generate the final output signal (**0**,**1**; **NO**/**YES**) according to a 'programmed' logic routine. In order to be suitable for diagnostic aims, the program should account for the complex relations between the inputs under analysis. As a simple example, if two signals should appear simultaneously and result in an unambiguous conclusion, logic gate **AND** should be implemented for analysis. More sophisticated logic schemes could be designed for multi-signal analysis. This approach could be of particular relevance to biomedical applications where the analysis of a single biomarker would be inconclusive.

Enzyme logic gates have emerged [42, 43, 47] as a promising avenue towards the realization of intelligent biosensing systems that are able to integrate and identify patterns in multiple biomarkers, thereby providing a more comprehensive and accurate assessment of pathophysiological state. As can be inferred from an

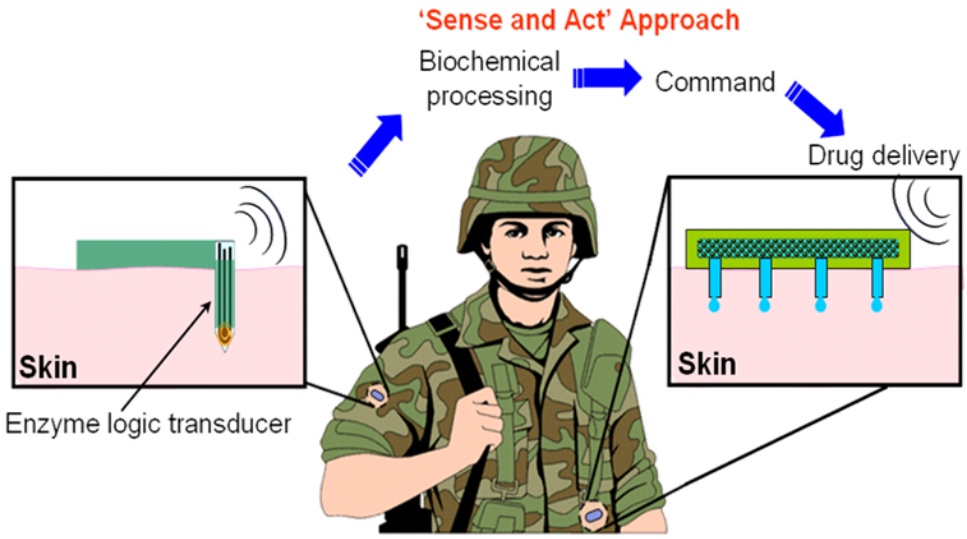

Figure 1.4: *Enzyme logic-based 'Sense-Act-Treat' system illustrating the transducer and drug delivery components.*

inspection of Fig. 1.5, the overlapping specificity of a number of biomarkers can be exploited to increase the reliability of the diagnosis through redundancy. The large dynamic range associated with the transition from physiological to pathological levels of the biomarkers can also be leveraged in order to lead to the construction of enzymatic logic gates with digital-like operation.

This dissertation is structured as an examination of the design methodology and component-level implementation required to construct practical enzyme logic-based biocomputing biosensors and thus varies widely in scope. Beginning from foundational principles – the fundamental properties of mass transport, electrochemistry, and enzymology – the thesis will then direct focus to the simulation of enzyme logic gates leading towards the optimization of the devices prior to their implementation on the laboratory benchtop. From there, emphasis will be placed upon the design and construction of such systems to yield optimal performance and operational figures of merit. Thorough evaluation of the synthesized devices will be the subsequent core thrust of the effort, thereby leading to the systems-level implementation of these gates into utilitarian 'Sense-Act-Treat' autonomous biosensing and drug delivery systems. Inline with the principles of Boolean logic, a decision

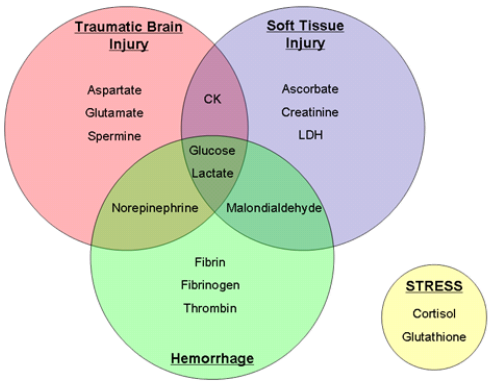

Injury	Biomarkers	Concentration	
		Phys. Level	Injury Level
Traumatic Brain Injury	Aspartate	1.5 µM	10 µM
	Glutamate	2 µM	15 µM
	Spermine	100 nM	500 nM
	Creatine Kinase	100 U/L	400 U/L
	Norepinephrine	2 nM	10 nM
	Lactate	1.6 mM	6 mM
	Glucose	4 mM	8 mM
Soft Tissue Injury	Ascorbate	40 µM	16.4 µM
	Cortisol	370 nM	643 nM
	Creatine Kinase	100 U/L	710 U/L
	Glucose	4 mM	6 mM
	Lactate Dehydrogenase	150 U/L	1000 U/L
	Malondialdehyde	1.1 µM	13.4 µM
Hemorrhage	Thrombin	10 nM	1000 nM
	Fibrinogen	8.8 µM	3.7 µM
Shock	Glucose	4 mM	29 mM
	Lactate	1.6 mM	13.7 mM
	Norepinephrine	2 nM	100 nM

Figure 1.5: *Left: Venn diagram illustrating the overlapping specificity of a collection of biomarkers as implicated by injury / trauma. Right: Table outlining the average levels of selected biomarkers identified in physiological and pathological serum samples.*

threshold will be instituted and the logic gates will be subject to systematic optimization such that their operation can be ascribed to a truth table, leading to high-fidelity unambiguous diagnoses of relevant pathophysiological scenarios. This methodological approach enables the realization of 'intelligent' bioelectronic devices able to respond to immediate physiological changes and provide autonomous corrective action. Unlike conventional biosensors and biosensor arrays, the new biocomputing diagnostic system is able to autonomously correlate the patterns of different clinically-relevant biomarkers according to pre-programmed Boolean logic operations, hence providing more rapid and reliable diagnoses of acute and chronic conditions, thereby substantially reducing device complexity via this novel architectural approach. Indeed, the aim of this dissertation is not to solve complex combinatorial problems via bio-/molecular computation, but rather to identify various biological and environmental scenarios in a plethora of relevant applications.

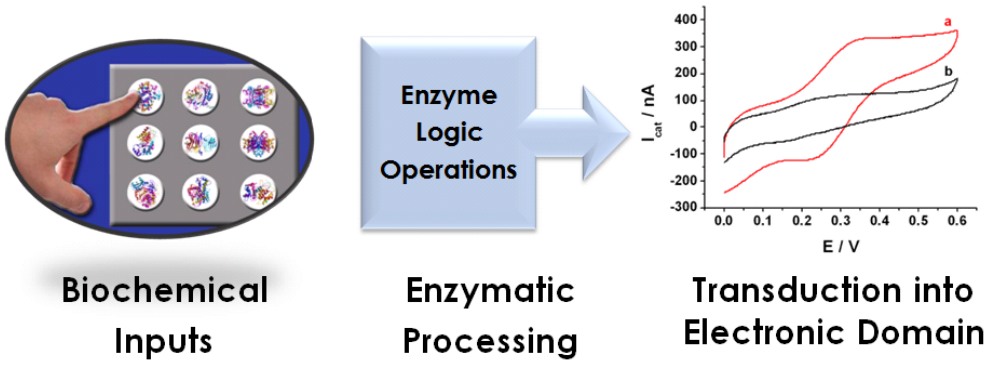

Figure 1.6: *Enzyme logic biosensing concept. Biochemical inputs are processed by the enzyme logic sensing contingent and the resulting chemical signal is transduced to the electrical domain via electrochemical principles for further processing.*

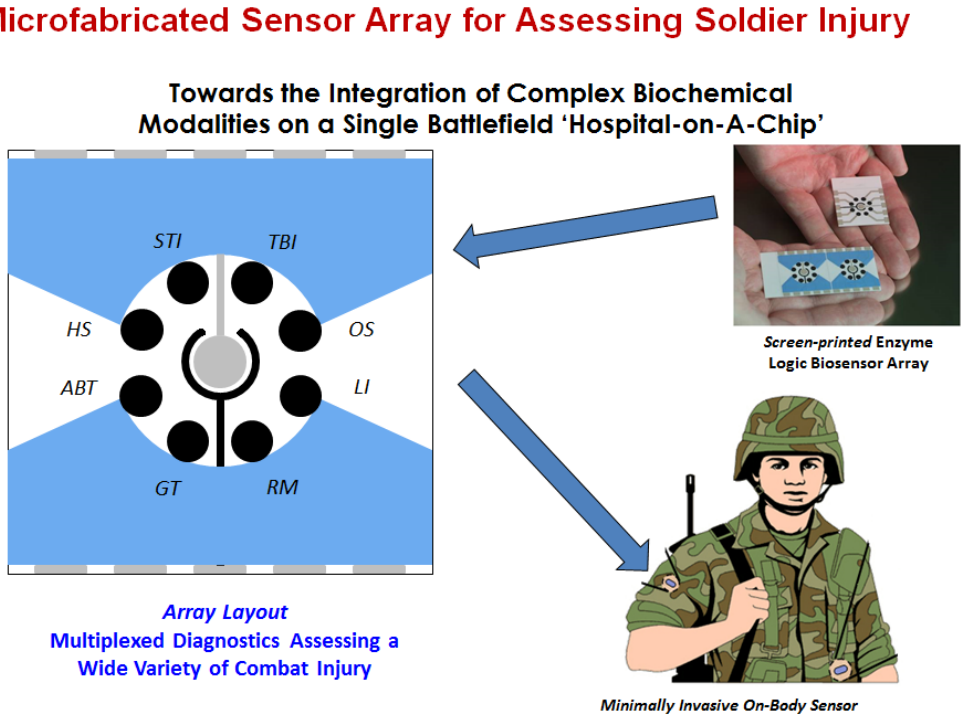

Figure 1.7: *Microfabricated sensor array for injury diagnosis. Each sensor in the array can be functionalized to enable the detection of a unique injury / trauma scenario.*

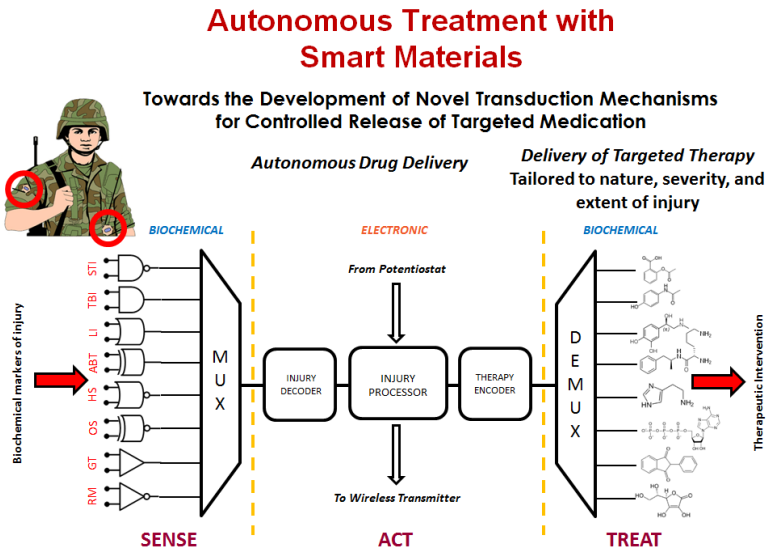

Figure 1.8: *Autonomous treatment of various injury / trauma scenarios under a 'Sense-Act-Treat' approach.*

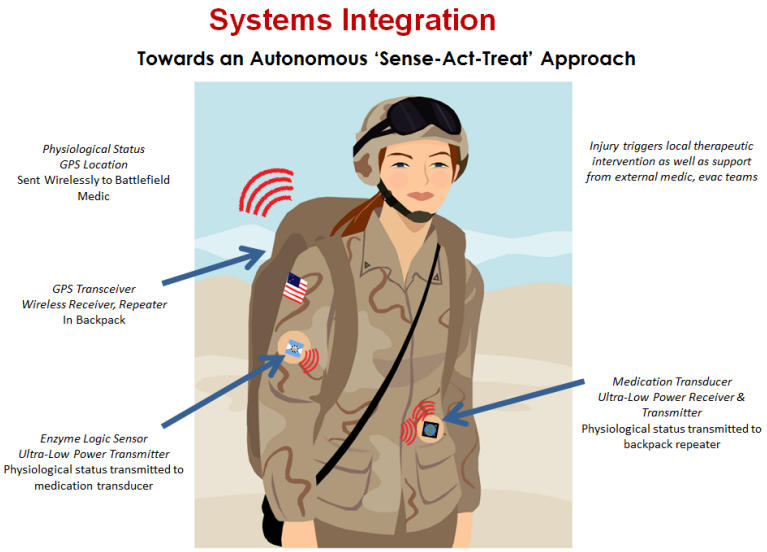

Figure 1.9: *Systems integration of sensing and therapy modalities onto a warfighter.*

Figure 1.10: *Towards rapid assessment and localization of injured soldiers. The wireless infrastructure may be leveraged to enable the real-time monitoring of individual solider health in the battlefield.*

Chapter 2

Fundamentals of mass transport, diffusion, and electrochemistry

After you see this approach, you wonder
why nobody thought of it before.
But thats what the best inventions are.
After you see them, they are obvious.

—Robert G. Gallager,
MIT Professor Emeritus in Communications Theory

The development of an understanding of the manner in which engineered chemical systems behave requires a rigorous excursion into the fundamental physical phenomena underlying mass transport. Indeed, a model must be delineated that integrates the mass transport effects observed in ionic solutions including the flux of ions under the influence of an ionic concentration gradient, electric field, and/or convective perturbation. To the detriment of this aim, such a model would invariably lack analytical solutions under relevant scenarios owing to its complexity. However, the sections that follow attempt to derive analytical expressions for the constituents of mass transport from first principles and we aim to, accordingly, apply the obtained mathematical relations to chemical systems of practical interest, particularly those in which oxidation-reduction reactions are instigated via external stimuli. The insights gleaned from this exercise enable us to make the first steps towards the construction of utilitarian chemical systems that emulate

their Boolean counterparts in the electronic domain.

2.1 Mass transport

Mass transport underlies nearly all phenomena in chemical systems and is accordingly of substantial interest in engineered systems. In order to generate a mathematical model for the movement of a finite mass of generalized substance, we begin by making the simple observation that the flux of a species i in a liquid solution is proportional to the gradient of its electrochemical potential $\bar{\mu}_i$ through the relation

$$j_i\left(\vec{r},t\right) \propto \bigtriangledown \bar{\mu}_i\left(\vec{r},t\right). \tag{2.1}$$

More specifically, we can reformulate the above equation by recognizing that, by the Einstein relation, the constant of proportionality is given by the relation -$C_i(\vec{r},t)D_i(C_i,\vec{r})/RT$ such that we form the *flux equation*

$$j_i\left(\vec{r},t\right) = \frac{-C_i\left(\vec{r},t\right) D_i\left(C_i,\vec{r}\right)}{RT} \bigtriangledown \bar{\mu}_i\left(\vec{r},t\right). \tag{2.2}$$

The species is migrating with velocity $v_i(\vec{r},t)$ such that we may perturb a term to the flux equation

$$j_i\left(\vec{r},t\right) = \frac{-C_i\left(\vec{r},t\right) D_i\left(C_i,\vec{r}\right)}{RT} \bigtriangledown \bar{\mu}_i\left(\vec{r},t\right) + C_i\left(\vec{r},t\right) v_i\left(\vec{r},t\right). \tag{2.3}$$

We recognize that the definition of the electrochemical potential $\bar{\mu}_i$ is given by

$$\bar{\mu}_i\left(\vec{r},t\right) = RT \ln\left\{C_i\left(\vec{r},t\right)\right\} + z_i F \phi\left(\vec{r},t\right) + \mu_i^0. \tag{2.4}$$

Substituting Eq. (2.4) into (2.3) we obtain the *Nernst-Planck equation* describing the simultaneous processes of diffusion, migration, and convection

$$j_i\left(\vec{r},t\right) = \frac{-C_i\left(\vec{r},t\right) D_i\left(C_i,\vec{r}\right)}{RT} \bigtriangledown \left[RT \ln\left\{C_i\left(\vec{r},t\right)\right\} + z_i F \phi\left(\vec{r},t\right)\right] + C_i\left(\vec{r},t\right) v_i\left(\vec{r},t\right), \tag{2.5}$$

$$j_i(\vec{r},t) = -D_i(C_i,\vec{r}) \bigtriangledown C_i(\vec{r},t) - \frac{z_i F}{RT} D_i(C_i,\vec{r})\, C_i(\vec{r},t) \bigtriangledown \phi(\vec{r},t) + C_i(\vec{r},t)\, v_i(\vec{r},t). \tag{2.6}$$

2.2 Diffusion

We proceed with a lemma to convert Eq. (2.6) to a more convenient form. We consider that the flux $j_i(\vec{r},t)$ of a chemical species i from within an arbitrary volume must equate to the rate of decrease of that species over time contained in that volume. This statement may be expressed mathematically as

$$\oint_S j_i(\vec{r},t)\, dS = -\frac{\partial \gamma(t)}{\partial t}, \tag{2.7}$$

where $\gamma(t)$ reflects the total amount of species i within the volume under consideration. We know that this term can be expressed by integrating the concentration of species $C_i(\vec{r},t)$ within the volume element

$$\gamma(t) = \oint_V C_i(\vec{r},t)\, dV. \tag{2.8}$$

Invoking Gauss' Theorem,

$$\oint_S j_i(\vec{r},t)\, dS = \oint_V \bigtriangledown \cdot j_i(\vec{r},t)\, dV \tag{2.9}$$

and combining Eqs. (2.7), (2.8), and (2.10) we obtain

$$\oint_V j_i(\vec{r},t)\, dV = -\frac{\partial}{\partial t} \oint_V C_i(\vec{r},t)\, dV = \oint_V \left[-\frac{\partial}{\partial t} C_i(\vec{r},t) \right] dV. \tag{2.10}$$

For an infinitesimally small volume element we have,

$$\bigtriangledown \cdot j_i(\vec{r},t) = -\frac{\partial C_i(\vec{r},t)}{\partial t}, \tag{2.11}$$

which can be rearranged to form the basic expression for the *Continuity equation*

$$\frac{\partial C_i\left(\vec{r},t\right)}{\partial t}+\bigtriangledown\cdot j_i\left(\vec{r},t\right)=0. \tag{2.12}$$

We can synthesize Eq. (2.6) from (2.12),

$$\frac{\partial C_i\left(\vec{r},t\right)}{\partial t}= \bigtriangledown\cdot\left[D_i\left(C_i,\vec{r}\right)\bigtriangledown C_i\left(\vec{r},t\right)+\frac{z_iF}{RT}D_i\left(C_i,\vec{r}\right)C_i\left(\vec{r},t\right)\bigtriangledown\phi\left(\vec{r},t\right)-C_i\left(\vec{r},t\right)v_i\left(\vec{r},t\right)\right]. \tag{2.13}$$

Assuming that $D_i(C_i,\vec{r})$ and $v_i(\vec{r},t)$ are constant in both space and time, we can recast Eq. (2.8):

$$\frac{\partial C_i\left(\vec{r},t\right)}{\partial t}=D_i\bigtriangledown^2C_i\left(\vec{r},t\right)+\left[\frac{z_iF}{RT}D_i\bigtriangledown^2\phi\left(\vec{r},t\right)-v_i\right]\bigtriangledown\cdot C_i\left(\vec{r},t\right). \tag{2.14}$$

If we further assume that the solution is quiescent, $v_i\rightarrow 0$ and

$$\frac{\partial C_i\left(\vec{r},t\right)}{\partial t}=D_i\bigtriangledown^2C_i\left(\vec{r},t\right)+\left[\frac{z_iF}{RT}D_i\bigtriangledown^2\phi\left(\vec{r},t\right)\right]\bigtriangledown\cdot C_i\left(\vec{r},t\right). \tag{2.15}$$

The addition of non-electroactive ions / supporting electrolyte will eliminate the contribution of migration to the mass transfer of the electroactive species such that *Laplace's equation* may be applied,

$$\bigtriangledown^2\phi\left(\vec{r},t\right)=0, \tag{2.16}$$

and therefore Eq. (2.10) becomes the *Diffusion equation*,

$$\frac{\partial C_i\left(\vec{r},t\right)}{\partial t}=D_i\bigtriangledown^2C_i\left(\vec{r},t\right), \tag{2.17}$$

which is the general formulation of *Fick's second law* for any geometry.[1]

We can arrange Eq. (2.17) for convenience

[1]The determination of the precise diffusion coefficient for the analyte of interest is essential for accurate solutions to Fick's second law. For a description on the manner in which these diffusion coefficients are predicted, the reader is referred to Appendix A.

$$\left(\frac{\partial}{\partial t} - D_i \bigtriangledown^2\right) C_i\left(\vec{r}, t\right) = 0, \tag{2.18}$$

or, in more compact form,

$$\pounds\left\{C_i\right\} = 0, \tag{2.19}$$

where

$$\pounds = \left(\frac{\partial}{\partial t} - D_i \bigtriangledown^2\right). \tag{2.20}$$

We recognize that Ficks second law describes a second-order, linear partial differential equation that is both separable and possesses constant coefficients. Accordingly, the principle of superposition applies implying that if,

$$\pounds\left\{C_{i,k}\right\} = 0 \tag{2.21}$$

for a particular solution $C_{i,k}$, then we can infer that

$$\pounds\left\{\sum_k A_{i,k} C_{i,k}\right\} \tag{2.22}$$

for an arbitrary set of independent coefficients $A_{i,k}$.

Since the diffusion equation is separable, we can begin by decomposing $C_{i,k}(\vec{r},t)$ into two decoupled components:

$$C_{i,k}\left(\vec{r}, t\right) = \widetilde{A}_i\left(\vec{k}, t\right) C_i\left(\vec{r}\right). \tag{2.23}$$

If we further assume that the spatial components of $C_i(\vec{r})$ possess solutions of the space-harmonic form

$$C_i\left(\vec{r}\right) = e^{-j\vec{k}\cdot\vec{r}}, \tag{2.24}$$

then we can superpose the solutions $C_{i,k}(\vec{r},t)$ across all spatial frequencies k such that we can construct the canonical concentration $C_i(\vec{r},t)$ profile through the following *Fourier transform* relations:

$$C_i\left(\vec{r},t\right)=\int_{-\infty}^{+\infty}C_{i,k}\left(\vec{r},t\right)d\vec{k}=\int_{-\infty}^{+\infty}\widetilde{A}_i\left(\vec{k},t\right)e^{-j\vec{k}\cdot\vec{r}}d\vec{k} \tag{2.25}$$

$$\widetilde{A}_i\left(\vec{k},t\right)=\frac{1}{(2\pi)^n}\int_{-\infty}^{+\infty}A_{i,r}\left(\vec{k},t\right)d\vec{r}=\frac{1}{(2\pi)^n}\int_{-\infty}^{+\infty}C_i\left(\vec{r},t\right)e^{j\vec{k}\cdot\vec{r}}d\vec{r} \tag{2.26}$$

where n refers to the number of dimensions that are being transformed. Recalling Eq. (2.18), we can begin by performing the temporal derivative of the particular solution $C_{i,k}(\vec{r},t)$,

$$\frac{\partial}{\partial t}C_{i,k}\left(\vec{r},t\right)=e^{-j\vec{k}\cdot\vec{r}}\frac{\partial}{\partial t}\widetilde{A}_i\left(\vec{k},t\right). \tag{2.27}$$

Performing the laplacian,

$$\bigtriangledown^2C_{i,k}\left(\vec{r},t\right)=-|\vec{k}|^2e^{-j\vec{k}\cdot\vec{r}}\widetilde{A}_i\left(\vec{k},t\right), \tag{2.28}$$

we thus obtain

$$\pounds\left\{C_{i,k}\left(\vec{r},t\right)\right\}=e^{-j\vec{k}\cdot\vec{r}}\frac{\partial}{\partial t}\widetilde{A}_i\left(\vec{k},t\right)+D_i|\vec{k}|^2e^{-j\vec{k}\cdot\vec{r}}\widetilde{A}_i\left(\vec{k},t\right)=0, \tag{2.29}$$

or simplifying,

$$\left(\frac{\partial}{\partial t}+D_i|\vec{k}|^2\right)\widetilde{A}_i\left(\vec{k},t\right)=0, \tag{2.30}$$

which is a first-order, linear partial differential equation with constant coefficients that can be solved in a straightforward fashion to yield

$$\widetilde{A}_i\left(\vec{k},t\right)=\widetilde{A}_i\left(\vec{k},0\right)e^{-D_i|\vec{k}|^2t}, \tag{2.31}$$

and the complete concentration profile can be analytically determined from the Fourier transform relation

$$C_i\left(\vec{r},t\right)=\int_{-\infty}^{+\infty}\widetilde{A}_i\left(\vec{k},0\right)e^{-D_i|\vec{k}|^2t}e^{-j\vec{k}\cdot\vec{r}}d\vec{k}. \tag{2.32}$$

Given that the analyte of concentration C_0 was added at a point-source $\vec{r}_0$ at $t=0$ we can formulate the impulse initial condition:

$$C_i\left(\vec{r},0\right)=C_i^0\delta\left(\vec{r}-\vec{r}_0\right). \tag{2.33}$$

We can determine the value of $\widetilde{A}_i(\vec{k},0)$ by performing the inverse Fourier transform with the initial condition above

$$\begin{aligned}\widetilde{A}_i\left(\vec{k},0\right)&=\frac{1}{(2\pi)^n}\int_{-\infty}^{+\infty}C_i\left(\vec{r},0\right)e^{j\vec{k}\cdot\vec{r}}d\vec{r}\\&=\frac{C_i^0}{(2\pi)^n}\int_{-\infty}^{+\infty}\delta\left(\vec{r}-\vec{r}_0\right)e^{j\vec{k}\cdot\vec{r}}d\vec{r}=\frac{C_i^0}{(2\pi)^n}e^{j\vec{k}\cdot\vec{r}_0}.\end{aligned} \tag{2.34}$$

Thus, we are left with the complete concentration profile,

$$C_i\left(\vec{r},t\right)=\frac{C_i^0}{(2\pi)^n}\int_{-\infty}^{+\infty}e^{-D_i|\vec{k}|^2t}e^{-j\vec{k}\cdot(\vec{r}-\vec{r}_0)}d\vec{k}. \tag{2.35}$$

In order to evaluate this integral, we can invoke Green's function and express the n-dimensional vector $\vec{k}$ in terms of its components:

$$C_i\left(\vec{r},t\right)=\frac{C_i^0}{(2\pi)^n}\int_{-\infty}^{+\infty}e^{-D_i\sum_{m=1}^{n}|k_m|^2t}e^{-j\sum_{m=1}^{n}k_m(\vec{r}_m-\vec{r}_{m,0})}\prod_{m=1}^{n}dk_m, \tag{2.36}$$

$$C_i\left(\vec{r},t\right)=C_i^0\left[\left(\frac{1}{2\pi}\right)\int_{-\infty}^{+\infty}e^{-D_ik^2t}e^{-jk(r-r_0)}dk\right]^n. \tag{2.37}$$

Performing this integral yields the n-dimensional fundamental solution of Ficks second law for the impulse initial condition,

$$C_i\left(\vec{r},t\right)=C_i^0\frac{e^{\frac{-|\vec{r}-\vec{r_0}|^2}{4D_it}}}{(4\pi D_it)^{\frac{n}{2}}}. \tag{2.38}$$

2.3 Electrochemical principles

Provided that this thesis is concerned with the electrical transduction of chemical concentration gradients *via* oxidation-reduction reactions in the presence of applied external stimuli, the mathematical insight gained above may be adapted to the special case of a hypothetical electrochemical system leading towards the

development of a time-dependent concentration profile and time-dependent current response in the presence of an applied voltage step, which is of noteworthy interest when amperometry is performed.

The fundamental couple for a reversible electrochemical oxidation-reduction reaction is given by the stoichiometric relation:

$$C_i^O O + ne^- \rightleftharpoons C_i^R R, \tag{2.39}$$

where C_i^O and C_i^R represent the initial concentrations of the oxidized (O) and reduced (R) chemical species, respectively, and n represents the stoichiometric number of electrons (e^-) that mitigate the reaction.

Basic thermodynamics indicates that the *Gibbs free energy* of the oxidation-reduction reaction is given by,

$$\Delta G = \Delta G^0 + RTln\left(\frac{C_i^R}{C_i^O}\right). \tag{2.40}$$

By definition, since ΔG=-$z_i F\phi$ and ΔG^0=-$z_i F\phi^0$ we can formulate the *Nernst equation*,

$$\phi = \phi^0 - \frac{RT}{z_i F} ln\left(\frac{C_i^R}{C_i^O}\right) \tag{2.41}$$

or,

$$\Delta\phi = \phi - \phi^0 = \frac{RT}{z_i F} ln\left(\frac{C_i^R}{C_i^O}\right). \tag{2.42}$$

This relation can be further generalized to model the time-dependent concentration of the electroactive chemical species at the surface of the electrode $(C_i^s(t))$ versus the initial bulk concentration $(C_i^{b,0})$:

$$\Delta\phi = \frac{RT}{z_i F} ln\left(\frac{C_i^s(t)}{C_i^{b,0}}\right). \tag{2.43}$$

Now assume that we apply a potential step at $t = 0$ such that

$$\Delta\phi u(t) = 0,\ t < 0, \tag{2.44}$$

$$\Delta\phi u\left(t\right)=\Delta\phi,\ t>0, \tag{2.45}$$

where *u(t)* is the unit step function. Thus Eq. (2.43) can be reformulated to

$$C_i^s\left(t\right)=C_i^{b,0}e^{\frac{z_iF}{RT}\Delta\phi u(t)}. \tag{2.46}$$

We can perturb this time-dependent concentration profile to Eq. (2.38),

$$C_i\left(\vec{r},t\right)=C_i^{b,0}\frac{e^{\frac{z_iF}{RT}\Delta\phi-\frac{|\vec{r}-\vec{r_0}|^2}{4D_it}}}{\left(4\pi D_it\right)^{\frac{n}{2}}}, \tag{2.47}$$

which is the complete formulation (valid for $t>0$) for the time-dependent concentration profile integrating both the diffusive and drift components of mass transport.

Directing focus at now developing an analytical relation for the temporal profile of the redox current, we begin by representing the charge q of species i in terms of the number of moles N of the chemical species as formalized by Faraday,

$$q_i\left(\vec{r},t\right)=z_iFN_i\left(\vec{r},t\right). \tag{2.48}$$

Since the conversion reaction is typically heterogeneous, we can normalize the rate of conversion to a more convenient form:

$$\bar{N}_i\left(\vec{r},t\right)=AN_i\left(\vec{r},t\right), \tag{2.49}$$

where $\bar{N}_i(\vec{r},t)$ represents the number of moles of chemical species i per unit area A. As such,

$$q_i\left(\vec{r},t\right)=z_iFA\bar{N}_i\left(\vec{r},t\right). \tag{2.50}$$

Taking the time derivative of the above equation,

$$\frac{\partial q_i\left(\vec{r},t\right)}{\partial t}=z_iFA\frac{\partial\bar{N}_i\left(\vec{r},t\right)}{\partial t}, \tag{2.51}$$

we recognize that the temporal derivative of the charge on the active chemical species yields the current,

$$i_i\left(\vec{r},t\right)=z_iFA\frac{\partial\bar{N}_i\left(\vec{r},t\right)}{\partial t}. \tag{2.52}$$

We also recognize that, by continuity, the rate of conversion $\frac{\partial\bar{N}_i(\vec{r},t)}{\partial t}$ of the active chemical species i is related to the flux $j_i(\vec{r},t)$ of this species by the relation,

$$\frac{\partial\bar{N}_i\left(\vec{r},t\right)}{\partial t}+j_i\left(\vec{r},t\right)=0, \tag{2.53}$$

such that we can recast Eq. (2.52) in terms of the flux,

$$i_i\left(\vec{r},t\right)=-z_iFAj_i\left(\vec{r},t\right). \tag{2.54}$$

In the absence of migratory and convective effects and assuming that the diffusion coefficient is constant, Eq. (2.6) becomes

$$j_i\left(\vec{r},t\right)=-D_i\bigtriangledown C_i\left(\vec{r},t\right). \tag{2.55}$$

Substituting Eq. (2.55) into (2.54) we obtain

$$i_i\left(\vec{r},t\right)=z_iFAD_i\bigtriangledown C_i\left(\vec{r},t\right). \tag{2.56}$$

As we are interested in the current arising from the oxidation-reduction reaction at the electrode surface (point of origin), we may simplify subsequent computations by setting $\vec{r}=\vec{r}_0=0$ such that Eq. (2.56) can be restated as

$$i_i\left(0,t\right)=z_iFAD_i\bigtriangledown C_i\left(0,t\right). \tag{2.57}$$

Taking the spatial derivative of $C_i(0,t)$ in Eq. (2.47) we obtain,

$$\bigtriangledown C_i\left(0,t\right)=C_i^{b,0}\frac{e^{\frac{z_iF}{RT}\Delta\phi}}{\left(4\pi D_it\right)^{\frac{n}{2}}}, \tag{2.58}$$

and Eq. (2.57) can be represented as:

$$i_i(0,t) = z_i F A D_i C_i^{b,0} \frac{e^{\frac{z_i F}{RT}\Delta\phi}}{(4\pi D_i t)^{\frac{n}{2}}}, \tag{2.59}$$

which represents the generalized current-time profile observed at an electrode under the application of a potential step $\Delta\phi$. In the absence of an applied potential at the electrode, $\Delta\phi = 0$ and Eq. (2.59) can be further reduced,

$$i_i(0,t) = \frac{z_i F A D_i C_i^{b,0}}{(4\pi D_i t)^{\frac{n}{2}}}, \tag{2.60}$$

and further simplifying to one dimension, we obtain

$$i_i(0,t) = \frac{z_i F A \sqrt{D_i} C_i^{b,0}}{2\sqrt{\pi t}}, \tag{2.61}$$

which is known as the generalized, one-dimensional *Cottrell equation*.

Amperometry is merely one example of a host of electroanalytical techniques that may be employed to ascertain the transport properties of an electroactive species at an electrode transducer. Other techniques include cyclic voltammetry,

$$i_i(0,t) = z_i F A C_i^{b,0} (\pi D_i \sigma)^{n/2} \chi(\sigma t), \tag{2.62}$$

where $\sigma = \frac{z_i F v_i}{RT}$ and $\chi(\sigma t)$ represents the normalized current lineshape function characteristic of the redox couple. Similarly, square wave voltammetry is a frequently used technique,

$$i_{i,m}\left(0, t_{p/2}\right) = \frac{z_i F A D_i C_i^{b,0}}{\left(4\pi D_i t_{p/2}\right)^{n/2}} \sum_{j=1}^{m} \frac{Q_{j-1} - Q_j}{\sqrt{m-j+1}} \tag{2.63}$$

where $t_{p/2}$ refers to half the pulse duration, m is the step index, and

$$Q_j = \frac{\left(\frac{D_{i,O}}{D_{i,R}}\right)^{1/2} e^{\frac{z_i F}{RT}(\phi_{j-1} - \phi_0)}}{1 + \left(\frac{D_{i,O}}{D_{i,R}}\right)^{1/2} e^{\frac{z_i F}{RT}(\phi_{j-1} - \phi_0)}}. \tag{2.64}$$

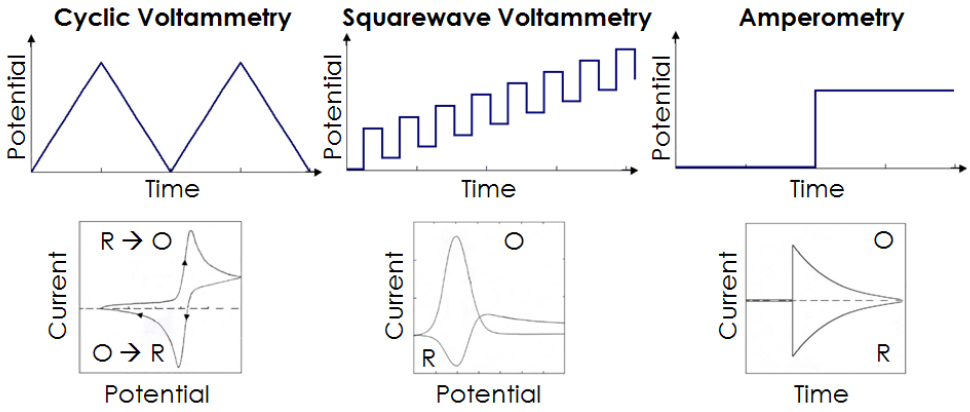

Figure 2.1: *Various controlled-potential electroanalytical techniques that are typically utilized to ascertain the transport properties of an electroactive species at an electrode transducer.*

Chapter 3

Introduction to enzymology and fundamentals of enzyme kinetics

Any piece of knowledge I acquire today has a value at the moment exactly proportional to my skill to deal with it. Tomorrow, when I know more, I recall that piece of knowledge and use it better.

—Mark Van Doren,
Professor of English, Columbia University
and Pulitzer Prize-winning poet

A fundamental understanding of the nature, kinetics, and role of enzymes in the metabolic pathway is imperative as one endeavors to design biocatalytic systems that emulate Boolean logic gates. Indeed, to harness the unique properties of enzymes, the reactions that these biomolecules facilitate must be engineered appropriately in order to achieve efficient biocatalysis marked by substantial dynamic range.

3.1 Role of enzymes in the metabolic pathway

Enzymes are specialized biomolecules possessing intricate (yet highly functional) folded structures that catalyze the interconversion of biochemical entities, making metabolic reactions, and ultimately life, possible [48]. Without known

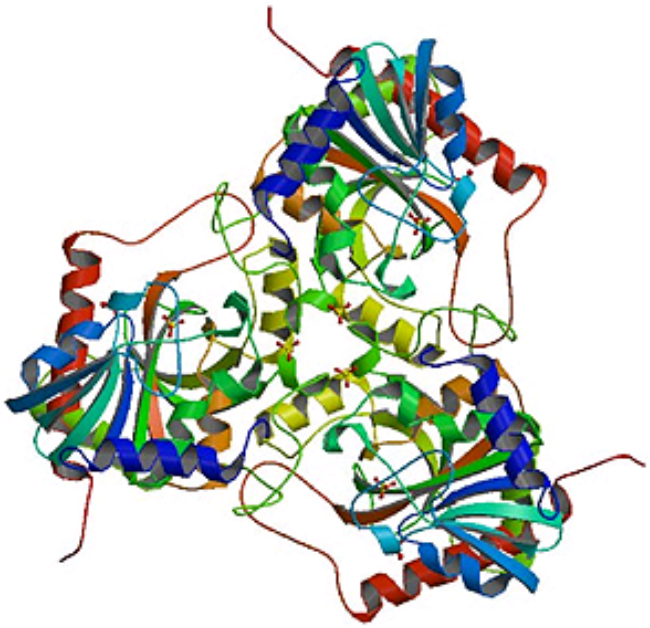

Figure 3.1: *Computer-generated structural model of the Thymidine phosphorylase enzyme (E.C. 2.4.2.4) illustrating the highly sophisticated tertiary structure. Image courtesy of the RCSB Protein Data Bank.*

exception, enzymes are ubiquitously present in every cell of every living organism [49]. A subset of proteins, enzymes are comprised of linear polymer chains of amino acids adjoined by peptide bonds between the carboxyl and amino groups of adjacent amino acid residues. The precise amino acid sequence of enzymes is determined by the nucleotide sequence of a gene within the organism's DNA that codes for the production of these specialized proteins. Twenty different amino acid entities comprise the chemical constituents of enzymes, which are defined by both their unique amino acid sequence *and* unique folded 'tertiary' structure [49].

By definition, enzymes act upon a specific substrate by undergoing a sequence of binding steps accompanied by a final catalytic (and subsequent release) step. It is this ability that often distinguishes enzymes from their protein counterparts [48]. A co-factor or co-substrate is often necessary to complete the biocatalytic reaction. Common co-factors / co-substrates include nicotinamide adenine dinucleotide (NAD^+) and free oxygen, to name a few.

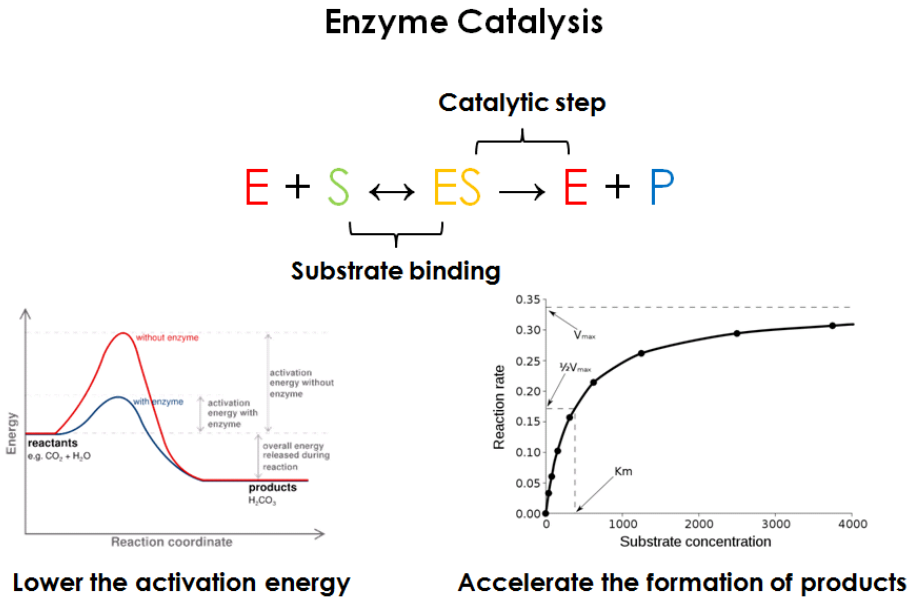

Figure 3.2: *Enzyme-mediated biocatalysis. An enzyme serves to accelerate the formation of a product by lowering the activation energy required for the chemical reaction to ensue.*

The singular role of enzymes in the metabolic pathway is to lower the activation energy E_A required for a biochemical reaction to ensue and, in this manner, enzymes serve to accelerate the formation of products that may be used further along the metabolic chain [48]. The most crucial component of the sophisticated enzymatic structure is the active site – the region where substrate / co-factor binding and catalysis occur – and therefore has been the most widely investigated constituent of these biomolecules in the context of biocatalysis and enzyme folding. Although the catalytic and folding mechanisms remain poorly understood, they are believed to originate from a combination of electrostatic interactions [50] and quantum tunneling [51].

Enzymes are extremely varied in nature and typically range in size from several dozen to several thousand amino acid residues [52, 53]. In spite of this lengthy sequence of amino acid constituents, only about three or four amino acids actually partake in the biocatalytic reaction, on average [54]. This remarkable property is further underscored by the astounding efficiency of enzyme-mediated

biocatalysis, which has been measured to enable as much as a 10^{17}-fold acceleration in the rate of the reaction [55]. Not surprisingly, enzymatic activity is highly influenced not only by the substrate and co-factor concentrations, but also by environmental parameters such as pH, temperature, and ionic strength, to name a few.

3.2 Enzyme types and functionalities

Given the plethora of known enzymes, systematic methods must be developed to attempt to classify (and group) these biomolecules into families for the sake of simplification. The International Union of Biochemistry and Molecular Biology has sought to address this need by assembling all known enzymes into six distinct classes or *families*, which are further stratified into sub-families for further specificity [56]. Each family is classified according to the nature of the chemical reactions that it catalyzes. Moreover, a certain nomenclature for the enzymes that populate each family is followed, with each entity also assigned a unique '*Enzyme Commission*' E.C. number consisting of four numbers. The six basic enzyme families are delineated in Tab. 3.1.

3.3 Use of an enzyme as a redox mechanism / electron interchanger

At a very fundamental level, an oxidoreductase enzyme (i.e. from the 1.X.X.X family) can be viewed as an electron interchanger, transfering an electron from an oxidation reaction to a corresponding reduction reaction via quantum tunneling. In this manner, an enzyme can be viewed as a molecular equivalent of a switch or gate.

The switching properties of enzymes may be leveraged in numerous information processing systems where truly molecular-scale processing is required. In this fashion, the construction of such information processing systems is not limited by the physical limitations of 'top-down' fabrication methodologies. Rather, such

Table 3.1: *The six enzyme families, nomenclature, and nature of the chemical reaction that is catalyzed.*

E.C. No.	Family Name	Nature of Chemical Reaction Catalyzed	Model
1	Oxidoreductases	Catalyze oxidation / reduction reactions	$A^- + B \rightarrow A + B^-$
2	Transferases	Transfer a functional group	A-X + B $\rightarrow$ A + B-X
3	Hydrolases	Catalyze hydrolysis reactions	A-B + $H_2O \rightarrow$ A-OH + B-H
4	Lyases	Cleave chemical bonds	A-B $\rightarrow$ A + B
5	Isomerases	Catalyze isomerization changes	A $\rightarrow$ A'
6	Ligases	Join molecules via covalent bonds	AB + C $\rightarrow$ A-C + B

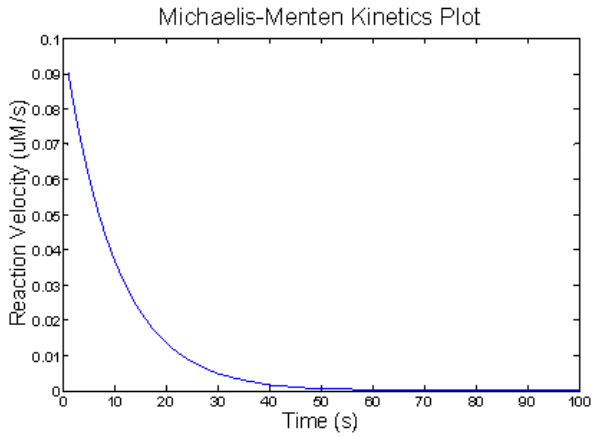

Figure 3.3: *Temporal dependence of the reaction velocity of an enzyme-biocatalyzed reaction.*

devices and systems can be synthesized according to 'bottom-up' realizations from completely organic constituents. Moreover, provided further development in the genetics and bioinformatics arenas, enzymes can be engineered via suitable gene sequencing, splicing, and replication technologies and produced *in situ* in high quantities in order to catalyze desired chemical and biochemical reactions. In effect, enzymes that are designed according to this paradigm can be 'programmed' to achieve the desired information-processing functionality, hence leading to the realization of a 'toolbox' of information processing embodiments at the molecular engineer's disposal.

3.4 Enzyme kinetics

Ever since the kinetic description of enzyme-mediated biocatalysis was formalized 100 years ago by Michaelis and Menten [57], efforts in enzymology have been directed at the development of kinetic models possessing greater accuracy. A noteworthy development in the field arrived over 50 years ago when King and Altman [58] introduced a graphical representation of enzyme behavior under steady-state conditions that made the derivation of the rate equations simple provided the mechanism of biocatalysis was known.

Although the precise mechanism of enzyme biocatalysis has yet to be fully understood, these mathematical formulations provide useful insight into the temporal evolution of biocatalytic processes. Take the case of the most simple enzyme-catalyzed reaction of a single substrate S, which is converted to a product P in two steps in the presence of an enzyme E:

$$E + S \underset{k_{-1}}{\overset{k_1}{\rightleftharpoons}} ES \overset{k_2}{\rightharpoonup} E + P \tag{3.1}$$

where k_n represents the *Rate constant* rate constant characterizing the rate of interconversion of one chemical species to another. We assume time-harmonic concentrations of the form

$$[S] = [S_0]\, e^{-kt}. \tag{3.2}$$

The velocity of the reaction is thus given by

$$v = -\frac{\mathrm{d}\,[S]}{\mathrm{d}t} = \frac{\mathrm{d}\,[P]}{\mathrm{d}t} = k\,[S_0]\, e^{-kt}. \tag{3.3}$$

In the steady-state model we assume that,

$$[E] = [E]_f + [ES]\,, \tag{3.4}$$

$$[S] >> [E] \text{ such that } [S]_f \approx [S]\,, \tag{3.5}$$

$$\frac{\mathrm{d}\,[ES]}{\mathrm{d}t} = 0. \tag{3.6}$$

The velocity at which the product is generated is given by,

$$v = k_2\,[ES] \text{ with } v_{MAX} = k_2\,[E]\,. \tag{3.7}$$

The two rate equations for the formation of the enzyme-substrate complex $[ES]$ may be expressed:

$$\frac{\mathrm{d}\,[ES]}{\mathrm{d}t} = k_1\,[E]_f\,[S]_f\,, \tag{3.8}$$

$$-\frac{\mathrm{d}\left[ES\right]}{\mathrm{d}t} = \left(k_{-1} + k_2\right)\left[ES\right]. \tag{3.9}$$

Under steady state conditions:

$$0 = k_1 \left[E\right]_f \left[S\right]_f, \tag{3.10}$$

$$0 = \left(k_{-1} + k_2\right)\left[ES\right]. \tag{3.11}$$

We are thus left with

$$k_1 \left[E\right]_f \left[S\right]_f = \left(k_{-1} + k_2\right)\left[ES\right]. \tag{3.12}$$

Rearranging,

$$\left[ES\right] = \frac{\left[E\right]_f \left[S\right]_f}{\left(k_{-1} + k_2\right)/k_1}. \tag{3.13}$$

We can formulate K_m as follows:

$$K_m = \left(k_{-1} + k_2\right)/k_1. \tag{3.14}$$

Substituting Eq. (3.14) into (3.13),

$$\left[ES\right] = \frac{\left[E\right]_f \left[S\right]_f}{K_m}. \tag{3.15}$$

Since the depletion of the substrate is insignificant during the steady-state phase $[S] = [S_f]$ and the free enzyme concentration is given by $[E_f]$ = $[E]$ - $[ES]$. With these relations, we can recast Eq. (3.15),

$$\left[ES\right] = \frac{\left(\left[E\right] - \left[ES\right]\right)\left[S\right]}{K_m} \equiv \frac{\left[E\right]\left[S\right]}{\left[S\right] + K_m}. \tag{3.16}$$

We recall that the velocity of the reaction is given by:

$$v = k_2 \left[ES\right] \equiv \frac{k_2 \left[E\right]\left[S\right]}{\left[S\right] + K_m}. \tag{3.17}$$

Recalling that $v_{MAX} = k_2[E]$, we can recast the above relation to obtain

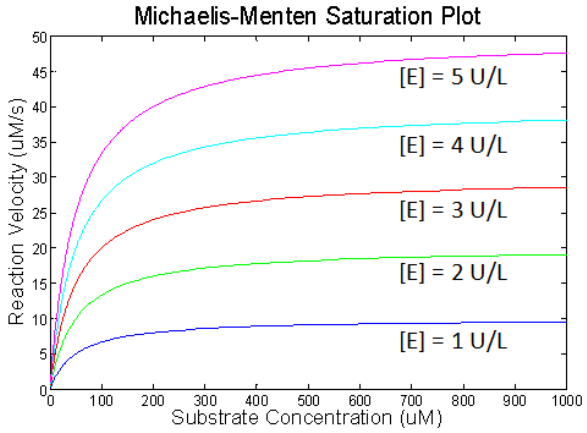

Figure 3.4: *Michaelis-Menten saturation plot for a hypothetical enzyme of varying concentration.*

$$v = \frac{v_{MAX}\,[S]}{[S] + K_m}. \tag{3.18}$$

The saturation plot of a hypothetical enzyme with behavior in accordance with the kinetic description of Eq. (3.18) is provided in Fig. 3.4 for several varying enzyme concentrations.

3.5 Similarities between electronic and biocatalytic systems

Upon a casual inspection of Fig. 3.4, one will notice that an enzyme obeying Michaelis-Menten kinetics possesses a similar transfer characteristic as a metal-oxide-semiconductor field-effect transistor (MOSFET). By controlling the enzyme $[E]$ and substrate $[S]$ concentrations, we can emulate the cut-off, linear, and saturation modes of operation of a MOSFET, the current mainstay of electronic technology. This analog is further corroborated in a comparison between the two switching paradigms, which is provided in Figs. 3.5 and 3.6. Curiously enough, the similarities can also be extended to other enzymatic entities that can imitate higher-order circuit functionality such as a CMOS inverter (Fig. 3.7), which serves as the foundational component of today's semiconductor industry.

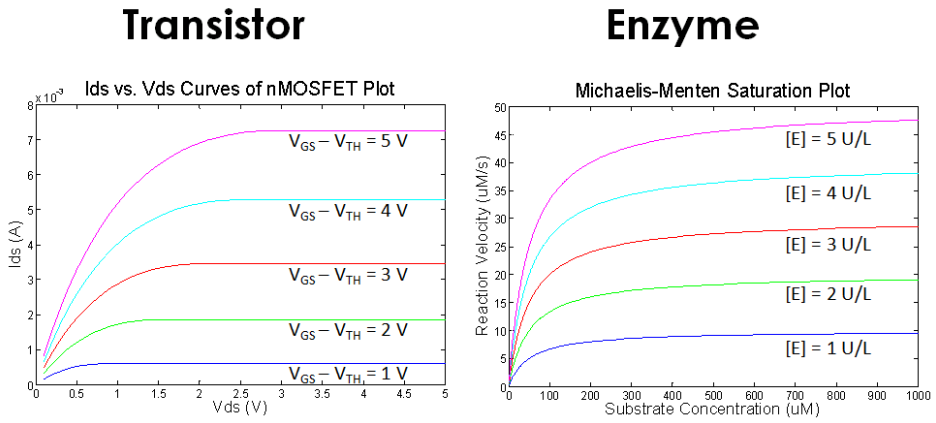

Figure 3.5: *Comparison between the transfer characteristics of a wide-channel silicon nMOSFET and a hypothetical enzyme.*

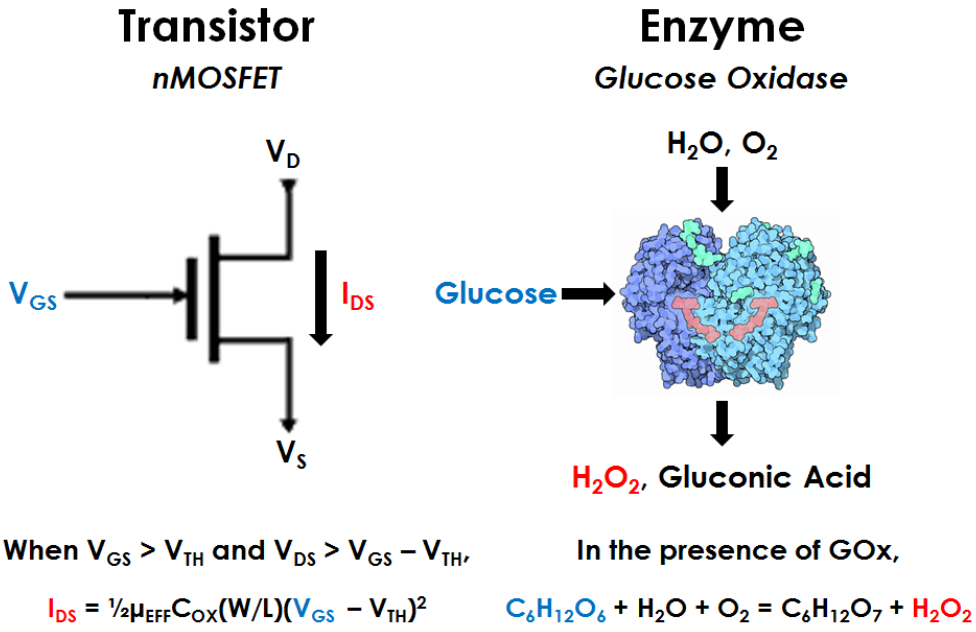

Figure 3.6: *Comparison between the behavior of an nMOSFET and glucose oxidase (E.C. 1.1.3.4).*

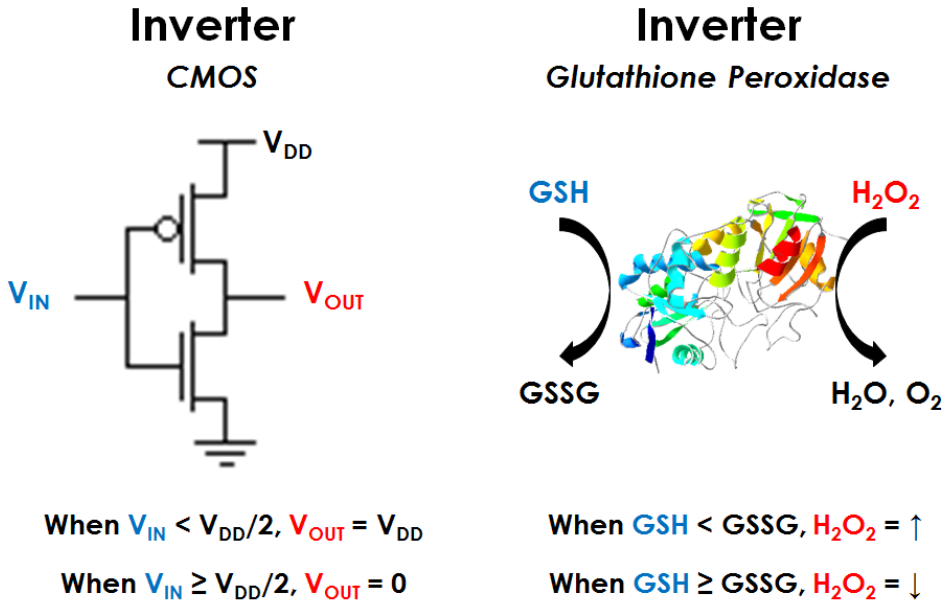

Figure 3.7: *Comparison between the behavior of a CMOS inverter and glutathione peroxidase (E.C. 1.11.1.9).*

3.6 A graph theory approach to enzyme kinetics

Here we propose the use of graph theory in an attempt to further augment the accuracy of the rate equation formulation of enzyme-mediated biocatalysis. This work extends the models established by King and Altman [57] and leverages the ordered substrate/co-substrate binding with the reversibility observed in most enzyme-biocatalyzed reactions considered in this thesis.

We begin by taking the case of a reversible enzyme (E) with ordered binding of the substrate / product (A and B) and co-substrate / co-product (Y and Z), which can be modeled according to the kinetic formulation of Michaelis, Menten, and Henri [57],

$$E + B + Z \underset{k_2}{\overset{k_1}{\rightleftharpoons}} EB + Z \underset{k_4}{\overset{k_3}{\rightleftharpoons}} EBZ \underset{k_6}{\overset{k_5}{\rightleftharpoons}} EAY \underset{k_8}{\overset{k_7}{\rightleftharpoons}} EA + Y \underset{k_10}{\overset{k_9}{\rightleftharpoons}} E + A + Y \tag{3.19}$$

where k_n denotes the kinetic (rate) constant of the conversion between one enzyme complex and another. We can formulate a closed geometric pattern to

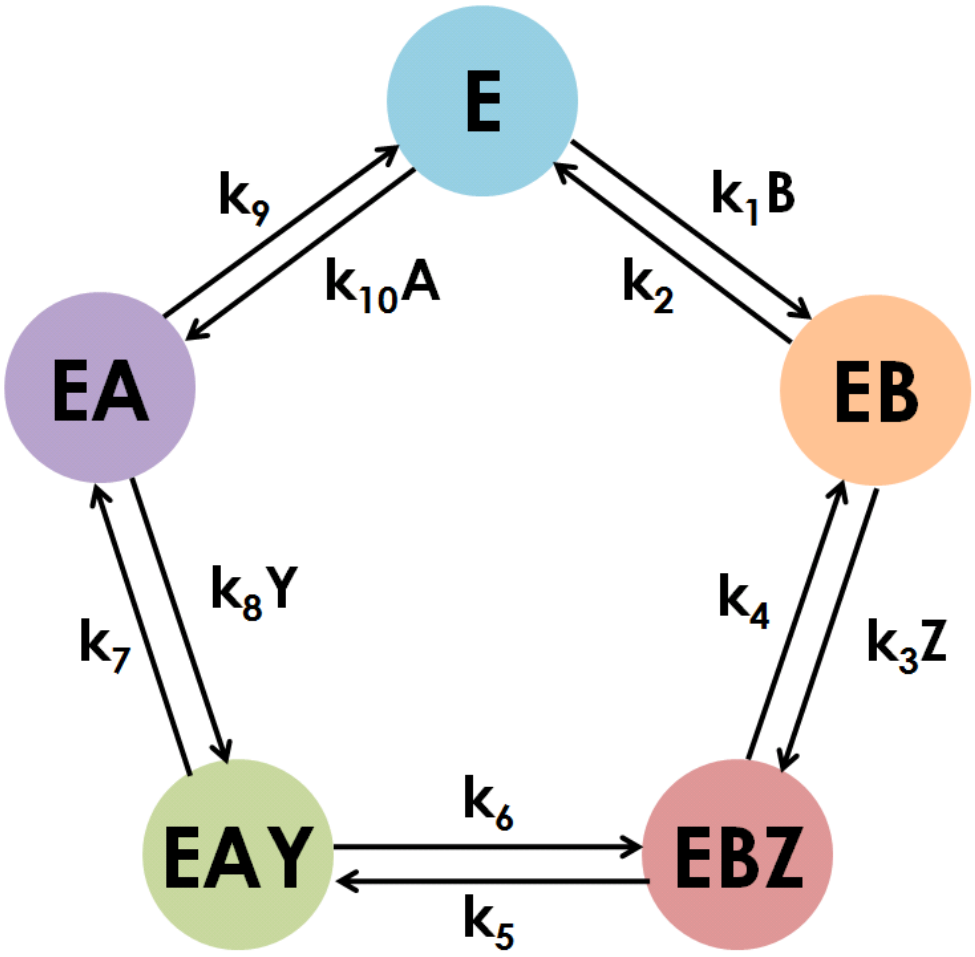

Figure 3.8: *King-Altman diagram describing the steps involved in a reversible, ordered biocatalytic reaction mediated by an enzyme biocatalyst.*

describe this system in connection with the graph theory approach to enzyme kinetics as originated by King and Altman [58], shown in Fig. 3.8.

From an inspection of the above figure, the time-dependent rate equations describing the formation of an enzyme-factor complex EX_i at a particular node in the graph will take the form

$$\frac{\partial\left[EX_i\right]}{\partial t} = -\sum_{i=1,i\neq j}^{n} \kappa_{ij}\left[EX_i\right] + \sum_{j=1,j\neq i}^{n} \kappa_{ji}\left[EX_j\right], \tag{3.20}$$

where $[EX_i]$ and $[EX_j]$ denote the time-dependent concentrations of the enzyme containing species under consideration EX_i and extraneous enzyme con-

taining species EX_j, respectively. κ_{ij} and κ_{ji} represent the kinetic constant of the conversion from EX_i to EX_j and from EX_j to EX_i, respectively.

The coupled non-stead-state (transient) equations with substrate depletion can thus be formulated from the above figure,

$$\frac{\partial [A]}{\partial t} = k_9 [EA] - k_{10} [A] [E] \tag{3.21}$$

$$\frac{\partial [B]}{\partial t} = -k_1 [B] [E] + k_2 [EB] \tag{3.22}$$

$$\frac{\partial [Y]}{\partial t} = k_7 [EAY] - k_8 [Y] [EA] \tag{3.23}$$

$$\frac{\partial [Z]}{\partial t} = -k_3 [Z] [EB] + k_4 [EBZ] \tag{3.24}$$

$$\frac{\partial [E]}{\partial t} = -k_1 [B] [E] + k_2 [EB] + k_9 [EA] - k_{10} [A] [E] \tag{3.25}$$

$$\frac{\partial [EA]}{\partial t} = k_7 [EAY] - k_8 [EA] [Y] - k_9 [EA] + k_{10} [E] [A] \tag{3.26}$$

$$\frac{\partial [EB]}{\partial t} = k_1 [E] [B] - k_2 [EB] - k_3 [EB] [Z] + k_4 [EBZ] \tag{3.27}$$

$$\frac{\partial [EAY]}{\partial t} = k_5 [EBZ] - k_6 [EAY] - k_7 [EAY] + k_8 [EA] [Y] \tag{3.28}$$

$$\frac{\partial [EBZ]}{\partial t} = k_3 [EB] [Z] - k_4 [EBZ] - k_5 [EBZ] + k_6 [EAY] \tag{3.29}$$

or, in matrix form,

$$\begin{bmatrix} \dot{A} \\ \dot{B} \\ \dot{Y} \\ \dot{Z} \\ \dot{E} \\ \dot{EA} \\ \dot{EB} \\ \dot{EAY} \\ \dot{EBZ} \end{bmatrix} = \begin{bmatrix} 0 & 0 & 0 & 0 & 0 & 0 & 0 & 0 & [EA] & -[A]\,[E] \\ -[B]\,[E] & [EB] & 0 & 0 & 0 & 0 & 0 & 0 & 0 & 0 \\ 0 & 0 & 0 & 0 & 0 & 0 & [EAY] & -[Y]\,[EA] & 0 & 0 \\ 0 & 0 & -[Z]\,[EB] & [EBZ] & 0 & 0 & 0 & 0 & 0 & 0 \\ -[B]\,[E] & [EB] & 0 & 0 & 0 & 0 & 0 & 0 & [EA] & [A]\,[E] \\ 0 & 0 & 0 & 0 & 0 & 0 & [EAY] & -[EA]\,[Y] & -[EA] & [E]\,[A] \\ [E]\,[B] & -[EB] & -[EB]\,[Z] & [EBZ] & 0 & 0 & 0 & 0 & 0 & 0 \\ 0 & 0 & 0 & 0 & [EBZ] & -[EAY] & -[EAY] & [EA]\,[Y] & 0 & 0 \\ 0 & 0 & [EB]\,[Z] & -[EBZ] & -[EBZ] & [EAY] & 0 & 0 & 0 & 0 \end{bmatrix} \cdot \begin{bmatrix} k_1 \\ k_2 \\ k_3 \\ k_4 \\ k_5 \\ k_6 \\ k_7 \\ k_8 \\ k_9 \\ k_{10} \end{bmatrix} \tag{3.30}$$

Solving the above set of coupled, first-order linear, inhomogeneous partial differential equations will yield the concentration-time profile of any unique chemical entity or intermediate partaking in the above reaction. In order to formulate a more comprehensive picture of the physical mechanisms that underlie the behavior of enzymatic reactions in the presence of freely diffusing chemical species, we must perturb the natural process of diffusion to our model. Therefore, a more rigorous mathematical description is justified.

Chapter 4

Integrative picture: Heterogeneous enzyme kinetics, mass transport, and diffusion

A goal without a plan is just a wish.

—Antoine de Saint Exupéry,
Writer, Poet, Aviator

Equipped with a detailed understanding of the kinetic properties of an enzyme, the synthesis of a generalized description of the diffusio-kinetic behavior of a biosensor device may be formulated in connection with how such effects manifest an electrochemical redox current arising at a polarized electrode interface. With a set of coupled differential equations formalized, the current-time response of an enzymatic electrochemical biosensor may be predicted prior to lab-bench implementation via a computer-based model, hence dramatically reducing optimization time and effort required on behalf of the experimentalist.

4.1 General formulation of the unified kinetic-diffusion equation

Proceeding to the generalized formulation of the *Unified kinetic-diffusion equation*, we realize that, in abstraction, our approach to deriving a wholistic description of enzymatic behavior can be envisioned as perturbation to the spatiotemporal concentration profile of the analyte under consideration $C_i(\vec{r},t)$:

$$\frac{\partial C_i(\vec{r},t)}{\partial t} = \langle Diffusion \rangle + \langle Kinetics \rangle , \tag{4.1}$$

or, in the formalism introduced earlier,

$$\frac{\partial C_i(\vec{r},t)}{\partial t} = D_i \bigtriangledown^2 C_i(\vec{r},t) - \sum_{i=1,i\neq j}^{n} \kappa_{ij} [EX_i] + \sum_{j=1,j\neq i}^{n} \kappa_{ji} [EX_j] . \tag{4.2}$$

The coupled equations introduced above can now be recast to contain diffusive terms:

$$\frac{\partial [A]}{\partial t} = D_A \bigtriangledown^2 [A] + k_9 [EA] - k_{10} [A][E] \tag{4.3}$$

$$\frac{\partial [B]}{\partial t} = D_B \bigtriangledown^2 [B] - k_1 [B][E] + k_2 [EB] \tag{4.4}$$

$$\frac{\partial [Y]}{\partial t} = D_Y \bigtriangledown^2 [Y] + k_7 [EAY] - k_8 [Y][EA] \tag{4.5}$$

$$\frac{\partial [Z]}{\partial t} = D_Z \bigtriangledown^2 [Z] - k_3 [Z][EB] + k_4 [EBZ] \tag{4.6}$$

$$\frac{\partial [E]}{\partial t} = D_E \bigtriangledown^2 [E] - k_1 [B][E] + k_2 [EB] + k_9 [EA] - k_{10} [A][E] \tag{4.7}$$

$$\frac{\partial [EA]}{\partial t} = D_{EA} \bigtriangledown^2 [EA] + k_7 [EAY] - k_8 [EA][Y] - k_9 [EA] + k_{10} [E][A] \tag{4.8}$$

$$\frac{\partial [EB]}{\partial t} = D_{EB} \bigtriangledown^2 [EB] + k_1 [E][B] - k_2 [EB] - k_3 [EB][Z] + k_4 [EBZ] \tag{4.9}$$

$$\frac{\partial [EAY]}{\partial t} = D_{EAY} \bigtriangledown^2 [EAY] + k_5 [EBZ] - k_6 [EAY] - k_7 [EAY] + k_8 [EA][Y] \tag{4.10}$$

$$\frac{\partial [EBZ]}{\partial t} = D_{EBZ} \bigtriangledown^2 [EBZ] + k_3 [EB][Z] - k_4 [EBZ] - k_5 [EBZ] + k_6 [EAY] . \tag{4.11}$$

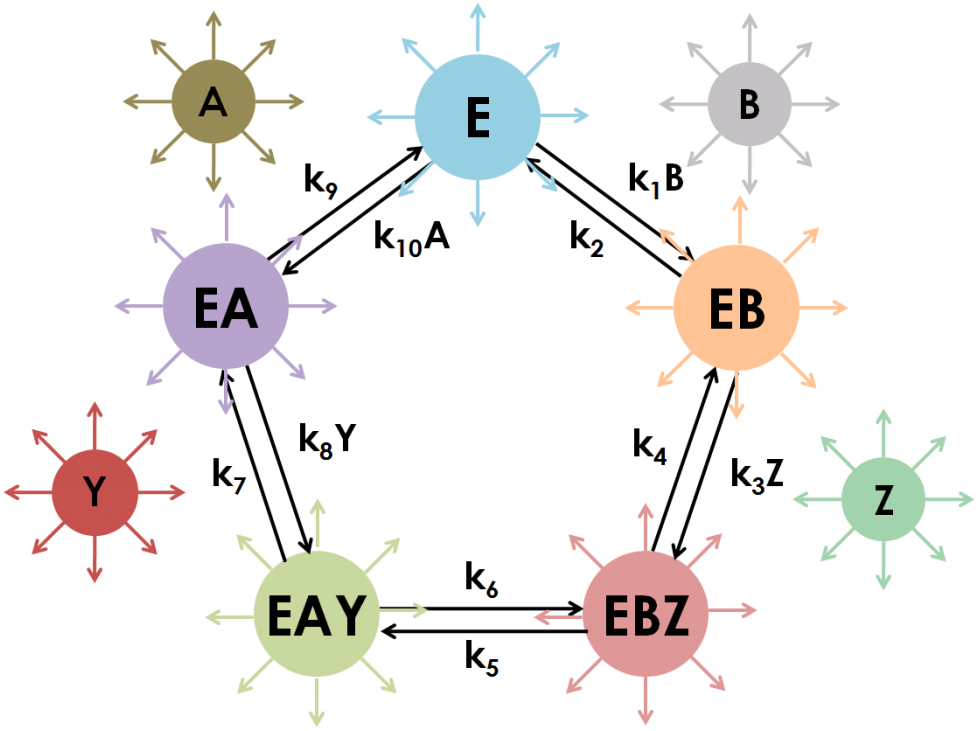

Figure 4.1: *King-Altman diagram incorporating both diffusion and kinetic effects.*

In more compact notation, we can form the generalized solution,

$$\left\{ \frac{\partial C_i\left(\vec{r},t\right)}{\partial t} + \sum_{i=1,i\neq j}^{n} \kappa_{ij} C_i\left(\vec{r},t\right) - \sum_{j=1,j\neq i}^{n} \kappa_{ji} C_i\left(\vec{r},t\right) \right\} \frac{1}{D_i} = \bigtriangledown^2 C_i\left(\vec{r},t\right), \quad (4.12)$$

$$\left\{ \frac{\partial C_i\left(\vec{r},t\right)}{\partial t} - D_i \bigtriangledown^2 C_i\left(\vec{r},t\right) + \sum_{i=1,i\neq j}^{n} \kappa_{ij} C_i\left(\vec{r},t\right) - \sum_{j=1,j\neq i}^{n} \kappa_{ji} C_i\left(\vec{r},t\right) \right\} \frac{1}{D_i} = 0. \quad (4.13)$$

The construction of analytical solutions to the above set of equations is not feasible. Instead of resorting to the derivation of complex solutions to these equations, we will choose to a construct a numerical computer model in order to reduce the relations to simple algebraic expressions that can easily be programmed and evaluated by a computer. This can be accomplished through the method of finite differences.

We must bear in mind, though, that A and B could be electroactive species, which can be oxidized / reduced via the application of a suitable redox potential, and thus they can be regenerated without the aid of enzyme-arbitrated biocatalytic reactions. Accounting for heterogeneous kinetics:

$$A + e^- \underset{k_b}{\overset{k_f}{\rightleftharpoons}} B \quad (4.14)$$

where the forward and backward rate constants k_f and k_b may be expressed as:

$$k_f = k_0 e^{-\alpha\theta} \quad (4.15)$$

$$k_b = k_0 e^{(1-\alpha)\theta} \quad (4.16)$$

with $\theta = \frac{nF\Delta\phi}{RT}$ and $\alpha \approx 0.5$ for perfectly reversible reactions. We can thus formulate the rate equations for both A and B that account for diffusion, homogeneous kinetics, and heterogeneous kinetics:

$$\frac{\partial\left[A\right]}{\partial t} = D_A \bigtriangledown^2 \left[A\right] + k_9\left[EA\right] - k_{10}\left[A\right]\left[E\right] - k_f\left[A\right] + k_b\left[B\right], \quad (4.17)$$

$$\frac{\partial [B]}{\partial t} = D_B \bigtriangledown^2 [B] - k_1 [B][E] + k_2 [EB] - k_b [B] + k_f [A]. \tag{4.18}$$

Practically speaking, both electrochemical kinetics and catalysis proceed at a very rapid pace, so the chemical system is typically limited only by mass transport through diffusion.[1]

4.2 Biosensor simulations

As mentioned earlier, the generation of closed-form analytical solutions to the relations introduced in previous sections represents a formidable, if not impossible, task. Accordingly, we must resort to the development of computer models to solve these relations numerically. Positioned with a model that integrates most physical-level perturbations that are expected to influence an enzyme-biocatalyzed reaction that is transduced in the electrochemical domain, we may assemble software routines that aim at predicting the response of a given biosensor system.

The first step in the construction of a biosensor simulator involves the definition of the precise boundary conditions, as delineated in Fig. 4.2, as well as the environmental parameters such as pH, temperature, and diffusion coefficients, to name a few. These quantities are employed as inputs into the appropriate main modules of the simulator - the diffusion solver, the kinetics solver, the immobilization solver, and the electrochemical solver. Each module attempts to deconstruct the complex cascade of electro-/chemical conversions into individual components that can be described by unique, decoupled relations, hence mitigating the complexity of the plethora of physical phenomena under investigation. This approach entails that the relations in each constituent module are solved and then perturbed to the next module, which is then solved before progressing to any subsequent models. This process may be iterated until all steps are complete and the desired precision has been achieved. The final result of this exercise would reside

[1] A more precise model for enzyme-mediated catalysis would account for the effect of pH, temperature, and ionic strength. For a more detailed description of the unique contributions of these physical parameters, the reader is referred to Appendix B, C, and D.

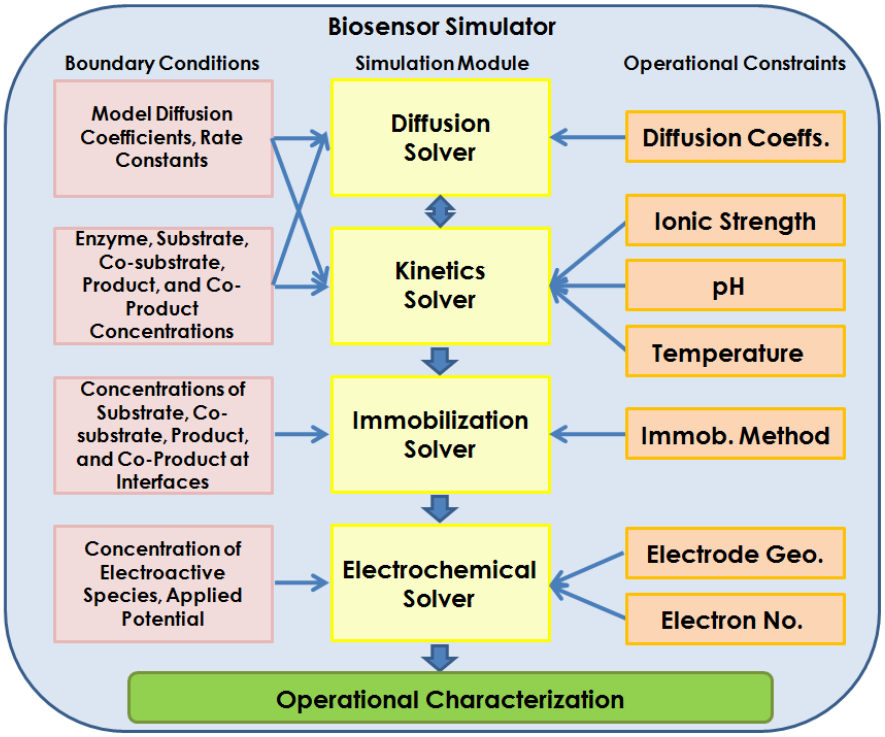

Figure 4.2: *Block-level architecture of the biosensor simulator engine delineating the modules that comprise the model.*

in the generation of a time-current profile that may be optimized *prior to* the implementation of such systems on the lab bench, hence saving the experimentalist a substantial amount of time and effort in their pursuit of optimal biosensor performance.

Chapter 5

Printed electrodes and simple enzyme assays

The most exciting phrase to hear in science,
the one that heralds the most discoveries,
is not "Eureka!" (I found it!)
but "That's funny..."

—Isaac Asimov

The cornerstone of electrochemical sensing resides in the implementation of an electrode transducer exhibiting some enhanced chemical affinity towards the compound(s) that are under transduction. Indeed, the transducer serves as the critical junction between reaction-based information manifested through concentration gradients and a redox current. This principle, in turn, leverages chemical oxidation and reduction reactions occurring at the electrode interface that give rise to an electron flux between oxidized and reduced chemical species. These reactions may either be electrolytic or galvanic in nature (discussed in further detail in the following chapters) and can facilitate the presentation of useful insight into the diffusive, convective, electromigrative, and/or kinetic properties of the system under investigation. Advantageously, much knowledge has been gathered over the past several decades regarding the rational design of the electrode transducer, both chemically and geometrically, in order to enhance its sensing capabilities and versatility.

A highly promising electrode transducer design methodology is introduced in the following sections and is then extended to the detection of simple enzyme biomarkers. The effect of chemo-/physical parameters is illustrated, underscoring the relevance of proper parametric optimization of the enzymatic system.

5.1 Screen printed electrodes

In order to mitigate the limitations encountered with solid-state electrodes, screen printed electrochemical sensors have been leveraged by the glucose monitoring [10], medical diagnostics [59, 60], environmental monitoring [61, 62], and analytical domains [63] for over three decades. Owing to the ease at which these printable sensing devices can be fabricated at an industrial scale, as well as their intrinsically low cost, robustness, and attractive electroanalytical performance [64, 65, 66], screen printed electrodes (SPEs) have proliferated in use. Moreover, the versatility of modern thick-film fabrication techniques enable the realization of different electrode geometries that can be designed to satisfy the requirements of the particular application at hand. Furthermore and more crucially, the inks that are employed in the screen printing process may be modified as necessary in order to impart selective chemical functionality [67] or improved catalytic behavior [68].

The fabrication of ceramic-based SPE sensors is detailed as follows. The fabrication of such sensors can easily be extended to plastic- (i.e. PET, PTFE, Kapton) and textile-based (i.e. cotton, nylon) substrates, as will be considered in further detail in subsequent chapters. Firstly, a design is implemented in AutoCAD® (Autodesk, San Rafael, CA) and the geometry of the electrode contingent is optimized per the unique specifications of the application at hand via numerically solving the mass transfer relations presented in the previous chapter. The design is then outsourced for fabrication on laser-cut stainless steel or chemically-etched polymeric mesh-screen stencils (Metal Etch Services, San Marcos, CA). Contingent upon the complexity of the design, the number of stencils required will vary, however, a three-layer design is the most common and consists of a conductive underlayer, a semi-conductive active layer, and an insulator layer.

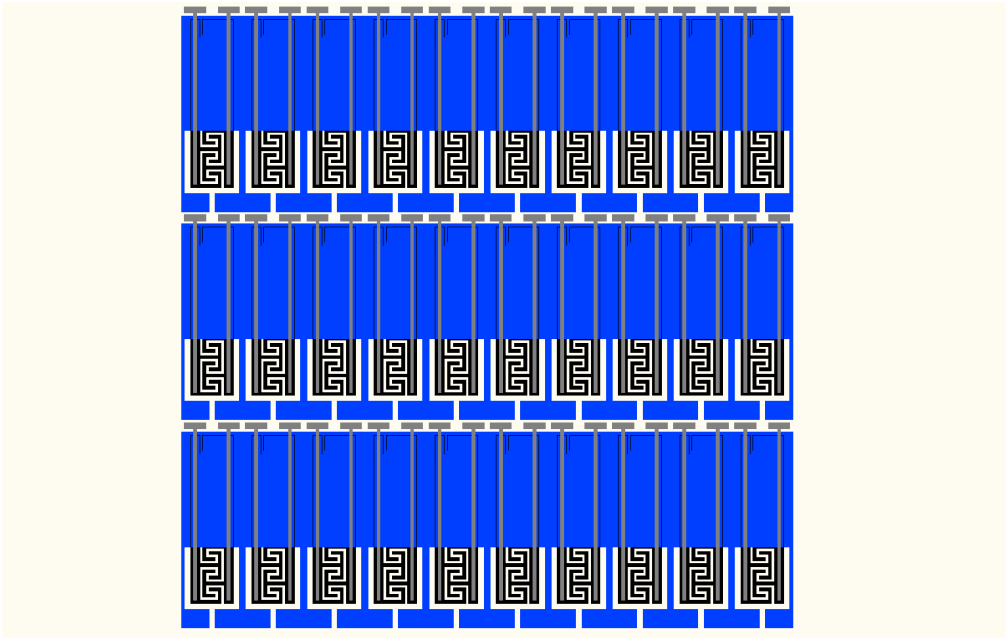

Figure 5.1: *AutoCAD®-rendered array of 30 two-electrode sensors for fabrication on through-hole or mesh-screen stencils. The layers are detailed as follows: grey (bottom conductive layer), black (interstitial active layer), and blue (top insulator layer).*

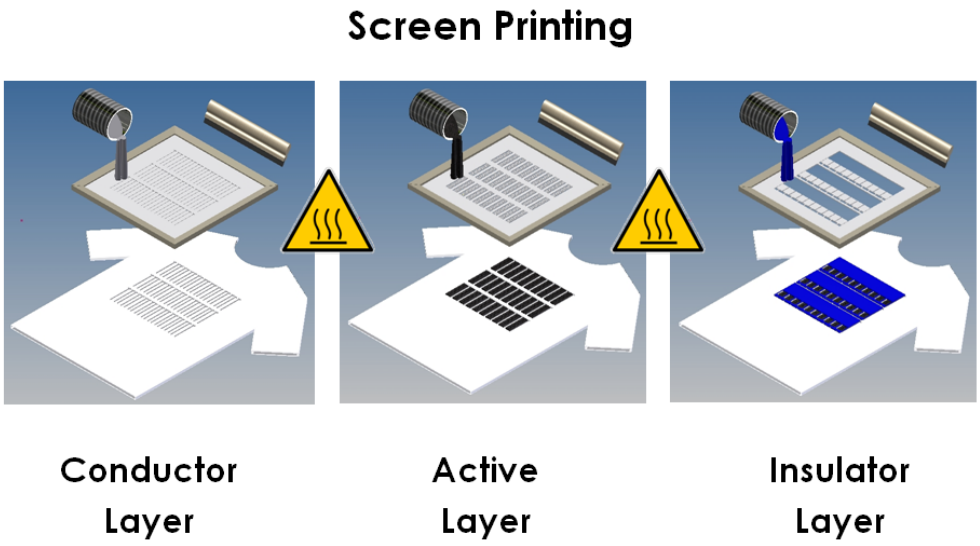

Figure 5.2: *Screen printing protocol detailing the steps and components required to fabricate an array of 3-electrode screen printed electrodes.*

Upon receipt of the framed stencil set, the operator programs a semi-automatic thick-film screen printer (Speedline Technologies MPM SPM, Franklin, MA) in order to adjust the height and stroke of the embedded squeegees to yield optimal pattern transfer quality.

Once the printing parameters are optimized, a laser-scribed alumina substrate (CoorsTek Inc., Golden, CO) is secured on the substrate platform. An Ag/AgCl-based ink is firstly employed to define the conductive underlayer as well as the reference electrode and patterned directly onto the substrate. Next, a carbon- or metal-based ink containing any associated catalytic or biocatalytic functionality is then overlaid on the conductor to define the working and counter electrode geometry. Finally, an insulator ink is overlaid on the Ag/AgCl and carbon layers to insulate all but the contact pads and the upper segment of the electrodes.

Subsequent to each printing routine, the patterned substrate is annealed in a temperature-controlled convection oven (SalvisLab Thermocenter, Rotkreuz, Switzerland) at 120° C for 20 min in order to evaporate the volatile-phase solvent such that the solids content and binder solely constitute the electrode matrix. The substrate is then cleaved into individual test strips for single use and possess over-

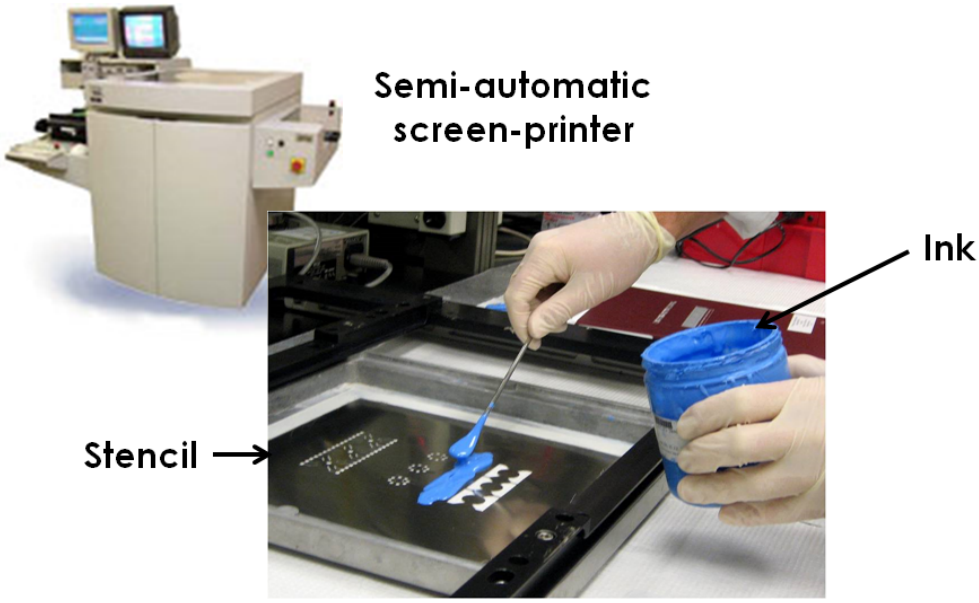

Figure 5.3: *Photographic image of a semi-automatic thick-film screen printer employed for the fabrication of screen printed electrodes. An exemplary stencil pattern (and application of an insulative ink) is shown in the inset.*

all dimensions of (typically) 5 mm × 34 mm, and can accommodate 30 μL sample volumes. Each screen printed three-electrode strip typically consists of a circular carbon working electrode (geometrical area: 3 mm^2) inscribed in a hemispherical counter (area: 10 mm^2) and reference electrode (area: 2 mm^2). Post-annealing electrochemical activation of the active material may be performed via repetitive cyclic voltammograms or extended duration amperometry. Cyclic voltammetry may also be executed in a sulfuric acid solution of moderate strength in order to electrochemically clean the electrode surface and attenuate any impurities that may interfere with measurements. Electrochemical deposition of conducting polymers (i.e. poly(pyrrole), poly(aniline)) or plating of metal catalysts (i.e. palladium, platinum, gold) may also be executed to functionalize / prepare the electrode surface for enhanced detection. Dry reagents, electroactive mediators, and/or permselective membranes may then be dispensed on the surface to achieve pH adjustment, reduce the overpotential required to excite the electroactive analyte of interest, and/or reject potential interfering compounds. Scanning electron microscopy can

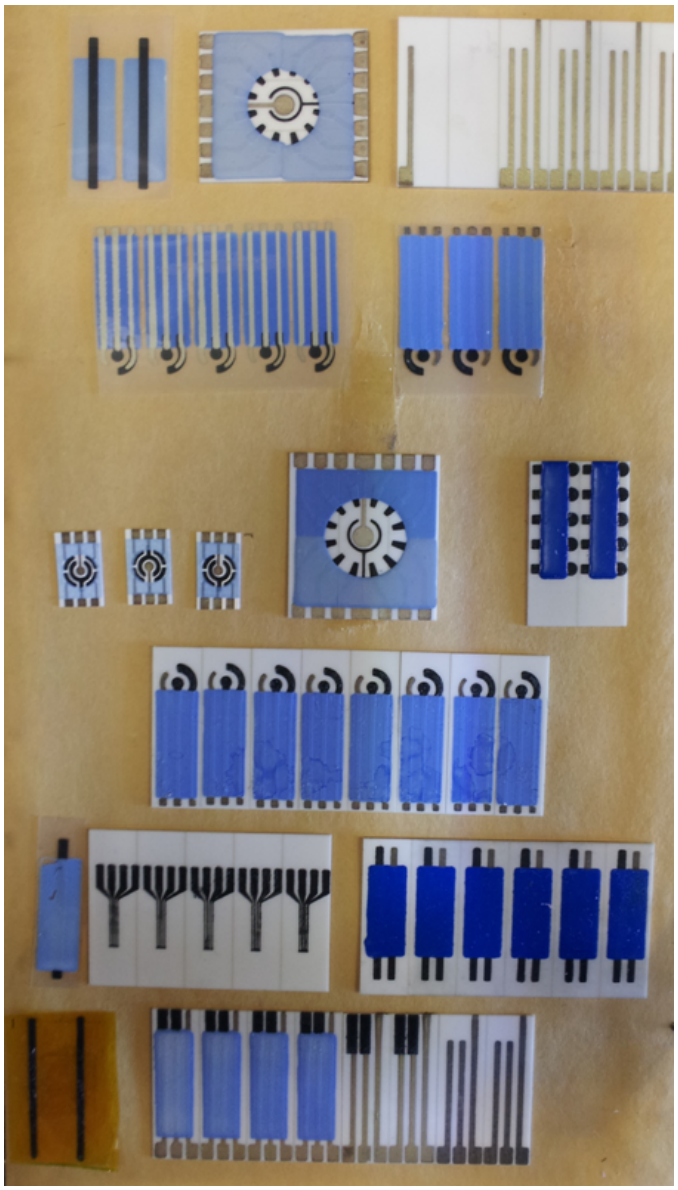

Figure 5.4: *Various design iterations of screen printed electrodes on rigid and flexible substrates.*

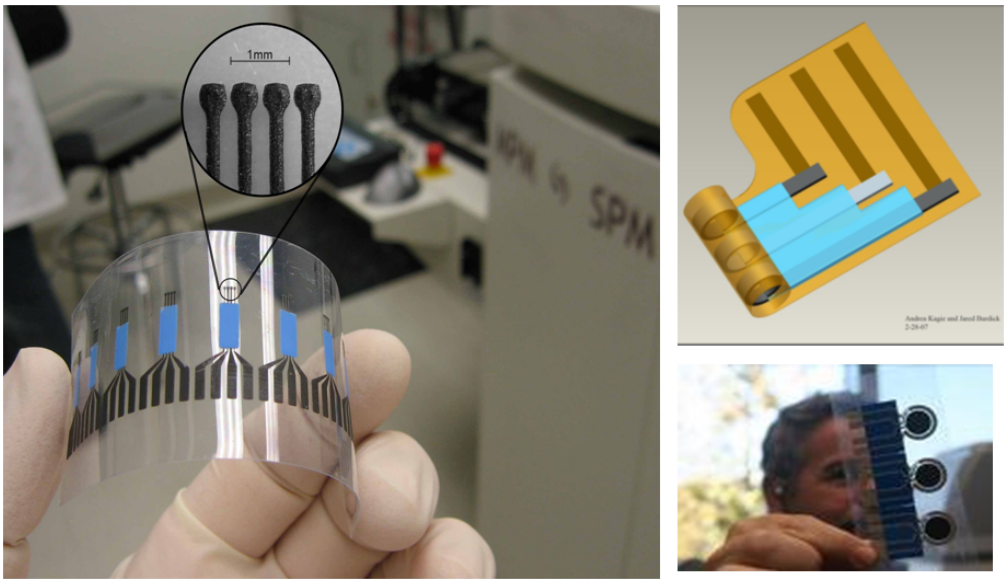

Figure 5.5: *Exemplary screen printed electrodes on flexible substrates for electrochemical biosensing. Left pane: 4-electrode micro-electrode array on PET for dopamine monitoring; top right pane: 3-electrode sensor on Kapton for insertion as a punctal plug into the lacrimal duct; bottom right pane: 3-electrode sensors on PET for epidermal monitoring.*

also be employed to characterize the electrode surface.

5.2 Stamp transfer electrodes for electrochemical sensing on non-planar and oversized surfaces

Despite the attractive merits of screen printed electrodes (SPEs), one noteworthy limitation of the screen printing fabrication methodology resides in its incompatibility with non-planar and oversized substrates. Indeed, screen printing has largely been confined to flat surfaces, which may restrict the potential utility of the method in the electrochemical sensors and biosensors fields. Recognizing this limitation as a fabrication challenge, printing electrochemical sensors on non-planar substrates would require an alternative fabrication strategy that is able to

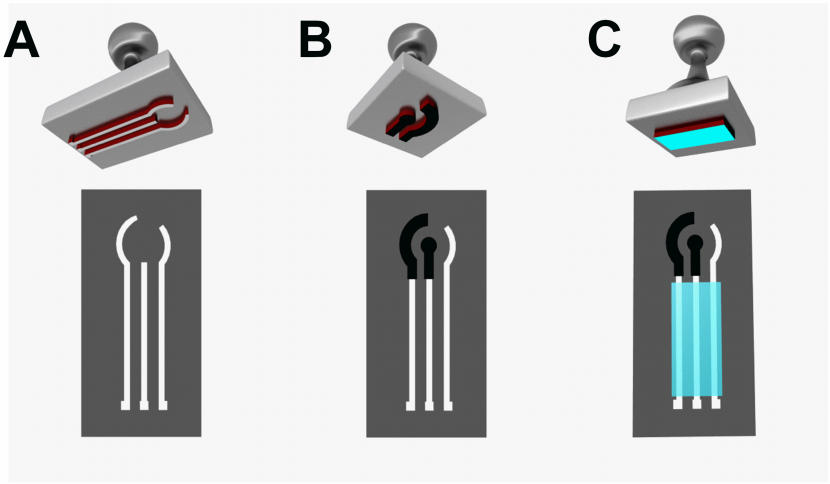

Figure 5.6: *Illustration detailing the steps involved in the stamp-transfer preparation of a common electrode pattern using elastomeric stamps with custom-designed surface reliefs containing the electrode pattern (top): (A) Ag/AgCl conductor layer, (B) carbon active layer, and (C) insulator layer.*

conform with the 'three-dimensional' features and surface irregularities that are characteristic of a wide array of substrate geometries and materials.

The formation of a versatile alternative to SPEs has been developed in order to impart electrochemical sensing abilities on a wide variety of rigid and flexible substrates. This simple, low cost, yet robust methodology is demonstrated to be well-suited for the formation of electrochemical sensors on non-planar substrates and large objects / structures, which have traditionally been off-limits to conventional screen printing techniques. Herein referred to as stamp transfer electrodes (STEs), this alternative to conventional SPEs exhibits similar analytical merits while addressing their limitations. Using a pattern-transfer technique, various conductive and insulating inks are applied to a sequence of elastomeric stamps with custom-designed surface reliefs containing the electrode pattern (Fig. 5.6) and directly applied to the substrate of interest in a fashion analogous to common soft-lithographic nanofabrication techniques [69, 70, 71]. In this manner, a complete layered electrochemical sensor contingent is transferred, hence leading to sensing devices that are highly compatible with irregular substrates (e.g. skin) possess-

ing diverse surface morphologies, without compromising the structural integrity of the pattern. As an illustration of the versatility of the fabrication technique, investigations to follow have demonstrated the ease at which complete electrochemical sensor patterns are transferred onto large structures (i.e. the side of a building), and three dimensional / curvilinear objects, such as balls and leaves, as well as conventional planar substrates, such as alumina. The concept is demonstrated towards the voltammetric detection of physiologically-relevant compounds (dopamine - DA, ascorbic acid - AA, acetaminophen - ACT) as well as compounds which are of substantial interest to the security and forensics community including residues originating from the discharge of ammunition (copper) and the handling of munitions and explosives (TNT). Further extending this unique concept to practical surfaces that are inaccessible with conventional SPEs, STEs are patterned on the skin and employed for the quantification of increasing levels of uric acid. Using this approach, the as-prepared sensors exhibit appealing electrochemical performance approaching that of their screen-printed counterparts. This simple and robust approach can enable the formation of ink-based printable electrodes on non-planar and oversized surfaces that are not compatible with standard screen printing protocols. The migration of printable electrochemical sensors to non-conventional (non-planar and/or oversized) surfaces provides new opportunities within the personal healthcare, fitness, forensics, homeland security and environmental monitoring domains.

An Ag/AgCl conductive ink and a graphite ink were diluted in isophorone in a 80 : 20 and 50 : 50 (ink : solvent w/w%) ratio, respectively, to reduce their intrinsic viscosity. The dielectric insulator ink was employed, but was not diluted. The sensor patterns were initially designed in AutoCAD and converted to bitmap files for fabrication on elastomeric rubber stamps (Simons Stamps, Turners Falls, MA). A separate stamp pattern was created for each layer (carbon, Ag/AgCl, insulator). Stamping pads were saturated with the appropriate inks and used for ink transfer.

In order to implement the STE, a custom-designed elastomeric stamp was firstly applied to a stamping pad saturated with a diluted Ag/AgCl-based ink and

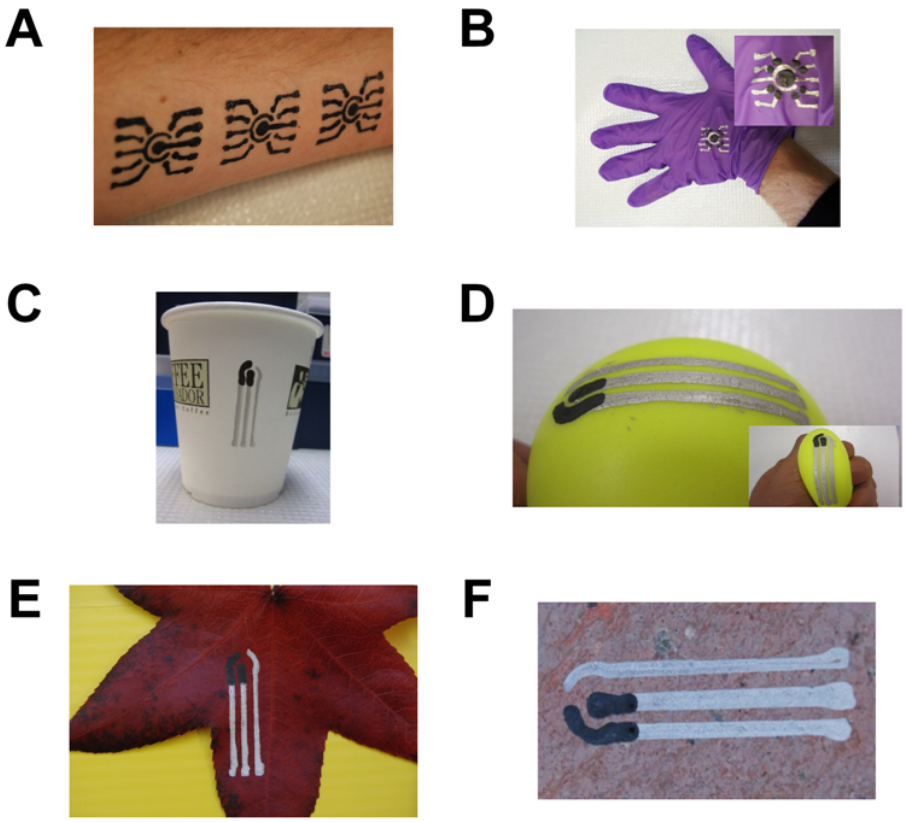

Figure 5.7: *(A) Three eight-electrode carbon ink-based arrays stamped on the epidermis for biosensing operation. (B) Eight-electrode array on a nitrile glove. Inset shows the array under flexion of the glove. (C) Three-electrode contingent on a disposable paper cup. (D) Three-electrode contingent on a Neoprene® stress ball. Inset illustrates the resiliency of the electrochemical sensor upon compression of the stress ball. (E,F) Images of three-electrode contingent on a maple leaf and a granite slab, respectively.*

then gently depressed against the substrate of interest, hence forming a conductive underlayer and reference electrode (illustrated in Fig. 5.6A). The process was subsequently repeated with a separate stamp design and diluted carbon-based ink to form the working and counter electrodes (Fig. 5.6B). Finally, as displayed in Fig. 5.6C, an insulator ink was applied using the same technique to define the active electrode geometry.

In order to interface the STEs with an electrochemical analyzer, a similar protocol to that described in the literature was followed [72, 73]. Namely, the pressure-contact method was implemented, whereby lead wires were applied to the contact pads of the STE via a tape-based adhesive, hence facilitating the interface with the electrochemical analyzer.

Epidermal STEs were realized using a similar procedure, although the ink was not diluted with isophorone in order to maintain suitable viscosity for epidermal transfer. Interface of the sensor with an electrochemical analyzer was realized with an elastic wristband containing screen-printed conductive contacts. In order to remove the sensor, a cotton ball saturated with rubbing alcohol was gently scrubbed over the surface of the electrode contingent. Exposure to the skin-based STE was minimized and proper conformance with the relevant safety protocols was maintained at all times. Although Ag/AgCl has been used in in vivo applications, including implantable biosensors [74, 75] and EEG / EKG adhesive dermal patch electrodes [76], prolonged exposure to the skin is not recommended. Alternatively, pure carbon STEs, as illustrated in Fig. 5.7A, may be employed as substitutes for Ag/AgCl-containing STEs in order to mitigate the wearers exposure to silver chloride.

Initial efforts endeavored at investigating the transfer of the stamped patterns onto a variety of nonconventional non-planar and curvilinear substrates. Fig. 5.7A illustrates three eight-electrode carbon-based arrays stamped on the forearm for monitoring the wearers perspiration and / or surrounding environment. Fig. 5.7B exemplifies the same design (containing a conductive Ag/AgCl underlayer and reference electrode) imprinted on a nitrile glove, with the inset of the figure illustrating the resiliency of the STE sensor under flexion of the hand. Minimal

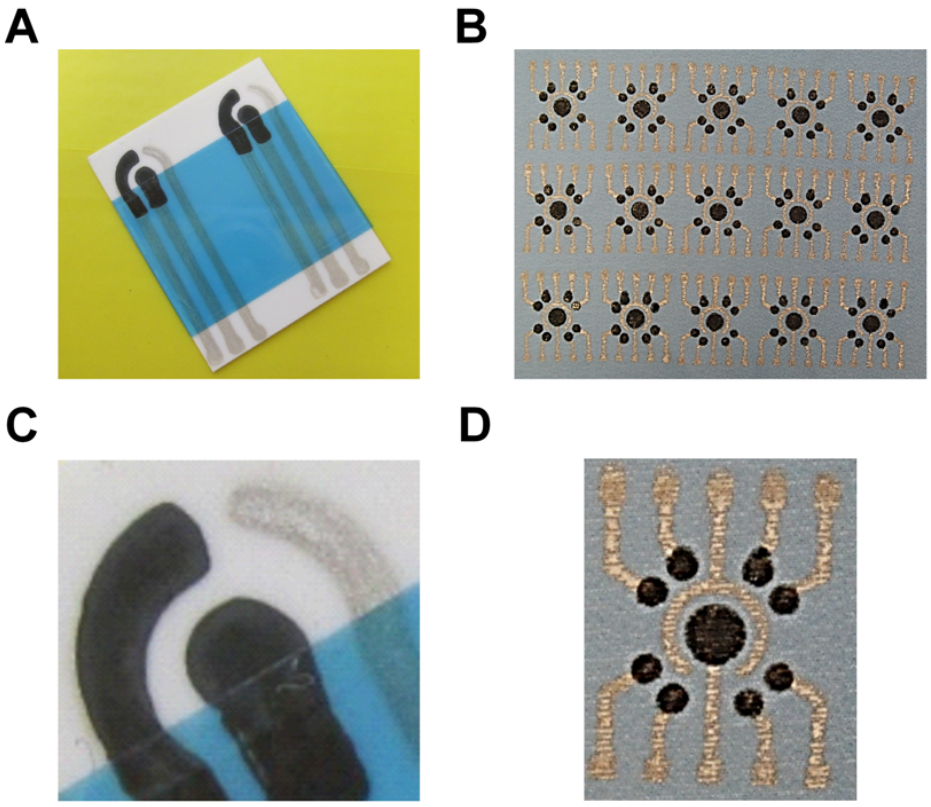

Figure 5.8: *(A) Image of stamp-transfer three-electrode contingent on alumina. (B) Image of stamp-transfer eight-electrode array on GORE-TEX® fabric. Close-up images of a single three-electrode element (C) and eight-electrode sensor array (D) on the alumina and GORE-TEX substrates, respectively, illustrating the well-defined borders and uniform surface morphology.*

deterioration of the stamped electrode pattern is observed following the application of various strain permutations, hence demonstrating the robustness of the stamp-transfer electrochemical system. Fig. 5.7C displays a three-electrode STE contingent on a paper cup while Fig. 2D shows the same STE system on a Neoprene stress ball; the inset of Fig. 5.7D epitomizes the resiliency of the electrodes even under severe compression. In order to realize sensors for remote environmental / security monitoring, a maple leaf (Fig. 5.7E) and granite slab (Fig. 5.7F) were patterned with the three-electrode contingent. As is evident from the images exhibited in Fig. 5.7, high-quality transfer of the electrode patterns onto various curvilinear, irregular, and oversized surfaces is achieved. As a consequence of the versatility of the transfer process and the ability of the elastomeric stamps to conform with uneven surfaces, well-defined electrode patterns are easily transferred to nearly any substrate.

Following optimization and demonstration of the stamp transfer process on non-planar substrates, the technique was migrated to planar substrates that have traditionally been used in the screen printing process. Fig. 5.8 illustrates several configurations of the stamped pattern on planar surfaces. Displayed in Fig. 5.8A is a pair of complete three-electrode electrochemical sensors stamped on an alumina substrate. Likewise, Fig. 5.8B presents 15 individually-addressable eight-electrode sensor arrays for multiplexed sensing operation on GORE-TEX fabric. Fig. 5.8C depicts a single three-electrode sensor in greater detail and is illustrative of the high-quality pattern transfer onto the substrate. Additionally, Fig. 5.8D displays a close-up image of a single exemplary eight-electrode array, illustrating that the structural integrity of the transferred pattern is maintained. The transferred pattern thus possesses uniform surface roughness, thickness, and coverage. Furthermore, line widening is not observed and the line edges are sharp and well-defined. Desirable electrode-to-electrode reproducibility is obtained as indicated from subsequent voltammetric measurements (described below).

Subsequent to a qualitative assessment and imaging of the STE sensors on various substrates, the electrochemical behavior of these devices was investigated in further detail. Fig. 5.9 compares the cyclic voltammetric response of the stamp-

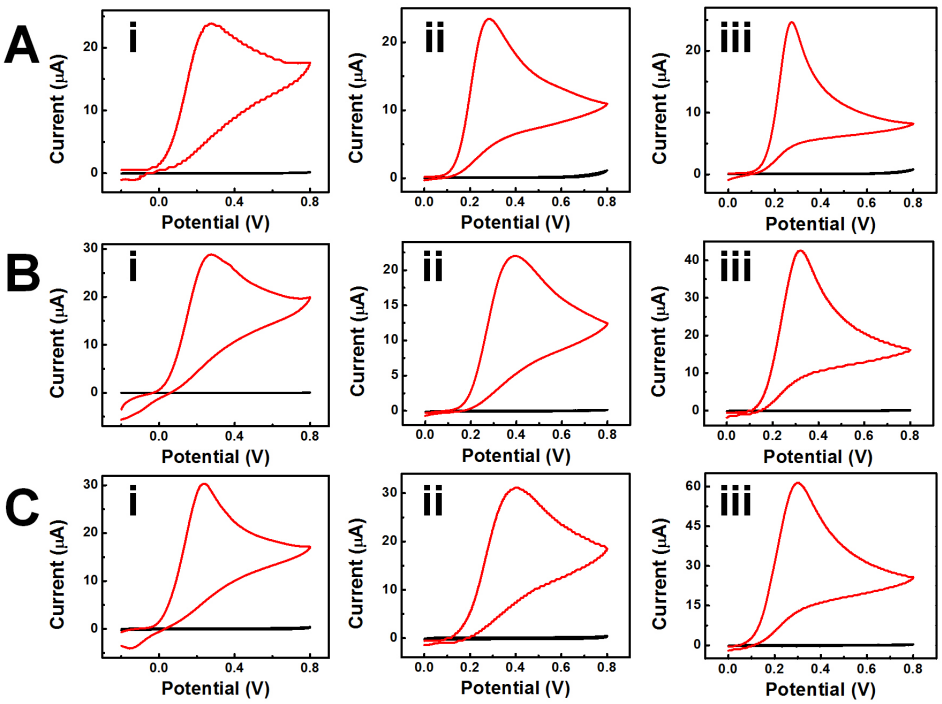

Figure 5.9: *Comparison between the voltammetric response of conventional screen printed electrodes on alumina (A) with stamp-transfer electrodes on alumina (B) and with stamp-transfer electrodes on a table tennis ball (C); scan rate = 100 mV* s^{-1}*. (i) 1 mM dopamine, (ii) 1 mM uric acid, (iii) 1 mM acetaminophen.*

transfer three-electrode contingent (working electrode area = 8.3 mm^2) on alumina substrates (B) and on a highly curvilinear table tennis ball surface (C) with that of a conventional SPE (area = 4.9 mm^2) on alumina (A). Three physiologically-relevant electroactive compounds were studied: dopamine (i), uric acid (ii) and acetaminophen (iii). The stamp transfer electrodes display well-defined oxidation peaks for all three analytes, similar to those observed at the conventional SPE (B,C vs A). Tab. 5.1 compares the peak potentials (E_p), initial potentials (E_i), peak currents (i_p), heterogeneous rate constants (k_s), and signal-to-noise ratios (SNR) produced by the SPE and STE embodiments for the three analytes under study. The heterogeneous rate constants k_s were interpolated from the experimental data using the *Butler-Volmer relation* [66],

$$k_s = \frac{i_p}{FA}\left[C_O e^{\frac{-\alpha F}{RT}\left(E_p - E^0\right)} - C_R e^{\frac{(1-\alpha)F}{RT}\left(E_p - E^0\right)}\right]^{-1} \tag{5.1}$$

where F is Faraday's constant, A is the electrode area (stated above), C_O and C_R refer to the concentrations of the oxidized and reduced species, respectively, α refers to the transfer coefficient, R is the ideal gas constant, T is the absolute temperature (in Kelvin), and E^0 represents the formal potential of the electrode. Under scenarios where the electrode is operated at a potential in the vicinity of E^0 and the concentration of the oxidized species exceeds that of the reduced species by a substantial margin, the following simplification to the above relation may be made:

$$k_s = \frac{i_p}{FAC_O}. \tag{5.2}$$

This approximation can also be applied to the converse scenario where the concentration of the reduced species far exceeds that of the oxidized form.

The similar voltammetric profiles and related peak parameters indicate that the electrochemical behavior is not compromised by the stamp transfer process nor by non-planar surfaces. As expected, this behavior depends primarily on the composition of the inks employed [77] and curing conditions [78].

The detection of heavy metals such as copper is of great relevance to the security [79] and environmental [80] monitoring domains. A widespread constituent

Table 5.1: *Comparison between the analytical figures of merit exhibited by stamp transfer electrodes and screen printed electrodes on alumina substrates.* E_i *indicates the 'initial' potential at which the current response for the electroactive species exceeds the baseline by a factor of 10.*

	DA		UA		ACT	
	SPE	STE	SPE	STE	SPE	STE
E_p (V)	0.28	0.27	0.28	0.39	0.27	0.32
E_i (mV)	-63	-24	124	156	143	132
i_p (μA)	23.9	22.8	23.4	22.1	24.6	41.5
k_s ($\times 10^{-3}$ cm s^{-1})	5.0	4.0	4.9	2.8	5.2	5.2
SNR (dB)	26.2	21.6	33.0	29.0	23.3	23.3

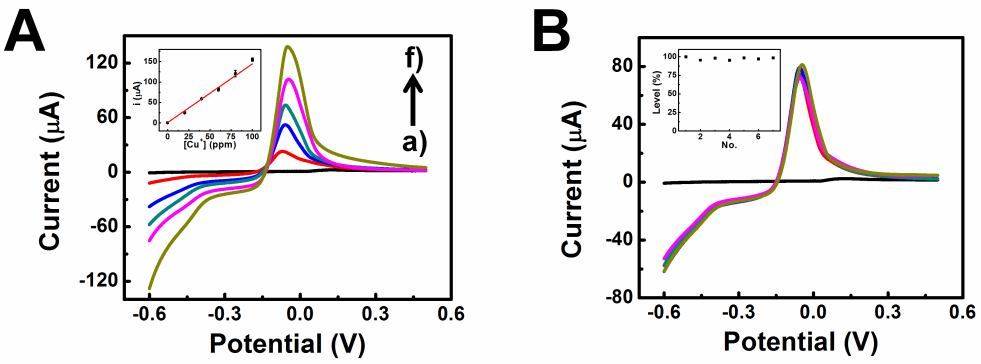

Figure 5.10: *(A) Square wave anodic stripping voltammograms generated by increasing levels of* Cu^+ *(a → f: 0 to 100 ppm) on alumina;* f = *20 Hz,* A = *25 mV,* ΔE = *4 mV,* t_{dep} = *15 s at -0.8 V* vs *Ag/AgCl. The corresponding calibration curve* (n = *7) is illustrated in the inset. (B) Repeatability of the detection of 60 ppm* Cu^+ *for seven different STEs. The inset displays the corresponding electrode-to-electrode uniformity profile based on measurements of the corresponding peak currents.*

of gunshot residue and antifouling paints, copper is of considerable interest to the forensics and naval communities [81]. Consequently, square wave anodic stripping voltammetry (SWASV) was performed in order to assess the electrochemical performance of the STE system. Following a surface cleaning routine, deposition was performed by placing 50 μL of the Cu solution on the electrode surface and applying a potential of -0.8 V (*vs* Ag/AgCl) for 15 s; stripping of the electrodeposited copper was executed by scanning the potential from -0.6 V to 0.5 V via SWASV. Fig. 5.10A displays stripping voltammograms for increasing Cu concentrations (b $\rightarrow$ f), along with the corresponding background response (a). Well-defined Cu stripping peak currents (E_p = -60 mV *vs* Ag/AgCl) are observed, along with a low background response. As indicated from the corresponding inset, the peak current increases linearly with the Cu concentration over this range (sensitivity, $s_x = 1.435$ μA ppm^{-1}; $R^2 = 0.992$). The favorable signal-to-noise characteristics is indicative of facile measurement of ppm levels of Cu following a short (i.e. 15 sec) deposition time. The SWASV response of the STE also exhibits good reproducibility and stability. Fig. 5.10B displays a series of 7 repetitive measurement of 60 ppm Cu that yielded a relative standard deviation of 5%, inline with results obtained from previous studies employing conventional screen-printed electrodes [72]. It is expected that the STE approach can be leveraged for the stripping-voltammetric detection of other trace metal constituents in diverse sample matrices.

Trinitrotoluene is frequently employed in the military as well as improvised explosive devices, roadside bombs, and mines and its identification is of considerable importance in for diverse security screening applications [82]. Consequently, the electrochemical performance of the STE was evaluated towards the voltammetric determination of TNT. As illustrated in Fig. 5.11, the STE displays a well-defined response for increasing TNT concentrations (20 - 60 ppm; a - c), which is in correspondence with other carbon electrodes [81]. Both reduction peaks (occurring at E_p = -0.71 V and -0.89 V *vs* Ag/AgCl) increase linearly with the TNT concentration. A highly linear calibration plot is observed in the left inset of Fig. 5.11 over the 20 $\rightarrow$ 100 ppm TNT concentration range ($s_x = 139$ μA / (μg mL^{-1}); $R^2 = 0.994$), reflecting the high sensitivity of the voltammetric STE system

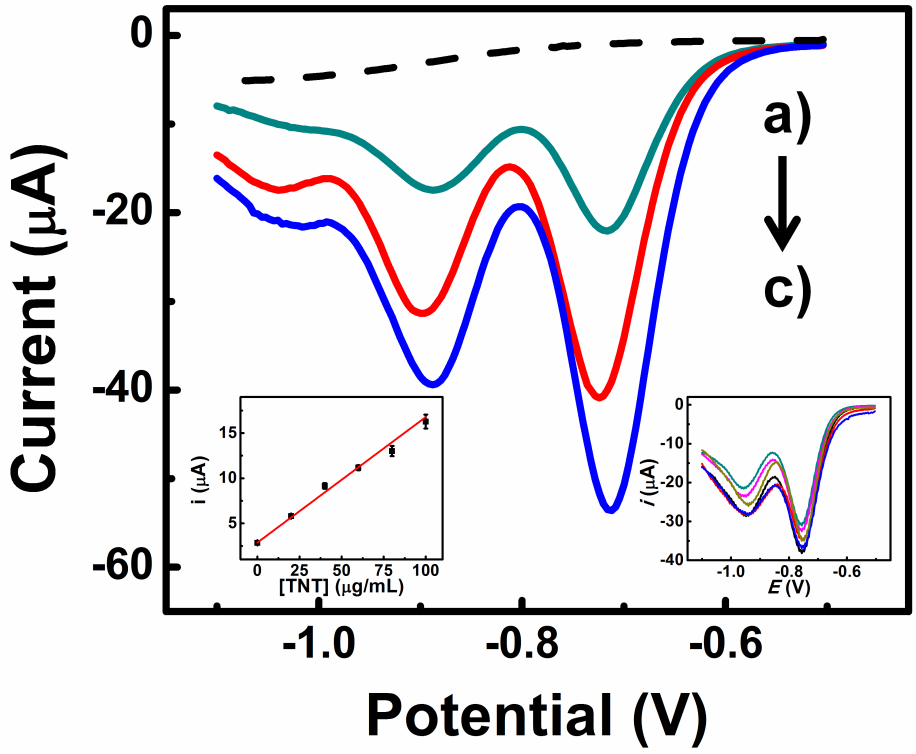

Figure 5.11: *Square wave voltammograms generated by increasing levels of TNT: 20 → 60 μg mL^{-1} (a-c), along with the background voltammogram (dotted line). A calibration curve (n = 7) for TNT is shown in the left inset. Repeatability of the detection of 60 μg mL^{-1} TNT for seven different STEs is displayed in the right inset. Other conditions, as in Fig. 5.10.*

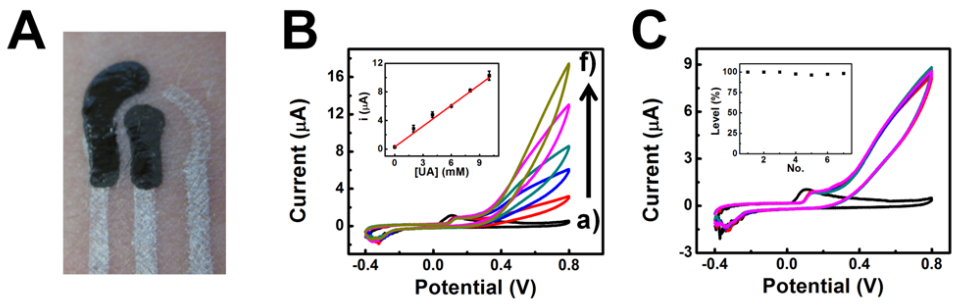

Figure 5.12: *(A) Image of the stamp-transfer three-electrode contingent on the skin. (B) Cyclic voltammograms generated by increasing levels of uric acid on the skin (0 → 10 mM; a - f); scan rate, 100 mV s^{-1}; inset illustrates the corresponding calibration curve* (n = 7). *(C) Repeatability of the detection of 10 mM uric acid for seven consecutive iterations (inset illustrates the corresponding stability profile at* E_{APP} = *0.6 V* vs *Ag/AgCl).*

under rapid SWV scans. Also shown in Fig. 5.11 (right inset) is the electrode-to-electrode precision data. Employing a 60 ppm TNT solution and 7 different STEs, this series yields similar TNT signals with a relative standard deviation of 9% with respect to the peak current. Although this figure is somewhat higher than those common for conventional SPEs [83], it is expected that further improvements and automation of the stamp-transfer fabrication process will serve to further improve the precision while leading to higher throughput.

In order to demonstrate the versatility of the fabrication methodology, stamp transfer electrodes were applied to the skin. Fig. 5.12A displays a common 3-electrode pattern on the epidermis prepared by stamping the forearm. Similar to the skin-based carbon STE arrays (of Fig. 5.7A), the epidermal 3-electrode pattern retains its structural integrity under mechanical strain as well as displays uniform coverage and well-defined lines and line edges. As illustrated below, the epidermal STE displays favorable voltammetric behavior and is highly resistant against common forms of mechanical strain expected on the epidermis. The electrochemical behavior of the epidermal STE was evaluated by employing uric acid as the model analyte. Uric acid is a common constituent in physiological fluids and a crucial component of the purine metabolism [84]. Fig. 5.12B displays cyclic

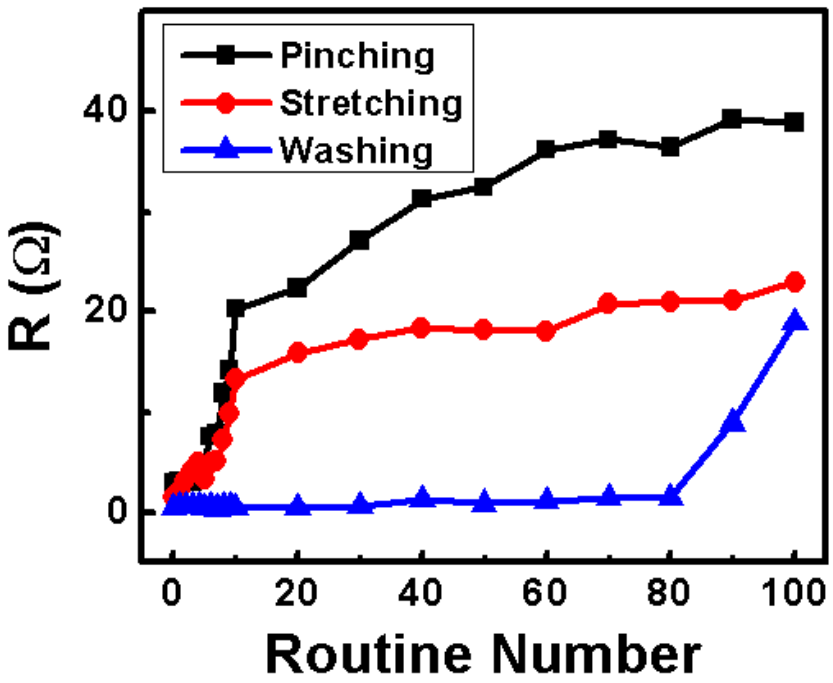

Figure 5.13: *Effect of various strain permutations on the resistance of a 1-cm Ag/AgCl electrode trace.*

voltammograms for increasing UA levels on the skin (2 $\rightarrow$ 10 mM; b - f) along with the background voltammogram (a). A well-defined voltammetric response is observed. As can be inferred from the inset of Fig. 5.12B, a highly linear calibration is obtained ($R^2 = 0.998$, $n = 7$) along with appreciable sensitivity ($s_x = 0.971$ μA mM^{-1}). A precision study using 6 mM UA at the epidermal STE (shown in Fig. 5.12C) demonstrates that the epidermal electrochemical sensor can achieve a relative standard deviation lower than 4% among repetitive measurements.

Following the voltammetric characterization of the transferred patterns on the skin, a methodical electrical characterization of the sensors was performed in order to ascertain the performance of the devices under repeated mechanical strain, deformation, and chemical degradation. Consequently, a detailed investigation of the resistance of a 1 cm segment of the epidermal Ag/AgCl electrode trace was performed under various mechanical and chemical influences. For example, Fig. 5.13

shows resistance measurements obtained in connection to 100 iterations of pinching (t_{pinch} = 5 s), stretching ($t_{stretch}$ = 5 s) of the forearm, as well as washing (t_{wash} = 5 s, soap and lukewarm water). Beginning from a value of ∼3 Ω prior to any mechanical deformation, the characteristic resistance of the STE trace increased steadily to ∼20 Ω and ∼13 Ω after 10 pinching and stretching cycles, respectively, after which the resistance stabilized, approaching ∼39 Ω after the 100^{th} pinching iteration and ∼23 after the 100^{th} stretching iteration. Accordingly, minimal deterioration in the resistive properties of the epidermal STE can be expected following repetitive mechanical deformations. A five second washing routine with soap and lukewarm water also resulted in negligible deterioration in the characteristic resistance of the sensor (3 Ω) until the ∼80^{th} iteration, after which the resistance gradually climbed to ∼20 Ω by the 100^{th} washing cycle. As a consequence of the sensors remarkable mechanical and chemical resiliency, the stamped device is expected to withstand the rigors of routine on-body use under diverse conditions. In an attempt to gain further insights, electrochemical impedance spectroscopy was performed (Fig. 5.14) in order to ascertain the boundary where mass transfer control of the electrochemical reaction transitions to kinetic control. Owing to the absence of straight line in the Nyquist plot, it can be inferred that the reactions occurring at the skin-electrode interface are purely governed by chemical kinetics rather than by mass transfer over the entire frequency range examined (1 Hz - 10 kHz). Mass transfer of the chemical species is thus not expected to dominate the charge transfer dynamics of the electrochemical system and therefore waveforms generated by voltammetric measurements may deviate somewhat from those expected at conventional solid-state electrodes (i.e. glassy carbon, screen printed carbon, etc.). Hence, the distortion imparted by the skin-based electrodes is equivalent to recording a voltammogram at high scan rates. Moreover, a solution and charge transfer resistance of R_Ω = 97 Ω and R_{ct} = 22.5 kΩ, respectively, can be extrapolated from the Nyquist plot of the experimental impedance data. Interpolating from these data, a double layer capacitance C_{dl} of 193.2 μF can be estimated (according to the Randles-Ershler model [6, 85]).

The work presented describes a novel stamp-transfer method for the man-

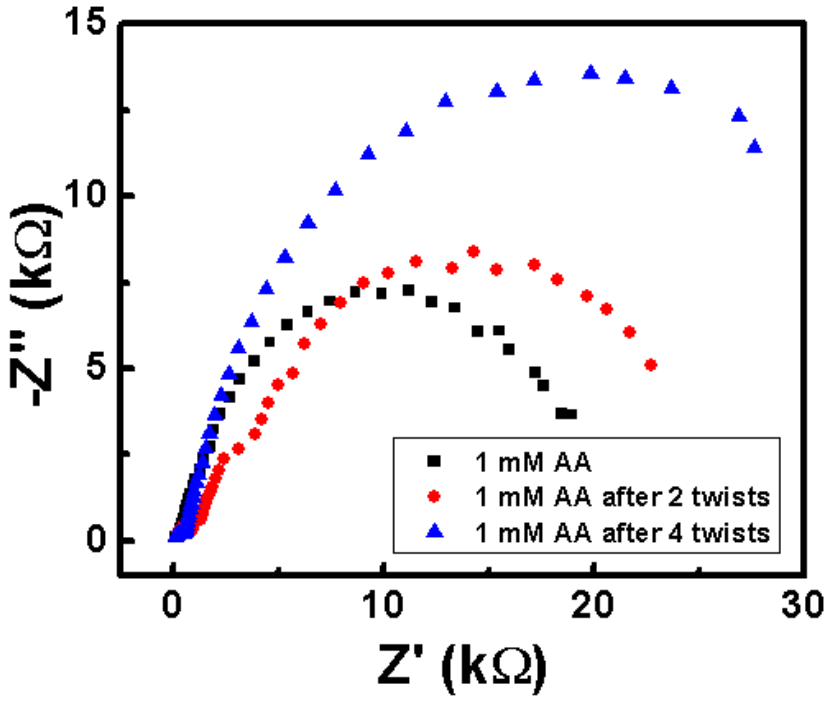

Figure 5.14: *Electrochemical impedance spectra of 1 mM ascorbic acid under increasing degrees of mechanical strain.*

ufacture of electrochemical sensors and biosensors on non-traditional substrates. Owing to the versatility of the pattern-transfer technique, the as-prepared electrochemical sensors are able to conform to a wide array of non-planar substrates possessing various surface irregularities, as well as large objects that are not compatible with conventional SPE fabrication techniques. The migration of printed electrochemical sensors to unconventional substrates characterized by a large surface area and/or a high degree of non-planarity creates new opportunities for the utilization of these devices in a wide array of applications in the healthcare, fitness, security-monitoring, and forensics domains. Although the approach is amenable to low-cost production, the stamp transfer technique can be implemented in high-throughput fabrication processes with the design of the appropriate automated equipment. The combination of the pattern-transfer paradigm with current developments in epidermal electronics would enable the realization of truly 'Lab-on-Skin'-type of embodiments for the control and readout of these sensor devices.

5.3 Screen printed electrodes for the amperometric detection of myeloperoxidase

Immediate and reliable diagnostic information regarding unpredicted cardiovascular events is crucial for providing timely, life-saving therapeutic intervention. Indeed, most acute cardiac events are life-threatening emergencies, and the length of time that transpires between the onset of the injury and treatment has been shown to be positively correlated with increased mortality rates [86]. For example, while patients exhibiting acute myocardial infarction (AMI) can benefit from new medications and treatments, in order to be effective, these drugs must be administrated rapidly after the first symptoms appear. Rapid and reliable diagnosis of cardiac abnormalities would allow for immediate medical intervention, leading to decreased mortality. Accurate diagnostic tools should also reduce unnecessary hospital admissions or discharges and reduce related healthcare costs. It is imperative to provide immediate and reliable diagnoses regarding unpredicted cardiovascular events and to identify those patients presenting such events in the

acute phase. Evaluation of patients arriving at the hospital with complaints of chest pain or related warning signs is time-consuming, costly, and inherently problematic. However, identifying patients with cardiac injury remains a primary challenge. Major emphasis has thus been given to point-of-care testing that provides a rapid means for early diagnosis [87]. Although advanced diagnostic tools such as the electrocardiogram offer a wealth of information regarding the cardiac pathophysiology [88], this technique is not amenable to point-of-care testing. Bioassays, however, show the promise for improved point-of-care evaluation and decision making for the diagnosis of acute cardiac events [89]. Despite extensive development in the field of bioassays, current assay tests performed in the hospital are still costly and time-consuming, thus placing an additional burden on the healthcare provider. A high-fidelity, low-cost point-of-care assay offering rapid results could enable a faster and better-suited treatment, thereby leading to decreased mortality rates from life-threatening cardiovascular events.

Cardiovascular disorders manifest a wide range of symptoms and characteristics, hence providing a challenging domain for diagnostics. Particular attention has been given to the development of blood tests for detecting injury to the heart muscle at the early stages among people with chest discomfort and for the diagnosis of acute coronary syndromes (ACS) [86]. Such blood tests for cardiac markers assist physicians in their assessment and diagnosis of ACS and aid them in identifying and managing high-risk patients. However, these tests must still be performed in hospital facilities requiring blood sample analysis, during which the most critical hours for therapeutic intervention may transpire. The reliable and rapid diagnosis of unpredicted cardiac events thus remains a paramount challenge in emergency healthcare today. Myeloperoxidase (MPO, E.C. 1.11.2.2), a heme peroxidase has been given much attention as a prognostic indicator of suspected ACS [90]. MPO catalyzes the conversion of hydrogen peroxide and the chloride ion to hypochlorous acid. As a pro-inflammatory enzyme biomarker, MPO becomes elevated upon neutrophil activation resulting from inflammation caused by eroded or ruptured arterial lesions [91]. Increased serum levels of MPO (11.9 U L^{-1} versus 6.6 U L^{-1} under normal cardiovascular conditions) have been shown to precede

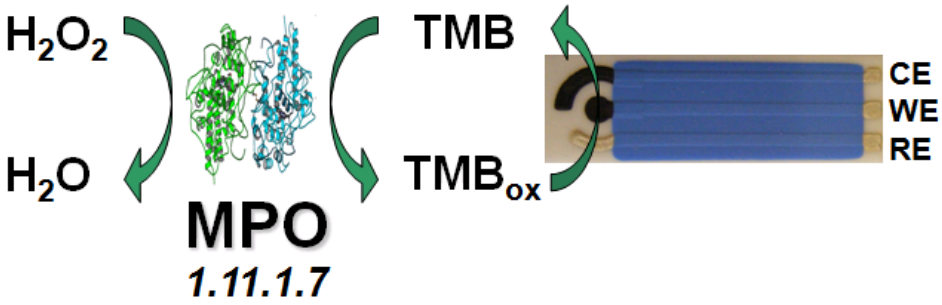

Figure 5.15: *Schematic representation of the enzymatic detection of MPO using a screen printed electrode (SPE).*

cardiac events such as acute myocardial infarction (AMI) [91] even in the absence of established indicators of myocardial necrosis [92]. Moreover, increased serum MPO has been shown to predict an elevated risk for subsequent cardiovascular events among patients with ACS and as a risk indicator for long-term mortality following AMI [93].

Numerous MPO immunoassays have been reported [94, 95, 96, 97] and are commercially available. These assays require long incubation times and entail complex, labor-intensive preparation and analysis. A strip-based sensor, analogous to those used for blood glucose monitoring [10], would allow for the immediate diagnosis of life-threatening acute cardiac events and facilitate timely therapeutic intervention, which will ultimately lead to increased survival rates.

The present study reports the development of a strip-based assay for the amperometric detection of physiologically relevant levels of MPO. The assay employs 3,3',5,5'-tetramethylbenzidine (TMB) as a redox mediator for the detection of MPO in the presence of a peroxide substrate (Fig. 5.15). The results demonstrate the feasibility of employing simple electrochemical techniques for the direct and highly-sensitive detection of MPO.

As a basis for the experimental realization of highly sensitive detection of MPO, several parameters including the applied potential, pH, concentration of TMB, incubation time, and temperature were investigated and optimized. The

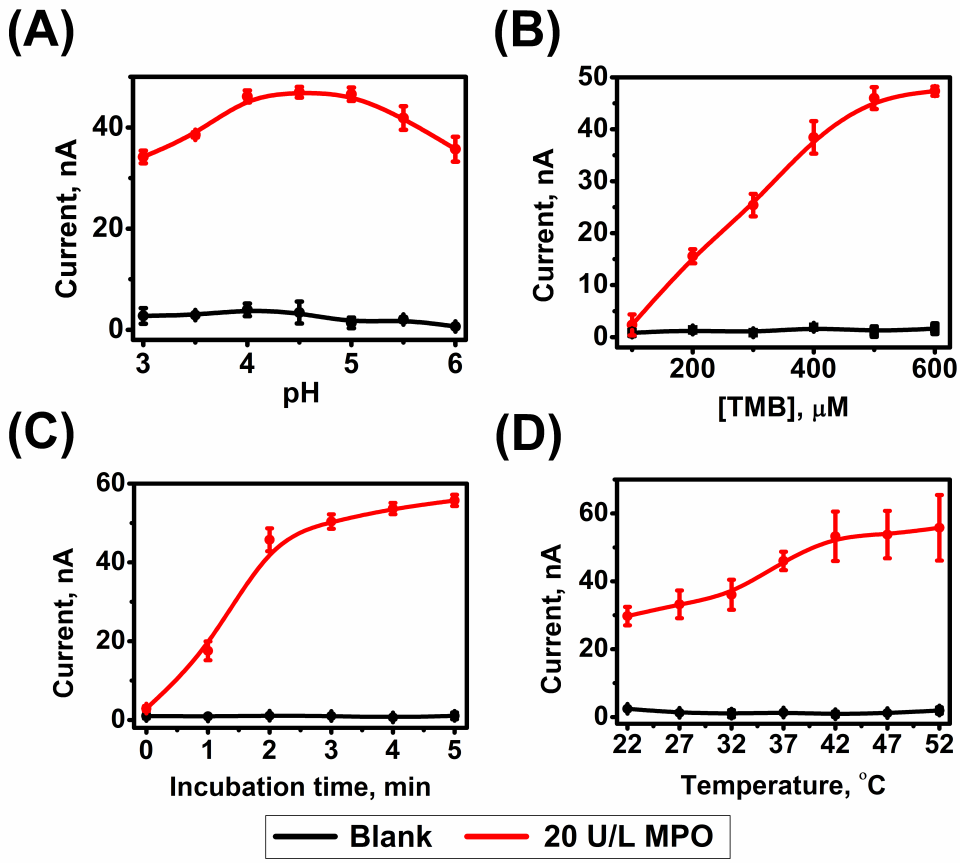

Figure 5.16: *Effect of (A) pH, (B) concentration of TMB, (C) incubation time, and (D) temperature on the detection of MPO (20 U L^{-1}) at SPE. All experiments were conducted in 0.1 M acetate buffer with an applied potential of 0 mV* vs *Ag/AgCl and 1.2 mM of H_2O_2.*

optimized parameters were utilized in calibration measurements employing physiological levels of MPO. Common interferents in serum were also investigated in the context of MPO detection fidelity. The results are as follows:

Effect of applied potential:

In order to determine the precise TMB reduction potential, the applied potential was scanned from -200 mV to 200 mV *vs* Ag/AgCl in 50 mV increments in an acetate buffer containing 0.6 mM TMB and 1.2 mM H_2O_2. At an applied potential of 0 mV *vs* Ag/AgCl, a highly sensitive current response for the reduction of the oxidized TMB product was observed. Therefore, this reduction potential

was selected to enable low-noise detection.

Effect of buffer pH:

With the reduction potential established at 0 mV *vs* Ag/AgCl, chronoamperograms were recorded for acetate buffer solutions with pH values of ranging from 3.0 to 6.0 in 0.5 increments. For each buffer pH value, current readings were extracted at the 10^{th} s following the application of 0 mV *vs* Ag/AgCl for both blank (0 U L^{-1} MPO) and 20 U L^{-1} MPO concentrations, as shown in Fig. 5.16A. The current response exhibited a negative parabolic profile with a maximum at pH 4.5. The decrease in the current response profile at pH values greater than 5 can be attributed to the instability of the TMB oxidation product near neutral pH values [94]. Accordingly, a pH 4.5 acetate buffer was selected for further measurements.

Effect of mediator concentration:

Subsequent to pH studies, the concentration of TMB was varied between 100 μM and 600 μM in 100 μM increments with a fixed concentration of H_2O_2 (1.2 mM). Chronoamperograms were recorded and a sampling time of 10 s was established. An increase in the magnitude of the current response was obtained for TMB between 100 μM and 500 μM, as elucidated in Fig. 5.16B. The onset of saturation in the current response was observed at 600 μM. Due to the diminishing returns afforded by increasing the level of TMB beyond 600 μM, ensuing experiments were performed with this concentration of TMB.

Effect of incubation time:

To determine the reaction duration that resulted in the optimal current response, the reagents (including 20 U L^{-1} MPO) were mixed and stored in a vial for 0 min to 5 min (in 1 min increments). Once the desired incubation time transpired, the sample was dispensed on the electrode surface and chronoamperometry was performed. As illustrated in Fig. 5.16C, an increase in the reduction current was observed for reaction durations from 0 min to 2 min. However, once the 2 min reaction duration was attained, the current response saturated and further escalating the incubation time had little effect on the current response. Thus, an incubation time of 2 min was chosen for subsequent investigations.

Effect of temperature:

Employing a temperature-controlled recirculating water bath, the reaction temperature was increased from 22° C to 52° C in 5° C increments. All reagents were incubated in this bath following preparation and allowed to reach the desired temperature. Once all the compounds to be analyzed were mixed, the solution was placed in a vial and incubated in the bath for two min prior to being dispensed on the electrode surface. Chronoamperograms were subsequently recorded and the results of these measurements (current sampled at $t = 10$ s) are shown in Fig. 5.16D. The measured current response increased from 22° C to 37° C. However, the current response saturated at temperatures of 42° C and greater.

As indicated from Fig. 5.16A - D, the measured background (blank) current was independent of TMB concentration, incubation time and temperature, although it displayed a slight pH dependence, as expected from the optimal assay conditions of TMB [94].

Calibration in buffer solution:

With the above mentioned optimization complete, all parameters were established at their respective optimal values and a calibration was performed between 0 U L^{-1} and 18 U L^{-1} MPO to emulate circulating concentrations of the enzyme in human serum. Acetate buffer solutions (pH 4.5) containing varying concentrations of MPO were mixed with TMB and H_2O_2, and allowed to incubate at 37° C for 2 min prior to dispensing on the electrode surface. A chronoamperogram was recorded for 30 s for the blank buffer solution and for each MPO concentration. The corresponding current-time signals are provided in Fig. 5.17A. The current was sampled at $t = 10$ s, and a linear regression shows a high degree of correlation among increasing levels of MPO with a correlation coefficient of 0.995 ($n = 3$). Extrapolating from the regression line intercept, the noise level was 1.05 nA and the regression line slope indicated a sensitivity of 2.72 nA (U $L^{-1})^{-1}$ (Fig. 5.17B). The detection limit of MPO was determined to be 0.4 U L^{-1} when considering a three standard deviation (3σ) separation from the blank buffer solution.

Interference investigation:

An interference study was conducted whereby the common serum-based

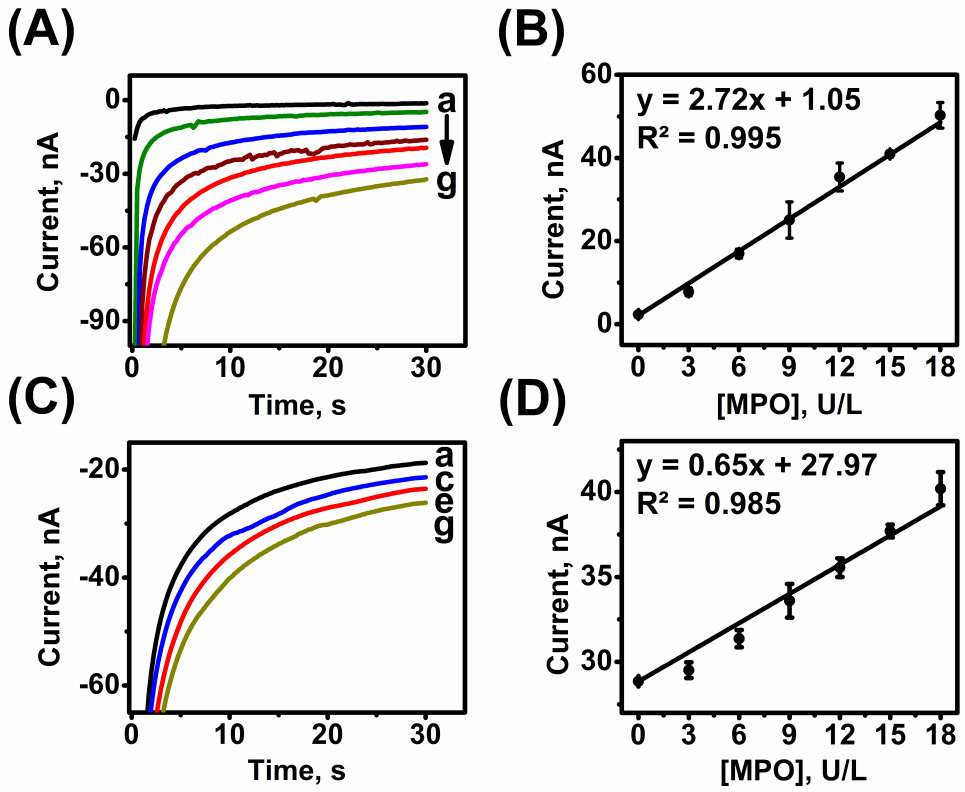

Figure 5.17: *Chronoamperograms recorded for the detection of MPO in (A) 0.1 M acetate buffer (pH 4.5) and (C) human serum at SPE; (B) and (D) show the calibration curves for MPO detection in buffer and serum, respectively; a → g: 0 to 18 U L^{-1} MPO (3 U L^{-1} increments). For clarity, only the 0, 6, 12 and 18 U L^{-1} MPO signals are displayed in (C). Experiments were conducted at 37° C with 600 μM of TMB, 1.2 mM of H_2O_2, 2 min incubation time, and an applied potential of 0 mV* vs *Ag/AgCl.*

compounds ascorbic acid (AA) and uric acid (UA) were employed to study their effect on the detection of MPO. The presence of 0.4 mM UA resulted in a slight deviation in the measured current of 20 U L^{-1} MPO in buffer while 0.1 mM AA yielded more than 100% deviation in the MPO signal. As such, AA served to directly reduce the TMB oxidation product generated by the presence of MPO. The study indicates that, even when adhering to the optimal conditions discussed earlier, the performance of the biosensor was noticeably altered by the presence of physiological concentrations of AA. This interference can be rectified through the inclusion of the enzyme ascorbate oxidase (AOx, E.C. 1.10.3.3) [98]. Consequently, further investigation into the remedial properties of AOx in the assay is warranted.

In order to mitigate the deleterious effect of AA, acetate buffer solutions (pH 4.5) were spiked with elevated levels of the circulating compounds under investigation: MPO (20 U L^{-1}) and AA (0.1 mM). The level of AOx in the buffer sample was optimized until the contribution of AA to the reduction current was negated. 650 U L^{-1} was identified as the most effective AOx level and this quantity was employed for further investigations. As in the calibration experiment, the reagents were incubated at 37° C for 2 min prior to dispensing on the electrode surface and chronoamperograms were recorded for 30 s. The current-time signals are shown in Fig. 5.18A for the assay with 20 U L^{-1} MPO (baseline) and the assay with 20 U L^{-1} MPO, 0.1 mM AA, and 650 U L^{-1} AOx (current sampled at 10th sec). As indicated from Fig. 5.18B, the response deviated by less than 15% from the baseline (MPO alone) when 0.1 mM AA and 650 U L^{-1} AOx were included in the assay. A low standard deviation of 3.4% ($n = 3$) from the mean value was obtained in these measurements. As such, sensitive detection of relevant levels of MPO in buffer using TMB was achieved even in the presence of a potent reducing agent such as AA.

In addition to a close examination of serum-based electroactive interferents such as AA and UA, the effect of other peroxidases that exist in the blood [99] was also explored. Given that peroxidases catalyze the reduction of H_2O_2 in the presence of a reducing substrate, many of these enzymes exhibit similar catalytic functionalities as MPO and therefore may be able to displace this compound in

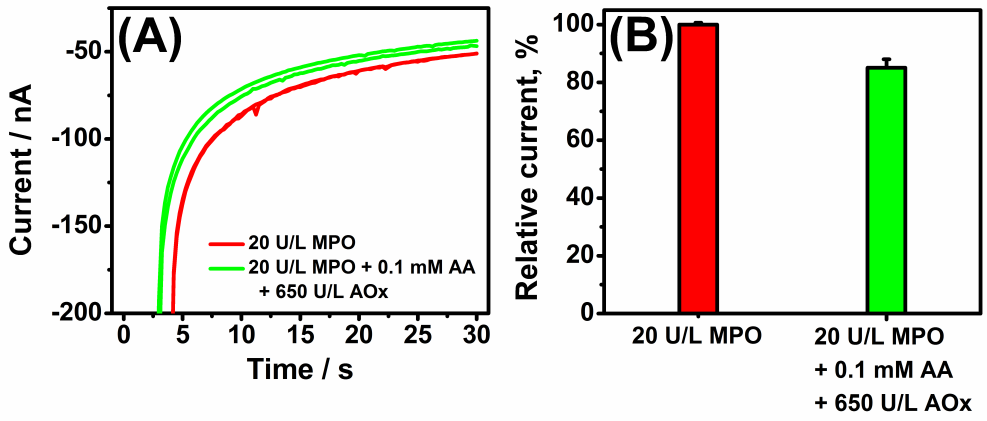

Figure 5.18: *(A) Chronoamperograms recorded for 20 U L^{-1} MPO (red) and with the addition of 0.1 mM ascorbic acid (AA) and 650 U L^{-1} ascorbate oxidase (AOx) (green). (B) Histograms showing the normalized output current with respect to 20 U L^{-1} MPO. Currents are sampled at the 10^{th} s.*

enzymatic detection schemes such as the one proposed. When multiple peroxidases are present (such as in serum), H_2O_2 will be consumed by each of these enzymes. However, by employing a sufficient concentration of H_2O_2 (1.2 mM) as in the aforementioned assay protocol, the interference effect of other peroxidases can be mitigated. In the present investigation, as an example, a human serum sample was spiked with a physiological level of glutathione peroxidase (GPx, E.C. 1.11.1.9), a common antioxidant enzyme found in the blood at relatively high levels (676 U L^{-1}) [100]. The measured current from the chronoamperometric experiments resembled baseline readings, thereby indicating that the presence of GPx could not be detected when employing the conditions used for MPO detection. Subsequently, a serum sample was spiked with both GPx and MPO (at physiological levels) in order to verify that TMB demonstrated specificity towards MPO alone. The measured current in this experiment was in close agreement with MPO signal obtained earlier and did not show an "additive" effect, thus confirming that the presence of GPx did not interfere with the detection of MPO. Reports have also indicated that Ellman's Reagent can be utilized to react with the thiol groups of the glutathione substrate, thereby inhibiting the catalytic oxidation of TMB [101].

Although the results imply that amperometry could lead to straightforward detection of MPO, the presence of other electroactive compounds and high levels of peroxidases (categorized under the E.C. 1.11.1.7 family) in serum could potentially interfere with the amperometric detection of this enzyme. Accordingly, the electrochemical detection of MPO should only be considered when it is evaluated in conjunction with other well-established prognostic indicators of acute myocardial conditions.

Detection of MPO in human serum:

In order to demonstrate the practical application of the new method, a calibration study was also performed in human serum. Serum samples were spiked with physiological levels of MPO (ranging from 0 U L^{-1} to 18 U L^{-1}), and the corresponding chronoamperograms were recorded. The corresponding current signals and the calibration curves are shown in Figs. 5.17C and D, respectively. The current was sampled at 10^{th} s following the initialization of the measurement. As with the buffer experiments, a favorable response is observed for these MPO increments, leading to a linear response with a correlation coefficient of 0.985 (n = 3). The noise level and sensitivity of the experiment were 27.97 nA and 0.65 nA, respectively. In this case, a limit of detection of 0.6 U L^{-1} was achieved (using the 3σ methodology).

An electrochemical biocatalytic scheme for the detection of MPO has been presented. A multivariate parameter optimization for this electrochemical strip-based assay was performed. Such optimization ensured effective amperometric detection of physiological levels of MPO at SPE in buffer and human serum using TMB as a redox mediator. It is anticipated that an inexpensive and easy-to-operate strip-based sensor, such as the one presented here, will yield a more rapid diagnosis than current methods provide, thereby leading to improved management of acute coronary syndromes. However, prior to its use as a diagnostic tool, extensive studies must be performed to examine and address all the potential interferences in relevant clinical serum samples.

Portions of Chapter 5, section 2 were taken from J.R. Windmiller, A.J.

Bandodkar, S. Parkhomovsky, and J. Wang. Stamp transfer electrodes for electrochemical sensing on non-planar and oversized surfaces. *Analyst*, 137(7):1570–1575, 2012. The dissertation author was the primary investigator and author of this manuscript.

Portions of Chapter 5, section 3 were taken from J.R. Windmiller, S. Chinnapareddy, P. Santhosh, J. Halámek, M.C. Chuang, V. Bocharova, T.F. Tseng, T.Y. Chou, E. Katz, and J. Wang. Strip-based amperometric detection of myeloperoxidase. *Biosensors and Bioelectronics*, 26(2):886–889, 2010. The dissertation author was the primary investigator and author of this manuscript.

Chapter 6

Enzyme logic biosensors and chemosensors

I was early taught to work as well as play,
My life has been one long, happy holiday;
Full of work and full of play-
I dropped the worry on the way-
And God was good to me everyday.

—John D. Rockefeller

The biocomputing approach to multi-signal processing biosensors with built-in logic is exemplified via the implementation of systems that integrate the complex patterns of biomarkers originating from pathophysiological scenarios. When an injury occurs due to mechanical or chemical damage to specific organs or tissues, chemical species (proteins and/or low molecular-weight compounds), normally present only in intracellular compartments, are released into various body fluids. Therefore, the rapid and sensitive detection of these biomarkers is essential in order to obtain a proper injury diagnosis. One disadvantage when detecting enzyme markers with the aim of injury diagnosis resides in the low specificity of the biomarkers due to the various pathological conditions underlying their release. However, the specificity of the enzyme-based diagnostic system can be achieved via the implementation of Boolean-based analysis of complex biomarker patterns via the implementation of biochemical logic gates. Rather than insisting on the

detection of a single injury biomarker, a biochemical system composed of enzyme logic gates can process two (or eventually several) physiologically-relevant inputs and thereby generate a corresponding output. The diagnostic capabilities of the biochemical detection system are enhanced when multiple logic gates are concatenated to increase the information processing capacity of the logic system. Hence, such systems can be optimized in order to detect specific injuries while diminishing the possibility of false alarms.

6.1 Boolean-format biocatalytic processing of enzyme biomarkers for the diagnosis of soft tissue injury

Soft tissue injury (STI) manifests a wide range of symptoms and characteristics, making an accurate assessment of pathophysiological states a key challenge. Much attention has focused on the development of blood tests for detecting injury to muscle tissues as early as possible among individuals who have presented outward indicators of STI [102]. Among clinically established indicators of STI, serum creatine kinase (CK, E.C. 2.7.3.2) and lactate dehydrogenase (LDH, E.C. 1.1.1.27) have been routinely employed in the assessment of muscular exertion, fatigue, injury, and trauma [103]. Tissue breakdown and hemolysis may be evaluated through the concomitant increase in LDH activity, which has been shown to rise from 150 U L^{-1} under normal physiological conditions to over 1000 U L^{-1} in cases where significant damage to the soft tissues has occurred [104, 105]. LDH catalyzes the conversion of pyruvate (PYR) and lactate (LAC) through the cycling of oxidation states of nicotinamide adenine dinucleotide (NAD^+). CK, which catalyzes the reversible phosphorylation of creatine (CRTN) in the presence of adenosine triphosphate (ATP), complements LDH as an indicator of rhabdomyolysis and can increase from 100 U L^{-1} under normal physiological circumstances to 710 U L^{-1} in pathological instances of STI [106]. When examined in tandem, both enzyme biomarkers overlap in their specificity for skeletal muscle, albeit elevated

levels of these enzymes can also indicate the presence of acute cardiac events and, therefore, a proper 'single-shot' STI diagnosis is traditionally not feasible. It has been shown that, in an acute cardiac event, individuals will typically exhibit a rise and fall of circulating CK levels followed by a rise and fall of circulating LDH, with the temporal offset between the two peaks at roughly 12 hours [107]. Accordingly, a detection concept that endeavors at identifying the presence of STI using this enzyme contingent must obviate the possibility of injury to the myocardium. Advantageously, the varying temporal concentration profiles of CK and LDH during acute cardiac events are ignored with the proposed **NAND** gate as only the *simultaneous* presence of elevated levels of these biomarkers would indicate the incurrence of STI.

The present investigation describes the development of a novel enzyme logic sensing concept for the detection of STI. Recent developments exploiting enzyme-based networks that mimic Boolean logic gates [108] have demonstrated considerable promise for the detection of physiologically relevant biomarkers [42, 43]. When compared with traditional biosensor concepts, this methodology merges the inherent redundancy and robustness of a Boolean logic approach in reaching 'True' or 'False' decisions with the specificity and dynamic range associated with biocatalytic processing. In this manner, multiple biomarkers of acute injury can be integrated and processed in a logical fashion to yield additional physiological information even in the presence of interfering compounds and unpredictable temporal concentration profiles of the biomarker inputs. Such a scheme also lends itself to established analytical electrochemical techniques in addition to harnessing the noise-mitigating capabilities of advanced digital signal post-processing algorithms. The resulting high-fidelity diagnostic route would facilitate a timely therapeutic intervention, which will ultimately lead to increased survival rates.

Employing CK and LDH as physiologically relevant enzyme inputs to a Boolean logic gate presents the opportunity to realize a high-fidelity detection concept for STI. Given that both inputs rise upon the incurrence of a meaningful pathological state, reasonable embodiments include the **AND** and **NAND** gate, whereby a concomitant increase in both biomarkers following injury would result

in an affirmative output. The latter embodiment lends itself to a more straightforward detection system that employs an enzyme cascade of CK, pyruvate kinase (PK, E.C. 2.7.1.40) and LDH in combination with their respective substrates: CRTN, ATP, phosphoenolpyruvate (PEP), and reduced nicotinamide adenine dinucleotide (NADH). Moreover, a NAND gate disregards the temporal delay between myocardial-induced rises of CK and LDH, as only the simultaneous presence of elevated levels of both of these enzymes would trigger a positive diagnosis, thereby negating potential interference that may arise as a result of an acute cardiac condition. By establishing a pathologically-meaningful decision threshold, relatively simple optical and amperometric assays tendered the diagnosis in a straightforward 'True'/'False' digital format. Only the *simultaneous* presence of elevated levels of both enzyme inputs would thus trigger a positive diagnosis. Moreover, an interference investigation has been performed that employs circulating levels of potential interferents. Such an enzyme cascade and enzymatically-processed biochemical information offer promise for point-of-care injury screening where a rapid determination of pathological situations is a prime consideration. In contrast with early work on injury diagnosis with enzyme logic gates such as **AND**, **OR**, and **XOR** [42, 43], the study presented represents the first example of a logic gate for injury detection employing the **NAND** architecture and the first demonstration of any logic gate operating in the presence of interferents.

The new protocol relies on measurements of physiologically relevant levels of CK and LDH processed through an enzyme cascade. Following an initial optical characterization and optimization of the enzyme logic STI machinery, the concept has been evaluated towards amperometric sensing at a disposable carbon screen printed electrode (SPE). The electrochemical assay employs methylene green (MG) as a redox mediator to realize the low-potential detection of the NADH output in the presence of physiologically relevant levels of both enzyme inputs along with potential interferences. In line with the **NAND** gate topology, a decision threshold is established at a pre-determined current, below which a positive diagnosis is made. This current magnitude, which corresponds to the aggregate concentration of CK and LDH normally found in serum, may be adjusted as required for high-

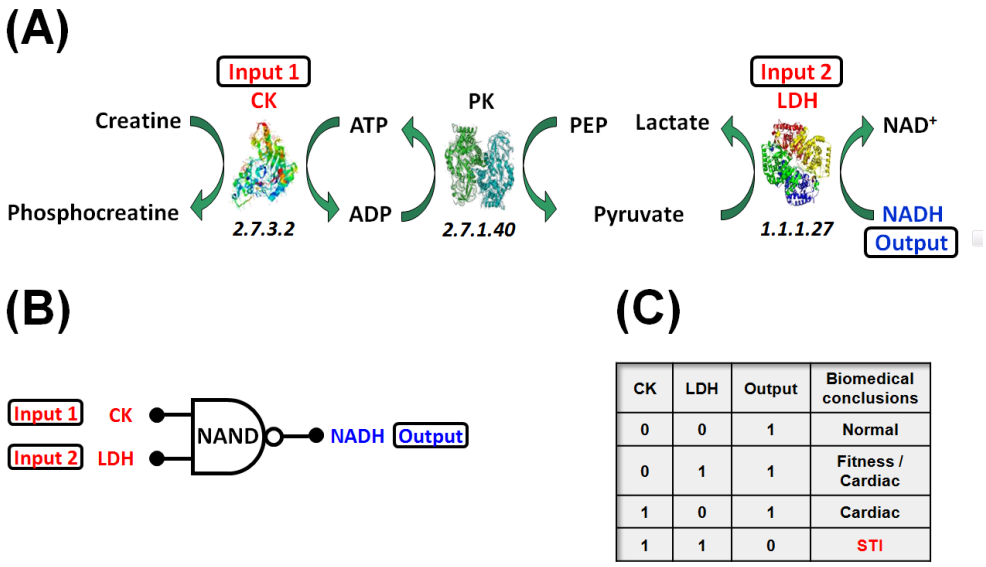

CK	LDH	Output	Biomedical conclusions
0	0	1	Normal
0	1	1	Fitness / Cardiac
1	0	1	Cardiac
1	1	0	STI

Figure 6.1: *(A) Biocatalytic cascade instigated by creatine kinase (CK) and lactate dehydrogenase (LDH) with the level of reduced nicotinamide adenine dinucleotide (NADH) as an indicator of* ***NAND*** *operation, (B) the equivalent logic system, and (C) the corresponding truth table with biomedical conclusions drawn from the combinations of the input signals. Note that the output signal with the logic value '****0****' implies an STI diagnosis, while logic output '****1****' corresponds to all other physiological scenarios.*

integrity readout under various pathological circumstances. The results delineated below indicate the potential of the new concept for the measurement of circulating levels of CK and LDH in the presence of physiologically-relevant interferents, thereby enabling the high-fidelity discrimination between normal (physiological) and abnormal (pathological) STI conditions. Accordingly, the proposed scheme offers great promise for the low-cost, rapid, and decentralized diagnosis of STI.

The fabrication of the carbon-based screen printed electrodes used in this investigation has been described in previous sections.

In order to comply with a 500 μL quartz cuvette, a total of 500 μL of reagents were employed in each optical experiment. This volume consisted of 100 μL of Gly-Gly and 50 μL of each of the reagents: NADH (3 mM), bovine serum albumin (BSA, 0.3%, w/v), ATP (20 mM), PEP (5 mM), PK (20 kU L^{-1}), CRTN (150 mM), along with 50 μL of each of CK and LDH. Logical '**0**' and '**1**' levels of CK (100 and 710 U L^{-1}) and LDH (150 and 1000 U L^{-1}) input signals were applied to the logic system in order to realize meaningful circulating levels of these enzymes. All reagents were dispensed in the cuvette and mixed by inversion. Immediately following mixture, an optical absorbance measurement was recorded continuously for 300 s at $\lambda = 340$ nm (at 37° C).

The electrochemical experiments were conducted by employing a sample volume of 160 μL in each measurement. This volume consisted of 16 μL Gly-Gly buffer and 16 L of each of the reagents used in the optical experiments along with an MG redox mediator (300 μM). In the interference study, the Gly-Gly buffer was spiked with physiological levels of the following compounds: LAC (6 mM), PYR (40 μM), phosphocreatine (PCr, 150 μM), adenosine diphosphate (ADP, 130 nM), and NAD^+ (30 μM). Circulating levels of the substrates and co-substrates already implemented in the enzyme cascade were several orders of magnitude lower than those employed and thus their effect was not considered. All reagents in both the optimization and interference studies (with the exception of MG) were mixed in a vial and incubated at 37° C in a heatblock for 180 s. Following this incubation period, MG was added to the solution, which was subsequently mixed and dispensed in the electrode reservoir held at 37° C. A chronoamperogram was

then recorded for 60 s with a stepped potential of 0.0 V *vs* Ag/AgCl.

Fig. 6.1A illustrates the enzyme logic cascade employed to realize the **NAND** gate operation as well as its equivalent logic gate (Fig. 6.1B) and the truth table (Fig. 6.1C). Using this operation, different combinations of the enzyme biomarker inputs lead to distinguishable patterns of the NADH output signal. In accordance with the **NAND** gate operational functionality, logical '**0**' and '**1**' levels of CK and LDH input signals, corresponding to normal or anomalous physiological conditions, respectively, ((CK,LDH) = (**0**,**0**), (**0**,**1**), and (**1**,**0**)), resulted in an output of logical '**1**'. On the other hand, logical '**1**' levels of both CK and LDH = (**1**,**1**) caused the output state to change from '**1**' to '**0**', indicating the occurrence of STI. It should be noted that the logic output signal '**0**' generated by the **NAND** gate and corresponding to the positive STI diagnosis does not imply that the signal is truly at a zero level. Rather, a '**0**' output implies that the system has transitioned from a state producing a signal of high magnitude to one that yields a low-level signal. In this regard, the logic output signal '**1**' indicates that the output signal is unchanged. The concentration of the reagents in the enzyme cascade were individually tailored to yield optimal dynamic range between the pathological level (**1**,**1**) and normal or anomalous physiological levels (**0**,**0**), (**0**,**1**), and (**1**,**0**). This enabled the unambiguous determination of the injury state (when the output signal '**0**' is generated) due to the establishment of a fixed decision threshold. Only the simultaneous presence of elevated levels of both enzyme inputs would thus trigger a positive diagnosis. On the other hand, the output signal '**1**' has undetermined meaning ranging from healthy conditions to various physiological anomalies not related to STI.

Assays for the individual analysis of serum CK and LDH are well-established [102, 109]. Commercially deployed assays for the determination of CK activity typically operate at an alkaline pH (8.8 - 9.0) as this is the level at which CK exhibits maximum activity [110]. However, assays that have been widely available for quantifying LDH activity operate at neutral pH values (7.2 - 7.4), the enzyme's optimum range for efficient PYR to LAC conversion [111]. This inherent pH incompatibility presents a unique challenge when endeavoring to employ both CK and LDH

as inputs into an enzymatic-processing system and requires a critical assessment of the optimal pH. A detailed investigation of the potential interferences is also of considerable importance in light of the fact that the enzyme cascade employs several compounds found in body fluids and in view of similar natural biochemical processes occurring within the body.

Based on established assay protocols [111, 112], the concentrations of the constituents of the logic-gate machinery were individually tailored to yield optimal dynamic range between the pathological level (**1**,**1**) and normal or anomalous physiological levels (**0**,**0**), (**0**,**1**), and (**1**,**0**). This enabled unambiguous determination of the injury state due to the establishment of a fixed decision threshold. Consistent with commercially available assays [112], a Gly-Gly buffer solution was identified as the most suitable experimental medium as other buffer solutions operating in similar pH regimes such as phosphate-buffered saline and tris(hydroxymethyl)aminomethane-hydrochloride contained ions that were noted as inhibitory to one or more of the enzymes. Furthermore, the enzyme activator ions Mg^{2+} (required for CK and PK catalysis) and K^{+} (required for PK catalysis) were included in this solution via the addition of magnesium acetate and potassium hydroxide, respectively. All experiments were performed at physiological temperature (37° C) due to the sub-optimal performance of the enzyme machinery at room temperature.

In order to identify the optimal pH that would enable the most favorable operation of the **NAND** gate, the pH of the Gly-Gly buffer was varied, as shown in Fig. 6.2. Commencing experiments with a physiological pH level, the pH value was increased from 7.40 to 8.50. Fig. 6.2A displays the optical absorbance of the **NAND** gate at pH 7.40 for three independent experiments at each logic level. In this case, the enzymatic reaction was sluggish to proceed as, little, if any, distinction was observed among the logic levels. The histogram shown in the inset demonstrates a comparative account of the **NAND** gate performance at this pH (at 300 s). In this case, the (**1**,**1**) logic level possessed nearly the same absorbance magnitude as the physiological logic levels (**0**,**0**), (**0**,**1**), and (**1**,**0**). Hence, an unambiguous decision threshold could not be established for diagnosis. A fur-

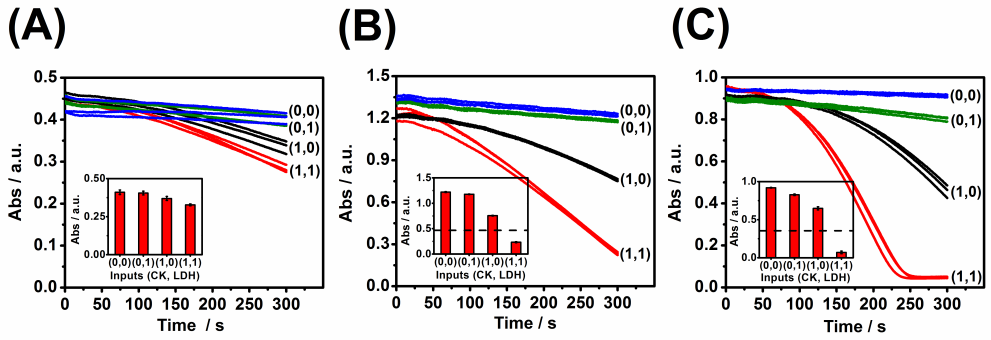

Figure 6.2: *Time-dependent optical signals corresponding to the consumption of NADH upon the application of various combinations of the CK and LDH input signals at pH (A) 7.40, (B) 7.95, and (C) 8.50. Insets show histograms featuring the* ***NAND*** *logic operation of the optical system at the specified pH. Dashed lines indicate decision thresholds for the realization of* ***NAND*** *gate operation. Optical absorbance measurements were performed at* $\lambda = 340$ *nm.*

ther increase in the pH improves the differentiation between the logic levels. For example, Fig. 6.2B presents the optical data obtained at pH 7.95 where a large differentiation between pathological and physiological logic levels is observed, reflecting the more rapid enzymatic reaction. From the corresponding histogram, the (**1**,**1**) logic level was separated by more than 0.52 O.D. from the nearest logic level. At this pH, an explicit decision threshold could be established at 0.49 O.D., leading to highly reliable **NAND** operation. Proceeding with a further elevated pH value of 8.50, which is routinely employed in CK assays [112], leads to further enhanced logic gate performance, although not as significant as in the transition from pH 7.40 to pH 7.95. Fig. 6.2C displays the optical absorbance of the **NAND** gate at pH 8.50. In this case, the conglomerate enzyme reaction proceeded at its fastest rate, with the (**1**,**1**) logic state consuming the NADH in its entirety prior to the conclusion of the experiment. The histogram chronicles the improvement in the **NAND** gate performance and the increased dynamic range at this pH level. In this case, the (**1**,**1**) logic level was extremely well-separated from the logic level in closest proximity, with a 0.58 O.D. separation between the two states. This enabled an explicit decision threshold to be established at 0.43 O.D., thus allowing

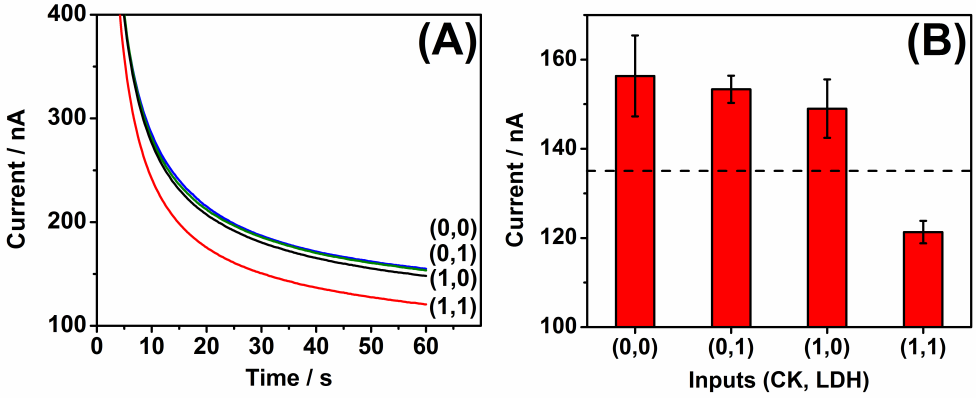

Figure 6.3: *(A) Chronoamperometric curves generated by the **NAND** gate upon application of various combinations of the CK and LDH input signals at pH 7.95. (B) Histogram featuring the **NAND** logic operation for the corresponding combinations of input signals. Electrochemical measurements were performed using a potential step to 0.0 V* vs *Ag/AgCl and the current was sampled after 60 s. Dashed lines indicate the decision threshold for the realization of **NAND** gate operation.*

for high-fidelity operation. In each measurement, regardless of the operating pH, the (**1**,**0**) logic level was in closer proximity to (**1**,**1**), while the (**0**,**0**) and (**0**,**1**) logic levels remained largely unperturbed and well-distanced from the two other levels. This reflects the Michaelis-Menten enzymatic kinetics, whereby the PYR substrate generated by physiological as well as pathological levels of CK were at saturating levels for both the LDH '**0**' and '**1**' levels, thereby giving rise to a non-proportional relationship. The challenge of physiological monitoring can be resolved in a strip-form embodiment by employing a mild pH adjustment using 'dry reagent' alkaline salts. In light of the reduced performance at pH 7.40, all subsequent experiments were performed at a pH of 7.95.

In accordance with the goal of low-cost decentralized screening of STI, the aforementioned protocol was migrated to the amperometric domain using a disposable SPE. Towards the goal of developing compact analytical devices and based on the results obtained above, the pH of the buffer was established at 7.95 and chronoamperometric measurements were performed for each logic level with MG

employed in the assay. The redox mediator MG offers a low-potential detection of NADH, hence minimizing potential electroactive interferences. The detection potential was varied between -0.2 V and 0.2 V *vs* Ag/AgCl in order to determine the optimal potential with the most favorable signal-to-noise ratio (SNR). Likewise, the MG concentration was varied from 100 μM to 10 mM in order to further maximize the SNR. This multivariate parameter sweep indicated that, in the presence of 300 μM of MG, an applied potential of 0.0 V *vs* Ag/AgCl resulted in the highest SNR figure-of-merit. Fig. 6.3A displays chronoamperograms (potential step to 0.0 V *vs* Ag/AgCl) obtained at the carbon SPE by the **NAND** gate upon application of various input combinations. At 60 s sampling time, the difference in current between the (**1**,**1**) logic and (**1**,**0**) logic levels was 27 nA, as shown in Fig. 6.3B. As in the optical experiments, the histogram indicates that a straightforward decision threshold could be instituted to realize high-fidelity **NAND** gate operation. This threshold was established at 135 nA.

Accordingly, satisfactory agreement was observed between the optical and electrochemical data, as indicated from a comparison of the histograms presented in Figs. 6.2 and 6.3, thereby confirming the validity of the transition of the experimental procedure from the optical to the electrochemical domain. With the electrochemical protocol in functional order, the effect of undesired (yet physiologically relevant) biomarkers and potential interference was subsequently investigated.

A biosensor using an enzyme cascade as its backbone employs many of the same compounds found within the body and operates under similar biochemical principles. One of the most well-established indicators of muscular fatigue and injury is a physiological rise in serum levels of LAC from 1.6 to 6.0 mM [113]. Any assay that employs LDH to assess STI must minimize the effect of LAC to yield reliable results. In addition to accounting for the influence of LAC on the operation of the logic gate, the effect of incorporating other physiologically relevant compounds is also a necessity even if they are not outward biomarkers of STI. Of the multitude of substances present in the blood, the most detrimental compounds to the operation of the system are those that also serve as the substrates and co-substrates for the enzyme reactions. Particularly, these interferents could

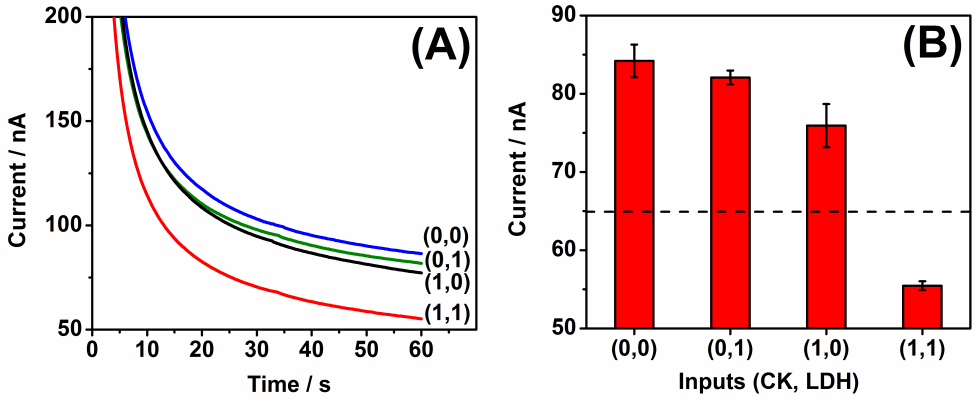

Figure 6.4: *(A) Chronoamperometric curves generated by the* ***NAND*** *gate upon application of various combinations of the input signals with physiological levels of 6.0 mM LAC, 40 μM PYR, 150 μM PCr, 130 nM ADP, and 30 μM* NAD^+ *at pH 7.95. (B) Histogram featuring the* ***NAND*** *logic operation for the corresponding combinations of input signals. Electrochemical measurements were performed using a potential step to 0.0 V* vs *Ag/AgCl and the current was sampled after 60 s. Dashed lines indicate the decision threshold for the realization of* ***NAND*** *gate operation.*

potentially hinder or even reverse the enzymatic reaction, thereby leading to complete operational failure of the logic gate. As such, PYR, PCr, ADP, and NAD^+ must be employed in the logic gate at their physiological levels in an attempt to emulate realistic sensing conditions.

Utilizing the same assay conditions as stated above, a comprehensive interference examination was performed with circulating levels of PYR, PCr, ADP, and NAD^+ as well as pathological levels of LAC. The resulting chronoamperograms are shown in Fig. 6.4A (average of three independent experiments). As apparent, the pathological logic level (**1**,**1**) was easily distinguishable and separated from the physiological logic levels by greater than 20 nA. The histogram shown in Fig. 6.4B illustrates the high-fidelity operation of the enzyme logic gate wherein a low standard deviation of less than 3 nA was obtained. With the logic threshold affixed at 65 nA, STI could be readily diagnosed under encumbering, yet realistic conditions. It should be noted that this logic threshold was reduced from the original value of 135 nA in the presence of interference. Although the standard deviation did not exceed 5% of the mean value, other intrinsic and practical physiological parameters will dictate the precision of each logic level and the position of the threshold. Such a system is expected to perform as intended for a large majority of the population with CK and LDH levels that fall within clinically-established ranges. Yet, due to the complex nature and variable extent of STI afflictions and of potential interferences, the execution of a large clinical study that integrates various forms of STI is imperative in order to select the most optimal threshold level for the general population.

The presented interference study underscores the robustness of the enzyme logic approach in assessing a pathologically complex and diverse affliction such as STI. The sizeable dynamic range of the **NAND** gate in the presence of high levels of interferents highlights the advantages of the concept when contrasted with traditional biosensor approaches. In light of the presence of interferents, the use of Boolean processing and a decision threshold for digital diagnosis enabled the assessment of proper diagnosis with a high degree of confidence under practical and varied conditions. Without the ability to establish a decision thresh-

old and Boolean-format digital processing of the inputs, a conventional biosensor would encounter serious challenges in discarding the noise arising from the presence of undesired biomarkers and extracting the signal of interest. Moreover, were a conventional biosensor approach to be used in this situation, the dramatically reduced background noise current in the presence of physiologically relevant interference would result in misdiagnosis, as can be inferred from a direct comparison of Figs. 6.3 and 6.4. Furthermore and more importantly, a traditional biosensor would experience great difficulty in resolving injury states under 'real-world' conditions when applied to STI, owing to the natural metabolic fluctuations of co-existing interferents and biomarkers. Therefore, the high dynamic range of the logic gate enabled the establishment of an unambiguous decision threshold and digital manipulation of the biomarker signals, thereby alleviating extraneous physiological effects, which allowed the system an enhanced ability to detect injury when compared with traditional biosensing concepts.

A novel enzyme logic system based upon the concert operation of an enzyme cascade has been designed to process biochemical information for the diagnostic assessment of STI. Such operation offers reliable information processing and generates distinguishable patterns of the NADH output signal arising from various combinations of the enzyme biomarker inputs. Following an optimization of the operating conditions, an interference investigation employing both physiological and pathological concentrations of potential interferents was also performed. The enzymatically-processed biochemical information presented in the form of a **NAND** truth table allowed for high-fidelity discrimination between normal (physiological) and abnormal (pathological) conditions even under extreme circumstances where interfering compounds were present at their pathological levels. The presented concept is the first demonstration, to the best of our knowledge, of successful enzyme logic gate operation applied to diagnostic merits in a physiologically relevant environment. While further development is required to realize an on-body sensor, the present system represents a first step towards the cost-effective and high-fidelity detection of enzyme biomarkers, thus enabling the decentralized diagnosis of injuries to the body's soft tissues.

6.2 Enzyme-based NAND gate for rapid electrochemical screening of traumatic brain injury in serum

Traumatic brain injury (TBI) is the leading cause of death and disability among the military and civilian population under 45, accounting for over 50 billion dollars in direct and indirect costs per annum in the US alone [114]. Early diagnosis of TBI is critical to improving the chances of survival among those who sustain these injuries as well as to mitigate prolonged cognitive impairments. To this end, the administration of treatment within the first 30 min following a TBI event can dramatically increase the odds for survival and substantially reduce long-term neurological disability [115]. However, at the present time, there is a deficit of robust diagnostic technologies that provide for the continuous monitoring of TBI, especially during the acute phase where long-term psychophysiological impairments may be reduced or prevented.

An enzyme-based logic gate that integrates the physiologically-relevant input biomarkers glutamate and lactate dehydrogenase has been developed to yield a rapid assessment of TBI, akin to the presentation of a blood glucose reading on a handheld glucose meter. Glutamate (GLU), a proteinogenic amino acid, is a freely-circulating metabolite and the most abundant excitatory neurotransmitter in the central nervous system (CNS) [116]. Conditions that have been implicated in glutamate abnormalities include ischemic neuronal injury [117], hypoglycemic injury [118], epilepsy [119], Alzheimer's disease [120], and traumatic brain injury [121, 122, 123]. Most notably, Suzuki and colleagues have observed statistically-relevant increases in circulating glutamate in blood samples from patients who have sustained TBI [124]. In this study, it was determined that circulating glutamate rises from nominal levels of 37.5 μM - 141.3 μM among patients who have sustained moderate to severe brain trauma.

Lactate dehydrogenase (LDH, E.C. 1.1.1.27), a cytoplasmic enzyme that catalyzes the interconversion of lactate and pyruvate in the presence of the coenzymes nicotinamide adenine dinucleotide (NAD^+) and its reduced form (NADH),

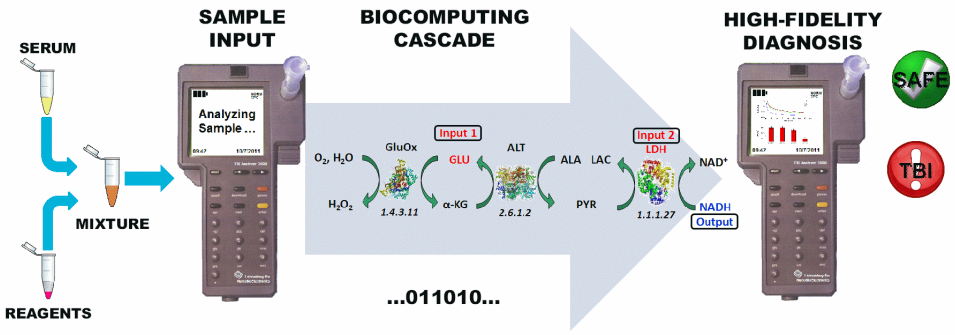

Figure 6.5: *Biocomputing concept illustrating the sample preparation and analysis routines.*

respectively, is normally present in high concentrations in the CNS [125]. Upon tissue damage and hemolysis, LDH activity has been shown to increase from normal circulating levels of around 150 U L^{-1} [126] to over 1000 U L^{-1} in pathological occurrences of tissue damage [105] and, more specifically, damage to the nervous tissue [127]. LDH complements glutamate as a biomarker of broader diagnostic scope and can be employed as a redundancy check on the assessment of a pathological state in an **AND** or **NAND** enzyme logic gate configuration, thereby significantly reducing the occurrence of false positives. In either configuration, the output of the logic gate would only change state when both inputs are 'high', i.e. at pathological levels or (**1**,**1**), thereby providing indication that a TBI has occurred. In the **AND** gate incarnation, the (**1**,**1**) level of the input biomarkers will result in a 'high' output, i.e. logic '**1**', and can be ascribed to a truth table. Conversely, the **NAND** gate will yield a 'low' output, i.e. logic '**0**' only when the (**1**,**1**) level of the input biomarkers is presented and its operation can also be ascribed to a truth table. Naturally, it is expected that the values reported for GLU and LDH will fluctuate among the general population. However, a distinct advantage of the enzyme logic-based approach is that an injury threshold is implemented between the normal and pathological levels of the biomarkers, above (or below) which a positive diagnosis for injury is presented. In this case, it is statistically expected that an overwhelming majority of cases will be identified, despite the wide distribution

inherent in the levels of the biomarkers among the population.

Enzyme-based biocatalytic cascades that implement Boolean functions have been shown to effectively integrate patterns of multiple biomarkers, thereby extracting a more detailed assessment of the nature and severity of injury [47]. In this regard, multiple biomarkers of varying specificity towards the injury can be integrated in the cascade to improve the reliability of the diagnosis and yield a simple '**YES**'/'**NO**' evaluation [73]. In this manner, enzyme-based logic gates have been previously employed for the assessment of such conditions as soft tissue injury, liver injury, abdominal trauma, hemorrhagic shock, and oxidative stress, to name a few [128, 129]. Moreover, studies have investigated the use of enzyme-based logic gates for the diagnostic assessment of TBI in buffer [130] and human serum samples [131]. However, these gates were relegated to operation in the optical domain (absorbance vs time), which requires a sophisticated benchtop spectrophotometer and therefore are not amenable to rapid, cost-effective evaluation. The evolution of an electrochemical analog that processes clinically-established TBI biomarkers would represent a significant diagnostic advancement - such logic gates can be integrated into rapid and easy-to-use strip-based diagnostic devices with an embedded reagent layer, akin to glucose test strips [10].

The study presented below describes the development of a rapid amperometric assay for screening patients suspected to have sustained traumatic brain injury. Specifically, a biocatalytic cascade operating in analogous fashion to a **NAND** Boolean logic gate has been designed, optimized, and characterized to process relevant fluctuations in the levels of the serum-based biomarkers GLU and LDH. Upon detecting pathological levels of both biomarkers that exceed a predefined threshold taken from clinical data, the gate is able to trigger an immediate alert. Moreover, the gate is shown to mitigate the effect of physiological and electroactive sources of interference that are normally found circulating alongside the biomarkers of interest. Owing to its robust design, the biocatalytic cascade is extended to operation in real human serum samples and is shown to function as intended at all logic states ascribed by a truth table. The electrochemical assay can readily conform to glucose meter-like technology (Fig. 6.5), thereby enabling

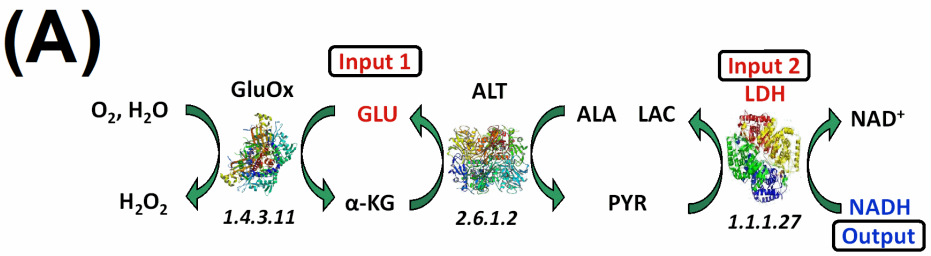

GLU	LDH	Output	Biomedical Conclusions
0	0	1	Normal
0	1	1	Tissue Damage
1	0	1	Anomalous
1	1	0	TBI

Figure 6.6: *(A) Biocatalytic cascade operating on the biomarkers glutamate (GLU) and lactate dehydrogenase (LDH) using a* ***NAND*** *gate topology with reduced nicotinamide adenine dinucleotide (NADH) as the output. (B) The equivalent logic system and (C) the corresponding truth table of the biocatalytic cascade. Biomedical conclusions are ascribed by the combinations of the input biomarkers. Note that the output signal with the logic value '**0**' implies a TBI diagnosis, while logic output '**1**' corresponds to all other physiological scenarios.*

rapid, on-the-spot assessment of TBI. Granted further clinical evaluation and validation, the logic gate TBI concept presented here could lead to improved survival rates and management of this debilitating condition.

Fig. 6.6A illustrates the biochemical cascade instigated by the GLU and LDH inputs. In this biocatalytic cascade, GLU is first converted to α-ketoglutarate (α-KG) via the enzyme glutamate oxidase (GluOx, E.C. 1.4.3.11). In the presence of α-KG, alanine transaminase (ALT, E.C. 2.6.1.2) will concomitantly convert the alanine (ALA) substrate to PYR, reconverting the α-KG back to GLU in the process. Finally, in the presence of PYR, LDH will oxidize the coenzyme NADH to NAD^+ while converting the PYR substrate to LAC. The Boolean logic gate equivalent to this cascaded process is shown in Fig. 6.6B. The biocatalytic process can be ascribed to a truth table, as represented in Fig. 6.6C. As is apparent from

the truth table, only the presence of elevated concentrations of both the GLU and LDH biomarker inputs will cause the output of the logic gate to change, thereby indicating that a TBI has been sustained. All other combinations of the biomarker inputs correspond to normal or anomalous physiological conditions and hence will not cause the output of the logic gate to change state.

The effect of pH was firstly investigated in a relatively simple system in the absence of GLU and GluOx. As such, the system employed two inputs: α-KG and LDH. Using NADH as the output signaling compound, a total sample volume of 350 μL was employed and consisted of 1 mM ALA, 300 μM NADH, and 4000 U L^{-1} ALT. Logical '**0**'/'**1**' levels of α-KG and LDH were established at 40 μM/140 μM and 150 U L^{-1}/1000 U L^{-1}, respectively. All constituents of the logic gate were dissolved in 0.1 M phosphate buffer (pH 7.40 and 7.97). All the reagents were dispensed in a quartz cuvette and mixed. Immediately following mixture, an optical absorbance measurement was recorded continuously at the characteristic absorption peak of NADH, 340 nm (at 37° C).

The electrochemical experiments were performed in a microcell and a sample volume of 60 μL was employed for each measurement. The following components were dissolved in 0.1 M phosphate buffer (pH 7.97) to realize **NAND** logic operation: 1 mM ALA, 300 μM NADH, 1500 U L^{-1} ALT, 250 U L^{-1} GluOx, and logical '**0**' and '**1**' levels of GLU (40 μM and 140 μM) and LDH (150 U L^{-1} and 1000 U L^{-1}). The reagents were mixed in a vial and incubated at 37° C in a heat-block for varying time periods (described below). Following the incubation period, methylene green (MG) was added to the solution to achieve a final concentration of 300 μM, and the solution was subsequently mixed and dispensed into the cell. A chronoamperogram was then recorded for 15 s with a stepped potential to -0.1 V *vs* Ag/AgCl. In order to investigate the interference of naturally circulating electroactive substances, 60 μM ascorbic acid (AA), 500 μM uric acid (UA), and 200 μM acetaminophen (AC) were spiked into the cell and the logic system was operated under the aforementioned protocol. Some constituents of the enzyme cascade exist within the circulatory system as metabolites, which may influence the proper operation of the gate. To study the effect of this class of interferents, physiologi-

cal levels of the following compounds were added to the reaction mixture: 6 mM LAC, 300 μM ALA, 40 μM PYR, 30 μM NAD^+, and 23 μM α-KG. The logic gate was operated as aforementioned in this study. In the serum experiments, ALA, NADH, ALT, and GluOx were dissolved in 0.1 M phosphate buffer (pH 7.97), and logical '**0**' and '**1**' levels of GLU and LDH were spiked in the serum sample (27 μL) to emulate physiological and pathological levels. Following this step, the reagents (27 μL) were added into the serum sample (1:1, v/v), and incubated for 6 min at 37° C. The concentrations of these components were identical to the previous experiments, with the exception of NADH, which was established at 600 μM due to the decreased electrochemical response in serum. Prior to electroanalysis, MG (6 μL)was added to the serum-reagent mixture to achieve a final concentration of 300 μM (total volume = 60 μL). Chronoamperograms were finally recorded for 15 s at a potential of -0.1 V *vs* Ag/AgCl.

The output of the **NAND** gate under investigation is represented by the concentration of NADH, which should be consumed to a greater degree at the (**1**,**1**) logic level than at any other logic level: (**0**,**0**), (**0**,**1**), and (**1**,**0**). Indeed, it is possible to detect NADH directly at the glassy carbon electrode (GCE) at a potential of 0.35 V *vs* Ag/AgCl with decent sensitivity, owing to the favorable oxidation of NADH at the electrode surface. The exact redox potential for the NADH oxidation may vary among glassy carbon electrodes and the surface treatment employed to prepare the surface for use. However, the presence of electroactive interferents in the serum such as AA, UA, and AC will produce significant levels of interference at this potential. Therefore, MG was employed as a redox mediator to facilitate the low potential selective detection of NADH at -0.1 V *vs* Ag/AgCl. At this low potential, physiological levels of UA (500 μM) and AC (200 μM) exhibited minimal influence on the current signal. However, physiological level of AA (60 μM) can produce a small, but perceptible contribution to the current signal, as shown in Fig. 6.7. Hence, from the results of this study, a potential of -0.1 V *vs* Ag/AgCl was selected to determine the quantity of NADH consumed by the gate (with the addition of MG).

Based on the logic gate machinery, optimal dynamic range between the

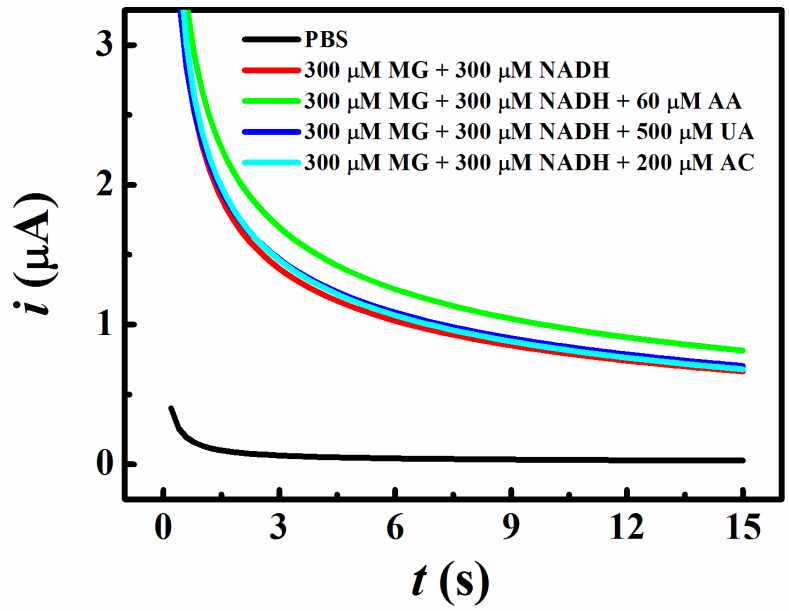

Figure 6.7: *Chronoamperograms of potassium phosphate buffer solution, 300 μM NADH in the absence and presence of different electroactive interferents (AA - ascorbic acid, UA - uric acid, AC - acetaminophen) with the methylene green (MG) mediator. Applied potential: -0.1 V* vs *Ag/AgCl.*

pathological level (**1**,**1**) and normal or anomalous physiological levels (**0**,**0**), (**0**,**1**), and (**1**,**0**) can be achieved through the optimization of the reaction conditions. Such optimization can result in a large difference in the NADH concentration between the (**1**,**1**) logic level and the others, thereby enabling the unambiguous determination of the injury state due to the establishment of a fixed decision threshold.

Preliminary experiments were performed in a relatively simple system without GLU and GluOx. Instead, α-KG and LDH were employed as the two inputs. The logical '**0**' and '**1**' levels of α-KG were the same as those for GLU (40 μM and 140 μM). The system also included 1 mM ALA, 300 μM NADH, 4000 U L^{-1} ALT, and logical '**0**'/'**1**' levels of LDH (150 and 1000 U L^{-1}), all dissolved in 0.1 M phosphate buffer. The effect of pH was studied for this system using optical absorbance measurements. The consumption profiles of NADH at four combinations of the logic levels were monitored at 340 nm with respect to time. The optimal pH of ALT and LDH is around 7.4 [111, 132], and between 7 and 9 for GluOx [133]. Although a pH 7.40 buffer was firstly selected as the reaction solution, the difference in the outputs between the logic levels (**1**,**0**) and (**1**,**1**) was not sufficient to discriminate them with high fidelity, as can be observed in Fig. 6.8A. Based upon the literature, we speculate that the activity of LDH in the enzyme cascade is comparatively high even at logical '**0**' level [134]. In order to obtain greater differentiation between the (**1**,**0**) and (**1**,**1**) logic levels, the pH of the system was adjusted to 7.97. At this pH, LDH exhibits reduced activity towards its substrate, albeit the activity of ALT is impacted to a lesser extent. From the optical absorbance profiles displayed in Fig. 6.8B, the consumption of NADH at the (**1**,**1**) level was well separated from the other logic levels. The pH 7.97 buffer was concomitantly selected as the host solution for further **NAND** gate investigations.

The activity of each enzyme employed in the biocatalytic cascade has a profound influence on the performance of the logic gate. With respect to the gate under study, one of the three enzymes in the cascade, LDH, serves as one of the inputs of the gate and its concentration must be established at specific values that correspond with physiological and pathological levels. The other two enzymes,

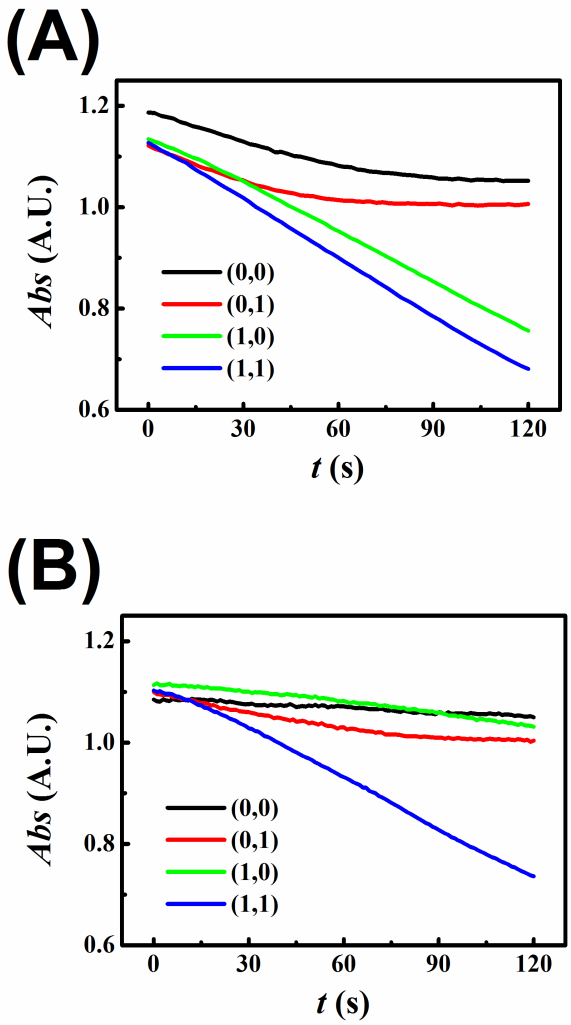

Figure 6.8: *Time-dependent optical signals illustrating the effect of pH upon the functionality of the α-ketoglutarate / lactate dehydrogenase (α-KG/LDH) enzyme cascade. The following components were dissolved in (A) pH 7.40 and (B) pH 7.97, 0.1 M potassium phosphate buffer: 1 mM alanine (ALA), 300 μM NADH, 4000 U L^{-1} alanine transaminase (ALT), 40 μM (logic '**0**') or 140 μM (logic '**1**') α-KG (37° C), and 150 ('**0**') or 1000 ('**1**') U L^{-1} LDH. The mixture was incubated at 37° C. Optical absorbance measurements were performed at λ = 340 nm.*

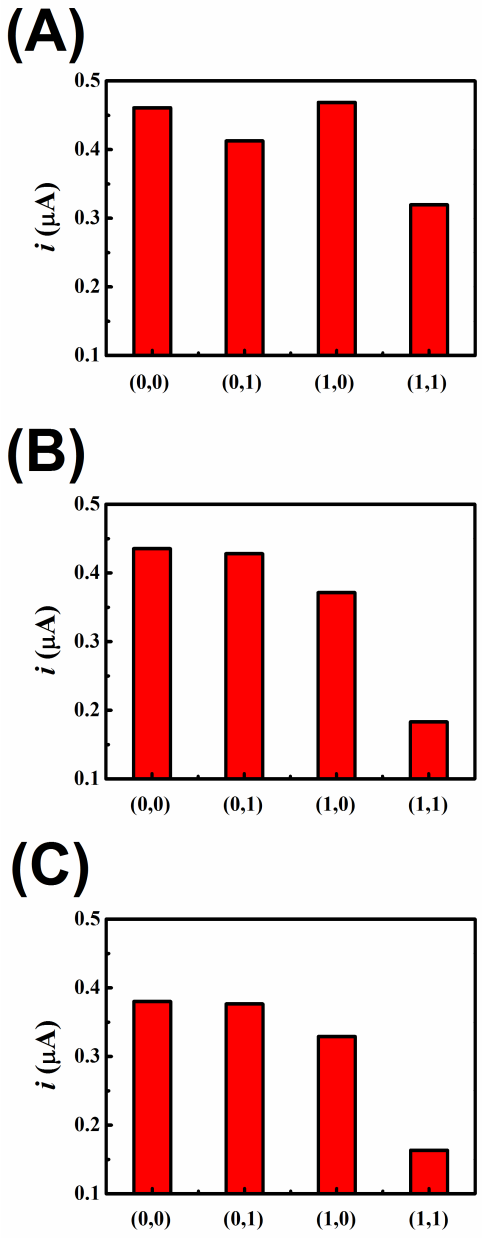

Figure 6.9: *Histogram of **NAND** logic operation for the corresponding combinations of input signals with different incubation time (4, 6 and 8 min). Electrochemical measurements at -0.1 V emphvs Ag/AgCl and the current was sampled at 15 s following the application of the potential step.*

ALT and GluOx, can be adjusted as desired to obtain satisfactory performance. Typically, high enzymatic activity can shorten the incubation time and enable rapid detection of the biomarker inputs. However, the excess usage of enzyme increases the cost of assay and, more importantly, may impose negative influence on the performance of the entire system. For example, although incubation time can be reduced if a greater quantity of ALT is employed in the assay, the electrochemical data indicate that increased ALT levels result in a decreased NADH electrochemical signal detected by the GCE. When varying concentrations of ALT are added to the 300 μM NADH solution, the amperometric response of the GCE is observed to decrease with increasing levels of ALT. As such, by employing ALT concentrations of 400, 1000, 1500. 2000, and 4000 U L^{-1}, the amperometric response to NADH on GCE decreased to 99.1, 89.2, 88.5, 68.3, and 45.4% of the original value, respectively. Conversely, varying the LDH within the pathophysiological range resulted in nearly no change of the amperometric signal obtained from the experiments. In order to achieve a comparatively fast assay and obtain a highly-sensitive response, 1500 U L^{-1} ALT was chosen as the final concentration in the reaction mixture. Meanwhile, the concentration of GluOx was also optimized. 125, 250, and 500 U L^{-1} GluOx were added to the reagent-enzyme solution, and the mixture employing 250 U L^{-1} GluOx exhibited optimal performance in terms of speed and sensitivity. Thus, 250 U L^{-1} GluOx was chosen for subsequent investigations.

The incubation time of the enzyme cascade is also a critical parameter that has profound effect on the operation of the enzyme logic gate. On the one hand, if the incubation time is not of sufficient duration, the difference between the (**1**,**1**) logic level and the other three would not be large enough to differentiate them unambiguously. On the other hand, an excessive incubation time would not only reduce the appeal of the enzyme logic assay methodology, but would also exhaust the supply of NADH in the cascade, which would also result in detection ambiguity.

Various incubation times (4, 6, and 8 min) were studied using a gate with fixed enzyme and substrate concentration. The results indicate that a 4 min incubation time will not yield satisfactory discrimination between the physiological and

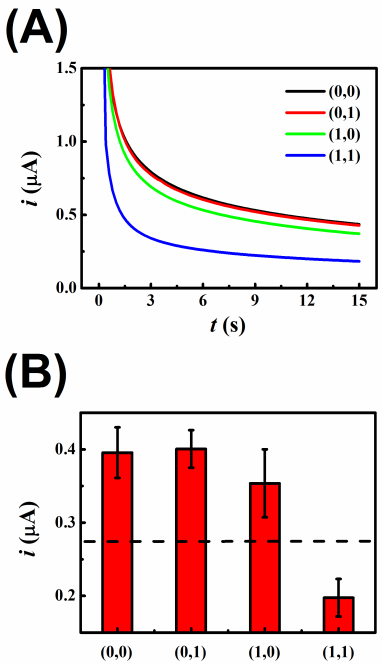

Figure 6.10: *(A) Chronoamperometric curves generated by the TBI gate upon application of various combinations of the GLU and LDH logic inputs (in buffer solution). (B) Histogram featuring the* ***NAND*** *logic operation for the corresponding combinations of the input signals. Electrochemical measurements were performed at -0.1 V* vs *Ag/AgCl and the current was sampled at* t *= 15 s. Dashed line indicates the decision threshold for the realization of* ***NAND*** *gate operation.*

pathological logic levels. With an incubation time established at 6 min, optimal performance is achieved (Fig. 6.9).

Inline with the goal of developing analytical methods that can identify TBI status (i.e. logic level (**1**,**1**)), from other physiological states, and based on the results obtained above, the pH of the reaction mixture was established at 7.97. The concentrations of the substrates, co-substrates, co-enzymes, and enzymes in the cascade were established at optimal levels: 1 mM ALA, 300 μM NADH, 1500 U L^{-1} ALT, and 250 U L^{-1} GluOx. Subsequent to mixture of these reagents, the mixture was incubated at 37° C for 6 min. Following incubation, MG was added to achieve a final concentration of 300 μM. Chronoamperograms were subsequently recorded for 15 s at -0.1 V *vs* Ag/AgCl (the oxidation potential exhibiting the greatest signal-to-noise ratio (SNR)).

Fig. 6.10A displays chronoamperograms obtained at the GCE by the TBI gate upon application of various input combinations. A sizeable separation between the chronoamperograms representing the (**1**,**1**) logic level and the three other levels is observed. At 15 s sampling time, the difference in current between the (**1**,**1**) and (**1**,**0**) logic levels is 156 nA, as shown in Fig. 6.10B, which enables the unambiguous determination of the TBI state. The histogram indicates that a straightforward decision threshold, which was fixed at 276 nA, could be instituted to realize high-fidelity **NAND** gate operation.

In order to migrate the enzyme logic gate diagnostic concept to real serum samples, the effect of various undesired co-existing biomolecules that could pose a substantial obstacle to achieving high-fidelity detection of the biomarkers must be investigated in greater detail. Consequently, the relevant physiological interferents were introduced into the assay and their impact on the logic gate performance was assessed in detail.

As aforementioned, the presence of electroactive interferents such as AA, UA, and AC within the serum can exert notable influence upon the detection of NADH and hence the entire TBI gate. To study the interference of these electroactive compounds, 60 μM AA, 500 μM UA, and 200 μM AC were introduced into the optimized assay. Indeed, the addition of the electroactive compounds yields a

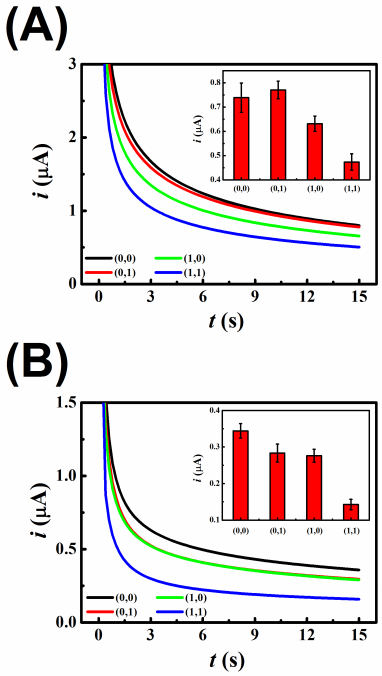

Figure 6.11: *(A) Chronoamperometric curves generated by the TBI gate upon application of various combinations of the GLU and LDH logic inputs (in buffer solution) in the presence of 60 μM AA, 500 μM UA, and 200 μM ACT. Inset represents the corresponding histogram for the combinations of input signals. Other conditions are the same as stated in Fig. 4. (B) Chronoamperometric curves generated by the TBI gate upon application of various combinations of GLU and LDH input in the presence of 6 mM lactate (LAC), 300 μM ALA, 40 μM pyruvate (PYR), 30 μM nicotinamide adenine dinucleotide (NAD^+), and 23 μM α-KG. Inset represents the corresponding histogram for the combinations of input signals. Other conditions are the same as stated in Fig. 6.10.*

notable change in the chronoamperograms (and corresponding histograms) of the various input combinations (Fig. 6.11A). While it is apparent that the magnitude of the background current increased (owing to the contribution of the electroactive substances), the relative difference between the logic levels (**1**,**0**) and (**1**,**1**) lessened. However, the absolute difference in current levels was 158 nA, which provides sufficient margin for differentiation.

Besides the presence of electroactive compounds within the serum sample, the existence of several other physiologically relevant co-existing compounds that naturally occur within the circulatory system may also interfere with the proper operation of the assay, especially those metabolites that serve as substrates and products of the logic gate. For example, lactate (LAC), a product of the gate, serves as an indicator of muscular fatigue and injury and has been shown to fluctuate between 1.6 mM and 6 mM during such events [113]. To investigate the effect of these metabolites, physiological levels of the following compounds were employed in the assay: 6 mM LAC, 300 μM ALA, 40 μM PYR, 30 μM NAD^+, and 23 μM α-KG. The results indicate that, in the presence of these metabolites, the logic (**0**,**1**) level migrated from the proximity of the logic (**0**,**0**) level to near that of (**1**,**0**). Nevertheless, the wide separation between the (**1**,**0**) and (**1**,**1**) logic levels (133 nA) enabled the establishment of a fixed decision threshold and unambiguous distinction between the logic levels (Fig. 6.11B).

To achieve the aim of real-time detection of TBI in clinical samples, the gate was migrated to operation in human serum. A similar protocol as that leveraged for the study in buffer solution was followed for the serum investigation. Four components of the gate, ALA, NADH, ALT, and GluOx were initially mixed in a 0.1 M phosphate buffer (pH 7.97) host. Thereafter, logic '**0**' and '**1**' levels of GLU and LDH were spiked into serum samples to emulate physiological and pathological levels. Subsequently, the mixture was added into the spiked serum sample (1:1 in volume) and the mixture was left to incubate for 6 min at 37° C. Following this routine, MG was added to the solution and chronoamperograms were recorded. The biochemical complexity of the serum matrix was found to severely hinder the detection of NADH. The initial NADH concentration of 300 μM was not of suffi-

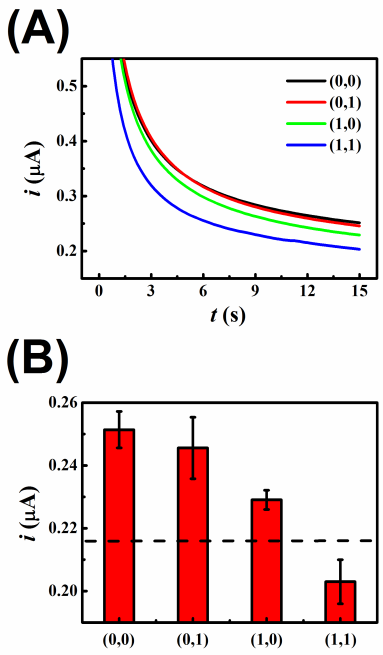

Figure 6.12: *(A) Chronoamperometric curves generated by the TBI gate upon application of various combinations of the GLU and LDH logic inputs in human serum. (B) Histogram featuring the* ***NAND*** *logic operation for the corresponding combinations of input signals. Other conditions are the same as stated in Fig. 6.10. Dashed line indicates the decision threshold for the realization of* ***NAND*** *gate operation.*

cient level to be detected using both input combinations. This can be attributed to both the efficient oxidation of NADH in serum and the blockage of the electrode surface by the proteins and other high-molecular weight biochemical species present in serum. For this reason, the concentration of NADH in the logic gate system was elevated to 600 μM. As shown in Fig. 6.12, at 15 s sampling time, the differential current magnitude between the (**1**,**1**) and (**1**,**0**) logic levels was 26 nA. From the results of six independent experiments, the relative standard deviation (RSD) of the output signals (using the four logic combinations) was in the range of 2.50% - 6.44%, which is indicative of good repeatability with respect to the biocatalytic operation and electrochemical detection. The histogram indicates that a fixed decision threshold of 216 nA could be instituted, which yields a straightforward and unambiguous diagnosis of pathophysiological status. The results of serum operation also indicate that the chemical constituents present in serum have a sizeable effect on the output levels. The differential current magnitude between the (**1**,**1**) logic level and the other three levels is reduced noticeably when compared with the buffer experiments. In particular, the difference in current between the (**1**,**1**) logic and (**1**,**0**) logic levels in serum is only one-sixth of that in buffer solution. However, the relative difference is still sufficiently large to produce an unambiguous determination of TBI, owing to the small RSD achieved.

A rapid amperometric assay for TBI screening in real human serum samples has been designed and evaluated. A biocatalytic cascade operating in analogous fashion to a **NAND** Boolean logic gate has been designed, optimized, and characterized to process relevant fluctuations in the levels of the serum-based biomarkers glutamate and lactate dehydrogenase. Upon detecting pathological levels of both biomarkers that exceed a pre-defined threshold taken from clinical data, the gate is able to trigger an immediate alert. Moreover, the gate has been shown to mitigate the effect of physiological and electroactive sources of interference that are normally found circulating alongside the biomarkers of interest. Owing to its robust design, the biocatalytic cascade has been extended to operation in real human serum samples and is shown to function as intended at all logic states ascribed by a truth table. For this reason, the concept presented in this study embodies

considerable potential for enabling the rapid assessment of TBI through a simple glucose-like blood test, eventually leading to blood glucose-like evaluation. As a result of the unification of robust amperometric techniques with new paradigms in the biocomputing domain, the presentation of a rapid assessment of TBI is facilitated, thereby opening new avenues to the detection of this injury in the acute phase. Further improvements, along with intensive clinical validation, are required before decentralized TBI testing can be achieved and employed for improving survival rates as well as the management of this debilitating condition.

6.3 High-fidelity determination of security hazards via Boolean biocatalytic cascades

Threat detection is a critical element in preventing terrorist attacks. Innovative sensor technology is thus urgently needed for the reliable and rapid assessment of threats imposed by chemical agents [135]. Most of the efforts towards this objective have focused on the development of field-based analytical instrumentation for the determination of trace levels of a single hazardous chemical compound [136]. However, despite considerable efforts in security screening technologies, there still remains an urgent need for an easy-to-use field-deployable kit that can assess multiple chemical threats (i.e. explosives and nerve agents) in a rapid manner and alert the operator when a hazard has been encountered [137].

A novel biocatalytic cascade has been introduced that is able to assess the presence of different types of threats in a rapid and reliable manner. Such unique bioprocessing of distinct classes of threat agents is illustrated for the first time for the detection of various nitroaromatic explosives and organophosphate nerve agents using an enzyme-based logic gate. In this manner, a simple assay can replace two different time-consuming test protocols commonly used for assessing each of these unique threats. Molecular substrates have been utilized as inputs to devices that exploit chemical computation [138, 139, 140]. Biocatalytic cascades that take the form of enzyme logic gates represent an attractive route for developing high-fidelity analytical devices [47, 108]. By forming biochemical cascades that

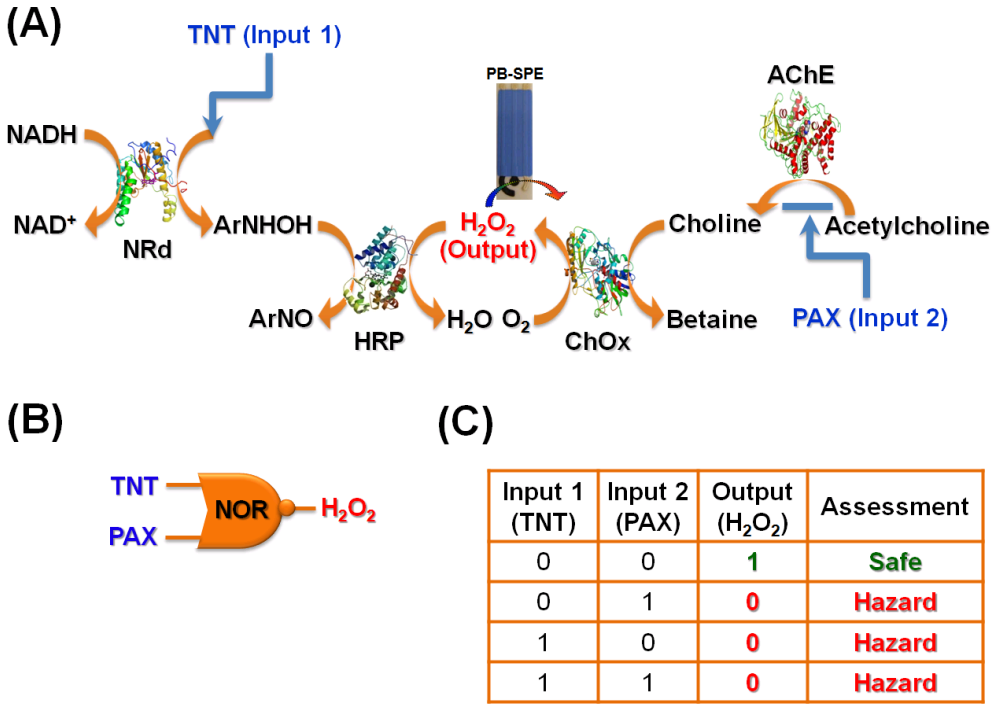

Input 1 (TNT)	Input 2 (PAX)	Output (H_2O_2)	Assessment
0	0	1	Safe
0	1	0	Hazard
1	0	0	Hazard
1	1	0	Hazard

Figure 6.13: *(A) Biocatalytic cascade used to perform **NOR** logic operation in connection to trinitrotoluene (TNT) and paraoxon (PAX) inputs; (B) the equivalent logic system, and (C) the corresponding truth table with assessment drawn from the combinations of the input signals.*

implement logical functions, according to Boolean principles, a threshold can be established above or below which a reliable indication of an abnormal event can be detected. A distinct advantage of enzyme logic gates is embodied in their innate ability to integrate several inputs and yield a rapid assessment of complex sensing scenarios in simple '**YES**'/'**NO**' terms. Such biocatalytic logic gates have recently been demonstrated to yield **XOR** [43] and **NAND** [134] operations, as well as higher-order logical functions in connection with several pathophysiological situations [128]. In the following section, the bioprocessing of distinct classes of threat agents via a **NOR** gate is illustrated, which can lead to a rapid '**YES**'/'**NO**' assessment and alert regarding the presence of either explosives and/or nerve agents in connection with the electrochemical monitoring of a single output at a disposable screen printed electrodes (SPE).

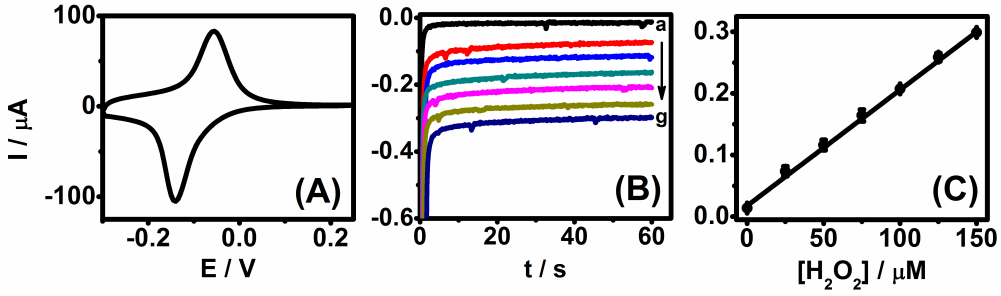

Figure 6.14: *(A) Cyclic voltammogram recoded at the PB-modified SPE in 50 mM phosphate buffer (pH 7.2); scan rate: 50 mV* s^{-1}*. (B) Chronoamperograms recorded for the detection of* H_2O_2 *at SPE (a* $\rightarrow$ *g: 0* μ*M to 150* μ*M, in 25* μ*M steps) in 50 mM phosphate buffer;* E_{APP} *= -0.2 V* vs *Ag/AgCl. (C) Calibration curve generated from (B).*

The present system is able to detect the presence of different security-relevant analytes, compared to conventional biosensors that commonly analyze only one specific substrate. The new enzyme logic capability is evaluated and illustrated using 2,4,6-trinitrotoluene (TNT) and paraoxon (PAX) as the model inputs to a **NOR** gate, as well as towards the detection of the 2,4-dinitrotoluene (DNT) explosive and methyl parathion (MPT) nerve agent. The enzyme logic approach harnesses the inherent selectivity of biocatalytic processing, thereby mitigating cross-reactivity and making the separation requirement unnecessary, leading to a greatly simplified and rapid assay. In this fashion, a qualitative alert can be tendered to the operator in regards to the presence of harmful agents. This approach is particularly attractive to address screening scenarios aimed to determine the presence of a harmful agent rather than to identify the exact nature of such threat.

As illustrated in Fig. 6.13A, the new logic gate employs a reaction cascade catalyzed by four enzymes: nitroreductase (NRd, E.C. 1.6.99.3), horseradish peroxidase (HRP, E.C. 1.11.1.7), acetylcholinesterase (AChE, E.C. 3.1.1.7), and choline oxidase (ChOx, E.C. 1.1.13.17). The four enzymes are leveraged as the backbone of the catalytic logic gate in order to process the TNT and PAX chemical inputs. On the right side of Fig. 6.13A, H_2O_2 is produced from the catalytic coupling of AChE/ChOx and acetylcholine. On the left side, H_2O_2 is partially depleted in the

presence of the nitroaromatic explosive substrate through a NRd/HRP biocatalytic cascade. An enabling feature of the cascade is the fact that the H_2O_2 level can also be reduced through the inhibition of AChE by an organophosphate nerve agent. Fig. 6.13B shows the equivalent logic gate of the cascade whereby H_2O_2 is used as the output signaling compound. Accordingly, as can be seen from the truth table in Fig. 6.13C, a decrease in the H_2O_2 level (and hence the current output) below a selected decision threshold is indicative of a "Hazardous" situation corresponding to the presence of an explosive and/or nerve agent, in line with the operation of a Boolean **NOR** gate.

The fabrication of screen printed electrodes has been described earlier. The generation of an oxidizable hydroxylamine product (from the NRd enzyme) necessitates lowering of the detection potential of the H_2O_2 output. Modification of the SPE transducer with a Prussian Blue (PB) mediator offers effective and selective H_2O_2 detection at an extremely low potential. Accordingly, SPEs were prepared in accordance with the procedure detailed by Karyakin et al [141]. Briefly, a 0.1 M KCl / 0.1 M HCl solution was prepared and the appropriate quantity of both $K_3Fe(CN)_6$ and $FeCl_3$ were dissolved in this solution in order to achieve 4 mM final concentration of each of these compounds. This solution was subsequently dispensed on the SPE and 0.4 V *vs* Ag/AgCl was applied for 2 min to the working electrode. After this step, the electrode was cured at 100° C for 1 hr in a convection oven. The PB-modified SPE was then electrochemically activated by performing 40 cyclic voltammetric scans from -0.2 V to 0.5 V *vs* Ag/AgCl in the 0.1 M KCl / 0.1 M HCl solution.

Based on the cyclic voltammetric characterization of the PB-modified SPE (provided in Fig. 6.14), a potential of -0.20 V *vs* Ag/AgCl was selected for the detection of H_2O_2, thereby minimizing potential electroactive interference and potential false results. Fig. 6.14A shows the cyclic voltammogram recorded using the PB-modified SPE in 50 mM phosphate buffer (pH 7.2) at a scan rate of 50 mV s^{-1}. A pair of redox peaks is observed at E_{pc} = -0.140 V *vs* Ag/AgCl and E_{pa} = -0.056 V *vs* Ag/AgCl, which is characteristic of PB electrochemistry. Further, the electrocatalytic activity of the PB-modified SPE was evaluated towards the reduc-

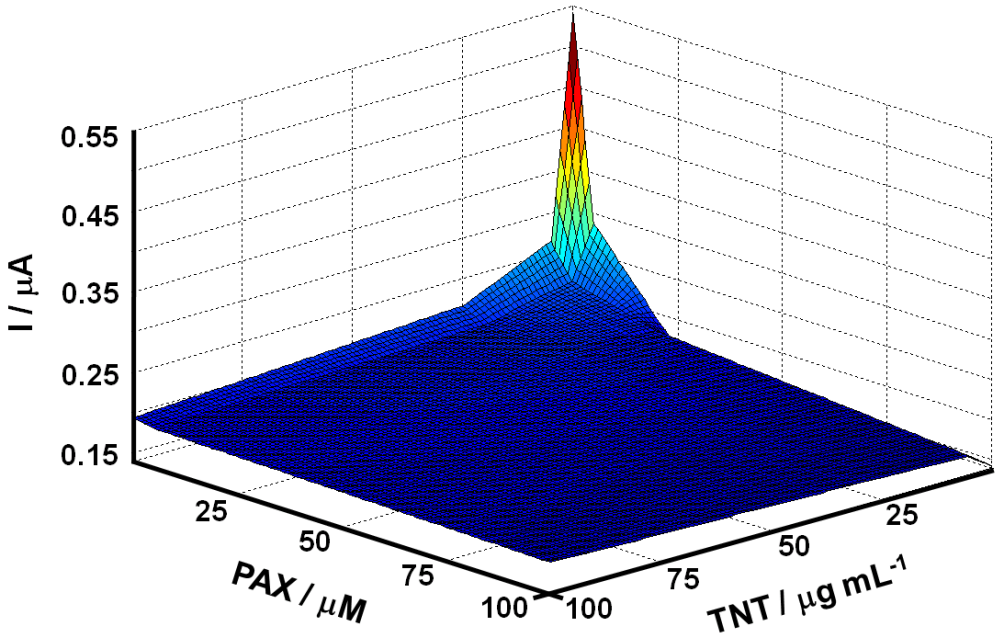

Figure 6.15: *Gate mapping illustrating the functional dependence between the levels of the TNT and PAX inputs and the output current obtained. The output currents are sampled using chronoamperometry (30 s) with inputs levels of 0, 5, 25, 100 (μg mL^{-1} and μM for TNT and PAX, respectively). The 2D linear interpolation was performed using a 20× oversampling algorithm in* MATLAB®.

tion of H_2O_2. Fig. 6.14B displays the chronoamperograms recorded for increasing concentrations of H_2O_2 (0 μM to 150 μM, in 25 μM increments). The corresponding calibration plot is shown in Fig. 6.14C. The current was sampled at $t = 60$ s, and a linear regression shows a high degree of correlation among increasing levels of H_2O_2 with a correlation coefficient of 0.998 ($n = 3$). The resulting PB-modified electrode strip offers highly selective and sensitive measurements of H_2O_2 down to the 5 μM level (Fig. 6.14B and C).

50 mM phosphate buffer (pH 7.2) containing 5000 U L^{-1} NRd, 300 kU L^{-1} HRP, 150 μM reduced nicotinamide adenine dinucleotide (NADH), 100 U L^{-1} AChE, and 5000 U L^{-1} ChOx was mixed with the desired concentrations of TNT and PAX to obtain the corresponding (**0**,**0**), (**0**,**1**), (**1**,**0**), and (**1**,**1**) logic levels. Following a 2 min inhibition period, 1 mM acetylcholine (ACh) was added and then incubated further for an additional 5 min to allow the reaction to ensue. The solution was then dispensed onto the electrode surface. Chronoamperometric detection of the H_2O_2 product was performed at the PB-modified SPE at a step potential of -0.2 V *vs* Ag/AgCl) and the current value was extracted at the 30^{th} s. Experiments were performed at least three times at each concentration to ensure the integrity of the results.

To validate the operation and optimize the performance of the constituent reactions of the logic gate, the complete system was mapped (via amperometric measurements) by 'scanning' the concentrations of the TNT and PAX inputs from 0 μg mL^{-1} to 100 μg mL^{-1} and 0 μM to 100 μM, respectively. The data points were subsequently interpolated to generate the smooth contour profile shown in Fig. 6.15. As expected for the operation of logic gates, the gradient of the current response ∇i([TNT],[PAX]) is maximized in the absence of both inputs (maximum current of 0.54 μA). In accordance with the operational functionality of a **NOR** gate, minor (low micromolar) increases in the levels of either of threat input yielded a dramatic decrease in the current response to less than 0.20 μA.

Four distinct operating points were selected from the gate mapping presented in Fig. 6.15 for further evaluation to validate that the behavior of the gate system at a given operating point was in agreement with its corresponding truth

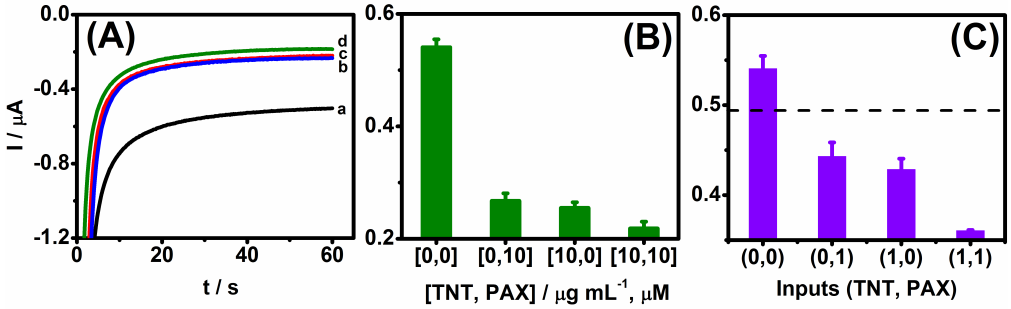

Figure 6.16: *(A) Chronoamperograms of the **NOR** enzyme logic gate corresponding to the [TNT (μg mL^{-1}), PAX (μM)] = (a) [0,0], (b) [0,10], (c) [10,0], and (d) [10,10] inputs for three independent trials. (B) Bar chart comparing the magnitude of the response for the four combinations of the inputs. (C) Bar chart of the **NOR** gate operating at its limit of detection for the four logic levels (TNT, PAX) = (**0**,**0**), (**0**,**1**), (**1**,**0**), and (**1**,**1**) for three independent trials. The '**0**' logic levels of both TNT and PAX represent the absence of these compounds in the assay while the '**1**' level corresponds to 1.5 μg mL^{-1} TNT/1.25 μM PAX. The dashed line indicates the decision threshold (0.49 μA).*

table. As such, chronoamperometry was performed for all four combinations of TNT/PAX corresponding to 0 μg mL^{-1} and 10 μg mL^{-1}/10 μM. Fig. 6.16A elucidates that a **NOR** behavior is obtained for [TNT (μg mL^{-1}), PAX (μM)] = [0,0], [0,10], [10,0], and [10,10], with the [0,0] 'Safe' level isolated from the other concentrations by 0.29 μA (sampling at 30 s). The corresponding bar chart, shown in Fig. 6.16B, illustrates the large dynamic range associated with the selected levels, along with a low standard deviation of 15 nA.

In order to demonstrate the versatility of the enzyme logic gate and its ability to process a wide array of inputs, the study was extended for the detection of other threats, such as the DNT explosive and MPT nerve agent. Fig. 6.17 illustrates the performance of the **NOR** gate in connection to various combinations of the TNT, PAX, DNT, and MPT inputs. DNT yielded a decrease in the H_2O_2 concentration comparable to TNT, owing to the broad catalytic specificity of NRd toward nitroaromatic substrates. MPT was slightly less inhibitive toward AChE than PAX, resulting in a 14% increase in the H_2O_2 level (compared with equivalent levels of PAX), although the dynamic range between the levels remained high. It should be noted that the proposed biocatalytic cascade exhibits broad specificity

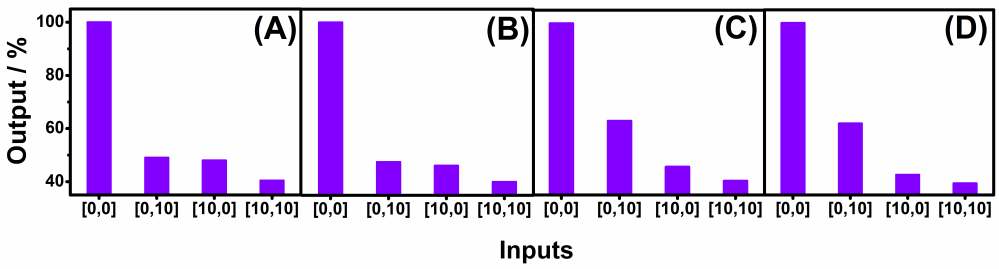

Figure 6.17: *Bar charts representing the magnitude of the response for four different combinations of the inputs [Input 1 ($\mu g\ mL^{-1}$), Input 2 (μM)] = (A) [TNT, PAX]; (B) [DNT, PAX]; (C) [TNT, MPT] and (D) [DNT, MPT]. The output current has been normalized to facilitate comparison.*

for substrates that comprise the nitroaromatic and organophosphate classes of compounds. Therefore, it is expected that the enzyme logic gate will function reliably for most of the compounds (explosive and nerve agent) that present a security hazard.

The first example of an enzyme logic gate able to issue a digital alert when assessing the presence of both explosive compounds and nerve agents has been presented. Leveraging **NOR** logic gate operation, an analytically relevant threshold could be implemented in accordance with a truth table in order to provide a qualitative '**YES**'/'**NO**' alert regarding the presence of different types of threats. The concept could be readily expanded towards rapid warning of other threats in connection to different logic gates, and should be coupled with a follow-up identification of the exact threat. The high sensitivity of the PB mediator towards H_2O_2 also facilitates the direct screening of peroxide -based explosives using the same field-deployable SPE assay (but without the logic gate machinery). The ability to assess the presence of different types of hazards holds considerable promise for enhancing and simplifying a variety of security screening protocols.

Portions of Chapter 6, section 1 were taken from J.R. Windmiller, G. Strack, M.C. Chuang, J. Halámek, P. Santhosh, V. Bocharova, J. Zhou, E. Katz, and J. Wang. Boolean-format biocatalytic processing of enzyme biomarkers for the diagnosis of soft tissue injury. *Sensors and Actuators B*, 150(1):285–290, 2010. The

dissertation author was the primary investigator and author of this manuscript.

Portions of Chapter 6, section 2 were taken from N. Zhou, J.R. Windmiller, G.V. Ramírez, M. Zhou, J. Halámek, E. Katz, and J. Wang. Enzyme-based NAND gate for rapid electrochemical screening of traumatic brain injury in serum. *Analytica Chimica Acta*, 703(1):94–100, 2011. The dissertation author was a co-author of the manuscript and had substantial original contributions to this work.

Portions of Chapter 6, section 3 were taken from M.C. Chuang, J.R. Windmiller, P. Santhosh, G.V. Ramírez, E. Katz, and J. Wang. High-fidelity determination of security threats via a Boolean biocatalytic cascade. *Chemical Communications*, 47(11):3087–3089, 2011. The dissertation author was a co-author of the manuscript and had substantial original contributions to this work.

Chapter 7

Systems-level considerations

The pessimist sees difficulty in every opportunity.
The optimist sees the opportunity in every difficulty.

—Winston Churchill

With a toolbox of proven, physiologically-relevant enzyme logic gates available at the designer's disposal, efforts must ultimately be directed at scaling the technology to enable increased processing capabilities and robustness. In this vein, the construction of useful enzyme logic-based systems demand that certain functionality (i.e. multiplexing, switching) and performance metrics (such as noise and dynamic range) are carefully considered in the design process, in direct analog to the aggregation of conventional logic gates into utilitarian digital systems. Accordingly, efforts were aimed at further increasing the level of sophistication and performance of the aforementioned logic gates via design, modeling, and optimization iterations to achieve the desired operational criteria.

7.1 Multiplexing of injury codes for the parallel operation of enzyme logic gates

Recent demonstrations of enzyme logic gates [27, 28, 29, 30, 31] and their networks [142, 143, 144, 145] have shown substantial potential for the determination of conditions characteristic of hemorrhagic shock (HS) and traumatic brain

injury (TBI) [42, 43]. Despite the current state-of-the-art in this field [108, 146], only single sensors / single gates have been proposed for injury diagnosis [47]. An array-like concept employing multiple enzyme logic gates would enable high-fidelity diagnosis while benefiting from the parallelization and inclusion of further diagnostic capabilities that a biosensor array provides. A cornerstone merit of enzyme logic-based sensors lies in the reduced complexity of the electronic backbone required for the determination of a pathophysiological state through the utilization of biocatalytic information processing.

A novel biocomputing 'injury coding' diagnostic technique has been developed that can multiplex multiple injuries and assign each pathophysiological state a distinct 'injury code', thereby enabling highly parallelized operation in the digital domain while minimizing the complexity of the analog electronic integration required for multiple-potentiostat electrochemical devices. Due to the Boolean nature of the enzyme logic concept [27, 28, 29, 30, 31], all normal physiological states (upon implementation of the **AND** logic operation) can be ascribed a logical '**0**' value in the biochemical domain, which accounts for most of the injury combinations, prior to the transduction of the signals to the electrical domain. Only pathological conditions causing a change in the outputs relative to a pre-defined threshold level would result in a logical '**1**' value, thereby alleviating the complex decision routines that must be performed in the electronic domain. It should be noted that the inverted logic values '**1**' and '**0**' should be applied for normal and pathological conditions, respectively, upon application of the **NAND** logic operation. As such, n outputs can be multiplexed into an n-bit word or 'injury code' for a comprehensive assessment of health conditions. A unique 'injury code' can thus be ascribed to a specific pathophysiological state in accordance with a truth table. A simple look-up table in digital logic circuitry could thus be employed to determine which injuries, if any, have been sustained in accordance with this distinct sequence of bits. In this manner, an array of n individual dual-input enzyme logic gates (each evaluating a separate injury) can assess 2^n possible pathological conditions among 2^{2n} possible physiological states. The new concept represents the first demonstration of the parallelization of enzyme logic gates applied to diag-

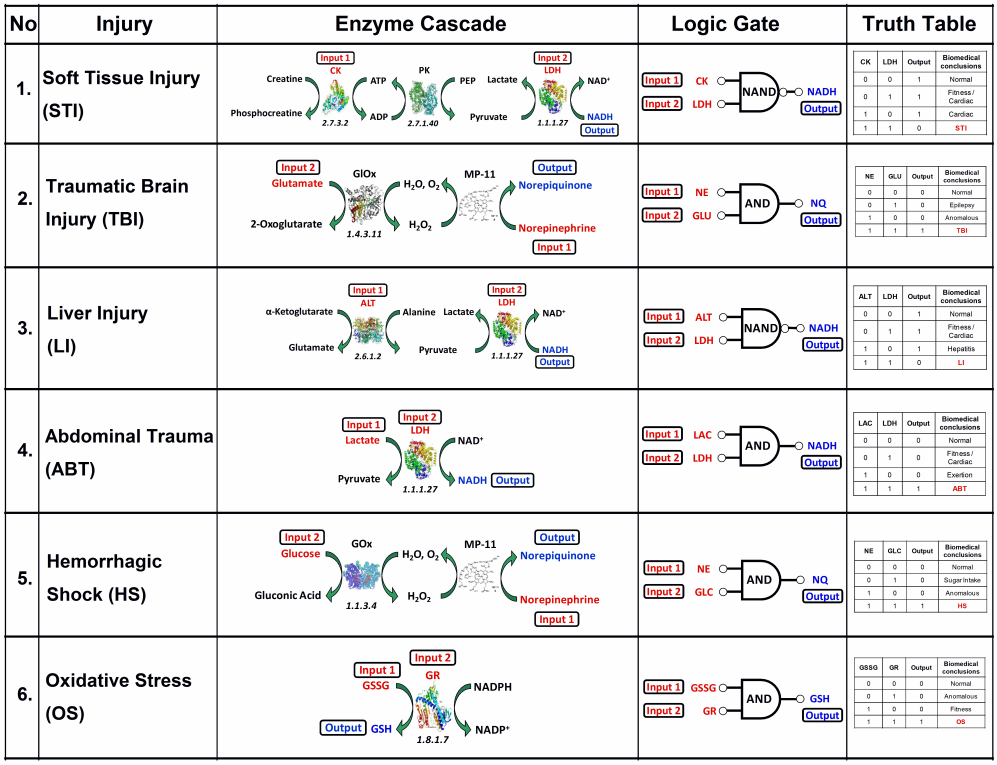

Figure 7.1: *Enzyme cascades, equivalent logic gates, and truth tables corresponding to six unique injuries: soft tissue injury (STI), traumatic brain injury (TBI), liver injury (LI), abdominal trauma (ABT), hemorrhagic shock (HS), and oxidative stress (OS).*

nostic merits, as well as the simultaneous multiplexing of the outputs of multiple logic gates in the biochemical domain into a binary injury code.

To illustrate the new concept and in accordance with the goal of rapid and reliable diagnosis of multiple injury states, an array of two **NAND** and four **AND** enzyme logic gates is assembled, as illustrated in Fig. 7.1. Six different pathological conditions are assessed including soft tissue injury (STI), traumatic brain injury (TBI), liver injury (LI), abdominal trauma (ABT), hemorrhagic shock (HS), and oxidative stress (OS) using twelve biomarker inputs. Optical absorbance and amperometric characterization of the six-gate system are conducted in order to verify compliance with a truth table as well as to ensure proper differentiation between the logical '**0**' and '**1**' output levels. The outputs of the six logic gates

were subsequently multiplexed to yield a distinct 6-bit injury code representing 64 unique pathological conditions among 4096 possible physiological scenarios. This leads to an additional (comprehensive) level of information on the overall nature of the injury, beyond the assessment of individual injuries performed by the individual gates. The system integration of clinically relevant enzyme logic gates and the subsequent multiplexing of their outputs into a cohesive injury code thus offer great promise for the rapid, reliable, and decentralized assessment of multi-injury and polytrauma conditions that typically occur in the battlefield (compared to traditional biosensing schemes). It should be noted that the system is comprised of separate channels individually tailored for specific biomedical needs. The modularity of the system allows for straightforward reconfiguration of the constituents to enable the device to adapt, expand, and meet new requirements and applications. The potential of the new modular biocomputing coding concept extends beyond the diagnosis of multiple injuries, as the concept could be readily extended for the reliable assessment of a wide array of other practical real-world scenarios involving multiple chemical changes.

The fabrication of the screen printed electrodes (SPEs) has been detailed in previous studies. Among pervasive battlefield injuries, STI, TBI, LI, ABT, HS, and OS are the most common sustained by soldiers in combat [147, 148, 149, 150], and were employed as the model injuries in this experimental study.

1.) Soft tissue injury (STI). Glycine-glycine buffer, 50 mM, with 6.7 mM $Mg(CH_3COO)_2$ was titrated by KOH to pH 7.95 and employed as a background solution (note that Mg^{2+} and K^+ cations are essential for activation of creatine kinase (CK, E.C. 2.7.3.2) and pyruvate kinase (PK, E.C. 2.7.1.40), respectively). The following components were dissolved in this solution to perform the **NAND** logic operation: reduced nicotinamide adenine dinucleotide (NADH, 0.3 mM), bovine serum albumin (BSA, 0.03 % w/v), adenosine triphosphate (ATP, 2 mM), phosphoenolpyruvate (PEP, 0.5 mM), PK (2 U mL^{-1}), creatine (15 mM). Logical '**0**' and '**1**' levels of CK (0.1 and 0.71 U mL^{-1}) and lactate dehydrogenase (LDH, E.C. 1.1.1.27, 0.15 and 1 U mL^{-1}) input signals were applied to the logic system in order to realize meaningful circulating levels of these biomarkers.

Immediately following mixture, optical absorbance measurements were recorded continuously for 300 s at $\lambda = 340$ nm. The solutions for the electrochemical measurements were incubated for 180 s at 37° C, then a methylene green (MG) redox mediator (0.3 mM) was added to catalyze the electrochemical oxidation of NADH on the SPE, and a chronoamperogram was recorded at E = 0.0 V *vs* Ag/AgCl.

2.) Traumatic brain injury (TBI). Potassium phosphate buffer, 50 mM, pH 7.4, containing glutamate oxidase (GlOx, E.C. 1.4.3.11, 1 mU mL^{-1}) and MP-11 (0.44 μM for optical and 5 μM for electrochemical measurements) was utilized to perform the **AND** logic operation. Logical '**0**' and '**1**' levels of norepinephrine (NE, 2.2 nM and 3.5 μM) and glutamate (GLU, 40 μM and 140 μM) were applied to the logic system in order to realize meaningful circulating levels of these biomarkers. The norepiquinone (NQ) produced *in situ* was optically measured at $\lambda = 487$ nm. Chronoamperometric detection of NQ was performed on the SPE at E = -0.4 V *vs* Ag/AgCl.

3.) Liver injury (LI). Tris(hydroxymethyl)aminomethane-hydrochloride (TrisHCl) buffer, 100 mM, pH 7.4, was employed as a background solution. L-alanine (L-ALA, 200 mM), α-ketoglutarate (KTG, 10 mM), and NADH (136 μM) were dissolved in this solution to perform the **NAND** logic operation. Logical '**0**' and '**1**' levels of alanine transaminase (ALT, E.C. 2.6.1.2, 0.02 and 0.2 U mL^{-1}) and LDH (0.15 and 1 U mL^{-1}) input signals were applied to the logic system in order to realize meaningful circulating levels of these biomarkers. The output signal corresponding to the decreasing concentration of NADH was measured optically at $\lambda = 340$ nm. The solutions for the electrochemical measurements were incubated for 180 s at 37° C; chronoamperograms were recorded at a bare glassy carbon (GC) electrode at an applied potential of E = 0.8 V *vs* Ag/AgCl.

4.) Abdominal trauma (ABT). Potassium phosphate buffer, 50 mM (pH 7.15 for optical or pH 7.40 for electrochemical measurements), containing 0.2 mM $MgCl_2$, 0.01 mM $CaCl_2$, and NAD^+ (10 mM for optical or 1 mM for electrochemical measurements), was used to perform the **AND** logic operation. Logical '**0**' and '**1**' levels of LDH (0.15 and 1.0 U mL^{-1}) and lactate (LAC, 1.6 and 6.0 mM) input signals were applied to the logic system in order to realize

meaningful circulating levels of these biomarkers. The output signal corresponding to the formation of NADH was measured optically at $\lambda = 340$ nm. The mixture for electrochemical measurements was incubated for 180 s at 37° C, then the MG redox mediator (0.3 mM) was added to catalyze electrochemical oxidation of NADH and a chronoamperogram was recorded at E = 0.1 V *vs* Ag/AgCl.

5.) Hemorrhagic shock (HS). Potassium phosphate buffer (50 mM, pH 7.4 for optical or 100 mM, pH 7.0 for electrochemical measurements) containing glucose oxidase (GOx, E.C. 1.1.3.4, 2 mU mL^{-1}) and microperoxidase-11 (MP-11, 0.44 μM for optical and 5 μM for the electrochemical measurements) was used to perform the **AND** logic operation. Logical '**0**' and '**1**' levels of norepinephrine (NE, 2.2 nM and 3.5 μM) and glucose (GLC, 4 mM and 26 mM) were applied to the logic system in order to realize meaningful circulating levels of these biomarkers. The norepiquinone (NQ) produced *in situ* was measured optically at $\lambda = 487$ nm. Chronoamperometric detection of NQ was performed on the SPE at E = -0.4 V *vs* Ag/AgCl.

6.) Oxidative stress (OS). Citrate buffer (50 mM, pH 5.0) was employed as the background solution. 5,5'-dithiobis-(2-nitrobenzoic acid) (DTNB, 2 mM) and reduced nicotinamide adenine dinucleotide phosphate (NADPH, 180 μM) were dissolved in this solution to perform the **AND** logic operation. Logical '**0**' and '**1**' levels of glutathione disulfide (GSSG, 150 μM and 400 μM) and glutathione reductase (GR, E.C. 1.8.1.7, 0.55 U mL^{-1} and 0.65 U mL^{-1}) input signals were applied to the logic system in order to realize meaningful circulating levels of these biomarkers. Optical analysis of the reduced glutathione (GSH) produced *in situ* was performed at $\lambda = 412$ nm for 60 s. Electrochemical analysis of GSH was performed by chronoamperometric measurements at E = 0.5 V *vs* Ag/AgCl on a cobalt phthalocyanine (CoPC)-modified SPE.

The concentrations of the biomarker input used for the activation of the logic gates are summarized in Tab. 7.1.

The new concept of parallel and multiplexed enzyme logic gates is illustrated here in connection to a multi-injury diagnosis. Such biocomputing-based comprehensive diagnosis of multiple injury conditions harnesses the processing capabilities

Table 7.1: *Physiological and pathological levels of clinically relevant biomarkers for each logic gate with the output compound indicated.*

No.	Injury	Biomarkers	Physiological	Pathological	Output
1	Soft tissue injury (STI)	Creatine kinase (CK)	100 U L^{-1}	710 U L^{-1}	NADH ↓
		Lactate dehydrogenase (LDH)	150 U L^{-1}	1000 U L^{-1}	
2	Traumatic brain injury (TBI)	Norepinephrine (NE)	2.2 nM	3.5 μM	NQ ↑
		Glutamate (GLU)	40 μM	140 μM	
3	Liver injury (LI)	Alanine transaminase (ALT)	20 U L^{-1}	200 U L^{-1}	NADH ↓
		Lactate dehydrogenase (LDH)	150 U L^{-1}	1000 U L^{-1}	
4	Abdominal trauma (ABT)	Lactate (LAC)	1.6 mM	6.0 mM	NADH ↑
		Lactate dehydrogenase (LDH)	150 U L^{-1}	1000 U L^{-1}	
5	Hemorrhagic shock (HS)	Norepinephrine (NE)	2.2 nM	3.5 μM	NQ ↑
		Glucose (GLC)	4 mM	26 mM	
6	Oxidative stress (OS)	Glutathione disulfide (GSSG)	150 μM	400 μM	GSH ↑
		Glutathione reductase (GR)	556 U L^{-1}	650 U L^{-1}	

of six individual enzyme logic gates, realizing **NAND** and **AND** operations, for the detection of STI, TBI, LI, ABT, HS, and OS using clinically relevant combinations of the biomarkers: CK, LDH, NE, GLU, ALT, LAC, GLC , GSSG, and GR [103, 104, 151, 152, 153, 154, 155, 156, 157]. The output of each logic gate was subsequently integrated as one of the constituents of the injury code-generating system to enable a high-fidelity assessment of multiple injury conditions and hence a comprehensive analysis of the scope of injury.

Upon the optimization of the design parameters, the four unique combinations of the two biomarker inputs to each individual logic gate resulted in distinguishable patterns of its respective output. For two of the gates, and in accordance with the **NAND** gate operational functionality, logical '**0**' and '**1**' levels of the input biomarkers, corresponding to normal or anomalous physiological conditions, respectively ((Input 1, Input 2) = (**0**,**0**), (**0**,**1**), and (**1**,**0**)), resulted in an output of logical '**1**'. On the other hand, logical '**1**' levels of both of the biomarkers (Input 1, Input 2) = (**1**,**1**) caused the output state to change from '**1**' to '**0**', indicating that an injury has occurred. It should be noted that the logic output signal '**0**' generated by the **NAND** gate and corresponding to a positive diagnosis does not imply that the signal is truly at a zero level. Rather, a '**0**' output implies that the system has transitioned from a state producing a signal of high magnitude to one that yields a low-level signal. In this regard, the logic output signal '**1**' indicates that the output signal is unchanged. The remaining four **AND** gates functioned under a logical inversion of the above operation. In this manner, logical '**0**' and '**1**' levels of the input biomarkers, corresponding to normal or anomalous physiological conditions, respectively ((Input 1, Input 2) = (**0**,**0**), (**0**,**1**), and (**1**,**0**)), resulted in an output of logical '**0**' whereas logical '**1**' levels of both of the biomarkers (Input 1, Input 2) = (**1**,**1**) caused the output state to change from '**0**' to '**1**', thereby signifying that an injury has been sustained. Overall, the digital outputs of the six logic gates can be subsequently multiplexed to yield a comprehensive 6-bit injury code (e.g., **001101**), corresponding to 64 unique pathological conditions (i.e., various combinations of six unique injuries).

With respect to each logic gate, the concentrations of the reagents that

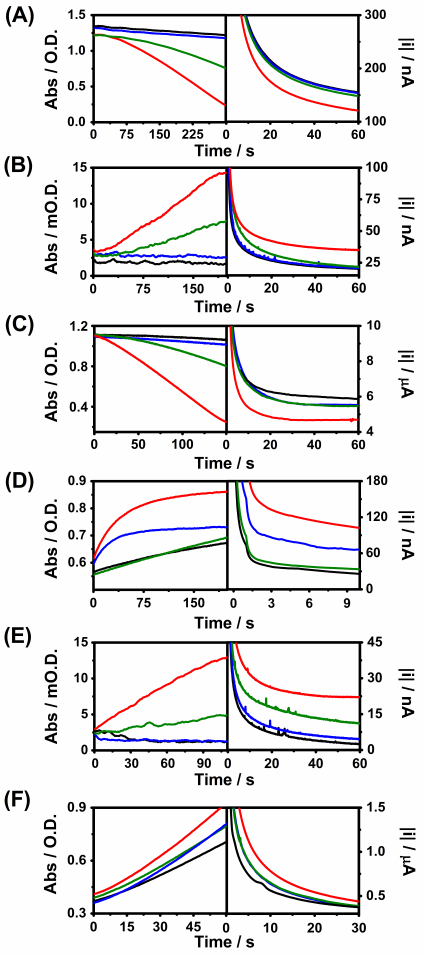

Figure 7.2: *Optical (left) and electrochemical (right) response generated by the (A) STI* ***NAND****, (B) TBI* ***AND****, (C) LI* ***NAND****, (D) ABT* ***AND****, (E) HS* ***AND****, and (F) OS* ***AND*** *logic gates upon various combinations of the input biomarkers (****0****,****0****) (black), (****0****,****1****) (blue), (****1****,****0****) (green), and (****1****,****1****) (red). Optical absorbance measurements were performed at* λ *= 340 nm, 487 nm, 340 nm, 340 nm, 487 nm, and 412 nm for the STI, TBI, LI, ABT, HS, and OS gates, respectively. Electrochemical chronoamperograms were performed at E = 0.0 V, -0.4 V, 0.8 V, 0.1 V, -0.4 V, and 0.5 V* vs *Ag/AgCl for the STI, TBI, LI, ABT, HS, and OS gates, respectively.*

served as the machinery (and not as inputs) were individually tailored to yield optimal dynamic range between the pathological level (**1**,**1**) and normal or anomalous physiological levels not related to injuries (**0**,**0**), (**0**,**1**), and (**1**,**0**). This enabled the unambiguous determination of the injury state (when the output signal '**0**' is generated by the **NAND** gate and '**1**' by the **AND** gate) due to the establishment of a fixed decision threshold. With respect to both gate archetypes, only the simultaneous presence of elevated levels of both inputs would trigger a positive diagnosis. On the other hand, the output signal '**1**' in the **NAND** topology and '**1**' in the **AND** embodiment imply extraneous pathophysiological states ranging from healthy conditions to various physiological anomalies not related to the injuries under investigation.

It should be noted that application of logic '**0**' and '**1**' input values corresponding to the physiologically relevant concentrations of the injury biomarkers required substantial optimization of the enzyme-based logic gates. For some of the injury scenarios under study, the concentration differential between logic '**0**' and '**1**' values was quite narrow, implying strict limitations to the threshold values. Thus, the design of the logic gate required a more careful consideration and optimization of the assay parameters compared with logic gates employed in previous studies, whereby logic '**0**' and '**1**' values were represented by truly zero and arbitrarily high concentrations of the input signals, respectively [27, 28, 29, 30, 31, 142, 143, 144, 145].

Soft tissue injury (STI):

Soft tissue injuries are among the most pervasive injuries sustained in combat and can be difficult to identify in numerous circumstances [158]. Among clinically established indicators of STI, serum CK and LDH have been routinely employed in the assessment of muscular exertion, fatigue, injury, and trauma [103].

Commencing experiments using optical assay methods, Fig. 7.2A (left) displays the optical absorbance of the **NAND** gate at $\lambda = 340$ nm. A large differentiation between pathological and physiological logic levels is observed, reflecting the rapid enzymatic reaction. From the corresponding bar chart (Fig. 7.3A (left)), constructed using the data at 300 s, the (CK,LDH) = (**1**,**1**) logic level was separated

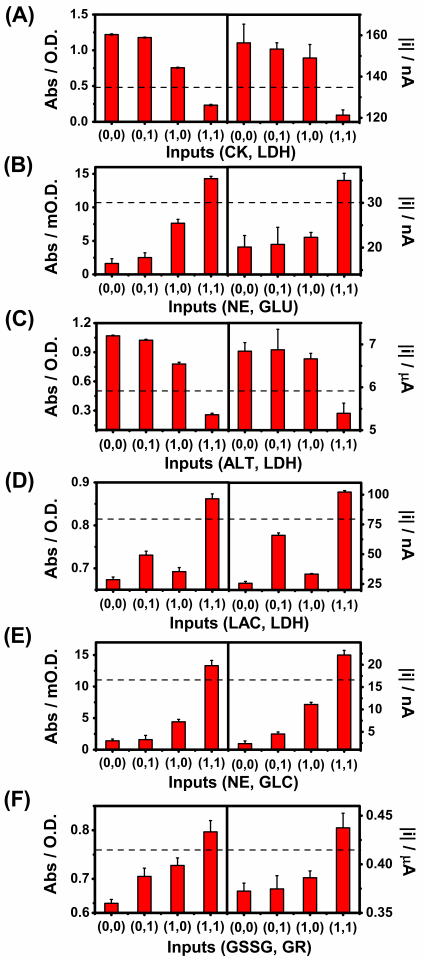

Figure 7.3: *Optical (left) and electrochemical (right) bar charts obtained by sampling the output of the (A) STI* ***NAND****, (B) TBI* ***AND****, (C) LI* ***NAND****, (D) ABT* ***AND****, (E) HS* ***AND****, and (F) OS* ***AND*** *logic gates upon various combinations of the input biomarkers (**0**,**0**), (**0**,**1**), (**1**,**0**), and (**1**,**1**). Optical absorbance measurements were extracted at* t *= 300 s, 200 s, 150 s, 200 s, 100 s, and 60 s for the STI, TBI, LI, ABT, HS, and OS gates, respectively. Electrochemical chronoamperograms were sampled at* t *= 60 s, 60 s, 60 s, 10 s, 60 s, and 30 s for the STI, TBI, LI, ABT, HS, and OS gates, respectively. Dashed lines indicate the decision threshold for the realization of Boolean logic gate operation.*

by more than 0.52 O.D. from the nearest logic level. An explicit decision threshold could hence be established at 0.49 O.D., leading to highly reliable **NAND** operation.

In accordance with the goal of low-cost decentralized screening of STI and developing compact analytical devices, the aforementioned protocol was subsequently migrated to the amperometric domain using a disposable SPE. Towards this goal, chronoamperometric measurements were performed for each combination of input signals with MG added to the assay, enabling the low-potential detection of NADH, hence minimizing potential electroactive interference. The detection potential was established at 0.0 V *vs* Ag/AgCl to maximize the signal-to-noise ratio (SNR) figure of merit. Chronoamperograms are shown in Fig. 7.2A (right) which were obtained at the carbon SPE by the **NAND** gate upon application of various input combinations. At 60 s sampling time, the difference in current between the (CK,LDH) = (**1**,**1**) logic and (**1**,**0**) logic levels was 27 nA, as shown by the bar chart, Fig. 7.3A (right). As in the optical experiments, the bar chart indicates that a straightforward decision threshold could be instituted to realize high-fidelity **NAND** gate operation. This threshold was fixed at 135 nA.

Traumatic brain injury (TBI):

Traumatic brain injuries are among the most debilitating injuries suffered in the battlefield [159] and have garnered much recent attention due to the wide range of symptoms and characteristics presented by individuals suffering from the condition [160]. NE, a catecholamine hormone neurotransmitter, and GLU, an amino-acid excitatory neurotransmitter, are among the most widely employed indicators of neurological damage and trauma [152].

Commencing experiments using optical assay methods, Fig. 7.2B (left) displays the optical absorbance of the **AND** gate at $\lambda = 487$ nm. As with the STI gate, a large differentiation between pathological and physiological logic levels is observed, reflecting favorable enzyme kinetics. From the corresponding bar chart (Fig. 7.3B (left)) constructed using the data at 200 s, the (NE,GLU) = (**1**,**1**) logic level was separated by 6.65 mO.D. from the nearest logic level. An explicit decision threshold could hence be established at 10.96 mO.D., leading to highly reliable

AND operation.

The aforementioned protocol was subsequently migrated to the amperometric domain using a disposable SPE. Accordingly, chronoamperometric measurements were performed for each combination of the input signals with the concentration of NQ serving as the output indicator. The detection potential was established at -0.4 V *vs* Ag/AgCl for SNR considerations. Chronoamperograms are shown in Fig. 7.2B (right) which were obtained at the carbon SPE by the **AND** gate upon application of various input combinations. At 60 s sampling time, the difference in current between the (**1**,**1**) logic and (**0**,**1**) logic levels was 13 nA, as shown by the bar chart in Fig. 7.3B (right). As in the optical experiments, the bar chart indicates that a straightforward decision threshold could be instituted to realize high-fidelity **AND** gate operation, which was established at 30 nA.

Liver injury (LI):

Screening of liver injury has routinely been employed in the clinical laboratory through enzyme-based assay tests [161] to assess sepsis – a secondary, but life-threatening condition arising due to such injuries [162]. This injury is especially prevalent in combat situations whereby damaged organs cause foreign matter to enter and circulate in the bloodstream [163]. Serum ALT and LDH have enjoyed widespread use as enzyme biomarkers in such assays [154] and are well-suited for integration as input biomarkers and enzyme backbones to the enzyme logic machinery.

Commencing experiments using optical assay methods, Fig. 7.2C (left) displays the optical absorbance of the **NAND** gate at $\lambda = 340$ nm. A large differentiation between pathological and physiological logic levels is observed, again a result of enhanced enzyme activity. From the corresponding bar chart (Fig. 7.3C (left)) constructed using the data at 150 s, the (ALT,LDH) = (**1**,**1**) logic level was separated by 0.52 O.D. from the nearest logic level. An explicit decision threshold could hence be established at 0.52 O.D., yielding the expected **NAND** operation.

Electrochemical experiments were subsequently executed by employing a bare GC electrode. Accordingly, chronoamperometric measurements were performed for each combination of the input signals and the level of NADH consumed

was monitored at 0.8 V *vs* Ag/AgCl. Chronoamperograms are shown in Fig. 7.2C (right) obtained at the GC electrode by the **NAND** gate upon application of various input combinations. At 60 s sampling time, the difference in current between the (**1**,**1**) and (**1**,**0**) logic levels was 1.3 μA, as shown by the bar chart in Fig. 7.3C (right). As in the optical experiments, the bar chart validates that a decision threshold could be unambiguously implemented to realize high-fidelity **NAND** gate operation, which was established at 6.0 μA.

Abdominal trauma (ABT):

As with liver injury, severe abdominal trauma frequently results in sepsis and must be addressed with little or no delay in order to improve survival [164]. In addition, ABT is another example of a common battlefield injury which has been linked to high mortality rates [165]. Serum LAC and LDH are well-established biomarkers of such injury [103, 104] in addition to serving extensive use in assays [166].

Initially, optical experiments were conducted and Fig. 7.2D (left) displays the optical absorbance of the **AND** gate at $\lambda = 340$ nm at each combination of the input signals. Pathological and physiological logic levels were easily differentiated, which confirmed that the assay conditions were favorable for this application. From the corresponding bar chart (Fig. 7.3D (left)) constructed using the data at 200 s, the (LAC,LDH) = (**1**,**1**) logic level was separated by 0.13 O.D. from the logic level in closest proximity. Accordingly, an unambiguous decision threshold could be established at 0.81 O.D. in order to yield **AND** functionality.

Following optical experiments, electrochemical investigations were then performed by employing a disposable SPE. Chronoamperometric measurements were performed for each combination of the input signals with MG serving as the output mediator to reduce the overpotential required for the detection of NADH. The detection potential was established at 0.1 V *vs* Ag/AgCl to maximize SNR. Chronoamperograms are shown in Fig. 7.2D (right) which were obtained at the carbon SPE by the **AND** gate upon application of various input combinations. At 10 s sampling time, the difference in current between the (**1**,**1**) logic and (**1**,**0**) logic levels was 36 nA, as shown by the bar chart in Fig. 7.3D (right). Upon examination

of the bar chart, it is apparent that a decision threshold could be unambiguously implemented to realize high-fidelity **AND** gate operation (as in the optical case), which was established at 84 nA.

Hemorrhagic shock (HS):

Hemorrhagic shock, a condition that arises due to uncontrolled bleeding, is another pervasive example of a high-mortality combat injury and frequently occurs as a result of the infliction of gun-shot wounds and blast injuries [167]. This critical condition must be assessed before desanguination ensues [168]. Serum GLC and NE have been identified as biomarkers of such injury [151, 155] and can increase many-fold upon presentation of this condition [169, 170].

Optical experiments were conducted and Fig. 7.2E (left) displays the optical absorbance at λ = 487 nm of the **AND** gate for each combination of the input signals. Pathological and physiological logic levels were well-separated, which again confirmed favorable assay conditions. From the corresponding bar chart (Fig. 7.3E (left)) constructed using the data at 100 s, the (NE,GLC) = (**1**,**1**) logic level was separated by 8.89 mO.D. from the logic level in closest proximity. Accordingly, a straightforward decision threshold could be established at 11.0 mO.D. in order to yield **AND** functionality.

Following optical experiments, electrochemical investigations were subsequently performed by employing a disposable SPE. Chronoamperometric measurements were performed for each combination of the input signals with the concentration of NQ serving as the output indicator. The detection potential was established at -0.4 V *vs* Ag/AgCl for SNR considerations. Chronoamperograms are shown in Fig. 7.2E (right) which were obtained at the carbon SPE by the **AND** gate upon application of various input combinations. At 60 s sampling time, the difference in current between the (**1**,**1**) logic and (**1**,**0**) logic levels was 11 nA, as shown by the bar chart in Fig. 7.3E (right). In accordance with these results, the decision threshold to realize high-fidelity **AND** gate operation (as in the optical case) was established at 16 nA.

Oxidative stress (OS):

Oxidative stress refers to a broad scope of pathological states and accompa-

nies nearly all forms of physical stress or strain experienced by the body [171, 172], including those acquired in battle [172]. GSSG and GR mitigate the body's biochemical response to oxidative stress and elevations in each compound in serum have been found to be associated with such events. Thus, GSSG and GR are excellent candidates for biomarkers [156, 157] that can enable highly reliable logic gate operation.

Optical experiments were first conducted and Fig. 7.2F (left) displays the optical absorbance of the AND gate at $\lambda = 412$ nm for each combination of the input signals using DTNB for optical analysis of the GSH produced in situ [173]. Pathological and physiological logic levels were easily differentiable, thereby validating high-fidelity operation. From the corresponding bar chart (Fig. 7.3F (left)) constructed using the data at 60 s, the (GSSG,GR) = (**1**,**1**) logic level was separated by 0.07 O.D. from the logic level in closest proximity. A decision threshold could hence be set at 0.76 O.D. in order to yield **AND** functionality.

Electrochemical investigations were then performed by employing a disposable SPE. Chronoamperometric measurements were performed for each combination of the input signals with CoPC serving as the output mediator to reduce the overpotential required for the detection of GSH. The detection potential was established at 0.5 V *vs* Ag/AgCl to maximize SNR. Chronoamperograms are shown in Fig. 7.2F (right) which were obtained at the CoPC-modified carbon SPE by the AND gate upon application of various input combinations. At 30 s sampling time, the difference in current between the (**1**,**1**) logic and (**1**,**0**) logic levels was 51 nA, as shown by the bar chart in Fig. 7.3F (right). As this figure illustrates, a decision threshold could be implemented to realize high-fidelity **AND** gate operation (as in the optical case), and was accordingly established at 412 nA.

Accordingly, good correlation was observed between the optical and electrochemical data in each of the six separate experiments, as indicated from a comparison of the bar charts presented in Fig. 7.3, thereby confirming the validity of the transition of the experimental procedure from the optical to the electrochemical domain. With the electrochemical protocol in functional order, the output of each logic gate could be integrated as one of the constituents of the injury

code-generating system.

Table 7.2: *Truth table and corresponding injury codes for all 64 possible combinations of STI, TBI, LI, ABT, HS, and OS.*

No.	STI	TBI	LI	ABT	HS	OS	Inj. Code	Biomedical Conclusions
1	0	0	0	0	0	0	000000	STI LI
2	0	0	0	0	0	1	000001	STI LI OS
3	0	0	0	0	1	0	000010	STI HS
4	0	0	0	0	1	1	000011	STI LI HS OS
5	0	0	0	1	0	0	000100	STI LI ABT
6	0	0	0	1	0	1	000101	STI LI ABT OS
7	0	0	0	1	1	0	000110	STI LI ABT HS
8	0	0	0	1	1	1	000111	STI LI ABT HS OS
9	0	0	1	0	0	0	001000	STI
10	0	0	1	0	0	1	001001	STI OS
11	0	0	1	0	1	0	001010	STI HS
12	0	0	1	0	1	1	001011	STI HS OS
13	0	0	1	1	0	0	001100	STI ABT
14	0	0	1	1	0	1	001101	STI ABT OS
15	0	0	1	1	1	0	001110	STI ABT HS
16	0	0	1	1	1	1	001111	STI ABT HS OS
17	0	1	0	0	0	0	010000	STI TBI LI
18	0	1	0	0	0	1	010001	STI TBI LI OS
19	0	1	0	0	1	0	010010	STI TBI LI HS
20	0	1	0	0	1	1	010011	STI TBI LI HS OS
21	0	1	0	1	0	0	010100	STI TBI LI ABT
22	0	1	0	1	0	1	010101	STI TBI LI ABT OS
23	0	1	0	1	1	0	010110	STI TBI LI ABT HS
24	0	1	0	1	1	1	010111	STI TBI LI ABT HS OS
25	0	1	1	0	0	0	011000	STI TBI

Table 7.2 – Continued

No.	STI	TBI	LI	ABT	HS	OS	Inj. Code	Biomedical Conclusions
26	0	1	1	0	0	1	011001	STI TBI OS
27	0	1	1	0	1	0	011010	STI TBI HS
28	0	1	1	0	1	1	011011	STI TBI HS OS
29	0	1	1	1	0	0	011100	STI TBI ABT
30	0	1	1	1	0	1	011101	STI TBI ABT OS
31	0	1	1	1	1	0	011110	STI TBI ABT HS
32	0	1	1	1	1	1	011111	STI TBI ABT HS OS
33	1	0	0	0	0	0	100000	LI
34	1	0	0	0	0	1	100001	LI OS
35	1	0	0	0	1	0	100010	LI HS
36	1	0	0	0	1	1	100011	LI HS OS
37	1	0	0	1	0	0	100100	LI ABT
38	1	0	0	1	0	1	100101	LI ABT OS
39	1	0	0	1	1	0	100110	LI ABT HS
40	1	0	0	1	1	1	100111	LI ABT HS OS
41	1	0	1	0	0	0	101000	*Normal*
42	1	0	1	0	0	1	101001	OS
43	1	0	1	0	1	0	101010	HS
44	1	0	1	0	1	1	101011	HS OS
45	1	0	1	1	0	0	101100	ABT
46	1	0	1	1	0	1	101101	ABT OS
47	1	0	1	1	1	0	101110	ABT HS
48	1	0	1	1	1	1	101111	ABT HS OS
49	1	1	0	0	0	0	110000	TBI LI
50	1	1	0	0	0	1	110001	TBI LI OS
51	1	1	0	0	1	0	110010	TBI LI HS
52	1	1	0	0	1	1	110011	TBI LI HS OS

Table 7.2 – Continued

No.	STI	TBI	LI	ABT	HS	OS	Inj. Code	Biomedical Conclusions
53	1	1	0	1	0	0	110100	TBI LI ABT
54	1	1	0	1	0	1	110101	TBI LI ABT OS
55	1	1	0	1	1	0	110110	TBI LI ABT HS
56	1	1	0	1	1	1	110111	TBI LI ABT HS OS
57	1	1	1	0	0	0	111000	TBI
58	1	1	1	0	0	1	111001	TBI OS
59	1	1	1	0	1	0	111010	TBI HS
60	1	1	1	0	1	1	111011	TBI HS OS
61	1	1	1	1	0	0	111100	TBI ABT
62	1	1	1	1	0	1	111101	TBI ABT OS
63	1	1	1	1	1	0	111110	TBI ABT HS
64	1	1	1	1	1	1	111111	TBI ABT HS OS

With the above six gates optimized to enable high-fidelity detection, a 6-bit injury code was concatenated from the outputs of each of the individual gates. Accordingly, $2^6 = 64$ unique injury combinations could be ascertained, as shown in Tab. 7.2., among $2^{12} = 4096$ possible pathophysiological scenarios. A comprehensive injury code could thus be constructed to account for various combinations of six unique injuries.

Such an encoding scheme enables a reduced dependence on analog circuitry required for the synthesis of high-integrity waveforms required for digital signal processing, as the outputs are generated with substantial differentiation between the digitally-defined physiological and pathological levels in the biochemical domain. Moreover, the binary nature of the output (indicative of injury) enabled multiplexing operations to be performed directly in the digital domain and could be appraised against a lookup table for the reliable evaluation of pathophysiological state. The sizeable dynamic range and high noise margins of the **NAND**

and **AND** logic gates facilitate such high-fidelity operation and serve to further underscore the advantages of the concept when contrasted with traditional biosensor and lab-on-a-chip approaches. Without the use of Boolean processing and the establishment of a concomitant decision threshold for digital diagnosis, a reliable assessment of injury could not be tendered nor could an injury code be constructed. In the absence of these merits, the approach would encounter serious obstacles in discarding the noise arising from extraneous interferents and anomalous pathophysiological conditions and extracting the signal of interest. Therefore, the operational merits of the logic gate architecture enabled the establishment of an unambiguous decision threshold and digital manipulation of the biomarker signals, thereby enabling the concatenation of an inclusive injury code to assess multiple injury conditions, which allowed the system an enhanced ability to detect injury when compared with traditional biosensing concepts.

Noise reduction, fault tolerance, robustness, and scalability are all factors to be considered when attempting to improve the performance of enzyme-based information processing systems. Experimental optimization was implemented in order to produce a reliable threshold between output = **0** and output = **1**. Although noise can be suppressed by logic network design, other intrinsic experimental parameters will dictate the precision of each logic level. When assessing the optical and electrochemical experimental results, the standard deviation for most of the values does not exceed 5 % of the mean value, demonstrating reproducibility within the chosen physiological and pathological input ranges. The chosen threshold lines separating logic output = **0** and logic output = **1** varied between 11 % and 60 % of the mean value; hence the as-designed logic gates can serve as reliable injury predictors for at least 90 % of the repetitions.

A new modular biocomputing coding concept based on parallel and multiplexed enzyme logic gates has been described. This enzyme logic coding approach has been demonstrated towards a multi-injury diagnosis in connection to twelve biomarker inputs. This system is able to assess 64 individual pathological conditions among 4096 possible pathophysiological states through multiplexing the outputs into a 6-bit 'injury code'. The new system, consisting of **AND** and **NAND**

gates, is able to evaluate a greater number of injuries than permitted by single enzyme logic gates while leveraging an electronic backbone of similar complexity. Moreover, due to the concept's Boolean biochemical signal processing architecture, the system is able to infer pathological conditions with a greater degree of reliability while enabling lower power consumption operation due to the reduced dependence on electronic operations than conventional biosensor arrays are currently able to offer. The concept represents the first demonstration of the parallelization of enzyme logic gates applied to diagnostic merits as well as the simultaneous multiplexing of the outputs of multiple logic gates in the biochemical domain into a binary injury code. Such devices hold considerable potential for future work in the advancement of low-cost, disposable biosensors. Further development is required to realize an on-body biosensing paradigm, albeit the injury code concept is well-positioned to enable the rapid and reliable assessment of multiple life-threatening injuries away from the hospital setting. Moreover, in addition to its connection to multi-injury diagnosis, the concept could be extended to the reliable assessment of a wide range of other practical medical, industrial, security and environmental scenarios.

7.2 Multi-enzyme logic network architectures for the assessment of injury

In order to further augment the complexity of bioanalysis systems, logic operations may be concatenated and represented by a multi-enzyme system capable of processing a contingent of variable biomarker signals. In this embodiment, bimodal functionality is desired through the implementation of a **SWITCH** feature activated by the presence or absence of switching inputs in specific gates. Switching between two unique subsystems provides a solution for the control of biochemical pathways and performance correlation for multiple logic gates in a given system. The **SWITCH** feature enables the simultaneous analysis of different physiological conditions within a biochemical logic system operating as a single aggregate. This concept is illustrated via a model enzyme logic-based system for the analysis of biomarkers characteristic of the two common injuries: traumatic brain injury (TBI)

and soft tissue injury (STI).

A graphical representation of the multi-enzyme biocatalytic system operating in a single solution is outlined in Fig. 7.4. The input concentrations that activate the biocatalytic system are summarized in Tab. 7.3. The system operates in two different modes: (i) for the analysis of TBI (employing 31 mM potassium phosphate buffer (PBS), pH 7.58, containing 6.7 mM magnesium sulfate) and (ii) for the analysis of STI (evaluated in 50 mM triethanolamine buffer (TEA), pH 7.4, containing 0.2 mM magnesium acetate). The persistent component of the system (the 'machinery' of the logic network) included the following compounds: pyruvte kinase (PK, E.C. 2.7.1.40, 10 U mL^{-1}), pyruvate oxidase (POx, E.C. 1.2.3.3, 5 U mL^{-1}), pyruvate dehydrogenase (PDH, E.C. 1.2.4.1, 2 U mL^{-1}), horseradish peroxidase (HRP, E.C. 1.11.1.7, 5 U mL^{-1}), creatine (Crt, 15 mM), nicotinamide adenine dinucleotide (NAD^+, 10 mM), thiamine pyrophosphate (TPP, 450 μM), L-cysteine (L-Cys, 3.96 mM), flavin adenine dinucleotide (FAD, 10 μM) and O_2 (in equilibrium with air). The output signal generated under TBI sensing operation was measured via an absorbance differentials at $\lambda = 655$ nm (corresponding to the generation of the oxidized form of the redox mediator, 3,3',5,5'-tetramethylbenzidine, TMB_{ox}) [174]. The output signal generated under STI operation was measured via absorbance differentials at $\lambda = 340$ nm (corresponding to the formation of reduced nicotinamide adenine dinucleotide, NADH) [175]. The absorbance measurements were recorded immediately following the combination of the reagents in a cuvette and the final absorbance value was extracted at 800 s following the initiation of the reaction. This sampling time was optimized for the effective discrimination of the logic **0** and **1** output signals generated by the system.

The assessment of two common battlefield injuries, STI and TBI, was performed by a multi-enzyme biocatalytic cascade, Fig. 7.4, which can be described as a comprehensive concatenated logic system and its gate equivalent is diagrammatically represented in Fig. 7.5. The system architecture includes eight networked logic gates of the **AND** variety. The biocatalytic system operates in two unique modes: one for the analysis of TBI and another for the analysis of STI (with the ability to switch between them). The system is designed to analyze five unique

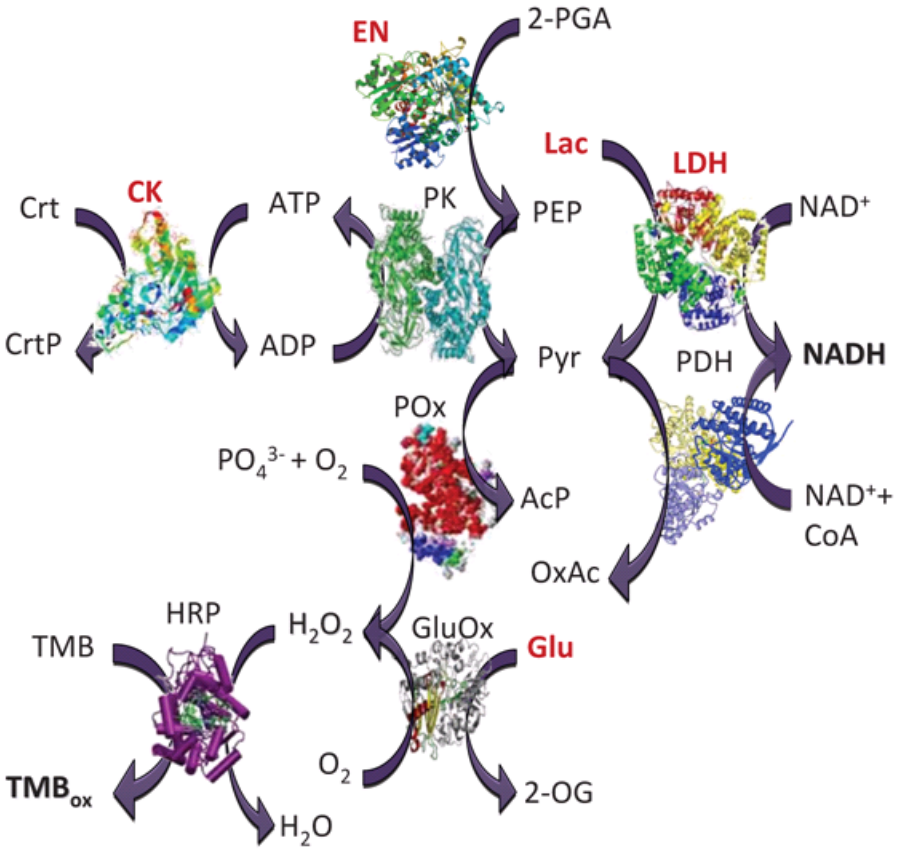

Figure 7.4: *Multi-enzyme biocatalytic cascade for the analysis of soft tissue injury (STI) and traumatic brain injury (TBI). Biomarker inputs for STI (creatine kinase, CK; lactate, LAC; lactate dehydrogenase, LDH) and TBI (enolase, EN; glutamate, GLU) are labeled in red. Output signals for STI and TBI are reduced nicotinamide adenine dinucleotide (NADH) and oxidized 3,3',5,5'-tetramethylbenzidine (TMB_{ox}), respectively. Other products of the biocatalytic cascade are the following: acetyl phosphate (AcP), oxaloacetate (OxAc), 2-oxoglutarate (2-OG), and creatine phosphate (CrtP). Note that, for the sake of simplicity, the scheme does not include some reacting cofactors, promoters, and byproducts; for the full composition of the system refer to the Experimental section.*

Table 7.3: *Concentrations of the input biomarkers that activate the biocatalytic cascade for the logic-based analysis of STI and TBI.*

Inputs	Logic '**0**'	Logic '**1**'	Ref.
CK	0.10 U mL^{-1}	0.71 U mL^{-1}	[103]
LDH	0.15 U mL^{-1}	1.00 U mL^{-1}	[103]
LAC	1.6 mM	6.0 mM	[104]
EN	0.42 mU mL^{-1}	1.20 mU mL^{-1}	[151]
GLU	40 μM	140 μM	[176]
ATP	0 mM	2 mM	–
2-PGA	0 mM	8 mM	–
GluOx	0 mU mL^{-1}	0.30 mU mL^{-1}	–
TMB	0 mM	0.45 mM	–
PEP	0 mM	2 mM	–
ADP	0 mM	2 mM	–
Phosphate	0 mM	31 mM	–
CoA	0 mM	0.5 mM	–

biomarker entities appearing at different combinations, thereby leading to a logic-based assessment regarding the presence or absence of TBI or STI conditions. Three biomarkers, creatine kinase (CK, E.C. 2.7.3.2), lactate dehydrogenase (LDH, E.C. 1.1.1.27) and lactate (LAC) , correspond to the physiological conditions characteristic of STI, while two other biomarkers, enolase (EN) and glutamate (GLU), represent an affirmative TBI diagnosis.

All five biomarkers were applied as biochemical input signals (labeled in red in Fig. 7.5) and activated the logic network at two different concentration levels: logic '**0**' corresponding to the normal physiological concentrations of the biomarkers, while logic '**1**' was selected at the elevated pathophysiological concentrations corresponding to the respective injuries, as provided in Tab. 7.3. The simultaneous processing of multiple biomarkers via the complex biocatalytic cascade requires optimization of the biocatalytic reactions by tuning the reaction rates in order to yield comparable output signals for various combinations of the biomarker inputs. The optimization was achieved by careful selection of the auxiliary inputs (labeled in green in Fig. 7.5): Adenosine triphosphate (ATP), 2-phosphoglycerate (2-PGA), glutamate oxidase (GluOx, E.C. 1.4.3.11), and TMB. In order to digitize the logic network operation, the auxiliary inputs were applied at two levels:

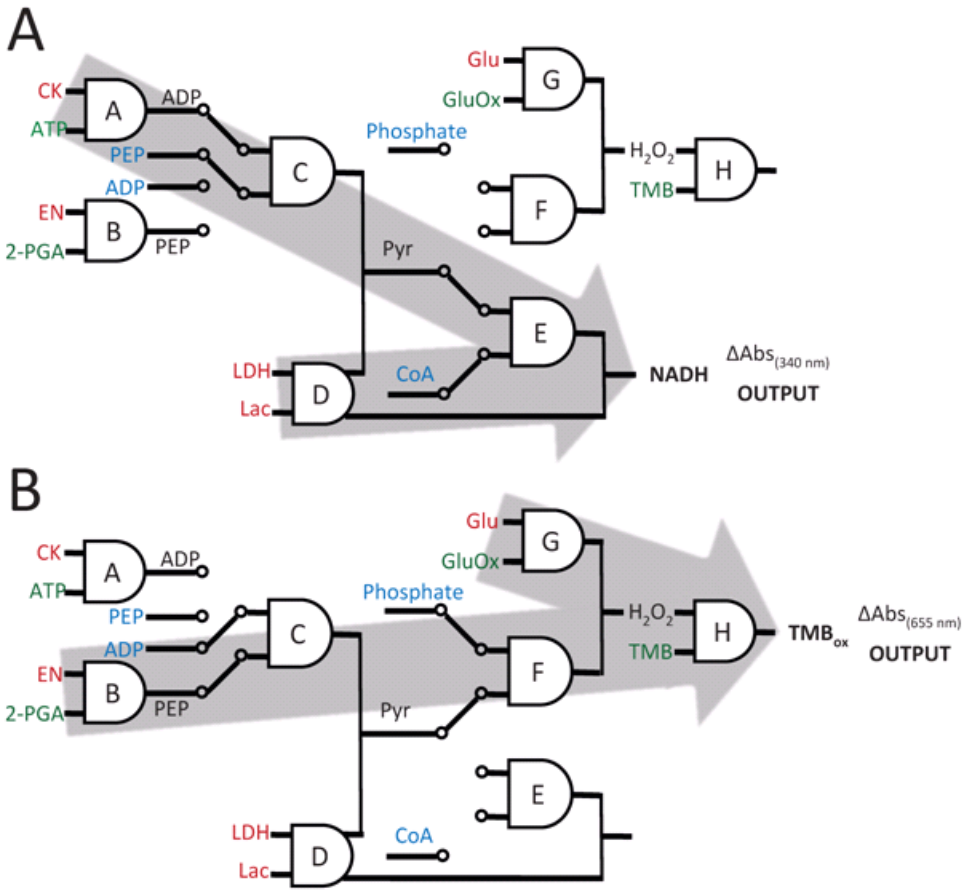

Figure 7.5: *Equivalent logic schemes for the concatenated logic gates designed to identify STI and TBI corresponding to the biocatalytic cascade provided in Fig. 7.5. (A) The system applied to STI diagnostic merits. (B) The system applied to TBI diagnostic merits. Biomarker inputs are labeled in red, auxiliary inputs in green, and switching inputs in blue. The switch-controlled pathways for the STI and TBI operational modes are indicated by the arrows.*

logic '**0**' corresponding to physical zero concentration, while logic '**1**' was selected experimentally upon optimization of the system, Tab. 7.3. The auxiliary inputs did not provide information concerning physiological conditions related to the injuries, but were necessary for optimal processing of the biomarker inputs. When applied at '**0**' levels, the auxiliary inputs muted the system response, and the system was concomitantly insensitive to the biomarker inputs. On the other hand, their application at '**1**' levels yielded optimal processing of the biomarker inputs applied in different combinations of '**0**' and '**1**' logic levels. Four additional inputs (labeled in blue in Fig. 7.5), phosphoenolpyruvate (PEP), adenosine diphosphate (ADP), phosphate (PO_4^{3-}), and coenzyme A (CoA) were used to switch the system operation between the TBI and STI modes. These inputs were applied at logic '**0**' levels corresponding to physical zero concentrations, while logic '**1**' levels were experimentally optimized, as provided in Tab. 7.3.

Biocatalytic logic network under STI operational mode:

In order to compensate for the lack of specificity among the biomarkers employed for STI diagnosis, only the concurrent appearance of all three STI-related biomarkers (CK, LDH, and LAC) at logic '**1**' values affirms the presence of symptoms characteristic of STI. Accordingly, the system operated under the following operational conditions (see Fig. 7.4 for the biochemical representation and Fig. 7.5A for the logic equivalent diagram - the STI pathway is highlighted): the biocatalytic reaction of CK (one of the STI biomarkers) and ATP (gate A) results in the production of ADP. Subsequently, the reaction of ADP with PEP biocatalyzed by PK (gate C) results in the formation of pyruvate (PYR), which then is biocatalyzed in the presence of CoA and PDH (gate E) to yield NADH, the output signal. Note that the pathway composed of A–C–E gates is activated only when the biomarker input CK, auxiliary input ATP, and switching inputs PEP and CoA appear at logic '**1**' values. The simultaneous application of the LDH and LAC inputs (STI biomarkers) at logic '**1**' (gate D) results in the reduction of NAD^+ and a further increase in the NADH output signal. It should be noted that this pathway results in the concomitant production of PYR, which traverses through gate E and produces a molar equivalent of NADH, thus further amplifying the output

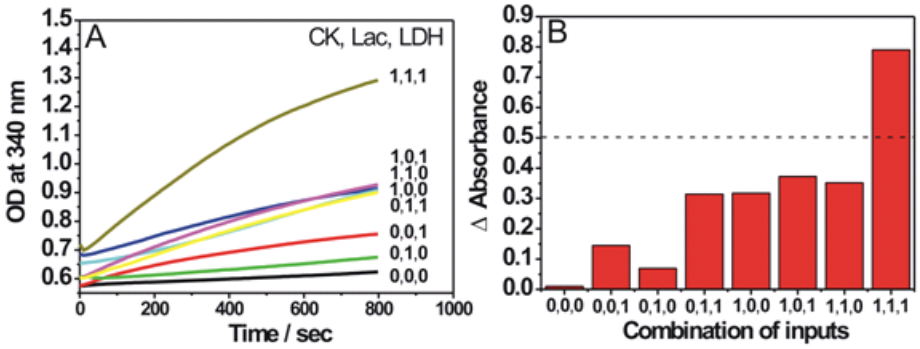

Figure 7.6: *(A) Optical detection of the output signal (NADH) generated by the logic system operating under STI analysis mode. The response was obtained following the application of all combinations of the injury biomarker input signals (CK, LDH, and LAC). (B) Bar chart comparing the output signals generated by the enzyme logic system for the analysis of STI at* t *= 800 s. The positive STI diagnosis corresponds to the output signal above the decision threshold (dashed line). The logic system composition is provided in the experimental section and the biomarker input concentrations corresponding to the logic '**0**' and '**1**' values are specified in Tab. 7.3. The auxiliary (ATP) and switching (PEP and CoA) inputs were applied at logic '**1**' levels for all combinations of the biomarker inputs.*

signal. Fig. 7.6A illustrates the optical changes in the system measured at λ = 340 nm (NADH absorbance) under the application of different combinations of the biomarker inputs. Only the simultaneous application of all three biomarker inputs at logic '**1**' values (input combination (**1**,**1**,**1**)) resulted in a substantial optical absorbance differential, hence allowing an unambiguous conclusion regarding the presentation of an STI event. The experimentally-corroborated threshold level of 0.5 O.D. enabled high-fidelity discrimination between the logic '**0**' and '**1**' levels, with the output signal differential greater than a factor of two, as presented in Fig. 7.6B. It should be noted that, in all measurements provided in Fig. 7.6, the auxiliary (ATP) and switching (PEP and CoA) inputs were applied at logic '**1**' values to enable optimal performance via the desired biocatalytic pathway. At the same time, the switching inputs, ADP and PO_4^{3-}, were applied at logic '**0**' levels to inhibit the alternative (undesired) TBI pathway.

Biocatalytic logic network under TBI operational mode:

In contrast to the biomarkers employed for the diagnosis of STI, the TBI biomarkers employed in the study (EN and GLU) are rather specific in nature and can report on the presentation of injury even when appearing alone. A generic EN enzyme was substituted in place of a neuron-specific EN variety, which is the isoenzyme released from damaged cortical tissues. The system operates in the following manner ((see Fig. 7.4 for the biochemical representation and Fig. 7.5B for the logic equivalent diagram - the TBI pathway is highlighted): the biocatalytic reaction of EN (TBI biomarker) and 2-PGA (gate *B*) results in the formation of PEP. Subsequently, the reaction of PEP with ADP (switching input) biocatalyzed by PK (gate *C*) results in the formation of PYR. Further reaction of PYR with PO_4^{3-} (switching input) biocatalyzed by POx (gate *F*) yields H_2O_2, which reacts with TMB in the presence of HRP (gate *H*). This reaction results in the oxidation of TMB, the redox mediator, and produces an absorbance increase at $\lambda = 655$ nm. In this fashion, TMB_{ox} is considered as the final output signal from the pathway composed of *B*–*C*–*F*–*H* gates. The same signal was generated through an alternative pathway composed of gates *G* and *H*: the biocatalytic reaction of GLU (TBI biomarker) and GluOx result in O_2 reduction and yields H_2O_2 (gate *G*). Subsequently, H_2O_2 reacts with TMB in the presence of HRP to yield TMB_{ox}, instigating a concomitant absorbance differential (gate *H*). Careful optimization of the system (by tuning the concentrations of the auxiliary inputs) enables a comparable output signal to appear in both the pathways. Fig. 7.7A represents the differential optical absorption in the system measured at $\lambda = 655$ nm (TMB_{ox} absorbance) for all combinations of the biomarker inputs. Any or both biomarkers appearing at the logic '**1**' level resulted in high absorbance differentials, hence signaling the presence of TBI conditions. The experimentally-derived threshold level of 0.02 O.D. enabled the high-fidelity discrimination among the logic '**0**' and '**1**' levels. The output signal differential for the input combination (**0**,**0**) and all other combinations ((**0**,**1**), (**1**,**0**), and (**1**,**1**)) is provided Fig. 7.7B. It should be noted that in all measurements shown in Fig. 7.7, the auxiliary (2-PGA,TMB and GluOx) and switching (ADP and PO_4^{3-}) inputs were applied at logic '**1**' values to facilitate optimal performance via the analytical pathway. At the same time,

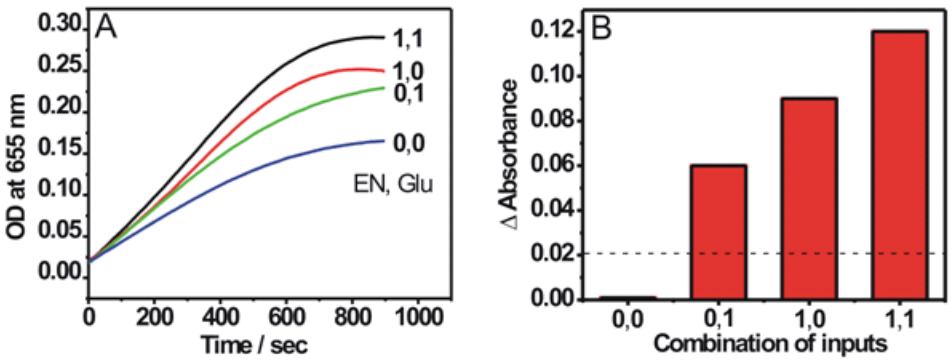

Figure 7.7: *(A) Optical detection of the output signal (TMB_{ox}) generated by the logic system operating under TBI analysis mode. The response was obtained following the application of all combinations of the injury biomarker input signals (EN, GLU). (B) Bar chart comparing the output signals generated by the enzyme logic system for the analysis of TBI at* t *= 800 s. The positive TBI diagnosis corresponds to the output signals above the decision threshold (dashed line). The logic system composition is provided in the experimental section and the biomarker input concentrations corresponding to the logic '**0**' and '**1**' values are specified in Tab. 7.3. The auxiliary (2-PGA, GluOx, TMB) and switching (ADP and PO_4^{3-}) inputs were applied at logic '**1**' levels for all combinations of the biomarker inputs.*

the switching inputs, PEP and CoA, were applied at logic '**0**' levels to inhibit the alternative (undesired) STI pathway.

Biocatalytic logic network under SWITCH operation:

Operation of the logic system in the STI mode results in production of ADP as a product of the biocatalytic reaction at gate *A*. Further reaction of ADP in gate *C* requires the presence of PEP, which is not produced by the system under operation in the STI mode (note that gate *B* is disabled because of the absence of the EN input). Therefore, PEP must be supplemented in order to activate gate *C*. Conversely, under operation in the TBI mode, PEP is produced, in situ, from gate *B* while ADP, which is required for operation of gate *C* is absent (note that gate *A* is deactivated due to the absence of CK). Hence, in this circumstance, ADP must be added in order to activate gate *C*. Finally, in order to activate the network to operate in the STI mode, the switching inputs PEP and ADP should be applied at logic '**1**' and '**0**' values, respectively, while they should assume the

opposite ('**0**' and '**1**') values under TBI operation. This switch enables gates *C* and *F* to selectively function under two unique modes of operation. Similarly, in order to switch between two operational modes, gates *F* and *E* must be selectively activated by the appropriate concentrations of PO_4^{3-} and CoA. Specifically, PO_4^{3-} and CoA were applied at logic '**0**' and '**1**' levels in the STI mode and at logic '**1**' and '**0**' levels in the TBI mode.

Although the objective of the investigation resided in the optimization of both the STI and TBI systems under identical experimental conditions, it was not possible to achieve the optimized operation of both modes under exactly the same conditions – the TBI system operated in a 31 mM potassium phosphate buffer solution (pH 7.58, containing 6.7 mM magnesium sulfate), while the STI system was realized in a 50 mM triethanolamine buffer (pH 7.4, containing 0.2 mM magnesium acetate). Further study will be required to enable the entire switching contingent to function under identical operational conditions in the *same* environment.

The present study substantiates that multi-enzyme / multi-step biocatalytic cascades of increased complexity (when compared to their single or dual gate counterparts) can yield reliable diagnoses of physiological conditions upon the logic-based analysis of the complex patterns of various biomarkers. The system presented exemplifies a novel approach to multi-signal processing biosensors that emulate and exploit natural biochemical pathways and operate according to a biocomputing concept. Further efforts will be required to translate the approach from the conceptual realm to practical biosensor applications. Granted, future biosensor devices will leverage electrochemical readout rather than optical analysis, as was used in the present study. Nevertheless, the insights gained from this study can be extended towards the design of various sophisticated bioelectronic systems and bioactuators controlled by complex patterns of multiple inputs.

7.3 Noise performance of enzymatic AND logic gates

Recent developments in the areas of chemical [177, 178, 179, 180, 181] and biomolecular [108, 182, 183, 184] computing, emanating from the broader framework of unconventional computing [185, 186], have resulted in the realization of various biochemical Boolean logic gates [27, 28, 187, 188, 189, 190, 191, 192, 193, 194] as well as other constituents of digital systems, including simple networks [195, 196, 197]. Functional units demonstrated thus far have included molecular memory units [198, 199, 200, 201, 202, 203], comparators [204], multiplexers/demultiplexers [205, 206, 207, 208], encoders/decoders [209], among others. Such devices and subsystems are expected to facilitate the assembly of concatenated systems able to process chemical information via chemical means. These systems are capable of performing simple arithmetic functions, for instance, operating as a half-adder/half-subtracter [209, 210, 211, 212, 213] or a full-adder/full-subtracter [214, 215]. Further extended these concepts to the aggregation of chemical digital processing elements, chemical systems can be designed to emulate keypad lock devices [216, 217, 218, 219, 220, 221, 222] and even to function as molecular automata [223, 224] based on networked logic operations.

Despite the current state of research pertaining to chemical computing, a majority of reported studies have been concerned with the demonstration of basic concepts, while aspects of practical applications have not been clearly addressed. In order to justify their studies, conjectures regarding possible relevance to molecular computer designs have been routinely emphasized. In reality, however, present-day chemical systems are not able to directly compete with conventional electronic computation devices. Indeed, biocomputing systems have, thus far, been connected only in simple 'circuits' capable of implementing basic arithmetic operations on the temporal scale of minutes or longer, which is largely unacceptable for most computation-based applications. On the other hand, the application of biomolecular logic systems for analytical purposes could provide utilitarian functionality in other domains, such as the development of a novel class of bio(chemical)

sensors which are able to accept multiple input signals and produce binary alert-type outputs in the form of a sequence of bits that can be used to identify relevant biomedical conditions [36, 41, 47, 146]. This approach has already been successfully applied towards the analysis of multi-parameter physiological conditions corresponding to different forms of injury [42, 43]. The biosensors under this thrust have leveraged enzyme-based biocatalytic cascades able to process targeted biomarker signals, which may deviate from normal physiological concentrations to elevated (or decreased) levels as a result of injury. Accordingly, in order for these systems to yield a reliable and high-fidelity assessment of life-threatening conditions, careful consideration must be directed at noise control in the gate- and network-level implementations of these enzyme logic gate archetypes [29, 30, 144].

In order to achieve the aforementioned aims, experimental and theoretical analyses of two unique **AND** logic gates embodying substantial kinetic similarities has been performed. These gates, activated by an enzyme and its corresponding substrate, consist of lactate dehydrogenase (LDH, E.C. 1.1.1.27) / lactate (substrate) and glutathione reductase (GR, E.C. 1.8.1.7) / glutathione disulfide (substrate) , which jointly constitute a definitive contingent of biomarkers for abdominal trauma (ABT) [151, 152, 153, 154] and oxidative stress (OS) [156, 157], respectively.

Previously-reported (bio)chemical computing systems have utilized arbitrary levels of the input signals (traditionally logic '**0**' has corresponded to a physically-zero concentration of inputs, while logic '**1**' was established at an arbitrarily high concentration) [225, 226, 227]. Novel biomedical applications require the operation of biochemical digital computing systems at specific logic input levels determined by physiological conditions with '**0**' and '**1**' corresponding to physiological and pathological concentrations, respectively. The logic '**0**' and '**1**' input signals may accordingly embody a minuscule range of variation, thus resulting in poor discrimination between the output signals generated by the gates. Furthermore, the output signal values interpreted as logic '**0**' and '**1**' can exhibit significant variation as compared to the difference between the two reference logic values. Finally, instituting operation at physiological concentrations imposes strict con-

straints on the possible values or ranges of concentrations and leaves little margin for the optimization of the process parameters. In order to infer the operational performance of the biochemical logic gate, the entire surface response function should be mapped and analyzed for the full possible concentration spread that the input signals can assume [29, 30, 31].

Biochemical logic gates presented in the literature typically utilize enzymes that operate as the machinery for higher-order logic systems, which serve to process signals represented by their corresponding substrates/cosubstrates [28, 194]. Alternatively, enzymes have been employed as input signals to activate biochemical logic systems comprised of the other required reactants [27, 31]. The present biocomputing gates are activated upon the simultaneous presentation of an enzyme and its corresponding substrate as inputs for the **AND** logic implementation. This imposes additional challenges for the accurate modeling of system performance, and, from this point of view, such gates can be regarded as examples of a novel, previously unexplored class of biochemical logic systems. Since input signals in these gates correspond to physiological conditions, there inevitably exists some uncertainty present in their values due to the innate physiological variations among human subjects. Owing to the stochastic nature of such systems, a random distribution of input signals (i.e. noise) is expected to exist in the system. As the presented systems can be applied to a broad range of biomedical applications, the analysis and understanding of the noise at the inputs and the manner in which it propagates through such logic gates are in order.

Experimental procedure for the LAC/LDH AND gate:

A graphical representation of the enzymatic **AND** logic gate is outlined in Fig. 7.8. The gate machinery consists of nicotinamide adenine dinucleotide (NAD^+) (10 mM and 1 mM for optical and electrochemical measurements, respectively) in a 50 mM sodium/potassium phosphate buffer (PBS) with 0.2 mM $MgCl_2$ and 0.01 mM $CaCl_2$, pH = 7.15. Methylene green (MG, 1 mM) was employed as an electroactive mediator in order to reduce the overpotential required to oxidize the reduced form of nicotinamide adenine dinucleotide (NADH). The **AND** logic gate was activated by presence of lactate (LAC) and LDH as inputs

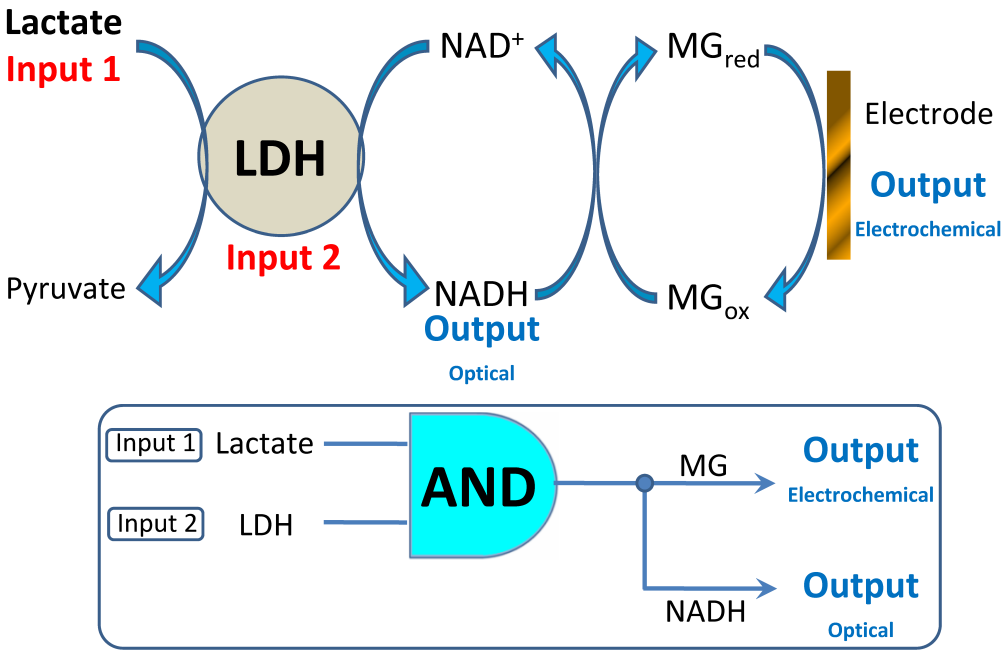

Figure 7.8: *Lactate / lactate dehydrogenase biocatalytic cascade and its **AND** logic gate equivalent*

1 and 2, respectively. Logic '**0**' and '**1**' levels of LAC (1.6 mM and 6.0 mM) and LDH (150 U L^{-1} and 1000 U L^{-1}) input signals were chosen according to the mean normal and elevated physiological concentrations of these biomarkers relevant for the diagnosis of abdominal trauma (ABT) [151, 152, 153, 154]. Optical absorbance measurements were performed at $\lambda = 340$ nm, and the electrochemical measurements were performed using amperometric techniques (0.1 V *vs* Ag/AgCl applied at the working electrode along with continuous agitation) in order to monitor the generation of the NADH product. In the optical experiments, the absorbance measurements were initiated immediately upon the combination of the reagents in a cuvette, and the final absorbance was extracted at 360 s from the beginning of the measurements. In the electrochemical experiments, the buffer, lactate, LDH, and MG solutions were dispensed in the microcell, and amperometric recording was initiated using a glassy carbon electrode Glassy carbon electrode. Following a 150 s settling period to allow the background current to decay to steady-state levels, the NAD^+ solution was added, and the recording continued for an additional 150

s. At 300 s following the initiation of the recording (150 s following the addition of NAD^+), the output signal current reading was extracted. In order to remove the contribution of the background current to the bona fide electrochemical signal arising from the biocatalytic process, the current obtained just prior to the addition of NAD^+ at 150 s was subtracted from the current reading at 300 s. In order to map the response surface of the **AND** gate, the LAC and LDH concentrations were varied across the maximum extent of their respective physiological-pathophysiological ranges, hence yielding an array of 6 $\times$ 6 experimental data points. With respect to electrochemical measurements, LAC was varied between 0 mM and 7.5 mM (in 1.5 mM increments) while LDH was varied between 0 U L^{-1} and 1250 U L^{-1} (in 250 U L^{-1} increments). On the other hand, optical measurements were conducted using the following parameters: LAC varied between 1 mM and 7 mM (in 1.2 mM increments) and LDH was varied between 100 U L^{-1} and 1100 U L^{-1} (in 200 U L^{-1} increments). To ensure that the entire range of possible levels of these biomarkers was included in the analysis, the concentrations of the input signals were scanned from levels somewhat below their respective logic '**0**' values to somewhat above their logic '**1**' values.

Experimental procedure for the GSSG/GR AND gate:

A graphical representation of the enzymatic **AND** logic gate is outlined in Fig. 7.9. The gate machinery consists of 0.18 mM nicotinamide adenine dinucleotide phosphate (NADPH) in a 50 mM citrate buffer, pH = 5.0. 2mM 5,5'-dithiobis-(2-nitrobenzoic acid) (DTNB, 'Ellman's reagent'), a photoactive dye, was included for optical measurements. The **AND** logic gate was activated by glutathione disulfide (GSSG) and GR as inputs 1 and 2, respectively. Logic '**0**' and '**1**' levels of GSSG (150 μM and 400 μM) and GR (556 U L^{-1} and 650 U L^{-1}) input signals were selected according to the mean normal and elevated physiological concentrations of these biomarkers in erythrocytes, motivated by studies of oxidative stress [156, 157]. Since GR and GSSG are mainly present in intracellular compartments of erythrocytes, maintaining a physiological pH (7.35 - 7.45 for serum) was not essential for the assay. Thus, in order to attenuate the enzymatic reaction and yield a high dynamic range between the output logic '**0**' and '**1**' lev-

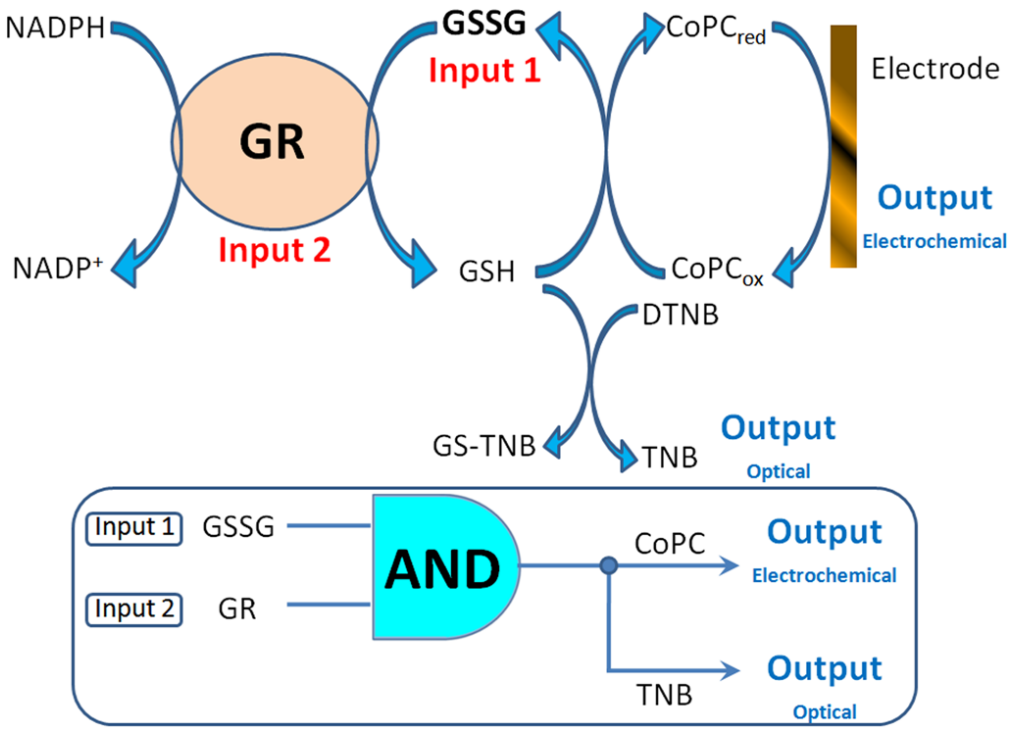

Figure 7.9: *Glutathione disulfide / glutathione reductase biocatalytic cascade and its **AND** logic gate equivalent*

els, the pH was experimentally optimized and established at an optimal value of 5. In the optical experiments, the thiol groups of the biocatalytically produced glutathione (GSH) irreversibly reacted with DTNB, resulting in the formation of 5-thio-(2-nitrobenzoic acid) (TNB) which was monitored by absorbance changes at $\lambda = 412$ nm. The absorbance differential was measured following the mixture of the reactants in a cuvette, and the final absorbance value was extracted at 100 s from the initiation of the reaction. In the electrochemical experiments, cobalt phthalocyanine (CoPC, 2 % w/w) was employed as a redox mediator to reduce the overpotential required for the detection of GSH at 0.5 V *vs* Ag/AgCl. The buffer, GR, GSSG, and NADPH solutions were dispensed on the CoPC-modified screen printed electrode (SPE), and an amperometric recording (in a quiescent solution) was initiated. Following a 30 s settling period to allow the transient current to decay to negligible levels, the recording was terminated, and the reading was extracted. In order to map the response surface of the **AND** gate, the two inputs were varied across the maximum extent of their respective physiological-pathophysiological ranges, hence yielding an array of 6 × 6 experimental data points. Optical measurements were conducted using the following parameters: GSSG varied between 67 μM and 483 μM (in 83 μM increments) and GR was varied between 524 U L^{-1} and 679 U L^{-1} (in 31 U L^{-1} increments). To ensure that the entire range of possible levels of these biomarkers was included in the analysis, the concentrations of the input signals were scanned from levels somewhat below their respective logic '**0**' values to somewhat above their logic '**1**' values.

Theoretical model of AND gate function:

As mentioned previously, the initial concentrations of both inputs vary between some minimum value (not equal to zero), [**Input 1**]$(t = 0) = C_{1,min}$, [**Input 2**]$(t = 0) = C_{2,min}$, and maximum value, [**Input 1**]$(t = 0) = C_{1,max}$, [**Input 2**]$(t = 0) = C_{2,max}$, determined by specific biomedical applications. The output product concentration, P, is measured as $P(t = t_{gate})$ at a specific reaction time, t_{gate}, and also varies between two values, P_{min} and P_{max}, as the input concentrations are swept from their minimal to maximal values. To analyze the logic gates, the input/output chemical signals are cast in terms of the dimensionless input (x,y)

and output z variables scaled to the logic ranges:

$$x = \frac{C_1 - C_{1,min}}{C_{1,max} - C_{1,min}}, \tag{7.1}$$

$$y = \frac{C_2 - C_{2,min}}{C_{2,max} - C_{2,min}}, \tag{7.2}$$

$$z = \frac{P - P_{min}}{P_{max} - P_{min}}. \tag{7.3}$$

The noise amplification properties of the **AND** gate has been thoroughly analyzed in previous work [29, 30, 31, 144, 225] by considering the function $z(x,y)$, termed the response surface, in the vicinity of the logic points $(x,y) = (\mathbf{0},\mathbf{0})$, $(\mathbf{0},\mathbf{1})$, $(\mathbf{1},\mathbf{0})$, and $(\mathbf{1},\mathbf{1})$. In general, the gate output is a function of not only the initial inputs and the duration of the reaction, but also on other endogenous parameters such as, in the present case, the initial concentration of the cosubstrate, c, and the operational pH level such that

$$P = F\left(C_1, C_2; c, pH, ...; t_{gate}, ...\right). \tag{7.4}$$

Note that the additional parameters, which can be either physical or bio/-chemical, are divided into two groups in Eq. (7.4). Certain parameters, here represented by c and pH, can be adjusted to some extent to improve gate performance. Other parameters cannot readily be adjusted as desired, for instance, t_{gate}, which was selected to yield the highest dynamic range between the output logic '**0**' and '**1**' levels, as well as most physical properties such as the temperature, which are inelastic variables specified by the intended application.

In order to calculate the function $z(x,y)$, the parameter dependence in Eq. (7.4) must be modeled. It is important to note [225] that there are several sources of noise to be considered in biochemical computing. In addition to the natural fluctuations in the inputs in the vicinity of the precise logic point values, systematic deviations may exist, as well as the uncertainty present in the physiological concentrations owing to human variability. The output of the stochastic system, similarly, is not precisely defined. In addition to the spread inherent in the output

levels, their absolute values may assume levels that are shifted from the selected reference. Furthermore, the logic level values assumed by the output signals will generally differ provided the various permutations of logic inputs. This is in direct contradiction to conventional electronic logic gates in which all Boolean-equivalent input combinations are expected to yield equivalent output signal levels.

It may not be feasible to precisely define the functional dependence in Eq. (7.4); hence, Eq. (7.4) should be viewed as an average with an inherent spread in the values assumed by the logic levels. One method that may be utilized to evaluate the function F resides in fitting empirically-derived data to solve a set of precise or phenomenological kinetic equations corresponding to the enzymatic reaction under evaluation; this approach was pursued in previous investigations for several biochemical systems [29, 30, 31]. In these studies, the kinetic parameters of the chemical systems under evaluation were treated as elastic parameters with values interpolated from the numerical fitting of the experimental data to the solution of the kinetic equations. Although insightful, this approach requires a working knowledge of the kinetics of the logic gate system, which is not the case for the present systems under investigation due to their complexity. Indeed, even a simplified kinetic description [226, 227, 228, 229, 230, 231] would require fitting an inordinate number of elastic parameters, which, consequently, cannot be accurately determined from the data map generated from the gate response.

Another approach [144] has called for the specification of a phenomenological fitting function for F based on expected solutions of the kinetic equations in addition to experimental observations. This approach has been developed [144, 225] for the general analysis of the noise performance inherent to biochemical logic gates and networks when detailed information regarding the system's kinetics was either unavailable or the set of the reactions was far too complex to determine fitting parameters uniquely.

Indeed, the extraction of the global features of the response surface function $z(x,y)$, sufficient to evaluate the biochemical logic gate's behavior in the vicinity of the four logic point values, is substantiated. However, an earlier phenomenological fitting form [29] developed for typical biochemical reactions encountered in

AND logic gate incarnations with the logic '**0**' values established at true zero concentrations actually reflects the features of the biochemical reaction rather than, more generally, those of the binary logic. Therefore, it is inappropriate to use such a form for gates with nonzero logic '**0**' values. To avoid this complication, the empirical data was not scaled to the logic ranges corresponding to Eqs. (7.1) - (7.3). Instead, the ambition is to fit the function F in Eq. (7.4) first by utilizing a phenomenological shape function suggested by earlier studies, [29] which here can be expressed as

$$F = \frac{\phi C_1 C_2}{(\alpha C_1 + 1)(\beta C_2 + 1)}. \tag{7.5}$$

The resulting function will subsequently be employed to derive an estimate for $z(x,y)$. It should be noted, however, that the overall constant in Eq. (7.5) is not a useful fitting parameter as it will be canceled in the calculation of $z(x,y)$. Therefore, the actual data fitting, described below, is performed for F normalized to its measured value at input concentrations at which it assumed a maximum value. This ratio was least-squares-fitted in order to determine the two fitting constants of interest, α and β.

Owing to the nonzero values that the minimum input concentrations assume, the output concentration concomitantly possesses somewhat different values for the combinations of the inputs $(C_{1,min}, C_{2,min})$, $(C_{1,min}, C_{2,max})$, as well as $(C_{1,max}, C_{2,min})$. In other words, the output at logic '**0**' level assumes three unique values. However, for a standard **AND** gate, the logic '**0**' output should be equivalent for all input combinations. This implies that the enzymatic gates considered in this work have some systematic noise built-in [225]. This noise is additive to the random noise that has been extensively analyzed in earlier work [29, 30, 31]. Thus, the demands for additional network elements with filtering properties [29, 225] will be even more stringent here if the present systems are to be employed as components of biochemical logic networks. The present modeling approach is also somewhat differs from earlier variants [31] in that the mean values defined as P_{min} and P_{max} are not unknown variables. Rather, Eq. (7.4) is first evaluated, which is then used to calculate P_{max} and the lowest magnitude logic '**0**' value as P_{min} (another

option would be, e.g., an average of the three logic '**0**' outputs as P_{min}). Indeed, the output signals to be utilized as reference '**0**' and '**1**' are not arbitrary but are established by the application, and care should be taken to minimize noise levels to yield high dynamic range performance of the **AND** function.

If the phenomenological fitting provided by Eq. (7.3) is indeed accurate, then α*(C, pH, ...; tgate,...)* and β*(C, pH,...;tgate,...)* should be functions of the chemical and physical parameters introduced in Eq. (7.2). The present approach, however, does not attempt to obtain this kinetic information and therefore offers no quantitative information on the dependence of the response surface function z on such parameters (in addition to its arguments x and y). Thus, this model cannot be utilized to directly optimize gate functionality. However, qualitative arguments [29, 225] can usually be utilized to decide whether to increase or decrease the overall gate activity in order to augment performance. These typically require a substantial modification in gate machinery because the response surface is obtained in terms of the scaled variables, Eqs. (7.1) - (7.3), and is not sensitive to the leading-order linear-response-type changes. For the present systems (i.e. those with chemical concentrations established at physiological levels), substantial alterations are not feasible nor practical, and, therefore, the performance of the gate cannot be readily optimized by varying the few degrees of freedom permitted under the experimental approach. Instead, the aim resides in the corroboration of an estimate of the degree of "noisiness" inherent in enzyme-based logic gate operation, with the expectation that, when networked with other elements (reaction steps) such as filters, will result in the demonstration of utilitarian enzyme logic-based systems with less noise.

To analyze random noise amplification from input to output, [31, 142] the noise amplification factor is computed as the ratio of the output noise distribution spread, σ_{ij}^{out}, to the fixed input noise distribution width, σ^{in}, with the definition

$$\sigma_{ij}^{out} = \sqrt{\langle z^2 \rangle_{ij} - \langle z \rangle_{ij}^2}, \tag{7.6}$$

where the averages at each logic point, (i,j) = (**0**,**0**), (**0**,**1**), (**1**,**0**), (**1**,**1**), are computed with respect to the input noise distribution $D_{ij}(x,y) = X_i(x)Y_j(y)$,

which, for the sake of simplicity, is assumed to be an uncorrelated product of two Gaussian distributions with equal widths, σ_{in}, in terms of the scaled variables. The straightforward expression

$$\langle z^n \rangle_{ij} = \iint z^n (x,y)\, D_{ij} (x,y)\, dxdy \tag{7.7}$$

is employed for numerical computations. In order to obtain a description of the effect of systematic noise, the inherent signal level jitter that translates into imprecise average values for z,the averages, $\langle z_{ij} \rangle$, are first computed. The spread interval ($\langle z_{ij} \rangle$ - σ_{ij}^{out},$\langle z_{ij} \rangle$ + σ_{ij}^{out}), which defines the region where the output corresponding to the specific logic point is most likely to be found for the assumed distribution of random noise at the input. If the combined spread region for the three logic **0** points overlaps with or is in close proximity to the logic **1** value, then the gates under evaluation in this study cannot be employed for systems with the degree of random input noise at levels near the σ_{in} value considered in this investigation.

Fitting of theoretical model to experimental data:

The catalytic reduction of NAD^+ to NADH that proceeds in the presence of lactate (**Input 1**) and LDH (**Input 2**) results in the increased production of NADH, which can be followed by optical and electrochemical means; as shown in Fig. 7.8. With respect to optical measurements, the absorbance increase characteristic of NADH formation was monitored at $\lambda = 340$ nm (note that the system's background absorbance was subtracted), as provided in Fig. 7.10A. In the electrochemical experiments, the NADH oxidation was mediated by MG [134], and the obtained current values corresponded to the concentration of NADH produced in the course of the biocatalytic reaction, Fig. 7.10B. The system emulated the **AND** logic gate when the reaction that ensued resulted in the formation of elevated levels of the product only in the presence of both reacting species: the substrate (lactate) and the enzyme (LDH) [input signal combination (**1**,**1**)], Fig. 7.10C. However, since the logic '**0**' values of both input signals do not correspond to truly zero concentrations of the reactants, the product is also generated at what should be considered '**0**' logic values [i.e. in the presence of input combinations (**0**,**0**), (**0**,**1**), (**1**,**0**)].

In order to analyze the output function of the biocatalytic system for the given logic values of the input signals, measurements were performed across an array of substrate (lactate) and enzyme (LDH) concentrations.

The normalized (to the maximum observed value) experimental response surface obtained by optical absorbance spectroscopy (top row) and electrochemical current measurements (bottom row) is illustrated in Fig. 7.11 for reaction times of t_{gate} = 360 and 300 s, respectively. As one can observe, both the measured, Figs. 7.11A and D, and fitted, Figs. 7.11B and E, surfaces obtained by the two methods are consistent. The logic surfaces extracted from optical and electrochemical measurements, provided Figs. 7.11C and F, exhibit noteworthy similarity. This is also confirmed via a comparison between the output logic values at four logic points from the two data sets; see Fig. 7.12. In this plot, the z-values corresponding to (**0**,**0**) and (**1**,**1**) logic input combinations are at '**0**' and '**1**', respectively, while z-values for two other logic input pairs, (**0**,**1**) and (**1**,**0**), fall in between. Note that the outputs from the latter pair are not in as close proximity to logic '**0**' as they should be for a true **AND** gate owing to the fact that these logic values correspond to different nonzero concentrations of the inputs and, as such, cannot be set equal to one another or to the output at (**0**,**0**).

The similarity between the two response surfaces is also manifested in similar noise characteristics evaluated for each response. Both the noise amplification factors (the degree to which the random input noise is amplified at a particular logic value), illustrated in Figs. 7.13A and C, and the spread regions (the separation between the logic points for a given value of the input noise distribution width), shown in Figs. 7.13B and D, are in good agreement with respect to both qualitative and quantitative measures. From the plots of $\sigma_{ij}^{out}/\sigma_{in}$, the response of the **AND** gate to noise present at its inputs can be gauged. If the maximum of $\sigma_{ij}^{out}/\sigma_{in}$ is greater / less than 1, then the logic gate amplifies / suppresses incoming random noise. In particular, one can observe that the logic point with the most inherent noise (irrespective of the input noise spread), in other terms, the input yielding the largest ratio $\sigma_{ij}^{out}/\sigma_{in}$, is (**1**,**0**). At this point, the LAC/LDH concentration is the greatest / least. Even though the noise is actually suppressed

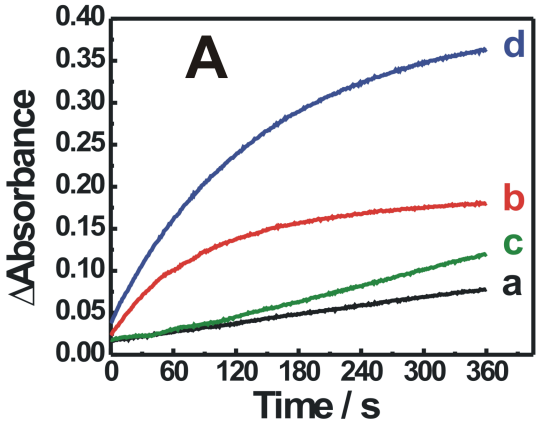

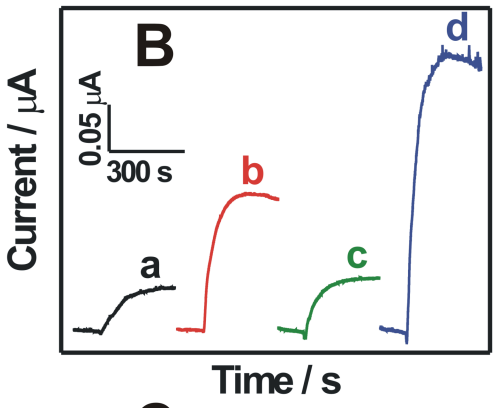

C

Input 1	Input 2	Output
Lactate	LDH	NADH/MG
0	0	0
0	1	0
1	0	0
1	1	1

Figure 7.10: *(A) Optical absorbance (λ = 340 nm) and (B) electrochemical amperometric (0.1 V vs Ag/AgCl) detection of the NADH output generated by the LAC/LDH biocatalytic cascade upon different combinations of the input signals, (a) (**0**,**0**), (b) (**0**,**1**), (c) (**1**,**0**), and (d) (**1**,**1**). (C) The truth table corresponding to the **AND** logic operational functionality of the system.*

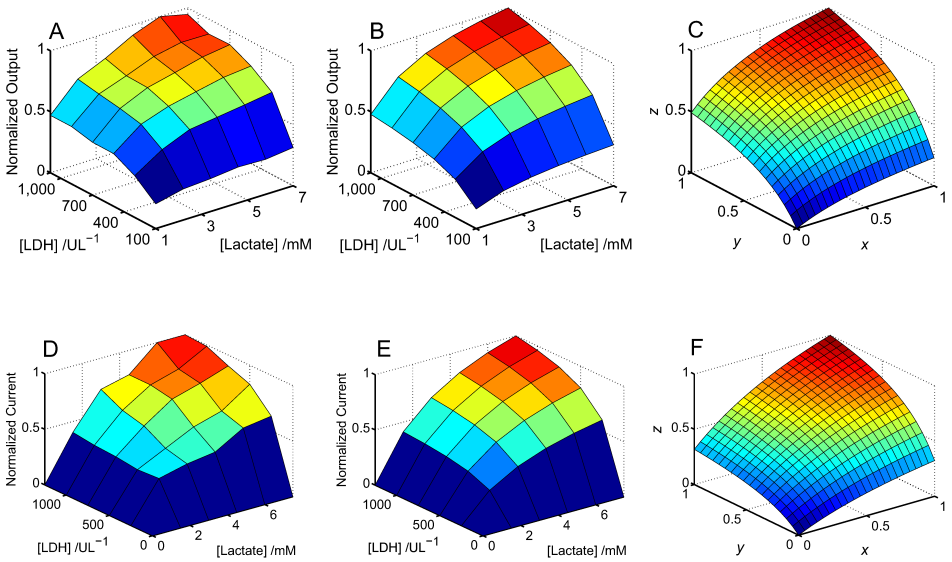

Figure 7.11: *Experimental data and their interpolation for optical (A-C) and electrochemical (D-F) measurements. Panels (A) and (D) illustrate the experimental response surface for the LAC/LDH-based* ***AND*** *gate; (B) and (E) provide the numerical fit according to Eq.* (7.5)*, with the resulting parameters* α *and* β *extracted as 0.645 (0.241)* $(mM)^{-1}$ *and* 3.68×10^{-3} *(*4.10×10^{-3}*)* $U^{-1}L$ *for optical and (electrochemical) datasets, respectively. Panels (C) and (F) exhibit the response surface in terms of the logic-range variables* x, y, *and* z*, which have undergone proper scaling and shifting to conform within the established limits (since the logic '****0****' values are not defined at zero concentrations).*

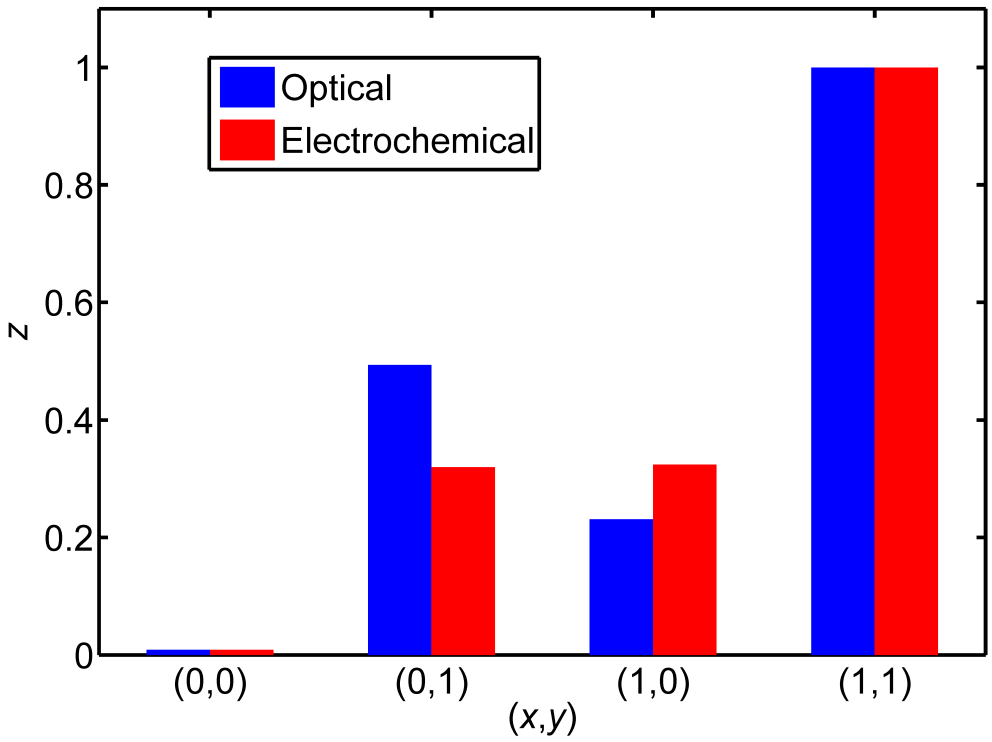

Figure 7.12: *Normalized output logic values* z *for the four logic input permutations to the LAC/LDH* ***AND*** *gate.*

at the (**1**,**1**) logic point ($\sigma_{ij}^{out}/\sigma_{in} \approx 0.5 < 1$), poor performance ($\sigma_{ij}^{out}/\sigma_{in} > 2$; see Fig. 7.13) at the (**1**,**0**) logic point implies that this system, in general, is not very suitable for incorporation in large networks of biochemical logic gates without the addition of filtering elements [31, 225] aimed at reducing noise.

The present approach of estimating the random noise amplification factor by assuming a Gaussian input distribution becomes inappropriate for σ_{in} exceeding ≈ 0.2, whereby the spread of the distribution becomes comparable to a sizable fraction of the unit interval. While the $\sigma_{ij}^{out}/\sigma_{in}$ profile tends to decrease for σ_{in} beyond 0.1, the overall shape of $z(x,y)$ in the present system is convex, which implies that the **AND** gate always amplifies analog noise [31].

In practice, the physiological spread of the input concentrations is substantially less than 20%, at least for the (**0**,**0**) logic input. Indeed, the observed concentrations for LAC are within the 0.5 - 2.25 mM range, while the LDH values

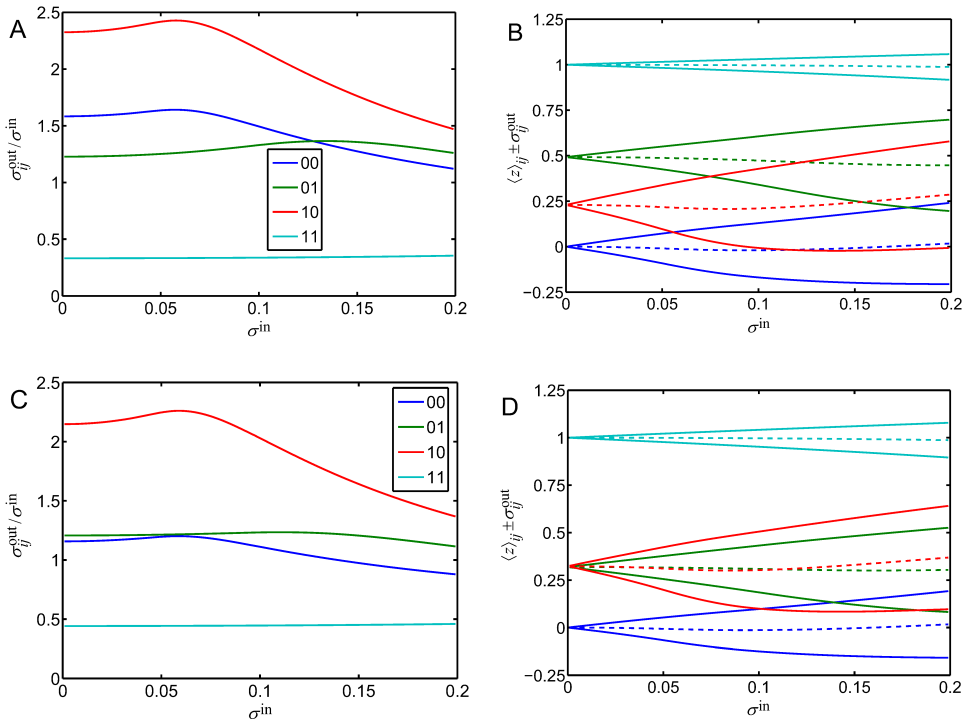

Figure 7.13: *Noise propagation properties of the LAC/LDH* ***AND*** *gate, as calculated from fits of the optical (A,B) and electrochemical (C,D) data. Panels (A) and (C) display noise amplification factors $\sigma_{ij}^{out}/\sigma_{in}$ versus the assumed width of the input noise distributions, σ_{in}. Panels (B) and (D) illustrate the spread region versus width of the input noise distribution σ_{in}. The dashed line denotes the average value, $\langle z\rangle_{ij}$, of the logic output, while the solid lines of the same color indicate the upper and lower bounds of the spread region, $\langle z\rangle_{ij} \pm \sigma_{ij}^{out}$.*

are distributed over the 42 - 180 U L^{-1} interval [232, 233]. The average values that are employed as the logic '**0**' inputs are 1.6 mM and 150 U L^{-1} for LAC and LDH, respectively. This indicates that the distribution of the inputs is not symmetrical and that the distribution spread is mutually exclusive for both LAC and LDH. Accordingly, calculations only yield a qualitative estimate of the noise amplification at this logic point. By taking $\sigma_{in} = 10\%$, which is the average of the data spreads for the x and y logic inputs (15% and 5%, respectively), it can be deduced that the intrinsic noise in the system will be amplified by 120% at this logic point. Assuming that the input noise spread remains constant and unperturbed for all other logic points, the maximum noise amplification produced by this gate would be roughly 3.6 dB when provided with the (**1**,**0**) input.

This degree of amplification of the incoming noise does not, however, preclude practical utilization of the presented gate. Analysis of the spread region plots in Figs. 7.13B and D, attests that, at $\sigma_{in} = 10\%$, the (**1**,**1**) logic point is well-separated from the other logic points by a margin of approximately 0.5 despite the fact that the average outputs at (**0**,**1**) and (**1**,**0**) are not 0. However, if σ_{in} increases to 30%, the spread regions of (**1**,**1**) and (**1**,**0**) points begin to overlap, and it may not be possible to distinguish between the '**0**' and '**1**' levels of the output signal.

Analagous to the previous system, the catalytic reduction of GSSG (**Input 1**) in the presence of GR (**Input 2**), which proceeds in the presence of NADPH (a constituent of the gate machinery), results in an elevated concentration of GSH in the solution, which can be monitored by optical and electrochemical means, Fig. 7.9. With respect to optical measurements, in order to convert GSH to a chromogenic product, DTNB (Ellman's reagent) was employed, which resulted in the formation of TNB, which was monitored optically at $\lambda = 412$ nm, Fig. 7.14A. With respect to the electrochemical experiments, GSH oxidation was catalyzed by a CoPC-impregnated SPE [234, 235]. The current obtained corresponds to the concentration of GSH produced in the course of the biocatalytic reaction, Fig. 7.14B. The system represents an **AND** logic gate when the reaction results in the formation of a product only in the presence of both reacting species, the substrate (GSSG) and the enzyme (GR) (i.e. input signal combination (**1**,**1**)),

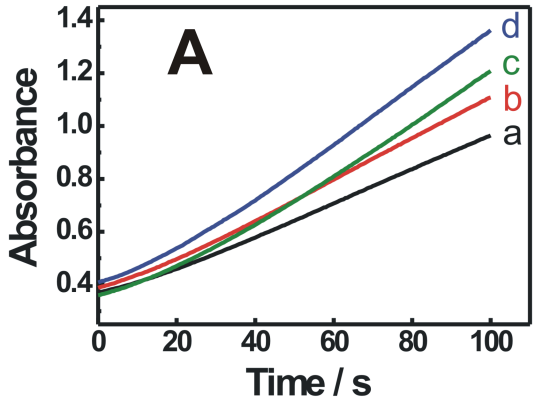

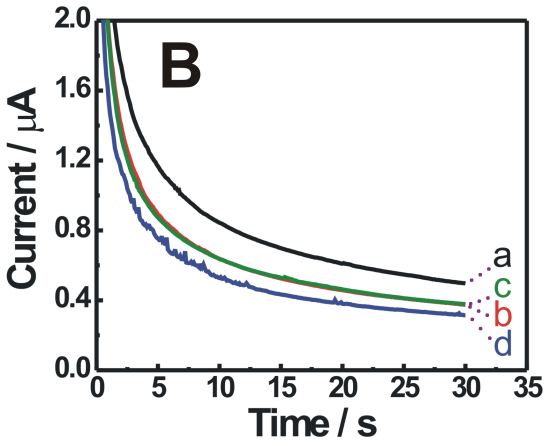

C

Input 1	Input 2	Output
GSSG	GR	TNB/CoPC
0	0	0
0	1	0
1	0	0
1	1	1

Figure 7.14: *(A) Optical absorbance (λ = 412 nm) and (B) electrochemical chronoamperometric (0.5 V* vs *Ag/AgCl) detection of the GSH output generated by the GSSG/GR biocatalytic cascade upon different combinations of the input signals, (a) (**0**,**0**), (b) (**0**,**1**), (c) (**1**,**0**), and (d) (**1**,**1**). (C) The truth table corresponding to the **AND** logic operation of the system.*

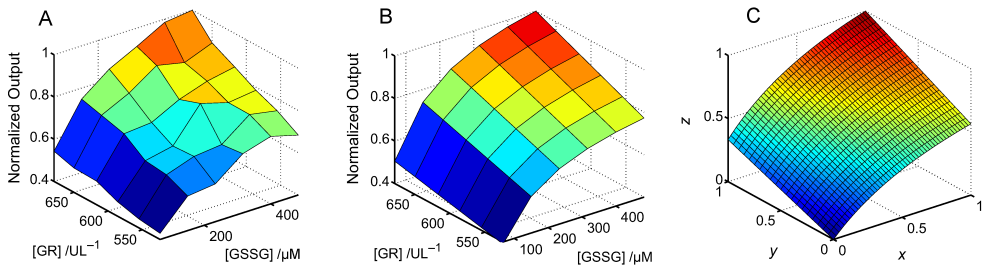

Figure 7.15: *(A) Optical measurements and numerical fitting of the response surface for the GR-based gate. (A) Experimental response surface. (B) Numerical fit of the surface in (A), according to Eq.* (7.5)*, yielding estimates of* $\alpha = 1.14 \times 10^{-2}(\mu M)^{-1}$ *and* $\beta = 0.00\ U^{-1}\ L$*. (C) Logic surface* z(x,y)*.*

Fig. 7.14C. However, analogous to the LAC/LDH system, logic '**0**' values of the input signals do not correspond to zero concentrations of the reactants, implying that some amount of the product is also generated at logic '**0**' values for one or both inputs. In order to analyze the output function of the biocatalytic system for the given input logic signals, measurements of the variable concentrations of both logic inputs (the substrate (GSSG) and enzyme (GR)) were performed. In contrast to the LAC/LDH system, which can directly serve as a logic gate injury detection paradigm for abdominal trauma [151, 152, 153, 154], GR/GSSG is an example of a system which shows potential for intracellular investigations. Concentrations of the enzyme (GR) and its substrate (GSSG) used in the present study correspond to those levels found within the intracellular space of erythrocytes. However, the presence of these biomarkers in blood occurs in scenarios where erythrocytes are ruptured, which can serve as a symptom of radiation exposure or severe oxidative stress [236]. Thus, further biomedical studies are required to determine the normal and pathophysiological concentrations of the biomarkers in blood.

In general, the optical response surface and noise properties of this logic system exhibited noteworthy similarities to the one discussed in the previous subsection. One can ascertain from the response surface provided in Fig. 7.15 and normalized logic outputs in Fig. 7.16 that the (**0**,**1**) and (**1**,**0**) points are displaced from '**0**', in direct correspondence with the results provided earlier in Figs. 7.11 and Fig. 7.12. Furthermore, the agreement between optical and electrochemical mea-

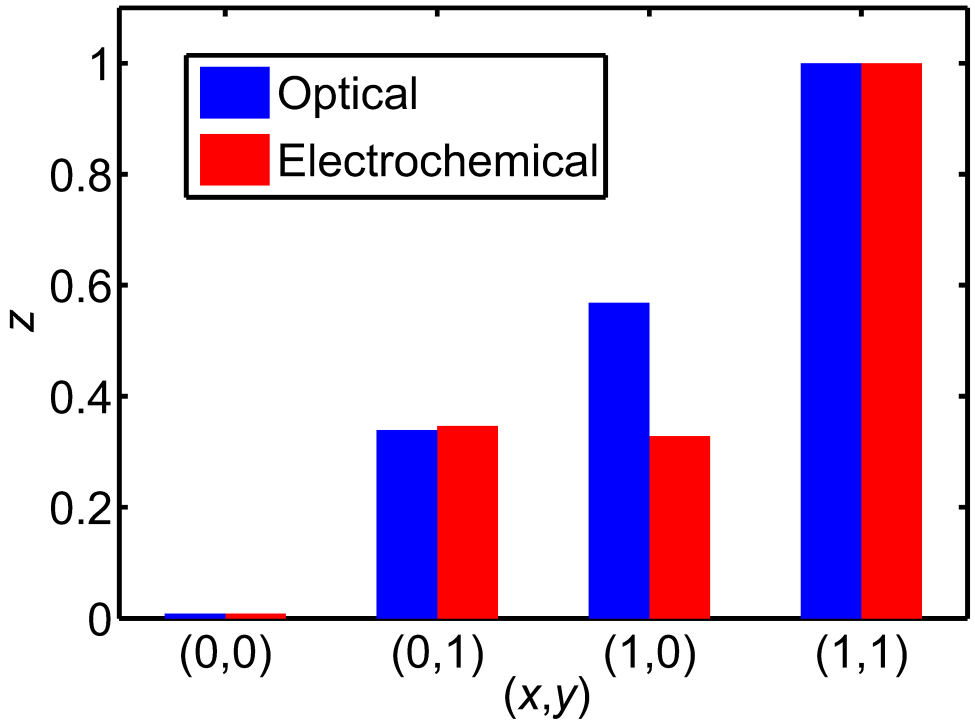

Figure 7.16: *(A) Normalized output logic values* z *for the four logic input permutations to the GSSG/GR* ***AND*** *gate.*

surements at the logic points is satisfactory, as is evident from Fig. 7.16. Therefore, for the GR/GSSG system, electrochemical measurements were performed only at the four logic points for validation purposes rather than proceeding with a mapping of the entire response surface.

The maximum noise amplification factor produced using this logic gate incarnation is greater than 100% (Fig. 7.17A), which is not surprising given the overall convex shape of the response surface in Fig. 7.15. The computed ratios $\sigma_{ij}^{out}/\sigma_{in}$ are actually less in magnitude than those calculated for the LAC/LDH system (see Fig. 7.13). This indicates that the system exhibits somewhat better noise performance, that is, it amplifies input noise to a lesser extent than the LAC/LDH logic gate (the maximum amplification factor here is 2.3 dB *vs* 3.6 dB for the LAC/LDH gate). However, owing to the larger variation in the average z-values at the logic '**0**' points (Fig. 7.16), the spread region void that differentiates the logic '**1**' from the logic '**0**' outputs is, in fact, reduced (0.3 *vs* 0.5 for the

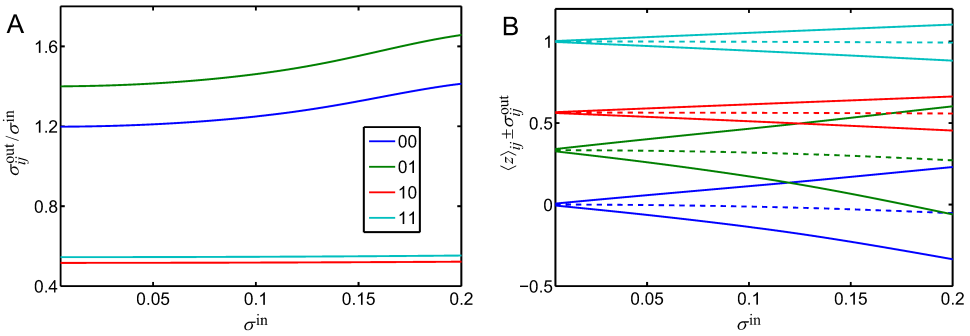

Figure 7.17: *Noise propagation properties of the GSSG/GR **AND** gate, as calculated from a fit of the optical data. Panel (A) displays noise amplification factors $\sigma_{ij}^{out}/\sigma_{in}$ versus the assumed width of the input noise distributions, σ_{in}. Panel (B) illustrates the spread region versus width of the input noise distribution σ_{in}. The dashed line denotes the average value, $\langle z\rangle_{ij}$, of the logic output, while the solid lines of the same color indicate the upper and lower bounds of the spread region, $\langle z\rangle_{ij} \pm \sigma_{ij}^{out}$.*

LAC/LDH gate), as seen in Fig. 7.17B. This is a direct consequence of the narrow physiological concentration profile embodied by GR, which effectively narrows the intrinsic separation between the '**0**' and '**1**' values.

From numerical analysis of the response surfaces, both the LAC/LDH and GSSG/GR logic gate implementations possess similar noise characteristics, that is, they amplify random noise present at their inputs with a maximum noise amplification factor of 2.3 (3.6 dB) and 1.7 (2.3 dB) for the LAC/LDH and GSSG/GR gates, respectively. Both of these gates also exhibit systematic noise due to the nonzero output product at logic '**0**'. However, at realistic values of the input noise distribution widths, on the order of 10%, it is nevertheless possible to distinguish the logic '**1**' output from logic '**0**' outputs even though the three logic '**0**' points (**0**,**0**), (**0**,**1**), and (**1**,**0**) embody substantial nonzero logic output values. This substantiates that a reliable detection of pathophysiological conditions [103, 126, 156, 157, 166, 171] can be achieved by such logic gates [128]. It is crucial to consider that, for wider distributions of the input noise or in a network of connected gates, noise suppression mechanisms, such as filtering, which lead to output products with sigmoidal dependence on the chemical inputs, must be deployed and utilized to enable further

information processing complexity with biochemical logic.

Portions of Chapter 7, section 1 were taken from J. Halámek, J.R. Windmiller, J.A. Zhou, M.C. Chuang, P. Santhosh, G. Strack, M.A. Arugula, S. Chinnapareddy, V. Bocharova, J. Wang, and E. Katz. Multiplexing of injury codes for the parallel operation of enzyme logic gates. *Analyst*, 135(9):2249–2259, 2010. The dissertation author was a co-author of the manuscript and had substantial original contributions to this work.

Portions of Chapter 7, section 2 were taken from J. Halámek, V. Bocharova, S. Chinnapareddy, J.R. Windmiller, G. Strack, M.C. Chuang, J.A. Zhou, P. Santhosh, G.V. Ramírez, M.A. Arugula, J. Wang, and E. Katz. Multi-enzyme logic network architectures for assessing injuries: Digital processing of biomarkers. *Molecular Biosystems*, 6(12):2554–2560, 2010. The dissertation author was a co-author of the manuscript and had substantial original contributions to this work.

Portions of Chapter 7, section 3 were taken from D. Melnikov, G. Strack, J.A. Zhou, J.R. Windmiller, J. Halámek, V. Bocharova, M.C. Chuang, P. Santhosh, V. Privman, J. Wang, and E. Katz. Enzymatic AND logic gates operated under conditions characteristic of biomedical applications. *Journal of Physical Chemistry B*, 114(37):12166–12174, 2010. The dissertation author was a co-author of the manuscript and had substantial original contributions to this work.

Chapter 8

Electronic support systems

In the realm of ideas everything depends on enthusiasm.
In the real world all rests on perseverance.

—Johann Wolfgang von Goethe

As discussed in previous chapters, enzyme logic gates have been leveraged to enable a high-fidelity assessment of pathophysiological status in unambiguous 'YES'/'NO' terms corresponding to the presence of one or more injuries [42, 43, 128, 129, 130, 134]. Advantageously, the enzyme logic paradigm facilitates straightforward chemical analysis since the output of these gates is truly binary and unambiguous in nature. Recognizing the unique ability of enzyme logic gates to integrate patterns in multiple biomarkers to yield a single output, a redesign of the supporting electronics is necessary due to the substantially dissimilar operational principles embodied by such logic gates when compared with conventional single-analyte amperometric biosensors relying on simple potentiostatic control. A new electronics sensing methodology is thus required whereby the binary nature of the chemical output can be exploited. Moreover, the enzyme logic architecture eliminates the requirement for scaling the number of sensing elements with the number of chemical analytes under investigation; the fluctuations in multiple biochemical markers can be integrated and processed to yield a single output, which can be monitored by a single electronic sensing element. This property can, in turn, alleviate the power consumption burden associated with multiple sensing

components. Thus far, however, microelectronic systems have not been adapted to meet the unique demands of digital sensors that exploit biocomputing principles.

Microelectronics have traditionally been leveraged to achieve the miniaturization that is a core requirement of modern electrochemical biosensors as well as to extend their operating times on battery power [237]. Advances in microelectronics have resulted in evolutionary changes to electroanalytical instrumentation, with miniaturized and inexpensive integrated circuits performing numerous functions. However, the interface between the electronic and chemical constituents of biosensors remains as one of the key limitations towards the realization of miniaturized, low power devices. Most notably, parallel detection must be employed when multivariate chemical analysis is required. In such schemes, a specific sensing element is required to monitor the level of each unique chemical entity [19]. Consequently, highly parallel sensor arrays necessitate the utilization of multiple electronic sensing elements for controlling multiple working electrodes, thereby scaling power consumption and device size accordingly. Alternatively, chemical reactions may be engineered to manipulate multiple chemical entities in the chemical domain prior to transduction to the electronic domain for further processing. In this manner, chemical signal processing can be exploited in order to enable the detection of several analytes with a single sensing contingent. This would enable a further degree of miniaturization and reduced power consumption while maintaining the overall functional capabilities of the complex system.

In order to properly interface with the enzyme logic paradigm, a new class of micro-/bioelectronic sensors has been designed, fabricated, and evaluated that are specifically configured to harness the bioprocessing capabilities of biomolecular logic systems and to provide amperometric transduction of signals generated by enzyme logic biosensors. The multivariate and versatile sensing capabilities of the concept are demonstrated, taking clinically relevant scenarios corresponding to combat injuries as a model. This biosensor is evaluated towards the amperometric determination of pathological levels of creatine kinase (CK, E.C. 2.7.3.2) / lactate dehydrogenase (LDH, E.C. 1.1.1.27) and lactate / lactate dehydrogenase for the diagnosis of soft tissue injury (STI) and abdominal trauma (ABT), respectively.

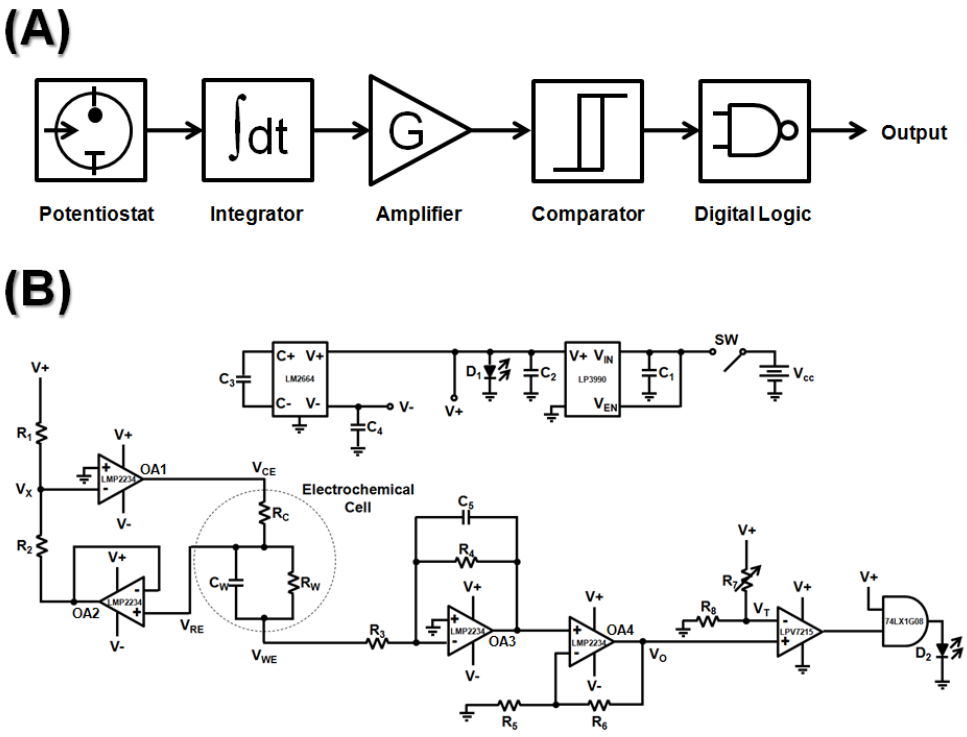

Figure 8.1: *(A) Process flow diagram outlining the equivalent functional behavior of the microelectronic sensing system and (B) the circuit-level schematic of the supporting electronics designed for the analysis of abdominal trauma. In order to realize correct logic operation, the CMOS AND logic gate in the figure is replaced with a CMOS NAND logic gate for the readout of the soft tissue injury system.*

The sensor employs enzyme cascades that emulate the operational functionality of **NAND** (STI) and **AND** (ABT) logic gates in connection with the detection of the biocatalytically processed chemical information via disposable carbon screen printed electrodes (SPE). The biosensor system enables a clinically relevant switching threshold to be pre-programmed into the device and configured as needed for the intended injury/application. The results presented clearly indicate the potential of the new concept for the unequivocal identification of pathophysiological conditions. It is anticipated that a user-friendly bioelectronic sensing system, such as the one discussed here, would be well-suited to empower a minimally-trained operator with the ability to identify a wide array of chemical agents of importance in various clinical, security, and environmental scenarios.

A linear voltage regulator (LP3990), switched capacitor voltage converter (LM2664), quad micropower precision amplifier with CMOS input (LMP2234), and micropower comparator with CMOS input (LPV7215) were procured from National Semiconductor (Santa Clara, CA). CMOS two-input AND (74LX1G08) and NAND (74LX1G00) gates were obtained from STMicroelectronics (Geneva, Switzerland). A CR1025 3 V manganese dioxide lithium-ion coin cell battery was purchased from Panasonic Corp. (Osaka, Japan). All other passives (resistors, potentiometers, capacitors, LEDs, switch, and battery holder) were acquired from Digikey Corp. (Thief River Falls, MN). Block-level and circuit-level diagrams are illustrated in Fig. 8.1A and B, respectively.

The linear voltage regulator was configured to generate a +1.8 V supply rail from the 3 V battery, which was fed into the switching voltage converter, thereby yielding a -1.8 V rail to implement fully differential voltage compliance at the potentiostatic unit. A NAND gate was employed for the STI experiments in order to invert the logic output generated by the comparator and consequently drive the status indicator LED. For the ABT experiments, an AND gate was used in the place of the NAND gate to drive the status indicator LED. The selection of resistors employed in the potentiostat was as follows: $R_1 = R_4 = R_6 = R_8 = 1$ MΩ, $R_2 = 1$ kΩ, $R_3 = 43$ kΩ, $R_5 = 100$ kΩ, and R_7 was adjusted in accordance with the switching threshold required by the application. The selection of capacitors

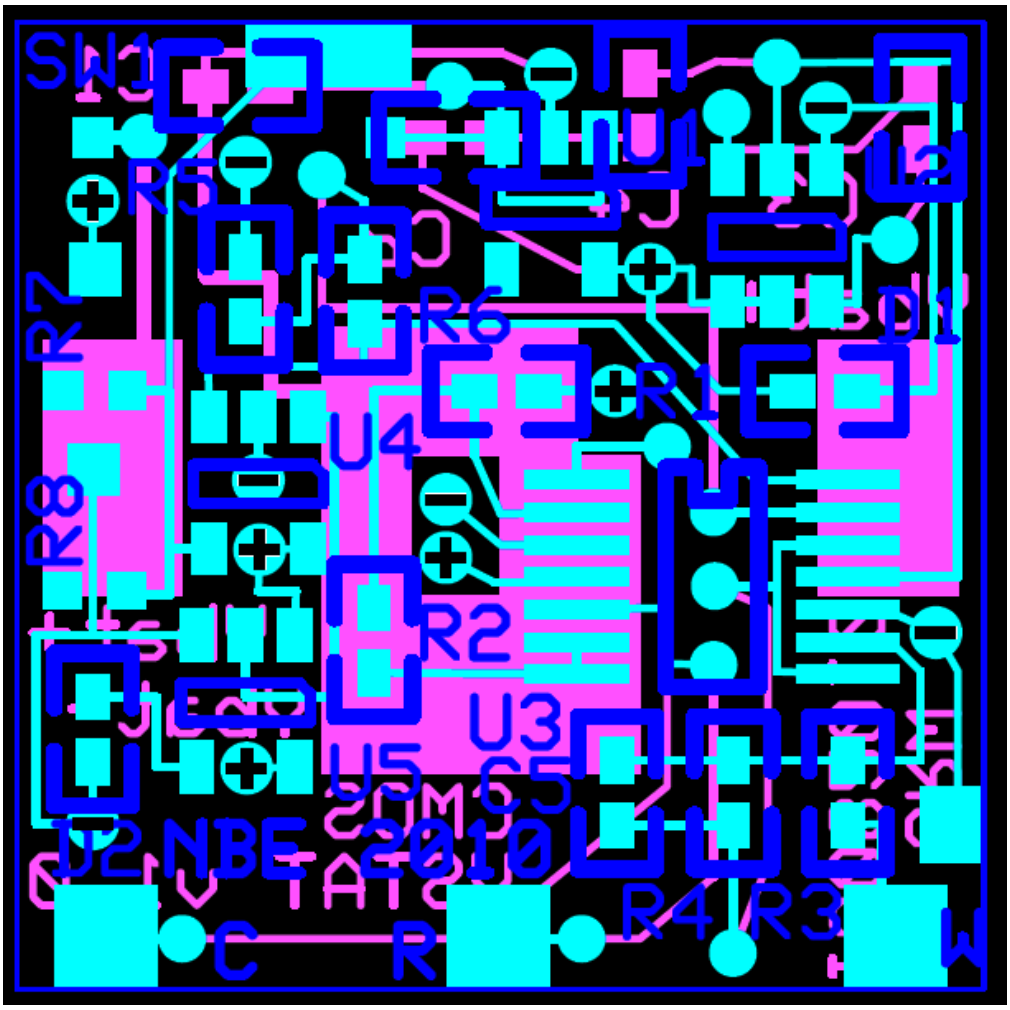

Figure 8.2: *Layout schematic of the microelectronic sensing system including the application plane, power and ground planes, and the reference plane.*

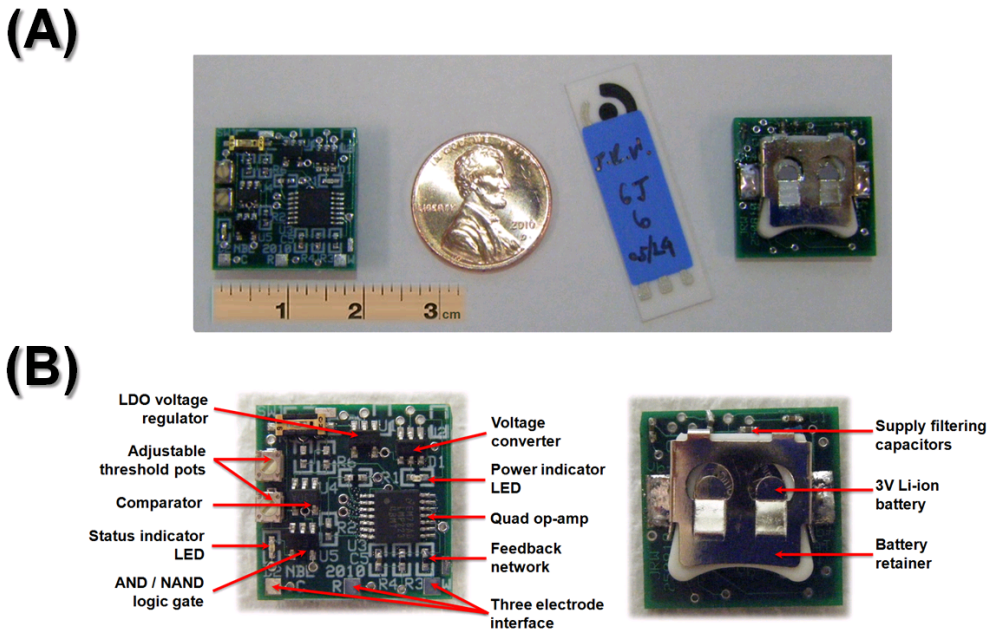

Figure 8.3: *(A) Image of the microelectronic system (US one cent and screen printed three-electrode strip shown for size comparison). (B) Obverse and reverse detail of the microelectronic system indicating the locations of the constituent components on the PCB.*

employed in the potentiostat was as follows: $C_1 = C_2 = 1\ \mu F$ (used for regulator stability), $C_3 = C_4 = 3.3\ \mu F$ (switched converter charge storage), and $C_5 = 1\ \mu F$ (low-pass filtering).

A 19 × 19 mm 4-layer printed circuit board (PCB) was custom-designed using an AutoCAD (Autodesk, San Rafael, CA) electrical layout editor and outsourced for fabrication. The PCB consisted of separate power and ground planes as well as a battery holder on the reverse side. A 4-layer board layout schematic, detailing the placement of all the traces, vias, and pads, is shown in Fig. 8.2. Photographs of the complete microelectronic device and its components are shown in Figs. 8.3A and B, respectively.

The fabrication of the screen printed electrodes employed in this study has been detailed earlier.

Among the plethora of relevant biomarkers implicated in soft tissue injury (STI), serum levels of CK and LDH become noticeably elevated under circum-

stances where muscular exertion, fatigue, injury, and trauma are sustained [103]. CK, a specific indicator of rhabdomyolysis, has been shown by Kaste *et al.* [106] to increase from an average serum level of 100 U L^{-1} under normal physiological conditions to around 710 U L^{-1} when an STI event has been incurred. Likewise, circulating levels of LDH, an enzyme frequently employed for the determination of tissue breakdown and hemolysis, can increase markedly from around 150 U L^{-1} under normal circumstances to over 1000 U L^{-1} under pathological states [104, 105].

Abdominal trauma (ABT), whether of the penetrating or blunt variety, represents a common class of combat injury whereby one or multiple organs in the abdominal cavity are ruptured or otherwise damaged [238]. In such scenarios, serum LAC and LDH are among the biomarkers of choice in the clinical setting when assessing organ damage and malfunction [154, 239]. Whereas LDH exhibits a similar concentration profile as indicated above under this class of injury [105], LAC has been shown to increase by Hara et al. from 1.6 mM to 6.0 mM [105, 238].

In both the systems under investigation (STI and ABT), the normal physiological concentrations of the selected biomarkers were employed as digital '**0**' input signals, while the elevated pathological concentrations were defined as '**1**' input signals. Thus, the systems were evaluated at four different combinations of the input signals: (**0**,**0**), (**0**,**1**), (**1**,**0**), and (**1**,**1**), where only the last combination corresponded to pathological scenarios, while the three other logic permutations reflected normal conditions or other irrelevant physiological anomalies. In addition to the binary levels of the input injury biomarkers, other reagents were experimentally optimized and employed at constant concentrations. These supporting chemicals served as the system "machinery" and therefore performed the biochemical analysis of the logic input signals.

The STI experiments were conducted by employing 0.3 mM reduced nicotinamide adenine dinucleotide (NADH), 0.5 mM phosphoenolpyruvate (PEP), 2 mM adenosine triphosphate (ATP), 15 mM creatine (CRTN), 0.3 mM methylene green (MG), 2000 U L^{-1} pyruvate kinase (PK, E.C. 2.7.1.40), 100 U L^{-1} ('**0**') / 710 U L^{-1} ('**1**') CK, and 150 U L^{-1} ('**0**') / 1000 U L^{-1} ('**1**') LDH in a 50 μL sample vol-

ume. All reagents were mixed in a tube and subjected to a 180 s incubation at 37° C in a heatblock. Following this incubation period, the solution was dispensed on the electrode surface and a chronoamperogram was subsequently initiated whereby a working electrode potential of 0.0 V *vs* Ag/AgCl was maintained for 60 s.

The ABT experiments were conducted by employing 10 mM nicotinamide adenine dinucleotide (NAD^+), 1 mM MG, 1.6 mM ('**0**') / 6.0 mM ('**1**') LAC, and 150 U L^{-1} ('**0**') / 1000 U L^{-1}L ('**1**') LDH in a 50 μL sample volume. All reagents were mixed in a tube and subjected to a 180-s incubation at 37° C in a heatblock. Following this incubation period, the solution was dispensed on the electrode surface and a chronoamperogram was subsequently initiated whereby a working electrode potential of 0.0 V *vs* Ag/AgCl was maintained for 60 s.

It should be noted that references to digital logic gates in bold typeface (i.e. **NAND**) represent enzyme-based manifestations of logic gates. On the other hand, references without a bold typeface (i.e. NAND) represent their CMOS counterparts.

The new electronic architecture has been designed to control biocomputing systems applied to diagnostic merits. To simplify analysis, a Randles-Ershler equivalent R-C circuit model [85, 240, 241] is employed to emulate the electrical behavior of the electrochemical system, as displayed in Fig. 8.1B. This model consists of a parallel capacitor (C_W, corresponding to the double layer capacitance arising from the accumulation of a net surface charge at the working electrode) and resistor (R_W, corresponding to the charge transfer / Faradaic resistance arbitrated by the electroactive species) in series with another resistor (R_C, the total solution resistance) [85, 242]. The potentials at the working, counter, and reference electrodes are denoted as V_{WE}, V_{CE}, and V_{RE}, respectively. The positive supply voltage is denoted as V^+.

As illustrated in Fig. 8.1B, the potentiostatic unit consists of two LMP2234 precision instrumentation operational amplifiers (OA) configured in the following arrangement: control amplifier OA1 amplifies the differential voltage seen between node V_X and ground (with gain A) and supplies current through the counter electrode. Upon sensing a voltage generated at the reference electrode, OA2, a voltage

follower/buffer, syncs sufficient current through R_2 in order to maintain its output voltage at the input (V_{RE}) value. In turn, V_X is adjusted and the output potential / current of OA1 is modified accordingly. The control amplifier thus functions as a voltage-controlled current source that delivers sufficient current to maintain the reference electrode at constant potential and arbitrate the electrochemical reaction. In implementing negative feedback, it is imperative that OA1 be able to swing to extreme potentials to allow the full voltage compliance required for chemical synthesis. Furthermore, it is crucial that OA2 possesses very high input impedance in order to draw negligible current; otherwise the reference electrode may deviate from its intended operating potential. In practice, the use of precision instrumentation amplifiers possessing 20 fA or less of input bias current enables unabated operation to the sub-picoampere level, which is suitable for nearly all electrochemical studies of practical interest.

Employing the equivalent circuit model of the electrochemical cell, the current through the cell may be expressed in the frequency domain (ω) as

$$i_{CELL}(\omega) = \frac{AV_X - V_{WE}}{R_C + (R_W / (1 + j\omega R_W C_W))}, \tag{8.1}$$

and the voltage established at the reference electrode is given by the relation

$$V_{RE}(\omega) = V_{WE} + i_{CELL}\left(\frac{R_W}{1 + j\omega R_W C_W}\right), \tag{8.2}$$

where i_{CELL} represents the current flowing from the counter electrode to the working electrode. The voltage at the counter electrode will follow the potential seen at node V_X,

$$V_{CE}(\omega) = AV_X = A\frac{(\zeta - 1)V_{WE} - (R_2/R_1)V^+}{\zeta A - 1 - (R_2/R_1)}, \tag{8.3}$$

and

$$\zeta = \frac{1}{1 + (R_C/R_W)(1 + j\omega R_W C_W)}. \tag{8.4}$$

The potential at the working electrode (with respect to the reference) must be specified as it is a crucial parameter in electrochemistry that dictates the excitation of the electroactive species. More specifically, the application of a suitable

potential at the working electrode will ensure that the electroactive substance within the medium is oxidized or reduced. Consequently, this will yield a Faradaic current proportional to the concentration of the analyte by the Cottrell equation [242]. Synthesizing the above expressions, network analysis may be performed, yielding the frequency-domain voltage at the working electrode,

$$V_{WE}(\omega) = \frac{-R_2 R_3}{R_1 \left(R_3 + \left(R_W / \left(1 + j\omega R_W C_W\right)\right)\right)} V^+ \tag{8.5}$$

and the DC response can be evaluated:

$$V_{WE}(DC) = \frac{-R_2 R_3}{R_1 \left(R_3 + R_W\right)} V^+. \tag{8.6}$$

The above relations indicate that, for a system with $R_W \gg \mathrm{R}_3$, the potential at the working electrode can be adjusted by modifying the ratio between R_2 and R_1. More crucially, Eqs. (8.5) and (8.6) elucidate that the working electrode voltage is inversely proportional to the Faradaic resistance and therefore directly proportional to the Faradaic current arising from the electrochemical reaction. Accordingly, by the Cottrell equation, the concentration of the analyte can be extrapolated and should be linearly related to the signal arising at the working electrode. It is imperative to note that R_3 is selected to enable best noise performance at the expense of response time. Increasing this value will enable lower noise readings, but longer response times. For quasi-real-time measurements where a reading is recorded on a non-continuous basis at some fixed interval, it is appropriate to employ a moderate R_3 resistance in order to enable the highly sensitive detection of the analyte.

OA3, an integrator (another LMP2234 precision instrumentation operational amplifier), implements a low-pass filtering operation and provides low-noise gain to the signal arising at V_{WE}. R_4 provides the necessary feedback at DC / low frequencies (where C_5 has large reactance) to maintain a stable output at the correct value. With suitable choice of R_4 and C_5, the integrator can mitigate the high-frequency oscillation / instability induced by the capacitive loading of the potentiostat. The output of the integrator is subsequently amplified by OA4 (LMP2234), a non-inverting voltage amplifier, in order to provide additional gain

to bring the signal to rail levels. The output voltage of the final amplifier stage is given by

$$V_0(\omega) = \frac{R_2\left(R_4/\left(1+j\omega R_4 C_5\right)\right)}{R_1\left(R_3+\left(R_W/\left(1+j\omega R_W C_W\right)\right)\right)}\left(1+\frac{R_6}{R_5}\right)V^+,\ \omega_c = \frac{1}{R_4 C_5} \tag{8.7}$$

and

$$V_0(DC) = \frac{R_2 R_4}{R_1\left(R_3+R_W\right)}\left(1+\frac{R_6}{R_5}\right)V^+. \tag{8.8}$$

As can be deduced from Eqs. (8.7) and (8.8), the output voltage of OA4 is inversely proportional to the Faradaic resistance and therefore directly proportional to the Faradaic current arising from the electrochemical reaction. The output voltage V_0 thus serves as an indicator of the amount of electroactive analyte present in the system.

Following the analog signal processing, V_0 is incident on a comparator, which compares this value with a pre-established voltage V_T that is implemented by adjusting the potentiometer R_7 in relation to a fixed resistor R_8. In the event that V_0 exceeds V_T, the comparator will output the full rail voltage (logical '1'); otherwise, the output of the comparator will be at ground potential (logical '0'). In this manner, the device operates as a 1-bit analog-to-digital converter with an adjustable switching threshold.

The output of the comparator is channeled to one of the inputs of a CMOS logic gate and the other input is tied to the supply voltage. The CMOS logic gate serves to source sufficient current to drive an LED. An AND logic gate is employed when the enzyme logic gate implements the **AND** operation. Accordingly, when the output of the potentiostat and supporting analog subsystem exceeds the pre-programmed threshold level, the comparator outputs a 'high' (logical '1') voltage, hence driving the output AND gate high and thereby illuminating the LED. Likewise, a NAND logic gate is utilized when the enzyme logic gate implements the **NAND** operation. In this case, the presence of a sufficient level of analyte would cause the output of the potentiostat and supporting analog subsystem to fall below the pre-programmed threshold level. As a consequence, the output of

(A)

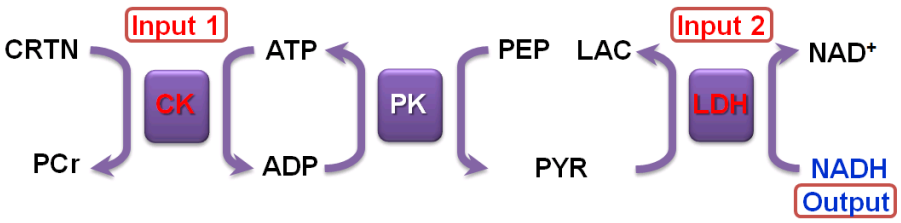

(B)

(C)

CK	LDH	Output	Biomedical Conclusions
0	0	1	Normal
0	1	1	Fitness / Cardiac
1	0	1	Cardiac
1	1	0	STI

Figure 8.4: *(A) Biocatalytic cascade instigated by creatine kinase (CK) and lactate dehydrogenase (LDH) emulating* ***NAND*** *operation, (B) the equivalent logic system, and (C) the corresponding truth table with biomedical conclusions drawn from the combinations of the input signals.*

the comparator would fall to the ground potential (logical '0'), hence driving the output of the NAND gate high and resulting in the illumination of the LED.

With the above implementation of the electronic hardware, the complete sensor system consumed 218 μA of current at 3.0 V, and thus the total power dissipation was 654 μW. Given a typical 30 mAh 3 V CR1025 coin cell battery, such a system could be sustained for over 45 h under continuous use. Applying a $\frac{1}{100}$ duty cycle, which may be sufficient for most remote sensing applications that do not mandate real-time readout, would result in the ability of the microsensor to sustain operation for over six months on a single battery charge, hence substantiating its integration into power- and space-constrained sensor implementations.

With a robust electronic backbone in place, the micro-/bioelectronic sensor system was applied towards diagnostic merits: the detection of STI with an enzyme-based **NAND** gate. Fig. 8.4A illustrates the biocatalytic cascade whereby

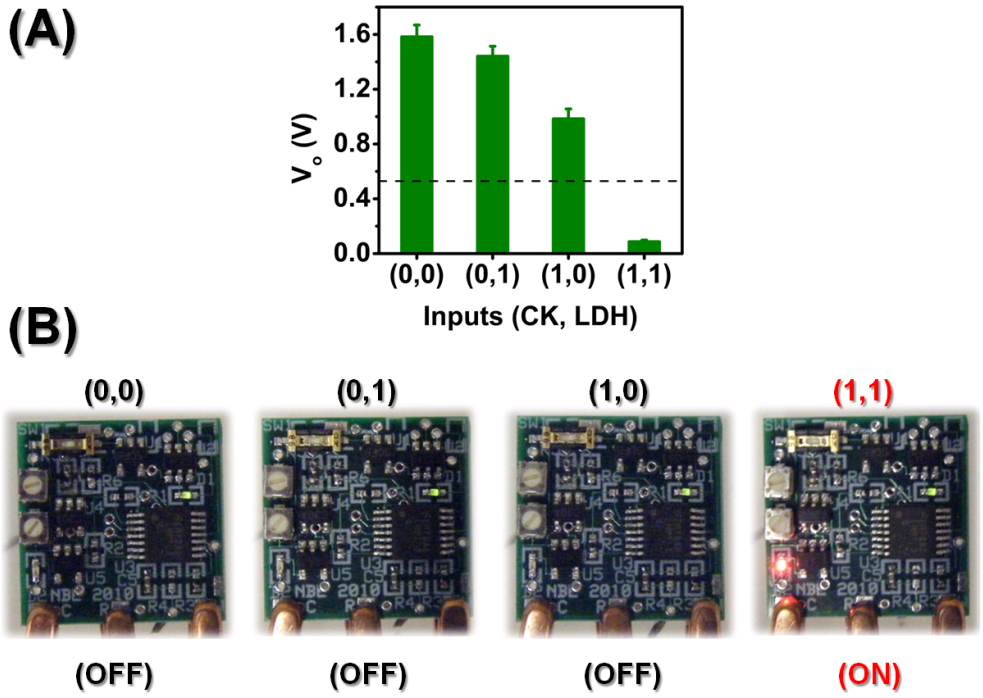

Figure 8.5: *(A) Bar chart featuring the* ***NAND*** *logic operation for the corresponding combinations of input signals. Electrochemical measurements were performed at E = 0.0 V* vs *Ag/AgCl. Dashed lines indicate the decision threshold for the realization of* ***NAND*** *gate operation. (B) Images of the microelectronic system under the application of various combinations of the input biomarkers CK and LDH. Only the pathological scenario involving high levels of both CK and LDH corresponding to the (**1**,**1**) logic level rendered an output logic **0**, resulting in the illumination of an LED.*

the enzyme inputs CK and LDH are processed to yield NADH as an output. The equivalent logic gate is shown in Fig. 8.4B. Upon the detection of abnormally high levels of both CK and LDH, the quantity of NADH present in the chemical system would decrease, as is evident from the truth table shown in Fig. 8.4C, thereby triggering the illumination of the LED.

In order to resolve the proper switching threshold that would indicate the occurrence of an STI event, the sensor was evaluated towards the operation of the **NAND** gate under four input logic combinations. Fig. 8.5A displays a bar chart obtained at the SPE by the **NAND** gate upon the application of all four of the input logic combinations for three independent trials. At 60 s sampling time,

the difference in mean voltage between the pathological logic level (**1**,**1**) and the physiological logic level in closest proximity (**1**,**0**) was 0.898 V. An exceptionally low standard deviation of less than 90 mV was maintained at every logic level.

Given the need to institute a threshold for the presentation of an affirmative diagnosis, the decision threshold was established as the midway point between the (**1**,**1**) and (**1**,**0**) logic levels, 0.535 V. As such, potentiometer R_7 was adjusted to 297 kΩ and accordingly a voltage divider (with respect to R_8) was implemented to realize a reference voltage (0.535 V) for the comparator. In pathophysiological circumstances that resulted in an output voltage V_0 below this threshold voltage V_T, light emission from the LED ensued. Fig. 8.5B displays photographs of the sensor under the application of the (**0**,**0**), (**0**,**1**), (**1**,**0**), and (**1**,**1**) logic levels once the programmable threshold was established. Clearly, only the pathological scenario (**1**,**1**) resulted in the illumination of the LED, thereby alerting the operator that an STI event has occurred and demonstrating the system's unambiguous assessment of the pathophysiological state.

Following the system-level validation of the micro-/bioelectronic sensor towards the evaluation of STI, the sensor was subsequently applied towards the detection of ABT with an enzyme-based **AND** gate. The biocatalytic cascade is displayed in Fig. 8.6A whereby the input biomarkers LAC and LDH are processed to yield NADH as an output. The equivalent logic gate is shown in Fig. 8.6B. In contrast to the STI system, upon the detection of abnormally high levels of both LAC and LDH, the quantity of NADH present in the chemical system would increase. This trend can be inferred from the truth table shown in Fig. Fig. 8.6C, and this process can be monitored by the operator via an LED display.

As in the STI system, in order to resolve the proper switching threshold that would indicate the occurrence of an ABT event, the sensor was evaluated towards the operation of the **AND** gate under four input logic combinations. Fig. 8.7A displays a bar chart obtained at the SPE by the **AND** gate upon the application of all four of the input logic combinations for three independent trials. At 60 s sampling time, the difference in mean voltage between the pathological logic level (**1**,**1**) and the physiological logic level in closest proximity (**0**,**1**) was 0.267 V. An

(A)

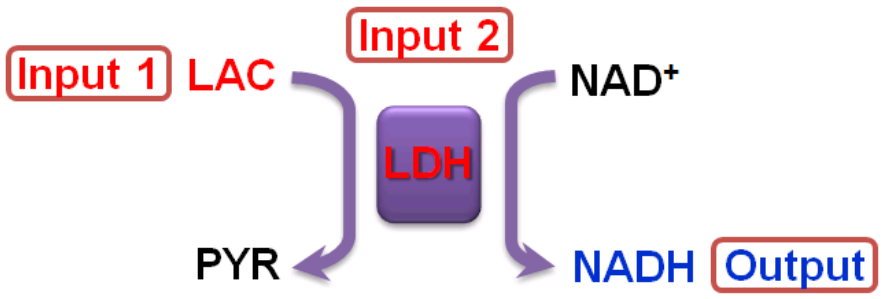

(B)

(C)

LAC	LDH	Output	Biomedical Conclusions
0	0	0	Normal
0	1	0	Fitness / Cardiac
1	0	0	Anomalous
1	1	1	ABT

Figure 8.6: *(A) Biocatalytic cascade instigated by lactate (LAC) and lactate dehydrogenase (LDH) emulating* ***AND*** *operation, (B) the equivalent logic system, and (C) the corresponding truth table with biomedical conclusions drawn from the combinations of the input signals.*

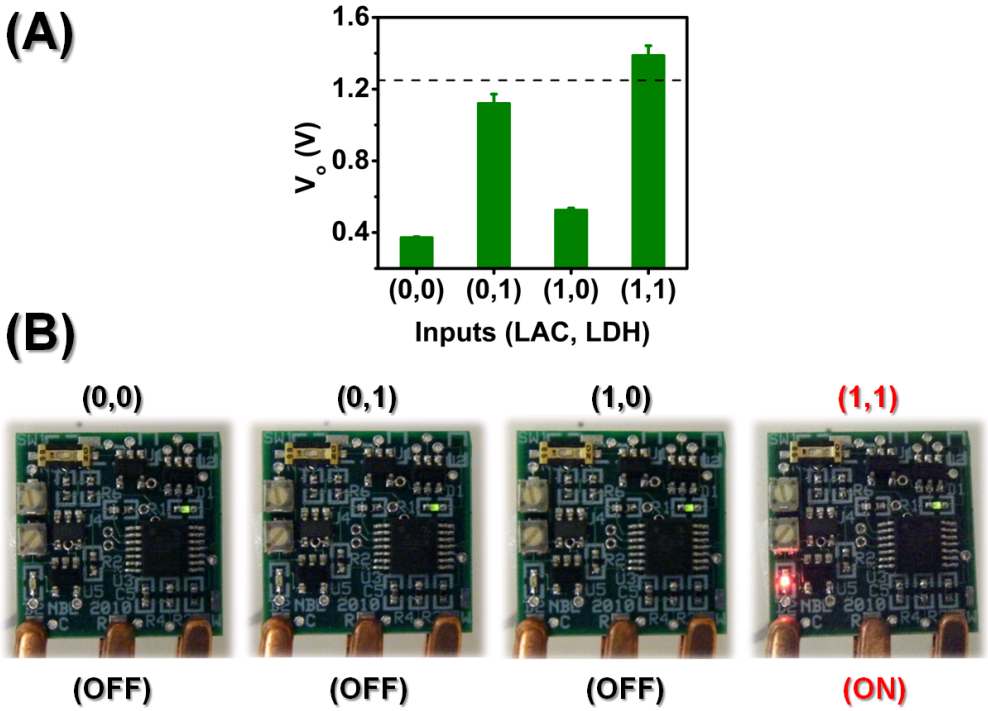

Figure 8.7: *(A) Bar chart featuring the* ***AND*** *logic operation for the corresponding combinations of input signals. Electrochemical measurements were performed at $E = 0.0$ V* vs *Ag/AgCl. Dashed lines indicate the decision threshold for the realization of* ***AND*** *gate operation. (B) Images of the microelectronic system under the application of various combinations of the input biomarkers LAC and LDH. Only the pathological scenario involving high levels of both LAC and LDH corresponding to the (**1**,**1**) logic level rendered an output logic **1**, resulting in the illumination of an LED.*

exceptionally low standard deviation of less than 60 mV was maintained at every logic level.

In order to achieve the highest-fidelity diagnosis possible, the decision threshold was established at the median between the (**1**,**1**) and (**0**,**1**) logic levels, 1.254 V. As such, potentiometer R_7 was adjusted to 697 kΩ and accordingly a voltage divider (with respect to R_8) was implemented to realize a reference voltage (1.254 V) for the comparator. In pathophysiological scenarios that resulted in an output voltage V_0 exceeding this threshold voltage V_T, light emission from the LED ensued. Fig. 8.7B displays photographs of the sensor under the application of the (**0**,**0**), (**0**,**1**), (**1**,**0**), and (**1**,**1**) logic levels once the programmable threshold was established. Clearly, only the pathological case (**1**,**1**) resulted in the illumination of the LED, thereby alerting the operator that an ABT event has occurred and again demonstrating the system's diagnostic integrity and utility as a versatile backbone for the readout of enzyme logic gates.

It is anticipated that the two systems presented here will function as intended for a majority of the population in circumstances where the biomarker levels fall within clinically established ranges. However, in both scenarios, owing to the variable extent of afflictions and the presence of a myriad of sources of potential interference, the execution of a large-scale clinical investigation that integrates various degrees of injury is imperative in order to select the most optimal decision threshold level for the population at large.

A microelectronic backbone has been designed towards the control and readout of digital biosensors with built-in enzyme logic and evaluated towards the diagnostic assessment of soft tissue injury and abdominal trauma. Upon sensing pathological levels of the biomarker pairs CK / LDH and LAC / LDH using **NAND** and **AND** enzyme logic gates, respectively, the sensor rendered an affirmative diagnosis via the illumination of an LED. Leveraging the intrinsic biochemical processing capabilities of enzyme logic gates, the sensor is designed to harness the quantized and binary nature of the chemical outputs generated by these gates, hence enabling decisive operational merits such as unambiguous 'YES'/'NO' readout, rapid measurement, small size, and extended battery lifetime. With a detailed understanding

of the analytical capabilities of enzyme logic gates and suitable methods of electronic transduction, high-fidelity biocomputing sensing systems can be constructed and implemented in a straightforward manner. In this vein, detailed multivariate chemical analysis can be tendered regardless of the nature or complexity of the enzyme logic gates utilized. The micro-/bioelectronic sensing concept represents the first instance of the development of an electronic system specifically tailored for the evaluation of biocomputing systems applied to diagnostic merits. The low-power, low-cost, and miniaturized embodiments of the sensor system make the design particularly attractive for diverse field operations and meets the requirements of field-deployable logic gate amperometric sensors. With further development of the supporting microelectronic systems, the sensor system would empower the non-technical end-user with the ability to assess the presence of chemical species in various clinical, security, and environmental scenarios in a straightforward and convenient manner. Such a reconfigurable micro-/bioelectronic logic-based multi-parameter sensing system shows considerable potential for the assessment of key analytes in a multitude of relevant applications where go/no-go readout, rapid measurement, device miniaturization, and extended longevity on battery power are core requirements.

Portions of Chapter 8 were taken from J.R. Windmiller, P. Santhosh, E. Katz, and J. Wang. Bioelectronic system for the control and readout of enzyme logic gates. *Sensors and Actuators B*, 155(1):206–213, 2011. The dissertation author was the primary investigator and author of this manuscript.

Chapter 9

Textile-based transducers

Any intelligent fool can make things bigger and more complex... It takes a touch of genius - and a lot of courage to move in the opposite direction.

—Albert Einstein

Wearable chemical sensors can provide pertinent information regarding the wearer's health or can be implemented for monitoring their surrounding environment [243, 244]. Accordingly, textiles represent an attractive class of substrates for the fabrication of such wearable chemical sensors [245, 246]. Advantageously, fabrics exhibit a plethora of unique chemical properties that can be exploited for various practical applications and are especially suited to handle the rigors of field-based use where durability and light-weight are core requirements [245, 246]. The integration of chemical sensing into textiles thus permits the wearer to receive extremely valuable and timely chemical information without compromising the functionality or comfort of the garment. To this end, reports have disclosed the fabrication of thick-film (screen-printed) amperometric sensors directly onto the elastic waistbands of undergarments [247]. Such studies have indicated that screen printing technology, which involves the selective patterning of conductors and insulators on planar substrates, is a viable option for the realization of wearable electrochemical sensors. However, little is known with regards to the compatibility of diverse varieties of fabrics with the thick-film sensor fabrication process. For example, textile-based sensing applications require a dense, hydrophobic outer

surface with desirable morphology, which can be realized by conventional screen-printing techniques provided that some relatively minor process modifications are made.

9.1 Electrochemical sensing on activewear

In addition to providing a means to monitor a wearers personal health, there are considerable demands for the development of wearable sensors that continuously assess the wearers local vicinity in order to identify potential hazards and threats, thereby providing a further layer of protection [248]. Monitoring the wearer's external environment is expected to increased survival rates in hazardous conditions. For example, growing concerns regarding terrorist activity have generated tremendous demands for innovative field-portable tools capable of detecting explosive compounds in a faster, simpler, and reliable manner [249].

Homemade explosives are, by far, the most common means to inflict death and destruction in terrorist attacks [250]. Common constituents of homemade explosives include urea nitrate [251, 252], ammonium nitrate [253], triacetone triperoxide (TATP) [254, 255], hexamethylene triperoxide diamine (HMTD) [255], 2,4-dinitrotoluene (DNT) [256], and 2,4,6-trinitrotoluene (TNT) [257, 258, 259, 260], among others. Due to the innate ability of DNT and TNT to withstand impact and friction, these compounds have proliferated in use in improvised explosive devices as a consequence of the reduced risk of accidental detonation during manufacture and handling [261]. Additional desirable properties of these nitroaromatic explosive materials are their stability, ease of mixture with other explosives, and water insolubility, making them especially useful for wet environments [262]. Electrochemical sensors offer unique opportunities for addressing the needs for field screening and identification of various nitroaromatic explosives [66]. In particular, the inherent redox activity of the widely used nitroaromatic explosives (e.g., TNT) makes them ideal candidates for electrochemical detection [66, 263].

The influence of various commercially-available textile materials upon the quality and performance of screen printed electrodes (SPE) has been examined in

an effort to identify an optimal fabric for the realization of high-fidelity electrochemical sensors for the detection of explosive agents of importance in security applications. In particular, differences in the hydrophobicity of the textile substrate are shown to have a profound effect upon the behavior of the corresponding SPE. Textiles are comprised of materials from numerous sources including animals (wool), plants (cotton), and synthetic formulations (nylon, polyester), all of which possess widely different morphologies and physical / chemical properties. The optimal textile candidate for supporting printable electrochemical sensors must possess inert properties and yield stable operation for extended periods of time under normal and heavy wear in circumstances where mechanical deformation can be extreme. Additionally, liquid-phase measurements require the utilization of water-proof fabrics, which would serve as excellent platforms for facilitating chemical reactions *in vitro*. The fabrics evaluated in the present study include cotton, polyester, and GORE-TEX®, a widely used constituent of outdoor garments. GORE-TEX fabric, a textile known for its exceptional gas-permeable and liquid exclusion properties, has been validated as a promising substrate for thick-film electrochemical sensors. The new GORE-TEX SPE offers high-fidelity detection of nitroaromatic explosives in the liquid- and gas-phases, and holds promise for monitoring hazardous scenarios.

Previous incarnations of printed textile electrodes exhibited favorable electrochemical behavior and mechanical / adhesion properties, although the textile detrimentally absorbed the sample solution due to its hydrophilic nature, hence leading to deteriorated sensing ability over time [247]. A fabric possessing water-repellant properties and a densely-woven structure would serve as an excellent candidate for use as the substrate to enable stable operation. It is thus a key consideration to examine different varieties of textiles as potential substrates for wearable screen-printed electrochemical sensors.

A few forms of widely-available fabric materials were evaluated in the study, 100% polyester and 100% cotton, as well as GORE-TEX, a completely waterproof and breathable fabric intended for outerwear. The wettability of a given substrate is often characterized by measuring the dynamic contact angle formed between a

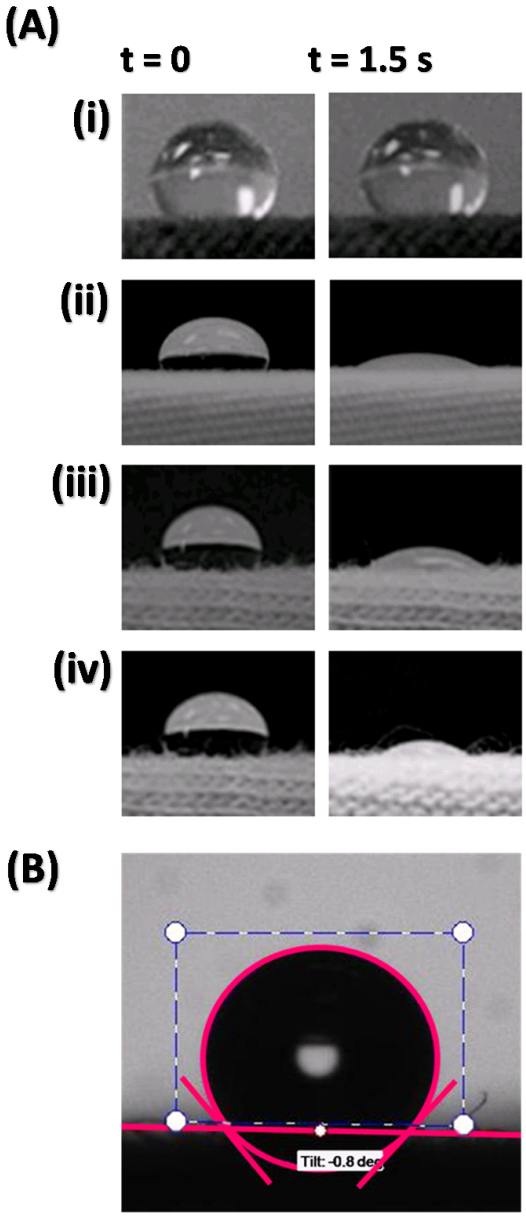

Figure 9.1: *(A) Dynamic optical contact angle measurements performed at* t = *0s (left) and* t = *1.5s (right) on (i) GORE-TEX, (ii) 100% polyester, (iii) 100 % cotton, and (iv) 35% cotton + 65% polyester fabrics. (B) Static contact angle measurement performed on GORE-TEX fabric.*

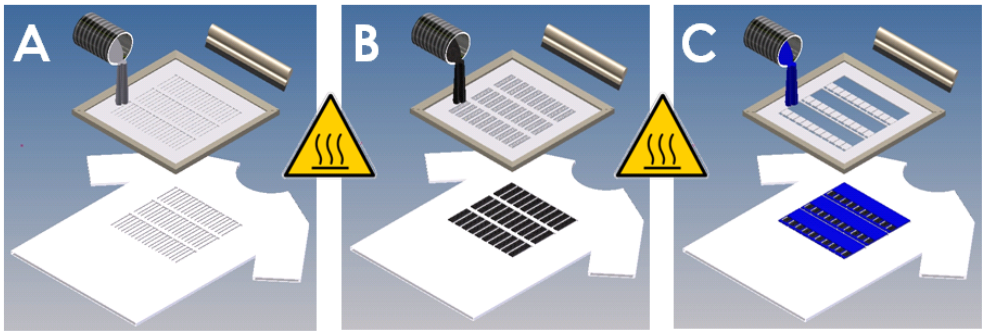

Figure 9.2: *Screen printing process flow diagram detailing the steps involved in the creation of complete electrochemical contingents on fabric substrates. (A) conductive underlayer (Ag/AgCl), (B) active layer (graphite), (C) insulative overlayer (polyvinyl chloride)*

liquid drop (typically water) and a solid surface. Wetting is favored by low interfacial, high solid surface- and low liquid surface-free energies. In greater abstraction, wettability is arbitrated by composition, pore size, surface structure and porosity of the fabric under investigation. Fig. 9.1A compares optical images captured in real-time contact angle measurements on (i) GORE-TEX, (ii) 100% polyester, (iii) 100% cotton, and (iv) 35% cotton + 65% polyester at 0 (left) and 1.5 s (right) following placement of a 10μL water droplet on the fabrics surface. These images indicate that, at an elapsed time of 1.5s, the GORE-TEX surface did not wet, whereas the droplets were almost entirely absorbed by the three other fabrics: 100% polyester, 100% cotton, and the 35% cotton + 65% polyester blend. As is apparent, the GORE-TEX fabric exhibited the greatest hydrophobicity among all the textiles examined.

Further, the apparent contact angle, θ_c, for each fabric was evaluated using a precision goniometer (CAM 100, KSV, Helsinki, Finland) and numerically fitted using the Young-Laplace equation:

$$\Delta P = -\gamma \nabla \cdot \vec{r} \tag{9.1}$$

where ΔP represents the pressure differential at the fluid-textile interface, γ is the surface tension, and $\vec{r}$ is the unit vector normal to the interface. Since

a polar liquid probe such as water penetrates rapidly through the hydrophilic matrices (i.e. (ii) 100% polyester, (iii) 100% cotton, and (iv) 35% cotton + 65% polyester), the measurement of contact angles between such probes is not feasible. The attractive hydrophobility / hydrophobicity of GORE-TEX is indicated from a casual inspection of the contact angle measurement shown in Fig. 9.1B. The contact angle was found to be 130° ± 5°. The distribution of fluorine atoms circumscribed around the carbon polymer backbone in GORE-TEX exhibits low surface energy, which yields non-polar characteristics. A strong surface tension is formed due to this difference in the surface energy between the water droplet and the GORE-TEX membrane. As a result, water beads form and the textile exhibits hydrophobic properties. It is important to note that the resistance to wetting observed on the GORE-TEX fabric corresponds to the waterproof property claimed by the manufacturer. The pores of GORE-TEX membranes are smaller (by several orders of magnitude) than the individual water droplets [264]. As the wetting rate exhibited by the other fabrics was quite rapid, the effect of wetting on the electrochemical behavior was evaluated further.

To further characterize the effect of wetting upon the electrochemical sensing performance, cyclic voltammetry was performed using various fabric-based electrodes, which were fabricated using a slight adaptation of the screen printing process described earlier (shown in Fig. 9.2). Fig. 9.3 displays hysteresis curves (repetitive cyclic voltammograms, CVs) recorded using the GORE-TEX (A), 100% polyester (B), and 100% cotton (C) fabric-based electrodes in both phosphate buffer (i) and 10mM potassium ferrocyanide solution (ii). To examine the dynamic transition of the wetting condition, repetitive CV experiments were conducted with a relatively high scan rate (300mV s^{-1}). With respect to the background measurements (in phosphate buffer), the GORE-TEX fabric-based electrode exhibited minimal changes in the current upon repetitive scans. As the number of scanning cycles is increased, a significant elevation in the recorded current is observed for both the 100% polyester and 100% cotton fabric-based electrodes (particularly at potentials greater than 0.4V *vs* Ag/AgCl). This can be ascribed to an increase in the active electrode area owing to the wetting effect. The wetting transition

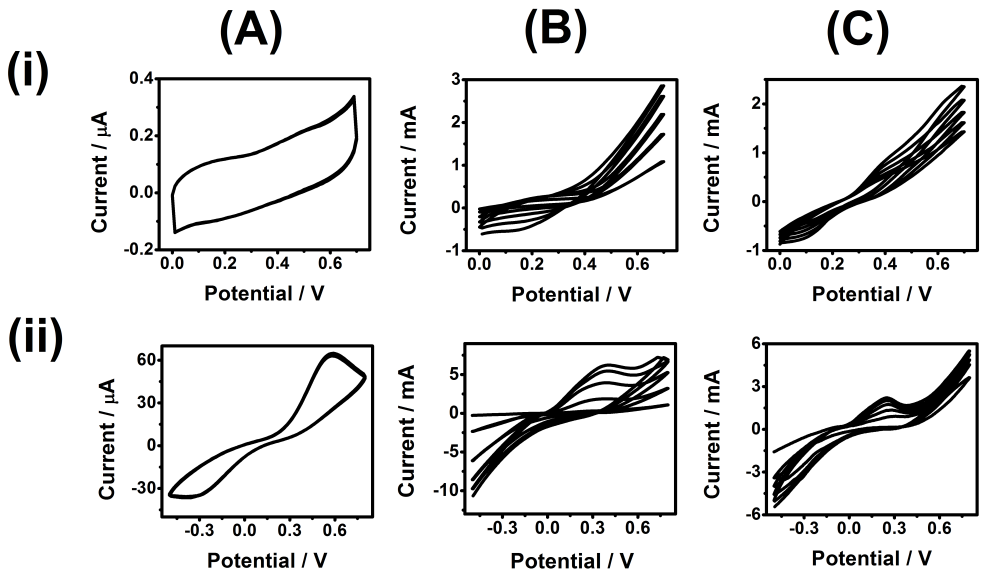

Figure 9.3: *Cyclic voltammograms of various fabric-based sensing devices in (i) 50mM phosphate buffer (pH7.4) and (ii) 10mM potassium ferrocyanide. First five initial scanning cycles are shown. Fabrics: (A) GORE-TEX, (B) 100% polyester, and (C) 100% cotton. Scan rate, 300mV* s^{-1}.

is also confirmed by observation whereby the entire fabric-based electrode strip was eventually wetted by the sample solution. A similar behavior also occurred in the ferrocyanide solution (ii), where the GORE-TEX fabric-based electrode possesses highly consistent CVs between subsequent cycles. On the other hand, a continually increasing current is observed in both 100% polyester and 100% cotton fabric-based electrodes. It is important to note that the GORE-TEX fabric-based electrode yields comparable redox properties as traditional carbon printed electrodes on inert solid substrates. However, only oxidation peaks at 0.4 V and 0.24V *vs* Ag/AgCl are recognizable in the polyester and cotton fabrics, respectively, whereas the reduction peaks are largely obscured. These results demonstrate the appealing electrochemical properties of the GORE-TEX fabric-based electrode. With a suitable substrate identified, all subsequent analytical investigations were thus executed with the GORE-TEX sensor.

Fig. 9.4A (left) exhibits an array of three eight-electrode electrochemical sensors on GORE-TEX fabric (each containing one counter (carbon) electrode

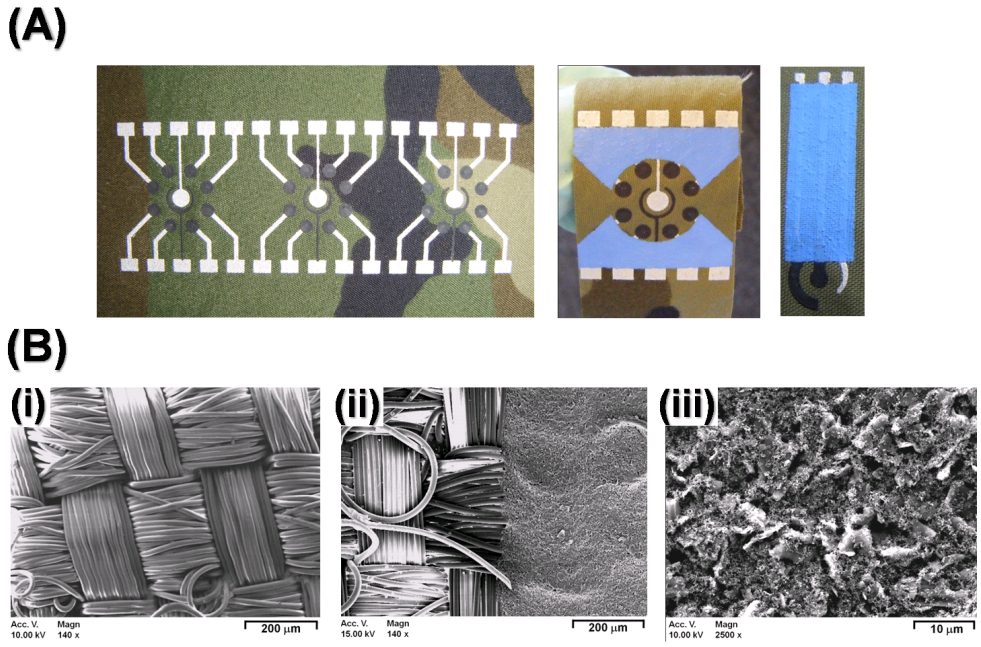

Figure 9.4: *(A) Photographic images of various sensor patterns printed on the GORE-TEX fabric. (Left) Integrated eight-electrode sensor array with silver conductive traces and carbon working electrodes; (Center) same array insulated by blue ink; (Right) single three-electrode electrochemical contingent. (B) Electron micrographs of (i) the GORE-TEX fabric, (ii) printed carbon electrode on the GORE-TEX surface and (iii) a magnified portion of the carbon electrode.*

and one reference (Ag/AgCl) electrode). Each sensor was insulated by printing an insulting ink around the active electrode area, thereby forming the complete GORE-TEX fabric-based electrode array (Fig. 9.4A, center). In addition, a typical three-electrode design is patterned on the GORE-TEX substrate (Fig. 9.4A, right), which is used in this study. The surface roughness and heterogeneous nature of the carbon layer is expected to affect the electrochemical behavior and hence it becomes essential to study the morphology of such surfaces. Micrographs of the surface morphology, the boundary of the printed carbon electrode, and a close-up of the printed carbon electrode surface on the GORE-TEX substrate are displayed in Fig. 9.4B (i), (ii), and (iii), respectively. Fig. 9.4B (i) depicts the typical morphology of a woven nylon protective layer that serves as the outermost layer of GORE-TEX-based fabrics. An electron micrograph presented in Fig. 9.4B (ii) illustrates the granular carbon layer, uniformly coated over the substrate. Note that the carbon electrode printed on the woven nylon fabric exhibits a well-defined appearance with relatively smooth conductor edges, as opposed to printed electrodes on polyester and cotton fabrics where the fiber structure is less organized, which serves to hamper the printing of high-quality carbon electrodes. No apparent defects or cracks are observed ((ii) and (iii)), which demonstrates the regularity of the printed electrodes on each fiber. A further magnified image of the carbon electrode is shown in Fig. 9.4B (iii) and illustrates the surface morphology in greater detail. The carbon layer possesses a non-porous surface and consists of two different sized carbon particles (3μm and $<1\mu$m diameters) embedded in the binder matrix.

Although GORE-TEX-based textiles are known to be less stretchable and more robust than other fabrics, normal wear and upkeep may affect the microstructure and morphology of the GORE-TEX fabric-based sensor and hence its performance. The influence of such mechanical deformation thus requires a detailed examination. The GORE-TEX fabric-based printed electrodes were hence subjected to successive bending operations and the influence of this mechanical stress upon the electrochemical performance was examined. Employing 10mM potassium ferrocyanide as a redox probe, CVs were obtained following repetitive bending of the fabric substrate (up to 60 bending iterations). A CV was recorded following

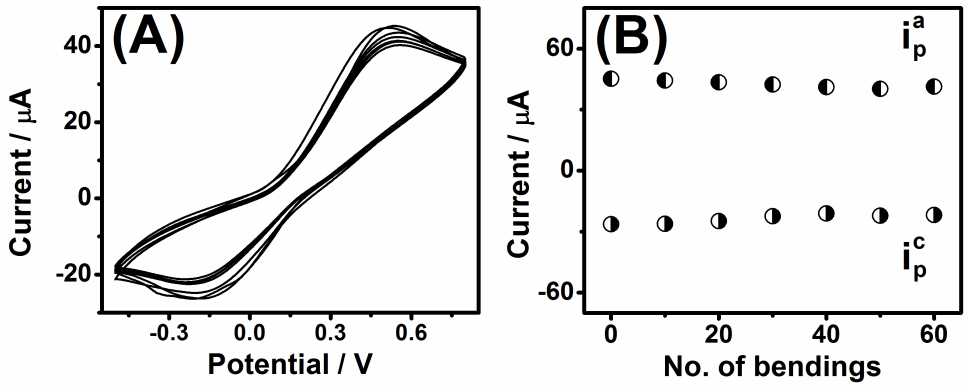

Figure 9.5: *(A) Effect of repetitive bending on the voltammetric waveform obtained at the GORE-TEX fabric-based sensor employing 10mM potassium ferrocyanide. Ten bending operations were conducted between consecutive cyclic voltammetric measurements. Bending time, 1s; release time, 1s. Bending was applied at an inward angle of 180° as the sensor was circumscribed around a mandrel with a 1mm radius. Scan rate: 100mV s^{-1}. (B) Characteristic current profiles recorded from the redox signal generated by ferrocyanide following ten such bending operations.*

10 bending operations. As illustrated in Fig. 9.5A, such repeated bending of the substrate does not appear to distort the voltammetric response in a noticeable manner. Fig. 9.5B reveals the current profiles recorded from the redox activity of ferrocyanide; the effect of this prolonged bending operation is minimal.

Although the rapid identification of deleterious healthcare conditions is of widespread concern [247], wearable textile sensors may also be extended to applications aimed at monitoring the wearer's surrounding environment. For example, textile-based printed electrodes may enable the sensitive detection of explosive compounds, hence providing an easily-deployable tool, particularly in field-based security and military applications. Inline with the goal of assessing the levels of DNT and TNT in the environment, the performance of the GORE-TEX fabric-based sensor was evaluated by employing a hypothetical analytical procedure that could be performed in the field (i.e. dispensing a drop of a liquid under test on a fabric-based sensor). Fig. 9.6 illustrates the square-wave voltammograms (SWVs) generated by increasing levels of DNT (A) and TNT (B) over the 0 to 50μg mL^{-1}

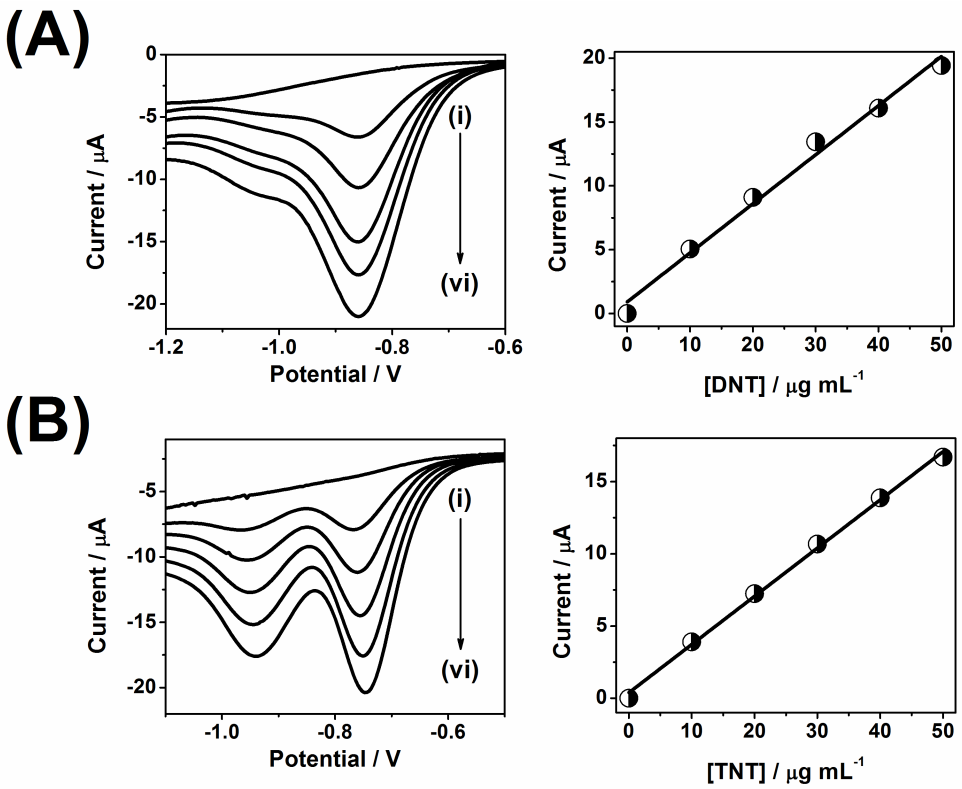

Figure 9.6: *Square wave voltammograms (SWV, left) recorded at the GORE-TEX fabric-based sensors towards the sensing of DNT (A) and TNT (B) in 0 - 50 $\mu g\ mL^{-1}$ (i → vi) and corresponding calibration plots (right). Potential step, 4mV; Amplitude, 25mV; Frequency, 20Hz. Current in calibration plots are sampled at -0.86V (A) and -0.75V (B)* vs *Ag/AgCl.*

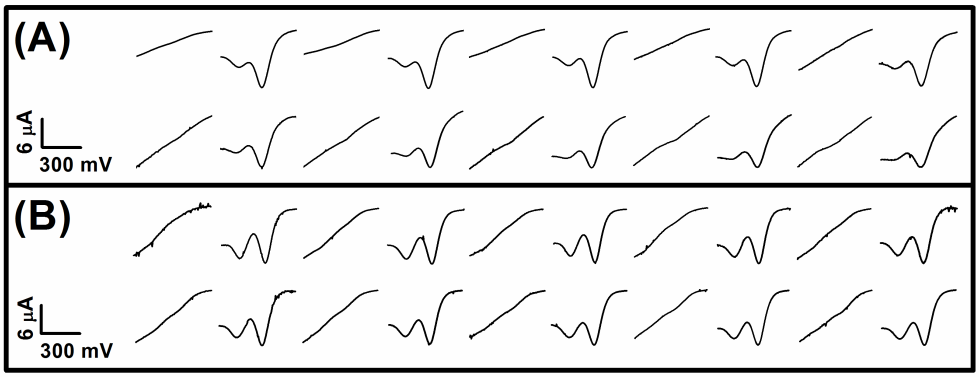

Figure 9.7: *Square wave voltammetric response of the GORE-TEX fabric-based sensor to alternating blank / DNT (A) and blank / TNT (B) samples with analyte levels at 20µg mL^{-1}. Scanned potential: -0.6 to -1.2V* vs *Ag/AgCl (A) and -0.5 to -1.1V* vs *Ag/AgCl (B); SWV parameters, as in Fig.9.6. The surface was rinsed with the blank buffer solution following each measurement.*

range at the GORE-TEX fabric-based sensor. In direct comparison with reported results in the literature [265, 266], the GORE-TEX fabric-based sensor exhibits a well-defined peak at -0.86V *vs* Ag/AgCl for DNT and two reduction peaks (at -0.75 and -0.95V *vs* Ag/AgCl) for TNT. Note also the appearance of a second reduction signal (around -1.02V *vs* Ag/AgCl) at higher DNT concentrations. For both nitroaromatic explosives, the first peak corresponds to the reduction of the nitro groups, whereas the second peak corresponds to the reduction of the hydroxylamine product to an amine-containg product. Owing to the relatively significant signal observed at the less negative potential, calibration curves are plotted correlating the current signals at -0.86V *vs* Ag/AgCl (Fig. 9.6A) and -0.75V *vs* Ag/AgCl (Fig. 9.6B) with the explosive concentration. These display high linearity ($R^2 >$ 0.99) along with the highly sensitive detection of DNT (0.38μA mL μg^{-1}) and TNT (0.33μA mL μg^{-1}). For both DNT and TNT, a low detection limit (LOD) of around 1μg mL^{-1} can be interpolated from the concentration given a signal equal to the blank level y_B (intercept) plus three standard deviations of y-residuals (s_y/x). These results indicate that the fabric-based electrodes possess appealing explosive sensing capabilities comparable to those of conventional screen-printed voltammetric electrodes.

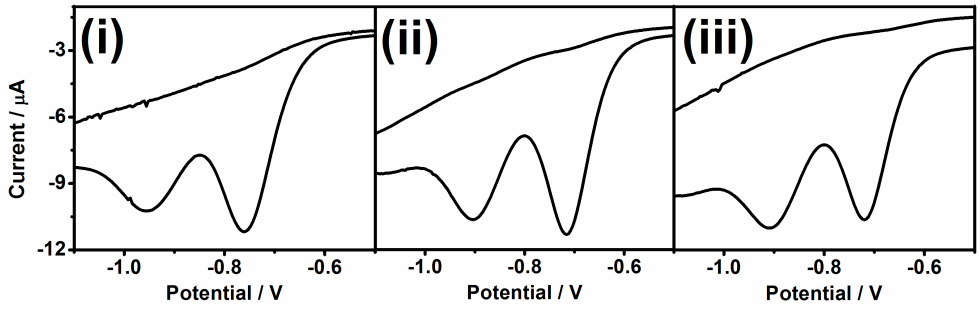

Figure 9.8: *Effect of laundry cycling on the square wave voltametrc response of GORE-TEX fabric-based sensors; 20 μg mL^{-1} of TNT is employed as the analyte. (i) SWVs recorded before (i) and following the 1st (ii) and 3rd (iii) laundry cycles; SWV parameters, as in Fig.9.6.*

The repeatability of the GORE-TEX fabric-based explosive sensor was subsequently examined. The investigation consisted of casting 60μL of 20μg mL^{-1} DNT or TNT solution onto the GORE-TEX fabric-based sensor, recording the sensor's response, and then replacing the test sample with phosphate buffer and measuring its response in the same manner. This 'live-blank' alternating cycle was then repeated for an additional nine iterations; the sensor response was recorded in each experiment over the potential window ranging from -0.6 to 1.2V *vs* Ag/AgCl (Fig. 9.7A) and -0.5 to 1.1V *vs* Ag/AgCl (Fig. 9.7B) for DNT and TNT, respectively. The fabric-based sensor demonstrates a well-defined response towards the detection of DNT and TNT and exhibits minimal waveform decay in the tenth evaluation of DNT (RSD = 8.5% for DNT and 2.6% for TNT). These results indicate the potential of the GORE-TEX fabric-based sensor to detect explosives in a repetitive fashion with minimal deterioration in the sensor response and underscore its utility as a reusable sensing modality rather than merely as a 'one-time-use' device.

Laundry washing represents another routine activity that may affect the performance of textile-based sensors. Here, chemical deterioration (originating from the detergent) in addition to mechanical deterioration may affect the sensor's electrochemical behavior. Fig. 9.8 illustrates the effect of laundry cycling the

GORE-TEX fabric-based electrodes upon their voltammetric response for 20μg mL^{-1} TNT. The GORE-TEX fabric-based sensors were subjected to a traditional laundry cycle in a typical household washing machine using commercially available liquid detergent along with additional 'filler' garments in the same load. As can be seen in Fig. 9.8 (ii and iii), the GORE-TEX fabric-based sensor exhibits similar voltammetric response following repeated washing. A slight shift in the reduction peak potential is observed subsequent to the first washing routing; however further washing iterations did not alter the peak potential. It should be noted that the majority of the GORE-TEX fabric-based sensors did not degrade to a significant extent following one laundry routine. However, upon submission to three laundry cycles, half of the original ten GORE-TEX fabric-based sensors remained functional and maintained their sensing properties. Common causes of laundry-induced degradation include splitting of the fabric, cracking / breaking of the carbon layer, and disconnection of the conductor traces.

Detection of explosive vapors is expected to meet the growing demands for remote security sensing. Vapor-phase electrochemical sensors are expected to address this challenge by enabling the detection of security hazards in a versatile, inexpensive, and miniaturized platform. In accordance with this overarching goal, the GORE-TEX fabric-based electrochemical sensor was adapted to meet the unique demands required for field-based analytical devices intended for security monitoring embodiments. In order to prepare the vapor-phase fabric-based sensor, a polyester film coated with a pressure-sensitive adhesive (ARcare 8259, Adhesives Research, Inc., Glen Rock, PA) that contained a 7mm diameter aperture was applied on the surface of the GORE-TEX fabric-based sensor to create a cavity for casting the solid electrolyte. A hydrogel electrolyte was prepared by dissolving 100mg of agarose into a 5mL potassium chloride solution (0.5M). The mixture was then brought to a boil (around 200° C) and remained at this temperature for 5 - 10min under continuous agitation until the agarose dissolved completely. Subsequently, the gel solution was cooled to 65° C and maintained at this temperature (with agitation applied) for further use. The solid electrolyte of the sensor was cast by dipping the fabric-based sensor into the agarose solution and promptly

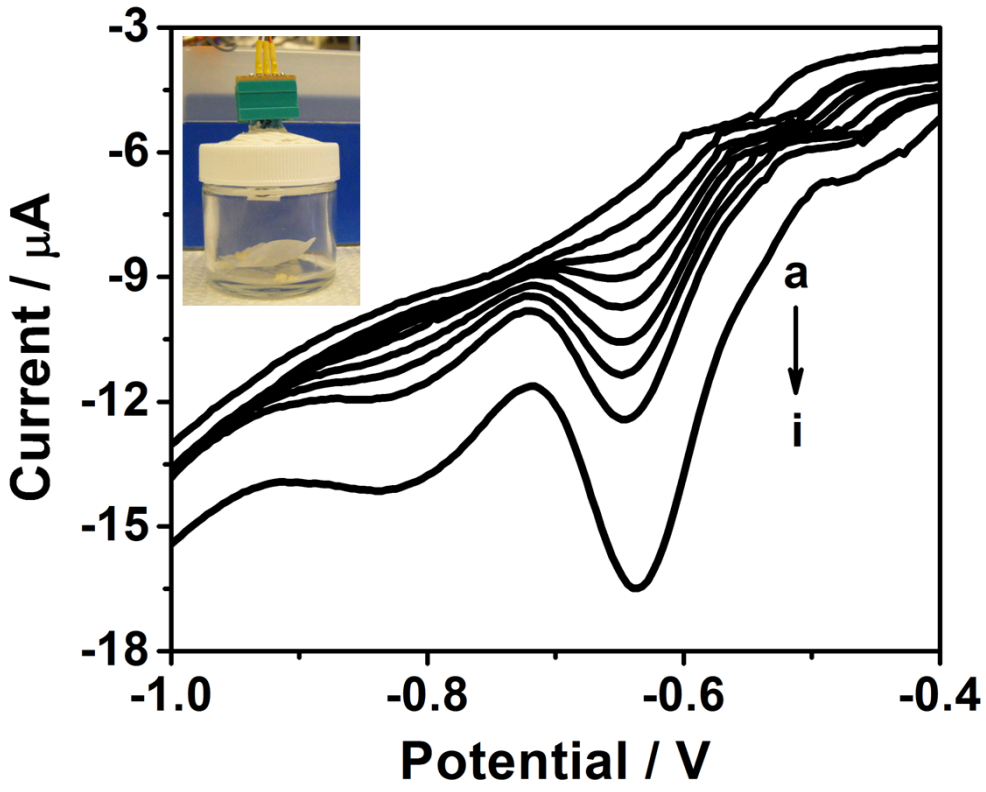

Figure 9.9: *Vapor-phase detection of DNT using the GORE-TEX fabric-based sensor at various exposure durations: a → i: 0, 4, 8, 12, 16, 20, 24, 28, and 60min; SWV parameters as in Fig.9.6. Inset: experimental setup.*

removing the sensor, allowing the agarose to solidify on the electrode surface at room temperature, thereby leading to the formation of a thick-film hydrogel layer on the exposed electrode contingent.

Preliminary experiments demonstrated the ability of the GORE-TEX fabric-based sensor, modified with a hydrogel electrolyte, to detect the presence of DNT in the vapor phase. 60 mg of DNT powder was placed in a 30 mL sealed glass vial to emulate a hypothetical situation whereby an explosive agent is concealed and transported within baggage. Fig. 9.9 illustrates the square wave voltammetric detection of DNT vapor at the GORE-TEX fabric-based sensor at increasing exposure durations. A characteristic reduction peak is observed (at -0.63V *vs* Ag/AgCl). As expected, the response to the DNT vapor becomes elevated upon increasing the exposure time from 0 to 60min.

The influence of various textile substrates upon the detection properties of thick-film electrochemical sensors has been examined in this study. Cotton, polyester, and GORE-TEX fabrics were compared in order to determine a suitable textile electrode substrate that would facilitate the direct patterning of an electrochemical sensor onto various fabrics using conventional screen printing methods. The superior water-proof properties of the GORE-TEX fabric were shown to be particularly attractive for fabricating and operating such printable textile-based sensors. Through rigorous physical and chemical characterization, the GORE-TEX fabric was determined to be an excellent substrate material for supporting screen printed electrodes owing to its inherently high degree of hydrophobicity, minimal sample absorption, and preservation of electrochemical activity against various forms of mechanical deterioration and chemical attack. The electrochemical sensing properties of such GORE-TEX based printed electrodes were examined and their ability to detect nitroaromatic explosives was demonstrated. Further assessment of the durability and reliability of the GORE-TEX substrate for extended periods of use will lead to the development of field-deployable security monitoring systems integrated onto conventional garments. The results indicate the potential of textile-based screen-printed sensors for future security and military applications. With further development, the same sensing paradigm can be applied towards the

detection of other classes of explosives, particularly widely-used homemade explosives. Current efforts are aimed at expanding the textile-based detection towards additional chemical agents of security relevance. This activity is expected to enhance survival rates among soldiers and first responders in hazardous situations. These future applications would benefit from the integration of the supporting electronic control, real-time information display, and alert functionality to enable field-based utility and to realize true 'lab-on-a-textile' functionality.

9.2 Electrochemical sensing on marine garments

The ability to continuously detect the presence of environmental contaminants and security threats within marine environments represents a major challenge to oceanographers, navies, local water-quality agencies and recreational surfers / divers throughout the globe [267, 268]. Conventional water quality analytical techniques mandate that the water sample be isolated and transported to the laboratory to undergo analysis, which is a costly, labor-intensive, and time-consuming proposition [269, 270]. To this end, electrochemical devices have been developed that enable real-time monitoring of seawater towards potential hazards such as explosive residues or toxic metals [66, 258, 271, 272, 273, 274, 275]. These devices include flow detectors for online shipboard monitoring [274, 275] and submersible sensors for remote detection [258, 271]. New hand-held analyzers have also been developed for underwater surveillance by divers [66]. The latter, however, is not compatible with military or recreational activities (e.g., surfing, diving) that commonly require 'hands-free' operation. A fully-integrated wearable sensor system that facilitates such marine operations while providing the user with a real-time assessment of their surroundings would thus be preferred.

In this investigation, wearable electrochemical sensors on underwater garments comprised of the synthetic rubber Neoprene® are described. Neoprene, which is synthesized from chloroprene [276], is a widely-employed synthetic rubber for dry- and wetsuits. While dense neoprene seals the openings of diving suits, foamed neoprene serves as an exceptional thermal insulator that encapsulates most

of the wearer's body. Its basic polymer, polychloroprene, is produced via emulsion polymerization before it is transferred into a foam-like material that consists of air bubbles and polymer arranged in a comb-like network [277]. Neoprene can be tailored to the desired application, ranging from nylon overlays intended to increase wearer comfort, to varying degrees of thickness to compensate for pressure and temperature variance at greater diving depths and / or cooler waters [278]. This, along with the elastic and superhydrophobic morphology of neoprene, makes underwater garments highly compatible with the thick-film (screen printing) fabrication process and for sensing operation in marine environments. Thick-film microfabrication has enjoyed widespread use for the mass production of highly reproducible electrochemical sensors (e.g., glucose strips for diabetics) [68, 10]. This process has recently been applied for printing electrochemical sensors on common textiles [247, 279], but not in connection to underwater garments. The integration of sensors directly onto underwater garments, such as those described in this study, would provide the wearer with the ability to continuously assess their surroundings.

The potential of neoprene-based printed electrochemical electrodes as wearable sensors has been demonstrated in this study for a wide range of marine monitoring scenarios. These results substantiate the potential of such devices to enable the wearer (surfer / diver) to continuously assess their surroundings for potential contaminants or hazards without being preoccupied with the transport and operation of cumbersome analytical equipment. Following characterization of noeprene's surface morphology, the role of mechanical stress on the redox activity towards ferricyanide at printed electrodes on the neoprene substrate is examined. Furthermore, the analytical performance of the new neoprene-based electrochemical sensor is evaluated for trace voltammetric measurements of heavy metals such as copper and nitroaromatic explosives such as TNT in untreated seawater. In addition, the enzyme tyrosinase (Tyr, E.C. 1.14.18.1) is incorporated within the sensor ink in order to facilitate the detection of phenolic pollutants in seawater. This represents the first example of electrochemical biosensing on textiles with printable enzyme-containing inks. Subsequently, the new wearable biosensor is integrated with an encapsulated potentiostat capable of providing the wearer with a visual

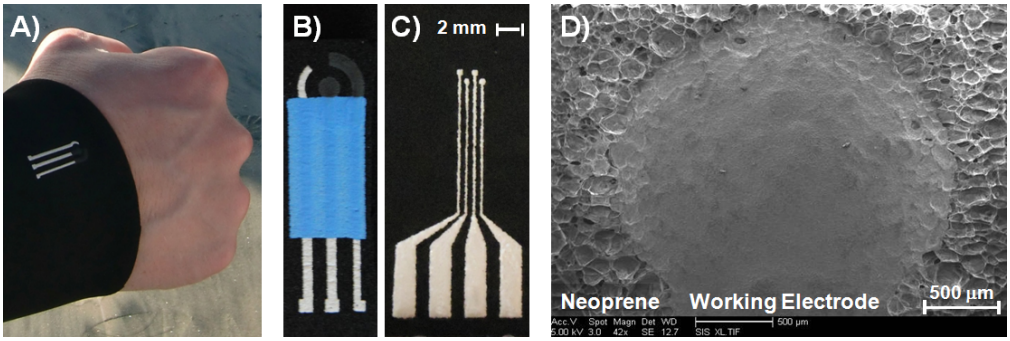

Figure 9.10: *(A) Screen printed electrode (SPE) on an underwater garment. The three-electrode configuration comprises an Ag/AgCl reference electrode as well as carbon working and counter electrodes printed directly onto neoprene. Center: Two SPE design varieties on neoprene - (B) three-electrode configuration equivalent to (A) comprising an additional insulator layer (blue); (C) an array of four silver electrodes (the feature width of each contact line is ∼195 µm, the pitch between adjacent electrodes is ∼280 µm, and the diameter of the active area of each electrode is ∼440 µm). (D) Scanning electrode micrograph illustrating the working electrode area on the neoprene substrate (42×, 5 kV).*

indication when the level of a target hazard or contaminant (e.g., phenols) has exceeded a pre-defined threshold. Under such operation, the wearer would be alerted to relocate to cleaner environments, inline with water quality and related health standards for recreational divers and surfers. The concept can be extended to other threat-assessment and environmental-monitoring applications of importance in marine environments.

The fabrication protocol required to produce thick-film electrochemical sensors has been described in previous studies. This procedure was adapted to the patterning of 4 mm-thick neoprene sheets. The design and fabrication of the microelectronic sensor has been described in the previous chapter, and the device was encapsulated in a watertight compartment and integrated into a wetsuit for water quality evaluation. The output potential of the potentiostat was established at -0.30 V (*vs* REF) and the device was operated in free-running chronoamperometric mode.

The utilization of a neoprene substrate enables the high-resolution printing of electrochemical sensors, characterized by well-defined borders, uniform ink

distribution, and no apparent defects. Diverse electrode configurations have been examined on various segments of commercially available wetsuits. For example, Fig. 9.10A displays a common three-electrode setup that was printed on the sleeve of such a wetsuit. This configuration, which compromises carbon working and counter electrodes, along with an Ag/AgCl reference, is used throughout most of this study. A more detailed optical image of this printed electrode assembly, along with an insulating layer, is depicted in Fig. 9.10B.

As a detailed understanding of the physical properties of the substrate material is crucial for the construction of high-fidelity wearable sensors, initial investigations were concerned with the characterization of the surface morphology, patterning resolution, and quality of the printed electrodes. To this end, Fig. 9.10C is representative of a well-defined array of four electrodes printed with Ag/AgCl ink; the feature width of each contact line is $\sim$195 μm, the pitch between adjacent electrodes is $\sim$280 μm, and the diameter of the active area of each electrode is $\sim$440 μm. Further insights into the surface morphology of the working electrode of the SPE contingent on neoprene are obtained from the scanning electron micrograph (42$\times$, 5 kV) shown in Fig. 9.10D. The rubber area surrounding the working electrode consists of comb-like polymeric subunits, which are characteristic of the neoprene substrate. The bare working electrode on neoprene exhibits an amorphous surface structure, defined by the micrometer-sized carbon flakes comprising the printed ink, along with defined boundaries. A similar morphology was observed for the carbon electrode printed on a rigid alumina-based SPE.

In order to confirm that the hydrophobic nature of the neoprene substrate was unaltered as a result of the screen printing process, contact angle measurements were performed (using seawater) on the bare neoprene substrate as well as on the printed carbon working electrode. The contact angles for the bare neoprene and for the carbon on neoprene were 138 $\pm$ 5° and 120 $\pm$ 5°, respectively, indicating that the carbon coating exhibits slightly better wettability when compared with the bare neoprene substrate. Moreover, the hydrophobic characteristic of the neoprene is maintained such that the electrode area can be maintained at a constant value.

Following the morphology investigation, the electrochemical behavior of the

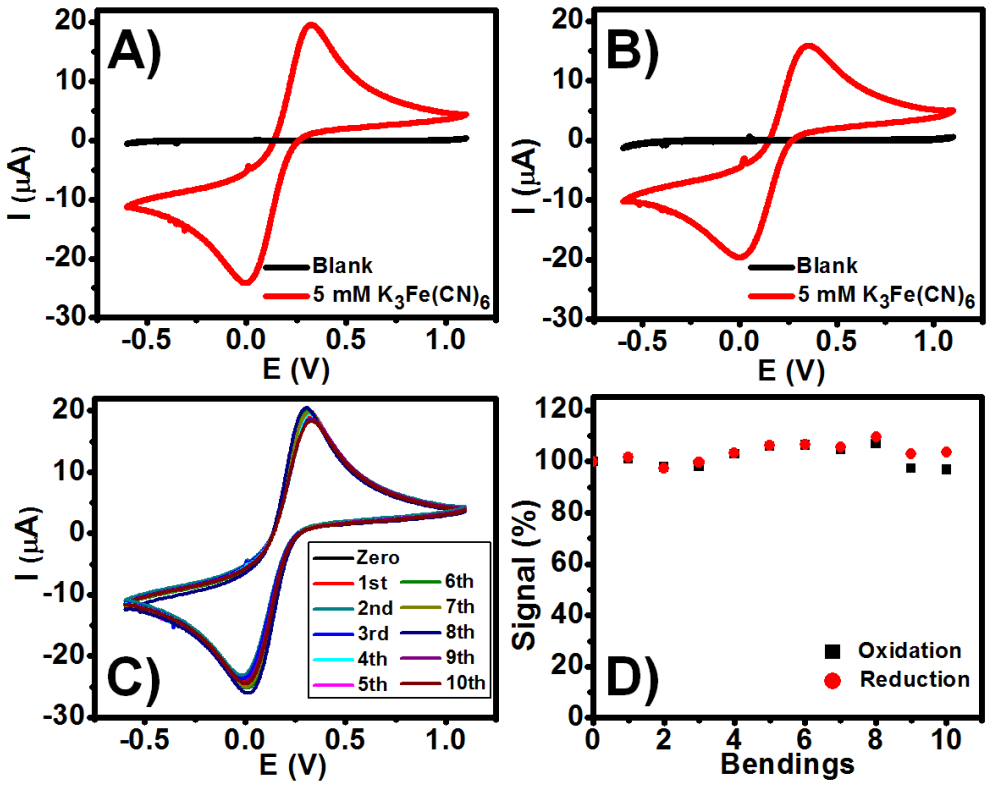

Figure 9.11: *Cyclic voltammograms for 5 mM ferricyanide at SPEs on flexible neoprene (A) and rigid alumina (B) substrates. (C) Voltammograms illustrating the effect of ten bending iterations. (D) Relative currents obtained for the redox peaks of 5 mM ferricyanide extracted from the repetitive bending data presented in (C). Scan rate: 50 mV s^{-1}.*

neoprene SPE was investigated employing a potassium ferricyanide redox probe. Fig. 9.11 displays representative cyclic voltammograms (CVs, 50 mV s^{-1} scan rate) for 5 mM ferricyanide as well as the blank solution (seawater) at the flexible neoprene SPE (A) and at a common rigid alumina-based SPE (B). These voltammograms indicate that the redox activity and the background response are not compromised by the neoprene substrate. The low background response indicates that the neoprene constituents do not contribute to the baseline. Both substrates yield two characteristic ferricyanide redox peaks, with similar peak potentials and separation. The oxidation peaks are located at 0.32 V and 0.35 V *vs* Ag/AgCl while the reduction peaks appear at 0.00 V and -0.02 V *vs* Ag/AgCl for the neoprene and alumina SPEs, respectively. As can be seen, the reversibility of the redox process is not affected by the neoprene substrate. Even though the geometric areas were identical for both SPE variants, the neoprene SPE displays higher anodic and cathodic peak currents, which can be attributed to a slightly larger active area on the neoprene substrate.

Wearable underwater sensors are expected to be deformed during routine use. Accordingly, the influence of mechanical deformation upon the voltammetric response was investigated in further detail. Figs. 9.11C and D illustrate the effect of repetitive 90° bending operations upon the CV response. Minimal changes in the peak potentials and currents are observed as a result of the mechanical deformation. The relative standard deviation (RSD) values were found to be less than 4 %, thus it can be concluded that the neoprene SPE is capable of withstanding repeated deformation without significant alteration of the electrochemical output signal. This is supported by consecutive resistance measurements that indicate that the conductivity of the trace did not deteriorate, although micro-fracturing is observed at the electrodes during prolonged bending. More specifically, while the resistance at the reference electrode increased by as much as 10 % following repeated mechanical deformation, the resistance of the counter and working electrode traces did not deviate by a quantity greater than the measurement error. As a matter of fact, even following multiple bending operations, the trace resistance measured at the neoprene SPE did not exceed the characteristic resistance of the

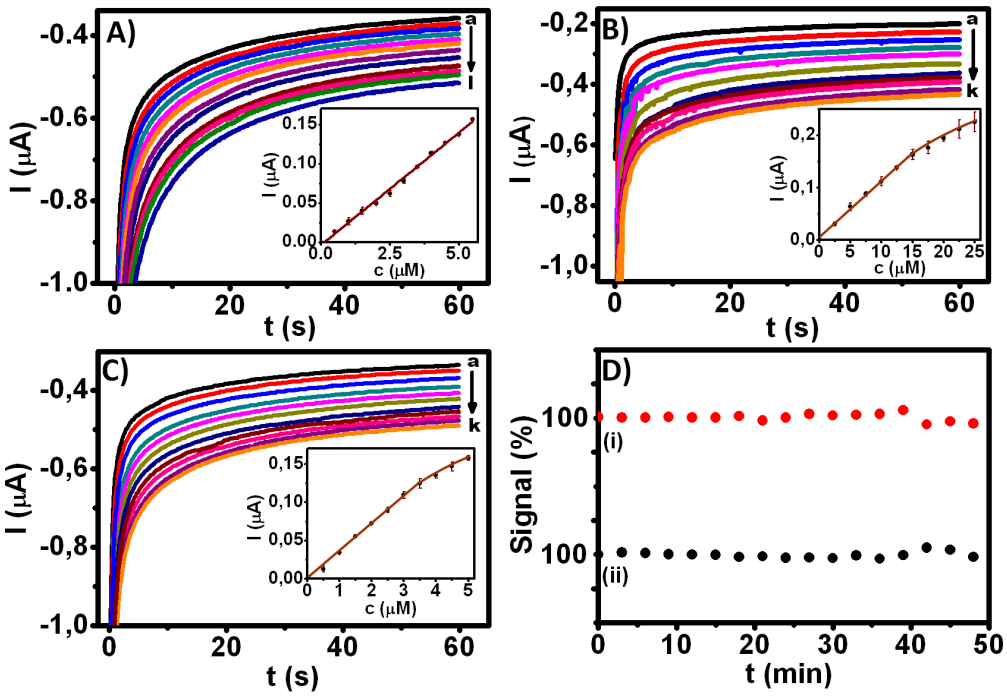

Figure 9.12: *Chronoamperograms of the tyrosinase-modified neoprene SPE in the presence of various phenolic compounds (step potential: -0.3 V* vs *Ag/AgCl). Samples were incubated on the electrode surface for 2 min prior to measurement: (A) phenol, (B) 4-chlorophenol, and (C) catechol. The insets show the corresponding calibration curves. (D) Stability of the signal over time with respect to the initial measurement at* t *= 0 min (100 %) for (i) 10 μM 4-chlorophenol and (ii) 2 μM phenol.*

traces at the common alumina-based SPE. It can hence be concluded that the conductivity of the traces was maintained through repeated deformation.

Following the initial electrochemical characterization, the study focused on the demonstration of the potential of the wearable sensing contingent for relevant water-quality applications using different model pollutants along with untreated seawater samples.

Phenols represent a pervasive class of organic compounds that are produced on an industrial scale and typically enter aquatic environments from the run-off generated by industrial and agricultural processing [280, 281]. The inherent toxicity of phenolic compounds creates urgent needs for their *in situ* monitoring in marine environments. The ability to continuously monitor the levels of such com-

pounds would thus prove extremely valuable as an alert for recreational divers and surfers.

In order to facilitate the trace detection of phenolic and catecholic contaminants, a tyrosinase-containing carbon ink was employed in the screen printing fabrication process and patterned directly on the wearable neoprene substrate. In order to quantify phenols and catechols, tyrosinase (Tyr) was mixed into the carbon ink (5 % w/w) and the enzyme-containing ink was printed onto the surface of the working electrodes of cured SPEs. The amount of enzyme in the bioactive layer was approximately 200 U per electrode. After the printing process, the Tyr-ink layers were dried at room temperature for one hour. The electrodes were subsequently stored at 4° C overnight. Following this procedure, 1 μL of aqueous Nafion solution (0.25 % v/v) was dispensed on the working enzyme electrode. Finally, the electrodes were kept overnight at 4° C prior to use.

The electrochemical response to micromolar changes of phenols (phenol, 4-chlorophenol, and catechol) was investigated using the neoprene-Tyr SPE biosensor. The biosensing route relies on the specificity of the enzyme that catalyzes the hydroxylation of phenols to enable the low-potential selective detection of the quinone products. In contrast, direct anodic measurements of phenols require high potentials and are vulnerable to interference caused by co-existing oxidizable species. Chronoamperometric measurements of the quinone product were executed by applying a reduction potential of -0.30 V *vs* Ag/AgCl. The corresponding chronoamperograms for increasing levels of phenol (0 to 5.5 μM in 0.5 μM increments), 4-chlorophenol (0 to 25 μM in 2.5 μM increments), and catechol (0 to 5 μM in 0.5 μM increments) are shown in Figs. 9.12A - C, respectively. Well-defined current signals are observed for these low micromolar concentrations; the limit of detection (LOD, using the $\mu + 3\sigma$ methodology) for phenol, 4-chlorophenol, and catechol are 0.25 μM, 0.43 μM, and 0.13 μM, respectively. The corresponding calibration plots are provided in the insets. As expected for biocatalytic reactions, the response for 4-chlorophenol and catechol increases linearly with concentration at first and then exhibits some curvature at elevated levels. A highly linear response is observed for phenol (A). The sensitivities are 28 nA μM^{-1}, 10 nA μM^{-1}, and 35

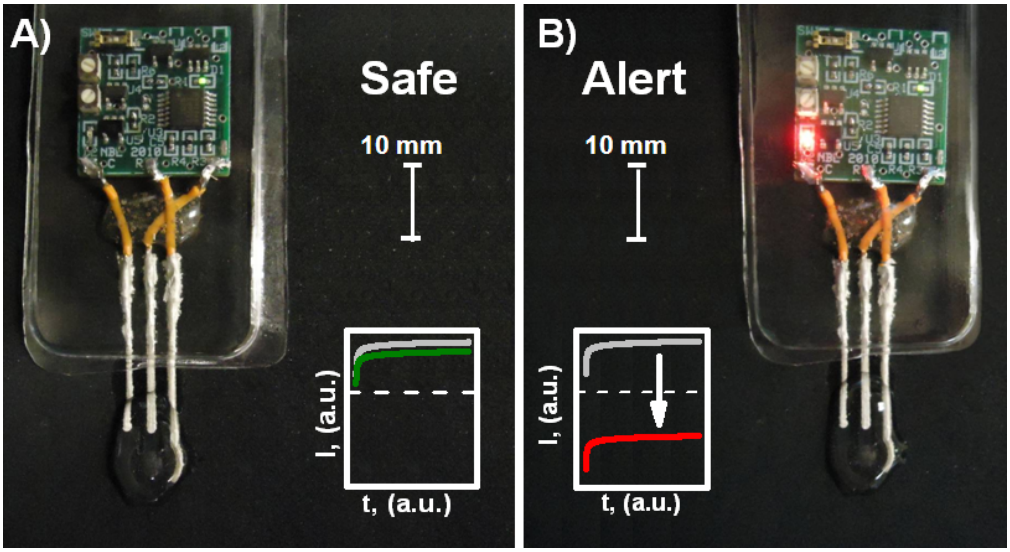

Figure 9.13: *Sealed, battery-operated electrochemical microsensor with an integrated potentiostat interfaced with a screen-printed three-electrode setup on a neoprene substrate. Safe environmental conditions are indicated in (A), whereas the additional illumination of a red LED (B) is indicative of a phenol content in seawater that exceeds a certain level (5.5 μM). E_{APP} = -0.3 V vs Ag/AgCl, $E_{Threshold}$ = 0.566 V. Insets show the outputs of the micropotentiostat block, illustrating the increased current magnitude caused by elevated phenol concentrations; a dashed line represents the threshold.*

nA μM^{-1} for phenol, 4-chlorophenol and catechol, respectively (R^2-values of 0.996, 0.996, and 0.997). The higher sensitivity towards catechol can be attributed to the single reaction step required for the enzymatic catalysis of catechol compared to the two-step reaction required for phenol and 4-chlorophenol. High stability is another important requirement for underwater marine monitoring. The response of the sensor was examined over a period of 50 minutes by performing 17 repetitive chronoamperograms (at three minute intervals). Fig. 9.12D examines the stability of the Tyr-SPE signal, relative to the first measurement (t = 0 min), for 10 mM 4-chlorophenol (i) and 2 mM phenol (ii). These experiments yielded a low RSD for each compound, ranging from 2.07 % to 1.73 %, respectively. Minor batch-to-batch variations (5 - 10 %) could be readily mitigated via initial calibration in the seawater matrix.

In order to provide a viable alternative to current sensing systems, an SPE

sensor was printed on the sleeve of a neoprene wetsuit. The working electrode was modified with Tyr and the entire printed contingent was mated with an encapsulated (watertight) miniaturized potentiostat (described in the preceding chapter) that is able to provide the wearer with a visual cue whether the level of phenolic compounds has exceeded a pre-defined threshold value. An image of the entire sensing system is shown in Fig. 9.13. In response to elevated levels of phenol (5.5 μM), the potentiostat-integrator-voltage amplifier analog system yielded an output potential of 0.797 $\pm$ 0.012 V, while the absence of phenols (0 μM) yielded a potential of 0.335 $\pm$ 0.008 V. Accordingly, by means of an adjustable voltage divider, the switching threshold for the comparator was established at 0.566 V, the arithmetic mean of the two extremes, and purely digital 'Safe'/'Hazard' analysis could be obtained. A 'Safe' (unpolluted) seawater environment is indicated by a green light, while in the case of hazardous levels of phenols, a red LED is illuminated (Fig. 9.13B). The output of the potentiostat block of the sensor (Fig. 9.13B inset) illustrates the increase in the current magnitude caused by elevated phenol concentrations; a dashed line represents the threshold.

As a consequence of war, military training, and the dumping of munitions, dangerous remains of undetonated ordnance still linger in numerous marine locales [258, 66]. In minesweeping missions, the detection of these explosive compounds could indicate the presence of naval mines or depth charges. Bearing in mind the abundance of dumped munitions and ordnance in the world's bodies of water, there is a pressing need to ascertain the presence of these hazards in aquatic environments. Underwater wearable sensors could monitor the electrochemical response of explosive agents in a continuous fashion and could alert the wearer to a potential threat. Accordingly, the neoprene-based electrochemical sensor was examined for voltammetric detection of the common model nitroaromatic explosive TNT.

Explosive detection experiments were performed by applying rapid square wave voltammetry (SWV). Fig. 9.14A displays representative voltammograms for an untreated seawater sample containing increasing levels of TNT in 100 ppb increments. The well-defined voltammograms illustrate a reduction peak at -0.54 V *vs* Ag/AgCl and a smaller shoulder at -0.74 V *vs* Ag/AgCl. The peak at -0.54

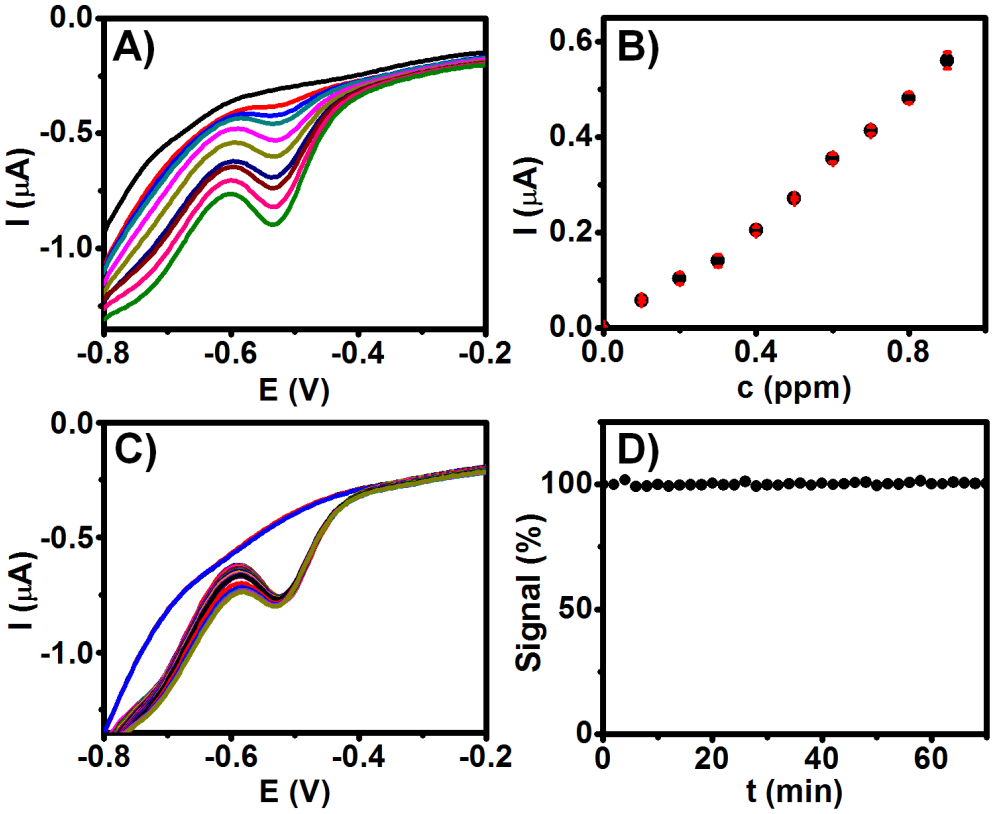

Figure 9.14: *Square wave voltammograms for TNT in seawater recorded at the neoprene SPE. (A) Response for increasing levels of TNT from 100 to 900 ppb. Potential step, 4mV; Amplitude, 25mV; Frequency, 20Hz. (B) Calibration curve corresponding to A. (C) Stability of the sensor with 500 ppb TNT over a period of one hour (*n *= 30). (D) Stability of the signal over time with respect to the initial measurement at* t *= 0 min (100 %). Also shown are the corresponding voltammograms for the unspiked seawater.*

V *vs* Ag/AgCl is attributed to the reduction of the nitro groups, while the minor shoulder at -0.74 V *vs* Ag/AgCl is due to the reduction of the hydroxylamine product [258]. Fig. 9.14B displays the corresponding calibration curve that illustrates linearity from 100 to 900 ppb of TNT (peak current at -0.54 V *vs* TNT concentration; $R^2 = 0.990$). The high sensitivity ($s_x = 6.5$ nA ppb^{-1}) and the low LOD of 42 ppb (estimated from the 100 ppb TNT response) substantiate the highly-sensitive detection capability of the neoprene-based SPE towards trace explosives in marine environments. No apparent peaks are observed in the corresponding background voltammograms, reflecting the high selectivity of the sensor.

The stability of the wearable explosive sensor was evaluated by performing 30 repetitive measurements of 500 ppb TNT at 2 min intervals. As indicated in the resulting voltammograms of Fig. 9.14C, this prolonged one-hour experiment yielded a highly stable voltammetric response using seawater. Fig. 9.14D illustrates the stability of the peak current (at -0.55 V *vs* Ag/AgCl) with respect to the initial measurement at $t = 0$ min (100 %). The low RSD of 0.59 % is indicative of a highly stable response, without apparent surface fouling.

Copper is an important constituent of antifouling paints utilized for maritime applications [80]. The release of copper from such paints greatly contributes to the contamination of harbors and to marine environments, in general. Hence, a wearable sensor that can be adapted for underwater trace-metal monitoring would be attractive for the detection of copper in aquatic environments.

To accomplish this goal, trace copper detection was performed using square wave stripping voltammetry [282] at the neoprene-based printed carbon sensor. In order to achieve trace copper detection, the carbon working electrode of the SPE was modified via the electrodeposition of gold at an applied potential of 0.0 V *vs* Ag/AgCl for 20 min. The plating solution employed for these experiments consisted of a phosphate buffer, pH 7.0, containing 50 ppm gold. Copper deposition was performed for 2 min at -1.00 V *vs* Ag/AgCl under quiescent conditions, followed by a square wave stripping voltammetric scan from -0.25 to 0.50 V *vs* Ag/AgCl, and a 2 min electrochemical 'cleaning' at this final potential. This represents the first example of the use of a wearable sensor for trace metal stripping-

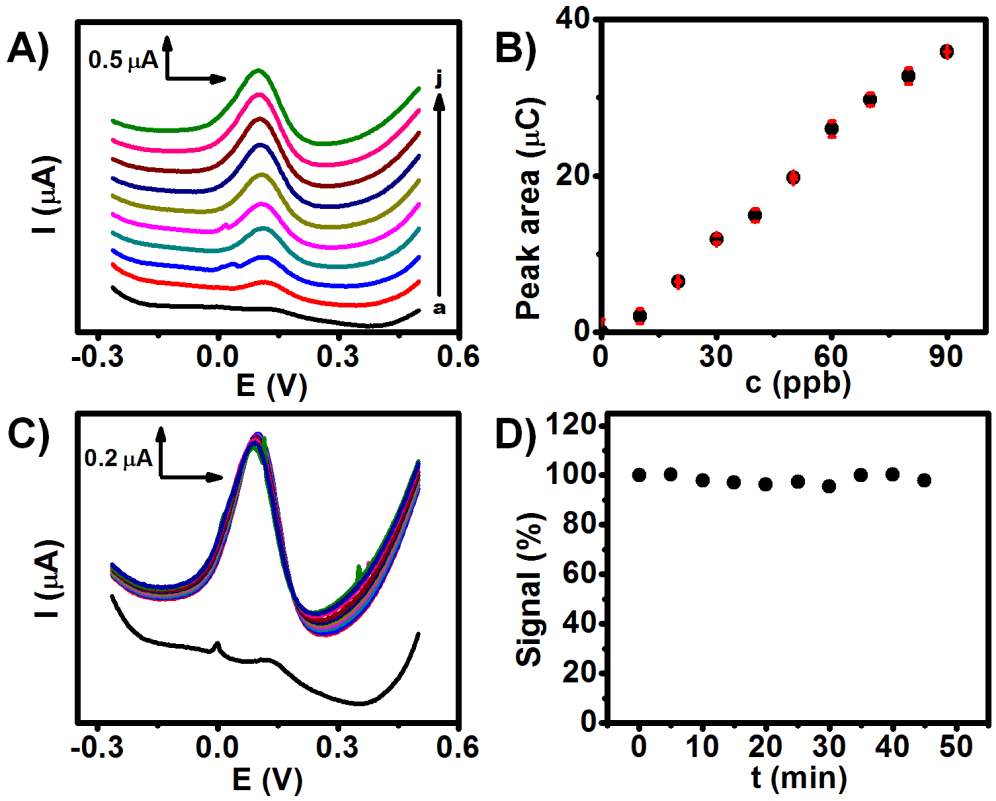

Figure 9.15: *Square wave stripping voltammograms for trace copper in untreated seawater at the Au-modified neoprene SPE. (A) Response to increasing copper concentrations in 10 ppb increments. Deposition for 2 min at -1.00 V* vs *Ag/AgCl under quiescent conditions followed by a square wave voltammetric scan from -0.25 to 0.50 V* vs *Ag/AgCl. Potential step, 4mV; Amplitude, 25mV; Frequency, 20Hz. (B) Calibration curve corresponding to the integrated stripping peak area versus the copper concentration (average of three repetitive measurements). (C) Stability of the system with 100 ppb copper over a 50 minute period. (D) Stability of the signal over time with respect to the initial measurement at* t *= 0 min (100 %).*

voltammetric measurements. A calibration curve was obtained through successive additions of copper into a cell containing untreated seawater. The copper was deposited on the electrode for 2 min at -1.00 V *vs* Ag/AgCl and was stripped from the electrode by scanning the potential to 0.50 V *vs* Ag/AgCl. Fig. 9.15A displays the voltammograms obtained at the Au-modified neoprene SPE for a seawater sample containing increasing concentrations of copper, while Fig. 9.15B depicts the resulting calibration curve for the integrated peak area versus copper concentration. Both experiments yielded well-defined copper peaks, with no overlapping signals. A linear range from 10 to 90 ppb levels of copper is observed ($R^2 = 0.988$), along with a sensitivity of 406 nC ppb^{-1} and an LOD of 13 ppb. The stripping copper response at the Au-modified neoprene SPE is also highly reproducible. Figs. 9.15C and D display a series of ten successive measurements of 100 ppb copper in untreated seawater over a 50 minute period. A highly reproducible copper peak is observed throughout this operation (RSD = 1.76 %).

As a final investigation, the complex-valued impedance profile (Nyquist plot) of the textile-based electrode was investigated in further detail. When compared with conventional SPEs on alumina, the electrode contingent on neoprene exhibited somewhat reduced charge transfer resistance, hence indicating more favorable reaction kinetics at the electrode interface within the frequency range evaluated (10 Hz - 10 kHz), Fig. 9.16. The imaginary component of the impedance spectrum, which is associated with the double layer capacitance originating from the electrode surface roughness, is substantially reduced with respect to the neoprene-based electrode. Consequently, this enables the neoprene sensor to function at elevated AC voltammetric modulation frequencies owing to the more rapid decrease in the non-Faradaic current due to the reduced capacitive loading .

Fig. 9.17 further reinforces the observations noted above. As can be inferred from the amplitude and phase responses provided in the Bode plots, the neoprene-based electrode contingent embodied a slightly reduced loss profile as well as slightly less phase change across the spectral range under examination when compared with its counterpart on solid alumina.

The development, evaluation, and demonstration of screen printed electro-

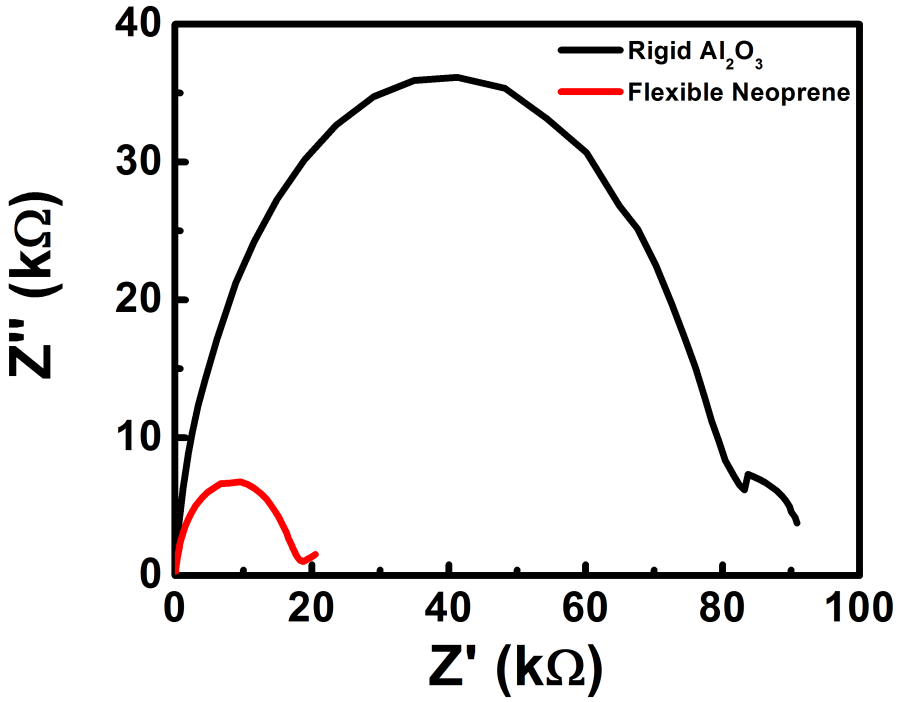

Figure 9.16: *Spectral comparison of the complex-valued impedance profile for screen printed electrodes on solid (Al_2O_3) and flexible (neoprene) substrates.*

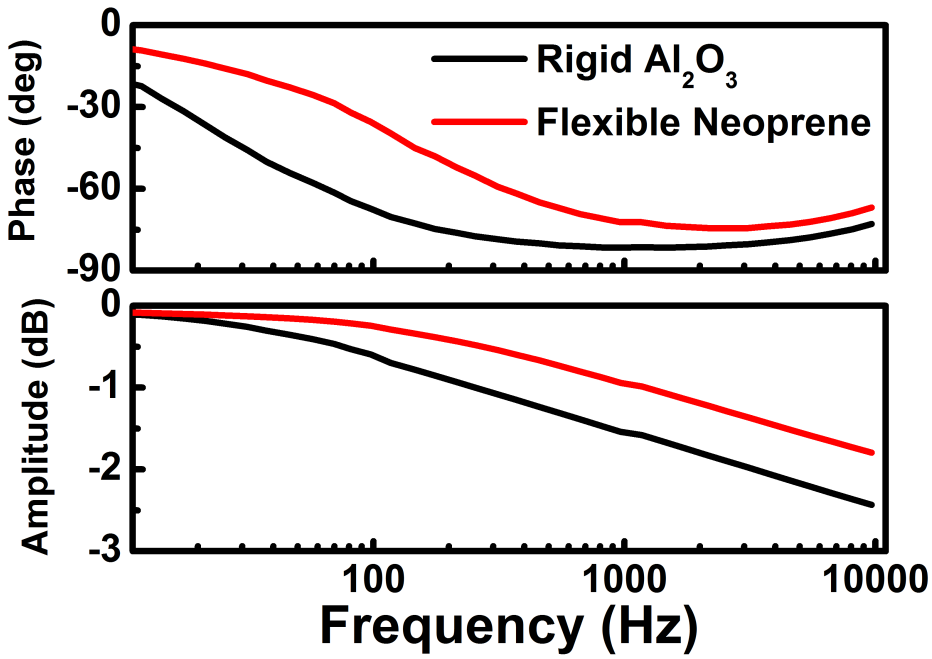

Figure 9.17: *Amplitude and phase response of impedance profile extracted from Fig. 9.16.*

chemical sensors on underwater garments has been discussed. These sensors are able to quantify trace levels of marine pollutants and explosive threats in seawater with high fidelity and repeatability. Wearable electrodes intended for in situ water analysis should alleviate the cumbersome process of sample preparation and analysis, hence allowing the wearer to monitor his / her surroundings for contaminants or hazards while performing other tasks. By printing the sensors on neoprene substrates commonly used in underwater garments, the real-time voltammetric detection of trace levels of Cu and TNT is attained. Moreover, the inclusion of an enzyme within the printed ink enables the biosensing of micromolar levels of phenolic contaminants. The neoprene-based printed electrodes can tolerate severe mechanical deformation that may be encountered during routine underwater activity. Whenever needed, an initial calibration in the seawater sample may be employed in order to address the potential matrix effects (such as changes in the temperature or oxygen level). The integration of printable sensors on underwater garments such as dry and wetsuits holds considerable promise for numerous marine sensing applications where real-time analysis and sensor miniaturization are core requirements. Using a similar design methodology, the concept can be further extended to other relevant threat assessment and environmental monitoring applications in marine environments.

Portions of Chapter 9, section 1 were taken from M.C. Chuang, J.R. Windmiller, P. Santhosh, G.V. Ramírez, M. Galik, T.Y. Chou, and J. Wang. Textile-based electrochemical sensing: Effect of fabric substrate and detection of nitroaromatic explosives. *Electroanalysis*, 22(21):2511–2518, 2010. The dissertation author was a co-author of the manuscript and had substantial original contributions to this work.

Portions of Chapter 9, section 2 were taken from K. Malzahn, J.R. Windmiller, G.V. Ramírez, M.J. Schöning, and J. Wang. Wearable electrochemical sensors for *in situ* analysis in marine environments. *Analyst*, 136(14):2912–2917, 2011. The dissertation author was a co-author of the manuscript and had substantial original contributions to this work.

Chapter 10

Microneedle-based transducers

We must become the change
we want to see.

—Mohandas Gandhi

The ability to continuously extract useful physiological information from transdermal fluids in a minimally invasive fashion has remained a pivotal goal within the biomedical devices community [283]. Such capability would prove valuable for a number of utilitarian physiological monitoring applications in the fitness [283], healthcare [284], and combat [285] domains. Electrochemical sensors have played a dominant role in the field of minimally invasive biosensors, with extensive development activity driven primarily by the challenge of continuous glucose monitoring [10, 286, 287, 288].

In an effort to achieve clinical translation of microdevices for the on-body monitoring of relevant bioanalytes, significant research activity has been devoted to the development of minimally invasive electrochemical biosensors [284, 10]. Microneedle arrays have been identified as a viable route to minimally invasive therapeutic delivery of vaccines [289], insulin [290], hormones [291], and other pharmacological agents [292, 293]. Accordingly, research pertaining to these devices has primarily focused on microneedle-mediated drug delivery rather than on employing microneedles for analytical sensing operations. In this regard, a few studies have applied hollow microneedles for transdermal glucose sensing merits [294, 295],

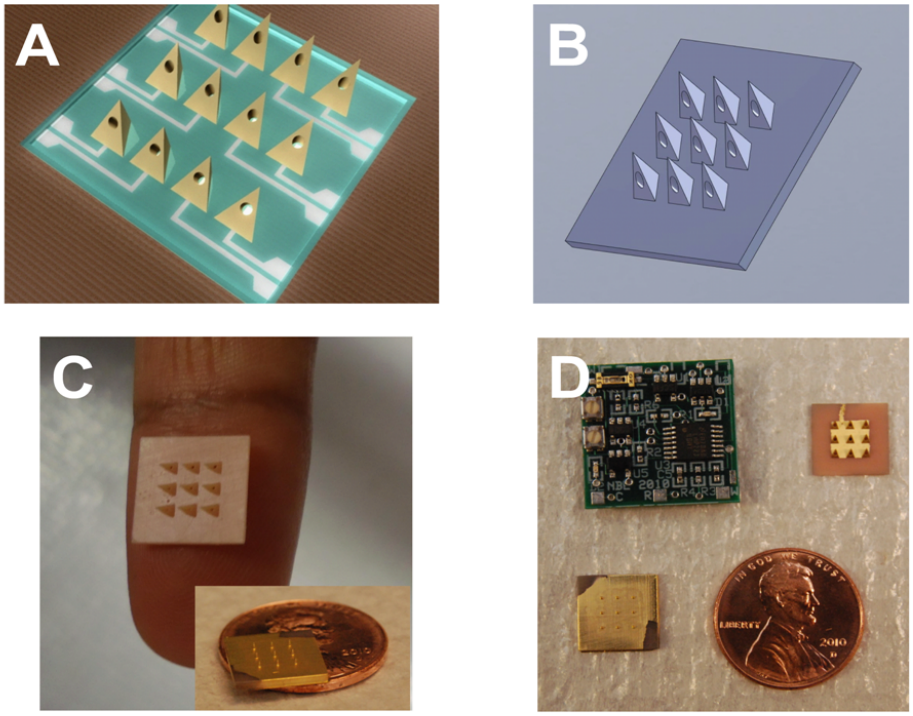

Figure 10.1: *(A) Computer-generated image of a 16-element individually-addressable microneedle array electrode contingent. (B) CAD file detailing a standard 9-element hollow microneedle array used throughout the investigations. (C) Size comparison of solid and hollow microneedle arrays. (D) Size comparison of microneedle arrays and the micro-/bioelectronic backbone employed for the control and readout of the sensor array.*

although these systems involve the integration of fluidic microchannels and the concomitant uptake of biological fluids, which complicate the process of on-body sensing.

The realization of minimally invasive transdermal sensing of biochemical analytes without the uptake of biological fluids demands that the execution of the sensing procedure be performed at the microneedletransdermal fluid interface. This, in turn, implies that the electrode transducer is directly employed at this interface. A key challenge materializes when this approach is taken: common solid electrode materials lack the plasticity required to conform with the micrometer-scale geometry and non-planar features that are the hallmark of mi-

croneedle array devices. Moreover, the electrode material must be amenable to the co-immobilization of enzymes, catalysts, mediators, and stabilizers. Such co-immobilization imparts selective recognition and transduction, in conjunction with the high stability essential for practical minimally invasive detection.

10.1 Microneedle array-based carbon paste amperometric biosensors

A carbon paste-loaded microneedle array has been designed, fabricated, and evaluated for minimally invasive biosensing applications. Of the plethora of electrode materials available, carbon paste is characterized by a high degree of plasticity that is essential for optimal loading of the transducer into the micron-scale geometries embodied by microneedle devices. Carbon paste electrodes (CPEs) have been widely employed in electroanalysis [296]. Such electrodes combine the advantages of low background current, low cost, as well as a straightforward means to regenerate the surface and impart selective catalytic abilities (via the inclusion of modifiers within the paste) [297]. The integration of a modified CPE within microneedle arrays has thus been demonstrated. The microneedle arrays utilized in the study consist of 9-element arrays of pyramidal-shaped hollow microneedles, which possess a 425 μm diameter aperture through which the modified carbon paste is extruded. In particular, a rhodium-dispersed carbon paste, known for its high affinity towards the low potential detection of hydrogen peroxide [297, 298, 299, 300], was packed within the microneedles to minimize the contribution of co-existing electroactive interferents. The resulting microneedle array CPE sensor design obviates the need for integrated microchannels and the extraction of the interstitial fluid. Enzyme-dispersed metallized carbon paste-loaded microneedle arrays are also shown to be useful for the selective detection of lactate at an extremely low potential of -0.15 V *vs* Ag/AgCl. This results in negligible contributions imparted by common physiological interferents (e.g., ascorbic acid, uric acid, and acetaminophen) upon the lactate response and simplifies the preparation of the sensor by precluding the need for an additional permselective layer. The

microneedle carbon paste sensor system thus represents an attractive platform to realize the continuous on-body monitoring of a multitude of relevant bioanalytes in a minimally invasive manner.

The microneedle designs were originally prepared using Solidworks (Dassualt Systemes S. A., Velizy, France). Substrate support structures were subsequently created with Magics RP 13 (Materialise NV, Leuven, Belgium). The microneedles were pyramidal in shape with a triangular base. The dimensions of each hollow microneedle were as follows: an edge length of 1174 $\pm$ 13 μm, a height of 1366 $\pm$ 15 μm, and a vertical cylindrical bore of 342 $\pm$ 5 μm diameter on one of the faces of the pyramid structure. The microneedles were arranged into 3 $\times$ 3 square arrays with 2 mm periodicity. Substrates for the microneedle arrays were 10 mm $\times$ 10 mm in extent and possessed a thickness of 2 mm. The three-dimensional computer models were transferred to a Perfactory SXGA Standard UV rapid prototyping system (EnvisionTEC GmbH, Gladbeck, Germany) for fabrication. This system uses computer models to precisely raster light from a 150 W halogen bulb over a photocurable material, resulting in the selective polymerization of the exposed material. Eshell 200 acrylate-based polymer (EnvisionTEC) was utilized as the constituent material to fabricate the microneedle arrays since the resin selectively polymerizes under visible light and exhibits a Youngs modulus of elasticity of 3050 $\pm$ 90 MPa [301]. Moreover, the polymer features Class-IIa biocompatibility per ISO 10993. A 550 mW output power beam (step size = 50 μm) with a zero-degree tilt was employed for the polymerization of the resin. Following the fabrication routine, the arrays were rinsed with isopropanol to remove the unpolymerized material. The arrays were later placed in an Otoflash post curing system (EnvisionTEC); post-build curing was performed for 50 s.

100 mg of rhodium on carbon (Rh/C, 5 wt %) and 10 mg of lactate oxidase (LOx, E.C. 1.1.3.2) were thoroughly homogenized via 10 alternating 5 min cycles of vortexing and ultrasonication. The mixture was then vortexed for an additional 1 hr. Following the homogenization process, 125 mg of the mineral oil pasting liquid and 15 mg of the poly(ethylenimine) (PEI) enzyme stabilizer were added to the solid mixture. Homogenization of the resulting paste mixture was accomplished

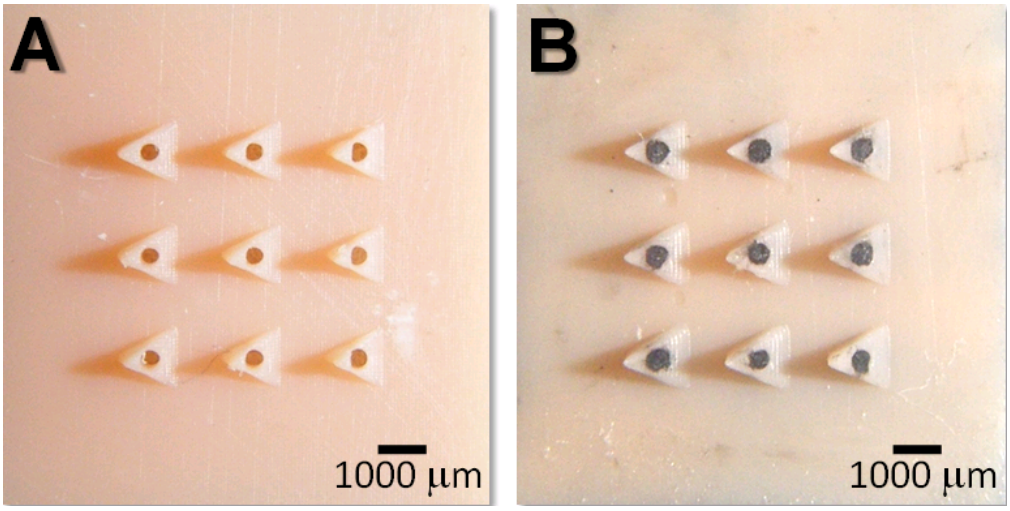

Figure 10.2: *Optical micrographs of the unloaded (A) and Rh-carbon paste-extruded (B) microneedle array.*

by grinding the mixture with a mortar and pestle for an additional 1 hr. The metallized carbon paste was subsequently extruded through the microneedle array with the aid of a plunger until the paste began to expel through the microneedle apertures. Excess paste was removed from each aperture; the surface was later smoothed using wax paper.

Initial studies were aimed at characterizing the morphology of the carbon paste-loaded microneedle array and initiated with a close examination of the microelectrode surface. An optical micrograph of the microneedle array is provided in Fig. 10.2A. This image displays uniform pyramidal microneedle structures (with triangular bases) possessing a height of approximately 1500 μm as well as cylindrical vacancies (425 μm diameter). Fig. 10.2B depicts a microneedle array that has been packed with carbon paste and subsequently polished. The figure indicates that the surface has been smoothly polished to obtain a highly uniform exposed area, thereby facilitating reliable electrochemical sensing. Excellent microelectrode-to-microelectrode uniformity is also observed, although the surface smoothing and paste removal protocols differ somewhat from those of conventional CPEs. This is attributed to the fact that the electrode apertures are located on the side of the pyramidal microstructure, thereby presenting additional challenges

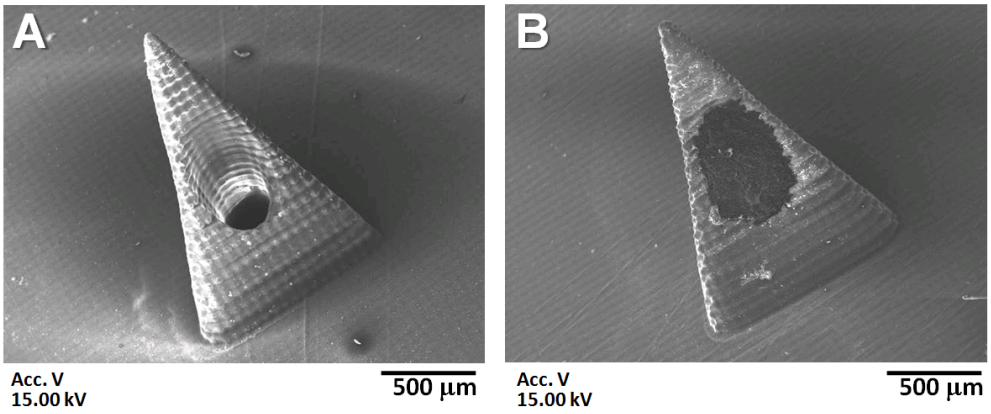

Figure 10.3: *Scanning electron micrographs of the unloaded (A) and Rh-carbon paste-extruded (B) microneedle constituent of the array.*

under polishing routines.

Pursuant to the characterization of the surface morphology, a closer inspection of the microneedle was performed using scanning electron microscopy (SEM). Fig. 10.3A depicts an electron micrograph of a single microneedle. The structure of the microneedle can clearly be observed, namely, the bored cylindrical vacancy and the ribbed structure created by the rastering of the light source over the polymer resin. Fig. 10.3B illustrates the surface details of a single microneedle loaded with carbon paste. A relatively smooth carbon paste morphology and a well-defined boundary between the carbon paste transducer and aperture are observed, which is attributed to the effective extrusion of the paste through the cylindrical aperture and subsequently polishing the surface. It should be noted that the microneedle and the opening appear to be elongated due to the oblique angle at which the SEM image was acquired.

Following the morphology investigation, the initial electrochemical experiments were performed to characterize the response of the carbon paste microneedle array towards hydrogen peroxide (H_2O_2). A hydrodynamic voltammogram (HDV) was recorded over the -0.20 to +0.60 V range in order to deduce a suitable operating potential and to demonstrate the strong catalytic ability of the Rh-carbon paste microneedle array towards the redox processes of H_2O_2. The results, illustrated in Fig. 10.4A, elucidate that the Rh-carbon paste microneedle array offers highly-

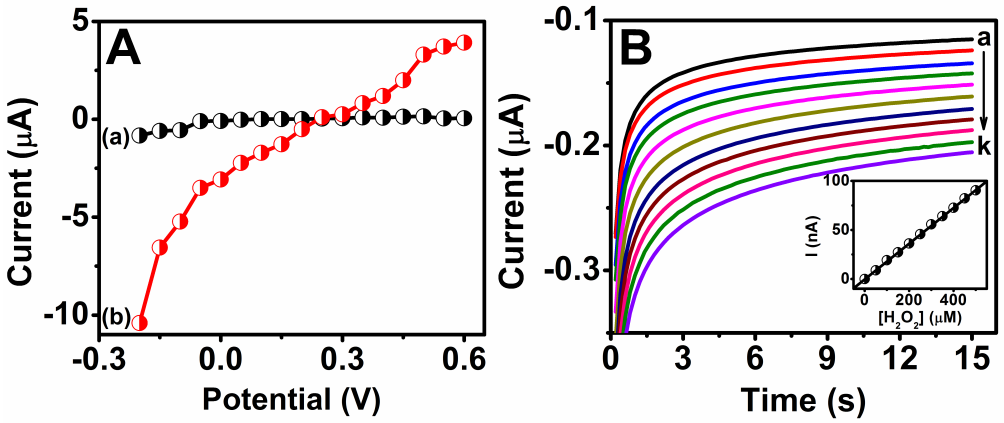

Figure 10.4: *(A) Hydrodynamic voltammogram of 0.1 M potassium phosphate buffer (a) and 10 mM H_2O_2 (b) at the rhodium-dispersed carbon paste microneedle electrode. (B) Chronoamperograms obtained using the rhodium-dispersed carbon paste microneedle electrode (0 → 500 μM H_2O_2 in 50 μM increments; a → k;* E_{APP} *= -0.15 V* vs *Ag/AgCl). The calibration curve* (n = 3) *is provided in the inset.*

catalytic detection of H_2O_2 over the entire range evaluated, with a crossover point occurring around 0.22 V (*vs* Ag/AgCl). The substantially reduced overpotential required to either reduce or oxidize H_2O_2 enabled the selection of a low operating (reduction) potential of -0.15 V *vs* Ag/AgCl for subsequent sensor investigations. At this potential, a reduction current of 5.95 μA could be achieved for 10 mM H_2O_2; the contributions imparted by common electroactive interferences at this potential are negligible (see data and discussion below).

The microneedle CPE exhibits a wide dynamic range for H_2O_2 quantification. Fig. 10.4B displays chronoamperograms for increasing levels of H_2O_2 to 500 μM (in 50 μM increments). Well-defined reduction currents, proportional to the H_2O_2 concentration, are observed. The resulting calibration curve, based on sampling the current at 15 s following the application of the potential step, displays high linearity (R^2 = 0.999; see inset). Interpolating from the experimental data, a limit of detection (LOD) of 20 μM (S/N = 3) could be achieved with the device, which is in agreement with the low-μM LOD values reported in the literature for bulk metallized carbon paste electrodes [298, 302, 303, 304]. The ability to detect H_2O_2 at low potentials is an appealing feature of the Rh-carbon paste microneedle

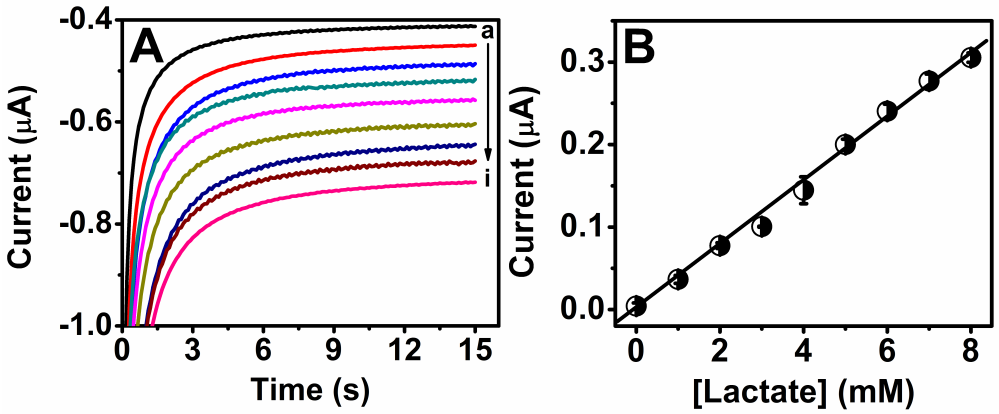

Figure 10.5: *(A) Chronoamperograms obtained for lactate concentrations from 0 to 8 mM in 1 mM increments (E_{APP} = -0.15 V* vs *Ag/AgCl). (B) Calibration curve corresponding to the chronoamperometric current at* t = *15 s.*

array when positioned for use in minimally invasive oxidase-based biosensors.

Following the optimization of the H_2O_2 detection, a microneedle array CPE biosensor for lactate was developed. Accordingly, lactate oxidase (LOx, E.C. 1.1.3.2)-dispersed metallized carbon paste was prepared employing PEI for the electrostatic entrapment of the enzyme within the matrix. Chronoamperometric calibration experiments were executed using the LOx-Rh-carbon paste microneedle array at -0.15 V *vs* Ag/AgCl for increasing levels of lactate (0 to 8 mM in 1 mM increments). Typical chronoamperograms are displayed in Fig. 10.5A; the corresponding calibration curve (for current sampling at t = 15 s) is shown in Fig. 10.5B. High linearity (R^2 = 0.990) and low deviation (σ < 10 nA) are observed. Although the estimated detection limit of 0.42 mM lactate (S/N = 3) is somewhat higher than the values reported in the literature for Rh-CPE biosensors, [299, 304, 305] it is still well below normal physiological levels and is therefore more than sufficient for relevant biomedical applications. It should be noted that the linear concentration range encompasses the entire physiological and pathological range of lactate in transdermal fluids [104, 105], indicating the potential diagnostic value of the microneedle-based lactate biosensor.

In order to ascertain the ability of the lactate biosensor to function as intended in the presence of common electroactive substances found in transdermal

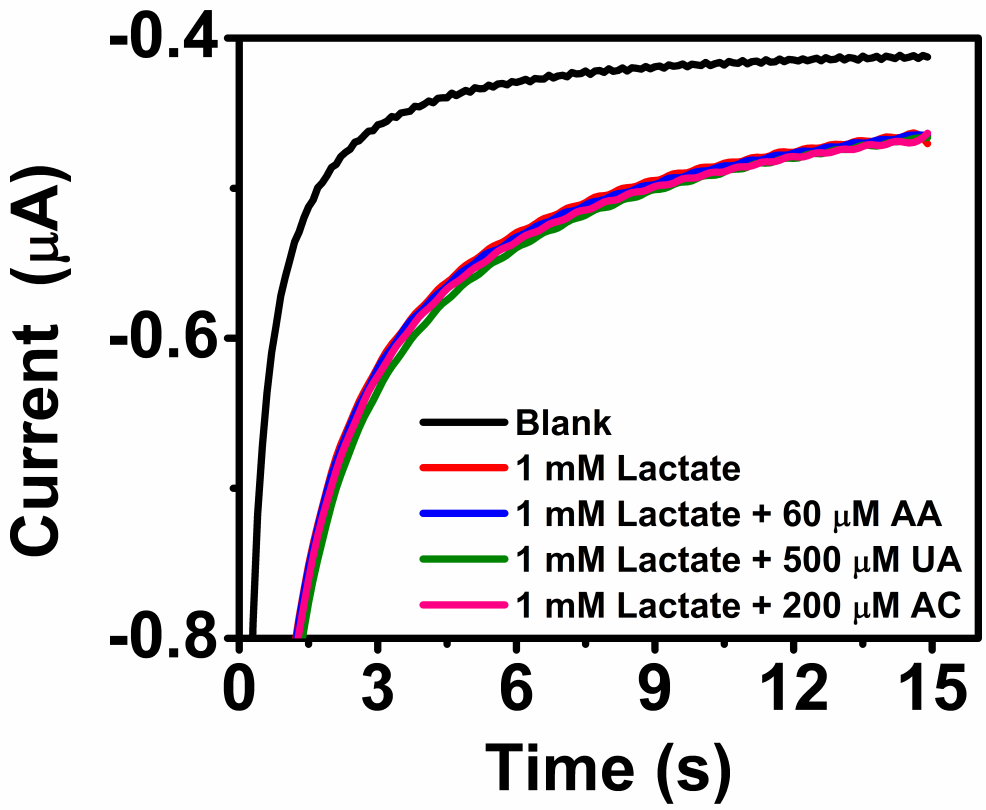

Figure 10.6: *Chronoamperograms illustrating the effect of physiologically relevant electroactive interferents upon the detection of lactate* (E_{APP} = *-0.15 V* vs *Ag/AgCl).*

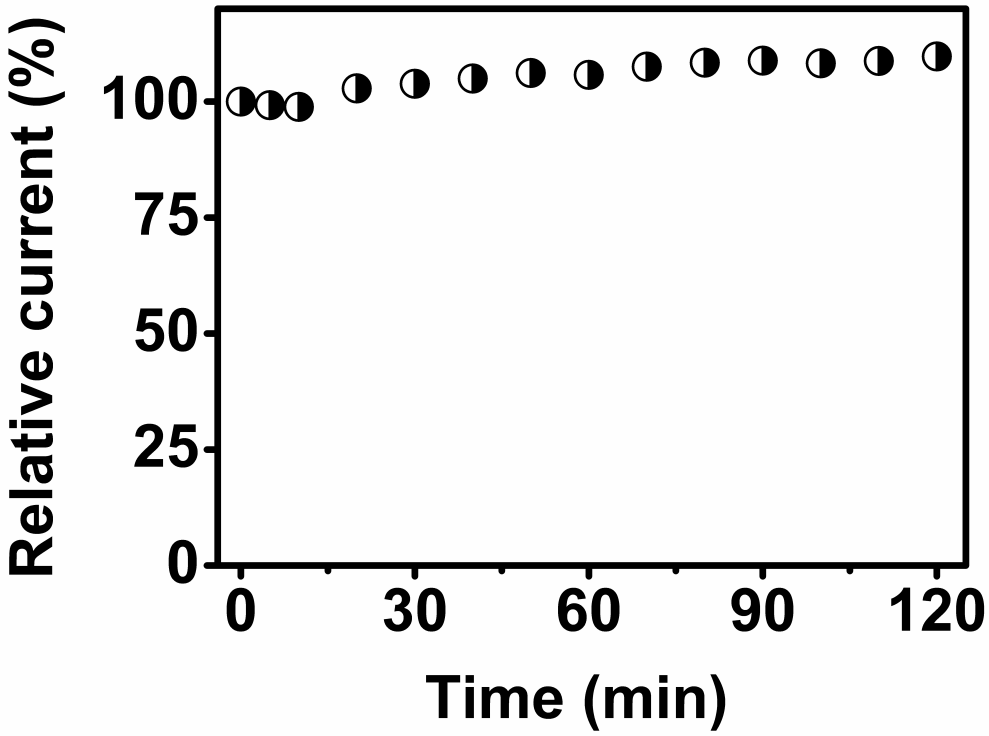

Figure 10.7: *Stability of the electrochemical response of the microneedle array for 2 mM lactate (E_{APP} = -0.15 V* vs *Ag/AgCl) over a 2 hour duration.*

fluids, an interference investigation was conducted using physiological levels of these compounds. Fig. 10.6 illustrates the results of the chronoamperometric experiments involving a potential step to -0.15 V *vs* Ag/AgCl and measurements of 1 mM lactate in the presence of 60 μM ascorbic acid (AA), 500 μM uric acid (UA), and 200 μM acetaminophen (AC). As evident, the addition of any of these common electroactive interferents resulted in a negligible effect on the lactate response. A maximum current deviation of only 1.5 % from the 1 mM lactate level was observed for the addition of AC. Such interference-free lactate detection reflects the strong, yet preferential electrocatalytic activity of the Rh-carbon paste microneedle array towards H_2O_2 [298, 299] and further supports the potential of the microneedle paste biosensor for lactate monitoring in transdermal fluids.

The stability of the microneedle array-based biosensor was examined from repetitive chronoamperograms for 2 mM lactate over a 2 hour period. The current

was sampled every 10 min over the entire 2 hour stability test period. Fig. 10.7 illustrates the time-course profile of the resulting current response (with the initial reading at $t = 0$ min normalized to 100 %). A stable current was achieved almost immediately following the initialization of the experiment, with only a slight increase (9.7 %) over the entire 2 hour time-course. The stable response reflects the integrity of the carbon paste microneedle array biosensor. Effective extrusion of the carbon paste, which prevents the potential accumulation of the enzymatic product within vacancies between the microneedle aperture and carbon paste transducer, is essential for the stable response.

Granted that the work represents one of the first instances of electrochemical sensing at microneedle-based devices, a detailed description of the amperometric profile of microneedle arrays is warranted. Consequently, a computational model was developed for the electrochemical detection of any arbitrary electroactive species at the microneedle array. Harnessing this model, the current response arising at a microneedle array of given geometry may be calculated a priori in systems that obey classical Fickian diffusion. Lactate was established as the model analyte in order to provide for the experimental verification of the model and correlate the numerical results with the empirical data.

Beginning with the relation presented in Eq. (2.59), a damping factor ξ may be included to account for the reaction kinetics (which are taken to be less facile than charge-transfer dynamics) and an empirically-defined background current *B(t)* may be appended to the relation arising from the charging of the double layer,

$$i_i\left(0,t\right) = z_i \xi g F A D_i C_i^{b,0} \frac{e^{\frac{z_i F}{RT}\Delta\phi}}{\left(4\pi D_i t\right)^{n/2}} + B\left(t\right) \tag{10.1}$$

where g represents the number of electrodes (microneedles) in the array and A represents the surface area of one electrode constituent. A summary of the values employed in the model is given in Tab. 10.1:

where $C_i^{b,0}$ is scanned from 0 to 10 mM (accounting for the physiological range of lactate), t is scanned from 0 to 60 s, and *B(t)* is found experimentally from a background current measurement. The results of the simulation, in the

Table 10.1: *List of values employed for Fickian diffusional model.*

Parameter	*Value*	*Units*
z_i	1	-
ξ	0.25	-
g	9	-
F	96485	Coul/mol
A	1.59E-7	m^2
D_i	8.88E-10	m^2/s
R	8.314472	J/mol/K
T	295	K
$\Delta\ \phi$	0.40	V
n	3	-

form of a contour plot, are provided in Fig. 10.8.

Fig. 10.9 presents an overlay of the simulated results with the empirical data obtained earlier for lactate. As is evident, excellent agreement is observed between the simulated and experimental results, with a residual sum of squares RSS $<$ 0.32 fA. Accordingly, the validated model, owing to its analytical fidelity and versatility, should be able to predict the electrochemical response of a given microneedle array electrode towards a bioanalyte or electroactive species of interest *a priori*.

The unison of CPE transducers with microneedle hosts addresses the challenges associated with the integration of solid electrodes with the non-planar features of microneedle arrays. Furthermore, it obviates the need for integrated microchannels as well as the extraction of the interstitial fluid and, therefore, the implementation of microfluidic and / or microelectromechanical systems is not necessary. Although the low-potential detection of lactate (H_2O_2) was illustrated using this microneedle system, highly linear detection of other pertinent bioanalytes over the entire physiological range is possible through the use of the appropriate biorecognition element, along with the high selectivity imparted by the very low cathodic detection potential. The high selectivity, sensitivity, and stability of the carbon paste microneedle array holds substantial promise for diverse on-body sensing applications. In light of these merits, the successful realization of a patch-type microneedle-based on-body sensor paradigm would require proper attention

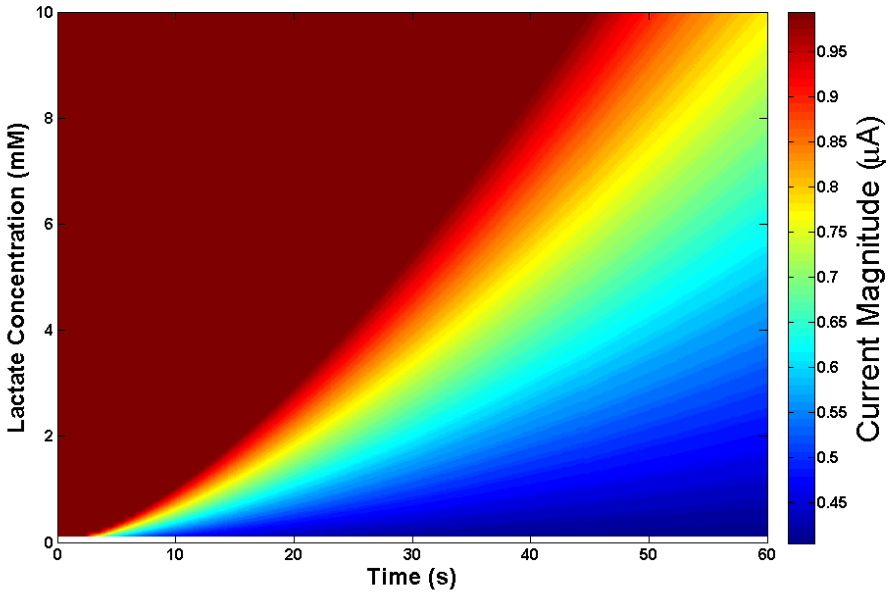

Figure 10.8: *Contour plot of the simulated amperometric profile produced by a lactate oxidase-functionalized 9-element microneedle array in the presence of various levels of lactate within the pathophysiological range.*

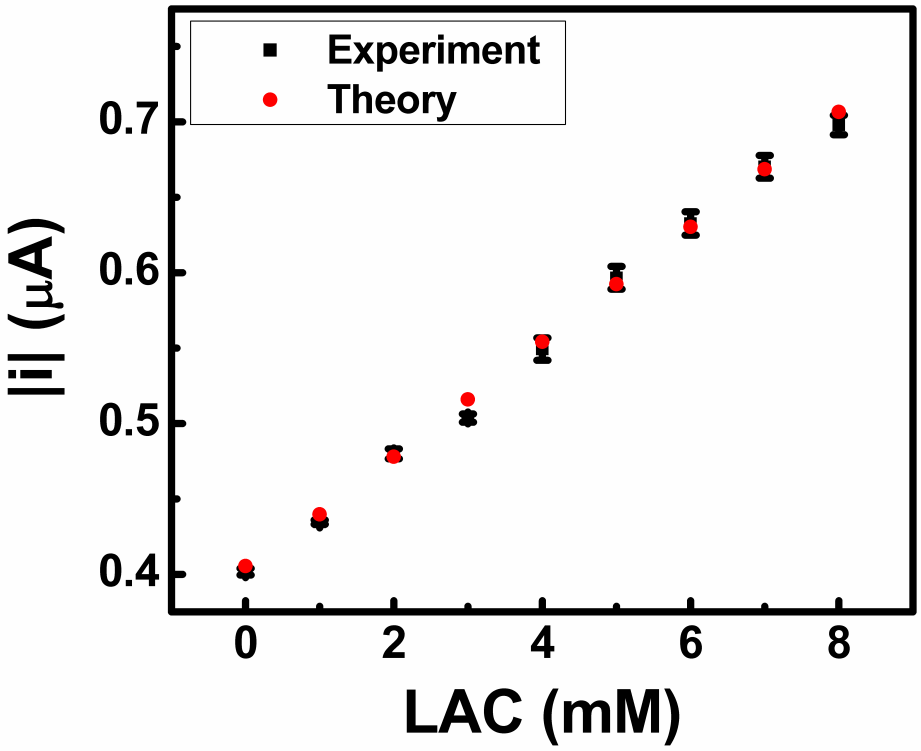

Figure 10.9: *Lactate calibration correlating simulated results using a Cottrellian analytical model with the empirical data.*

to the key challenge of biofouling at the tissue-device interface in connection with the selection of appropriate surface coatings and permselective membranes.

10.2 Bicomponent microneedle array biosensors utilizing conducting polymers

As discussed in the previous section, permselective membranes are necessary to impart improved rejection of co-circulating electroactive interferents and mitigate the natural process of biofouling via the accumulation of proteins on the electrode surface of the microneedle. To accomplish this objective, a microneedle array device employing a recess-based microcavity structure, which is intended to confine the recognition enzyme and protect it upon penetration of the epidermal layer, has been developed and evaluated. The bicomponent microneedle biosensor consists of an array of platinum-coated solid microneedles, which serve as the working electrode, and a hollow microneedle cover, which provides a microcavity that surrounds each solid microneedle, as diagrammatically represented in Fig. 10.10. The recess-based microneedle architecture enables the facile electropolymeric entrapment of a biocatalyst / enzyme within the individual apertures of the microneedle array. As a result, direct transdermal biosensing is accomplished without requiring the uptake of the transdermal fluid, thereby simplifying device construction. The bicomponent recess geometry of the microneedle biosensor also provides greater surface area for enzyme immobilization when compared with microneedles containing embedded planar electrodes [294, 306].

Electropolymerized poly(o-phenylenediamine) (PPD) thin films have been widely employed for the confinement of enzymes into miniaturized electrode transducers while imparting remarkable permselective properties and a stable response. In particular, PPD has been used for the entrapment of different oxidase enzymes such as glucose oxidase (GOx, E.C. 1.1.3.4) [307, 308, 309, 310], lactate oxidase (LOx, E.C. 1.1.3.2) [311, 312, 313], and glutamate oxidase (GluOx, E.C. 1.4.3.11) [314, 315, 316], along with permselective detection of the liberated hydrogen peroxide product. As a consequence of their remarkable permselective properties,

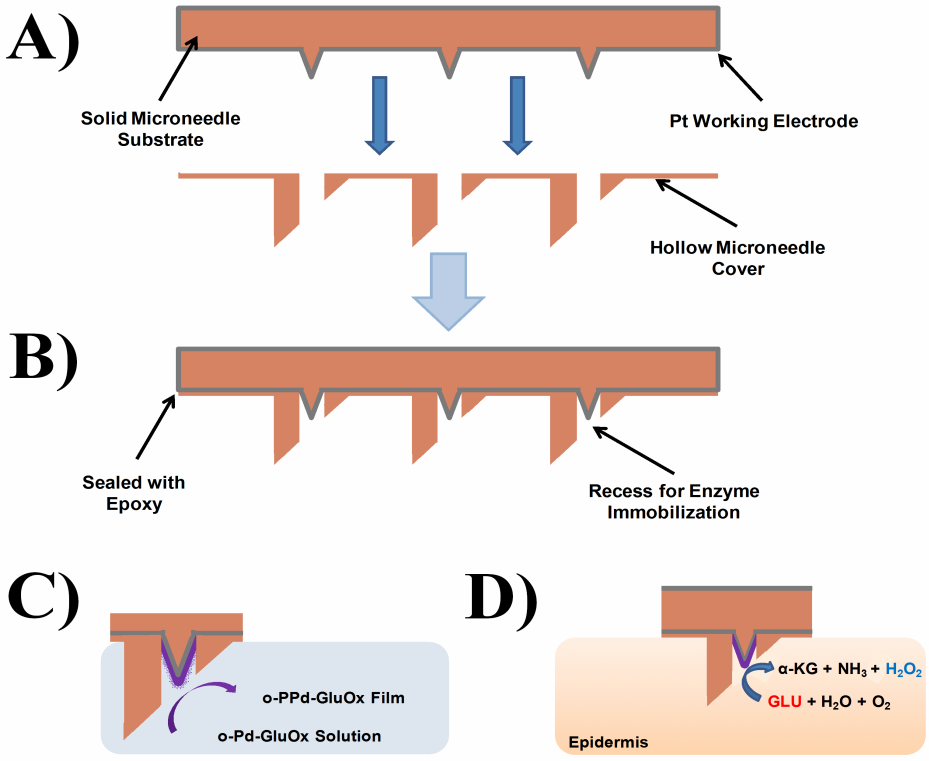

Figure 10.10: *(A) Solid and hollow microneedle constituents of the bicomponent microneedle array electrode. (B) Fully-assembled bicomponent microneedle array electrode. (C) Growth of the glutamate oxidase (GluOx)-functionalized poly(o-phenylenediamine) (PPD) film at the solid microneedle surface within the recess from the o-phenylenediamine (o-PD) monomer. (D) Biocatalytic behavior of the electropolymerized glutamate oxidasepoly(o-phenylenediamine) film (illustrated in purple), enabling the quantification of glutamate levels within the transdermal fluid. Glucose oxidase (GOx) is substituted in place of GluOx for the quantification of glucose.*

PPD films impart high selectivity and stability through the exclusion of co-existing electroactive interferences and proteins normally present within bodily fluids [317]. Biosensors that employ PPD films have thus been shown to facilitate the amperometric detection of hydrogen peroxide with high substrate selectivity, excellent sensitivity, operational stability, and rapid response time [310]. In this manner, biosensors that employ enzyme-functionalized PPD films commonly exhibit considerable advantages when compared with those based on other immobilization techniques [318].

To illustrate the versatility of the new bicomponent microneedle array platform, a biosensor for the amperometric quantification of physiological levels of the excitatory neurotransmitter glutamate has been demonstrated; this platform is subsequently extended to glucose monitoring for the management of diabetes mellitus. Clinical studies have revealed that blood glutamate levels rise from an average value of 37.5 μM among healthy patients to 141.3 μM among patients who have sustained moderate to severe trauma related to intracranial injury [124]. As such, serum glutamate levels can provide useful insight into the overall condition of the central nervous system following brain trauma.

Previous biosensors that have been developed for quantifying glutamate levels were characterized by a high degree of invasiveness; these devices have required the uptake of the cerebral spinal fluid (CSF) via a catheter [319] or a microdialysis probe [320, 321] for further analysis. Typically performed in a hospital setting, such clinical analysis is a painful, time-consuming, and costly proposition. In addition, these previously described methods are not amenable to on-body continuous monitoring, especially when access to the CSF is not feasible. However, as blood glutamate levels correlate well with the levels found in the CSF [322], its extraction from this hard-to-access bodily fluid is unnecessary.

A novel means to entrap the enzymes GluOx and GOx within the microcavities of a new microneedle geometry has been developed. The PPD-based confinement of the enzymes within the microneedle cavities enables the efficient quantification of glutamate and glucose at pathophysiological levels within buffer solutions and undiluted human serum. The minimally-invasive nature of the device, com-

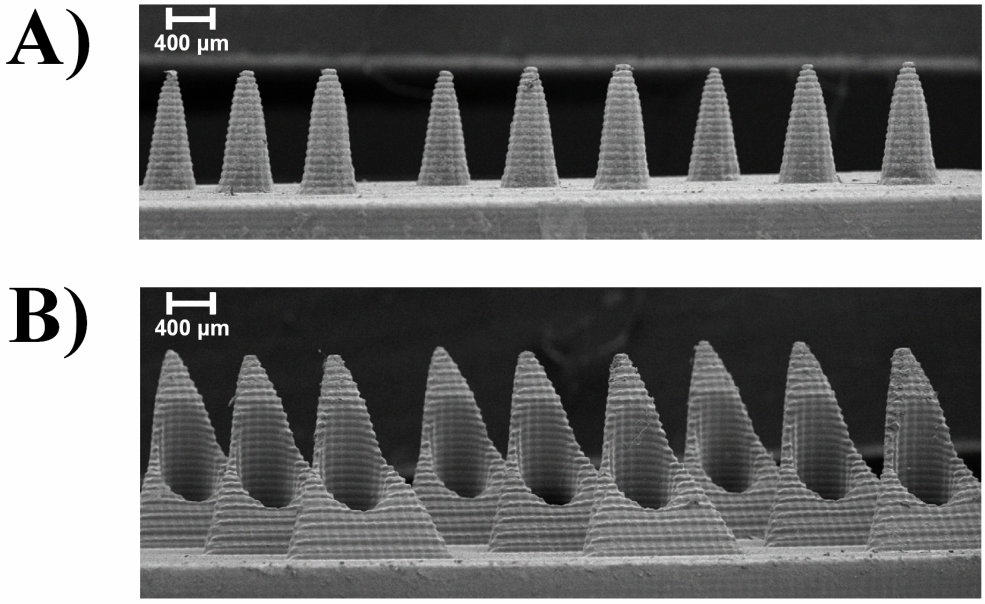

Figure 10.11: *Scanning electron micrographs of the solid (A) and hollow (B) microneedle arrays.*

bined with its convenient means to achieve enzyme entrapment and protection, as well as its attractive electroanalytical performance, demonstrates considerable potential as a practical patch-type on-body biosensor.

The fabrication of the hollow microneedle arrays has been described in the previous section. Solid microneedles, which were fabricated using the same technique, were conical in shape and possessed a base diameter of 390 $\pm$ 14 μm and a height of 818 $\pm$ 35 μm. The solid microneedles were arranged in 3 $\times$ 3 square arrays with 2 mm periodicity on 10 $\times$ 10 mm substrates possessing a thickness of 2 mm. A Compex 201 krypton-fluoride (KrF) excimer laser (Coherent, Santa Clara, CA), which operated with a 10 Hz repetition rate at a wavelength of 248 nm, was used to ablate a commercially-obtained high-purity Pt target. This process resulted in the deposition of thin films of Pt ($\sim$12 nm) on the surface of the solid microneedle array [323]. A background pressure of 5 μTorr was maintained during the 2 min pulsed laser deposition (PLD) routine, which was performed at room temperature.

Adhesive non-conducting epoxy was applied to the periphery of the solid microneedle substrate. A hollow microneedle cover was then placed over the solid microneedle substrate; this procedure is diagrammatically represented in Figs. 10.10A and B. The two components were then arranged under an optical microscope to align the solid microneedles within the hollow microneedle aperture. This formed the bicomponent microneedle array electrode (BMAE), as shown in Fig. 10.10C.

In order to immobilize the GluOx and GOx enzymes on the electrode surface and reject potential electroactive interferents, a poly(o-phenylenediamine) (PPD) film was electropolymerized from a solution of the o-phenylenediamine (o-PD) monomer Fig. 10.10C. Functionalization of the BMAE with GOx ensued, and a 0.1 M phosphate buffer (pH 7.40) solution containing 10 mM o-PD, 5 mM sodium sulfate, and 100 kU L^{-1} GOx was purged with nitrogen for 20 minutes at room temperature. The BMAE was subsequently immersed in the solution; a potential of 0.75 V *vs* Ag/AgCl was consequently applied for 20 min in order to deposit the GOx-entrapped PPD film [307], as represented in Fig. 10.10C.

To conserve the costly GluOx enzyme during the electropolymerization process, a slight variant of the aforementioned protocol was employed [315]. The BMAE was immersed in a solution of 0.1 M phosphate buffer (pH 7.40) containing 10 mM o-PD and 5 mM sodium sulfate; a potential of 0.75 V *vs* Ag/AgCl was subsequently applied for 5 min. The electrode was later rinsed and desiccated at room temperature. A 0.5 μL aliquot of 7.5 kU L^{-1} GluOx in 0.1 M phosphate buffer (pH 7.40) was then dispensed in each microcavity constituent of the BMAE; this step was repeated for an additional six iterations. Following this process, the solution was allowed to dry at room temperature. Subsequently, a solution of 0.1 M phosphate buffer (pH 7.40) containing 10 mM o-PD, 5 mM sodium sulfate, and 1 U/mL GluOx was dispensed in each microcavity. A potential of 0.75 V *vs* Ag/AgCl was subsequently applied for 15 min in order to electropolymerize the GluOx-entrapped-PPD film. Whereas the previous protocol was adapted for simplicity at the expense of increased enzyme utilization, this implementation facilitates the electropolymerization of more costly enzymes.

Following each electropolymerization routine, the BMAE was rinsed and

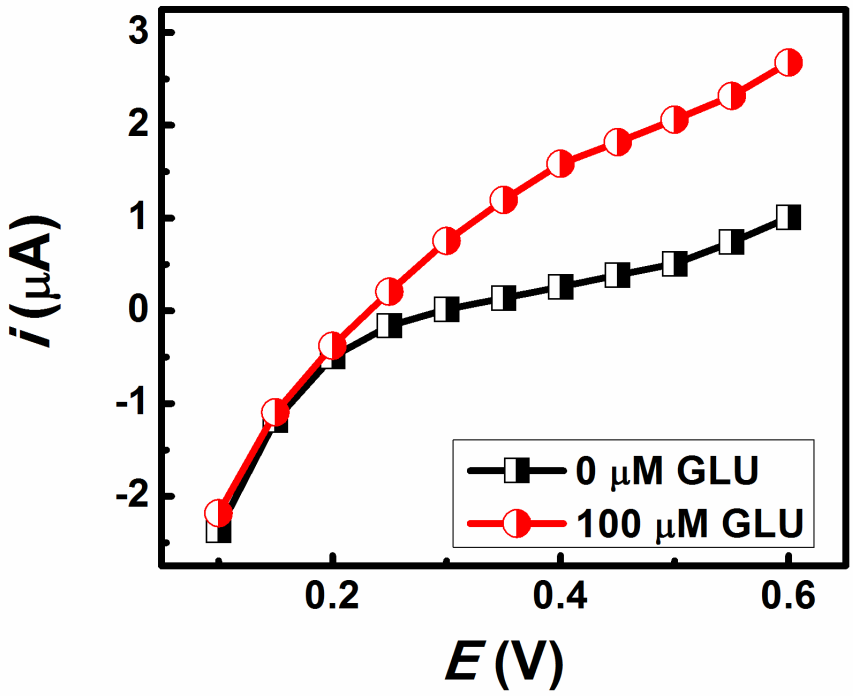

Figure 10.12: *Hydrodynamic voltammograms of the glutamate bicomponent microneedle array electrodes* (t = *15 s).*

immersed in a 0.1 M phosphate buffer solution (pH 7.40) for 30 min to remove monomeric residues from the microneedle structure as well as any non-bound enzyme. When not in use, the BMAE was stored in phosphate buffer at 4° C. This protocol, which is diagrammatically represented in Fig. 10.10D, enabled the quantification of glutamate and glucose, as shown.

An investigation of the surface morphology of the BMAE was first performed in order to ascertain the electrode geometry and surface features. A close examination of the BMAE surface morphology was executed using scanning electron microscopy (SEM). Figs. 10.11A and B display scanning electron micrographs of the solid and hollow microneedle arrays, respectively. As can be observed from the micrographs, the features of the microneedles closely corresponded with those

specified in the CAD file. With respect to the solid microneedles, a notable observation is the ribbed structure, which is attributed to the rastering of the light source that was utilized to polymerize the resin. A uniform pyramidal structure and a triangular base are observed at each component of the hollow microneedle array, along with apertures of uniform size distribution. Minimal microneedle-to-microneedle geometric variation was observed.

The initial electrochemical characterization of the BMAE was aimed at constructing hydrodynamic voltammograms (HDVs) in order to select the optimal detection potential of the generated H_2O_2 product. An HDV was obtained using chronoamperometry at varying potentials between 0.1 and 0.6 V *vs* Ag/AgCl (in 50 mV increments). These experiments were performed in the buffer solution containing 100 μM of glutamate. The redox currents were sampled at 15 s following the application of the potential step. An identical procedure was followed utilizing the GOx-BMAE for the detection of 10 mM glucose. The resulting HDV for glutamate is shown in Fig. 10.12. As is evident from the figure, the presence of glutamate caused a concomitant rise in the anodic current, corresponding to the oxidation of the H_2O_2 enzymatic product. The onset of the peroxide oxidation occurred at $\sim$0.25 V *vs* Ag/AgCl. To minimize the potential oxidation of interferents in real samples, a potential of 0.40 V *vs* Ag/AgCl was selected for further electrochemical studies of the BMAE biosensor.

Using chronoamperometric potential steps to the selected potential of 0.40 V *vs* Ag/AgCl, the sensitivity of the new BMAE biosensor was evaluated in detail. Fig. 10.13A illustrates the average of chronoamperometric experiments ($n = 3$) for increasing levels of glutamate over the entire pathophysiological range (0 140 μM in 20 μM increments, sampled at $t = 15$ s) in a buffer matrix. A linear calibration plot ($R^2 = 0.995$) is observed (shown in the inset of Fig. 10.13A) over the entire range under investigation. The calibration plot is indicative of high sensitivity ($s_x = 7.129$ nA / μM) and a low deviation (RSD = 3.51%); a limit-of-detection (LOD) of 3 μM can be extrapolated based on the signal-to-noise characteristics of the experimental data (S/N = 3). The LOD lies well- below normal physiological levels, reflecting the ability of the microneedle sensor to detect physiologic levels

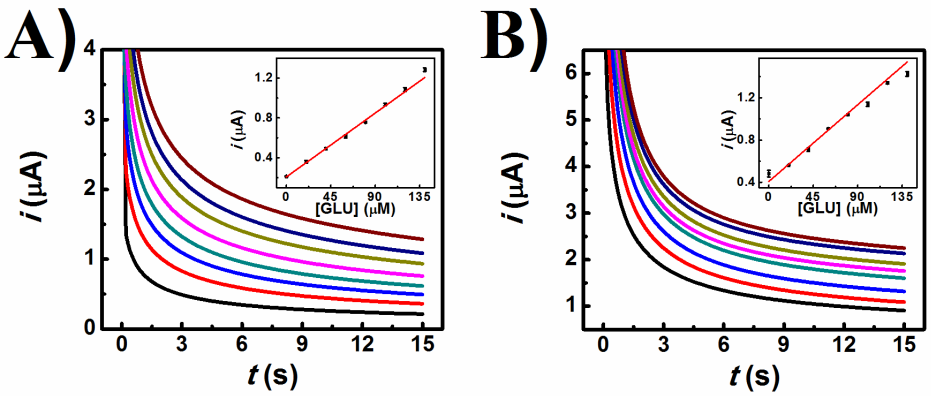

Figure 10.13: *(A) Chronoamperograms recorded for increasing concentrations of glutamate from 0 μM to 140 μM in 20 μM increments in (A) 0.1 M phosphate buffer (pH 7.40) and (B) human serum. All experiments were performed with E_{APP} = 0.40 V* vs *Ag/AgCl and* t = *15 s* (n = *3).*

of glutamate.

Following the calibration experiments in the buffer solution, the system was evaluated towards the quantification of glutamate in undiluted human serum samples. Fig. 10.13B illustrates the average chronoamperometric calibration experiments (n = 3) in human serum for increasing levels of glutamate over the 0 140 μM range (in 20 μM increments). As with the buffer study, a linear calibration plot is observed (inset of Fig. 10.13B; R^2 = 0.992) over the entire range. In addition, the calibration data exhibit high sensitivity (s_x = 8.077 nA / μM) and low deviation (RSD = 6.53%). An LOD of 21 μM can be extrapolated based on the signal-to-noise characteristics of the data (S/N = 3). As with the buffer experiments, the LOD obtained from the experimental data resides below the limit of normal physiological levels. The relatively unperturbed electrochemical behavior of the BMAE in untreated serum samples serves to emphasize the protective abilities of the PPD film against interfering substances naturally residing within serum. Furthermore, the similar sensitivity obtained for both the buffer- and serum-based trials again underscores the robustness of the PPD immobilization scheme despite the prolonged exposure of the biosensor to the protein-rich serum medium.

An additional advantageous feature of the PPD entrapment methodology

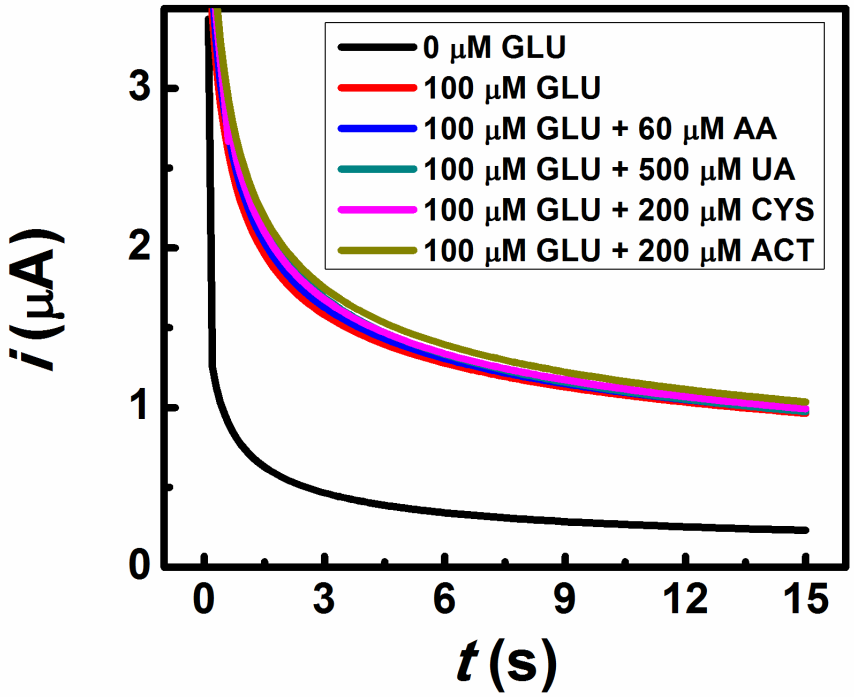

Figure 10.14: *Chronoamperograms recorded in 0.1 M phosphate buffer (pH 7.40) for the blank buffer solution, 100 μM glutamate, and 100 μM glutamate in the presence of the electroactive physiological interferents ascorbic acid (AA, 60 μM), uric acid (UA, 500 μM), cysteine (CYS, 200 μM), and acetaminophen (ACT, 200 μM). Conditions as in Fig. 10.13.*

resides in its ability to reject coexisting electroactive interferents even at moderate oxidation potentials [318]. Accordingly, the selectivity of the response was examined in the presence of physiological levels of ascorbic acid (AA, 60 μM), uric acid (UA, 500 μM), cysteine (CYS, 200 μM), and acetaminophen (ACT, 200 μM) [104]. Fig. 10.14 illustrates the negligible contribution imparted by the presence of these electroactive compounds upon the current signal for 100 μM glutamate. Physiological levels of ascorbic acid, uric acid, cysteine, and acetaminophen resulted in only 0.44%, 0.31%, 1.93%, and 6.37% average deviations from the 100 μM glutamate current response, respectively. Hence, natural metabolic fluctuations in the levels of these electroactive species are not expected to interfere with the in vivo quantification of glutamate in applications were the BMAE device is employed as an on-body biosensor.

The ability to operate over prolonged periods with minimal deterioration in the current response represents another major requirement of on-body biosensors. Accordingly, the stability of the BMAE response was examined using a 100 μM glutamate solution over an eight-hour period. The time-course profile, displayed in Fig. 10.15, indicates that the biosensor exhibited a highly stable current response, retaining 105% of the original signal level after eight hours of continuous sampling. The measured current never exceeded 110% of the original level over the entire duration of the investigation. Consequently, the BMAE is expected to perform reliably over extended periods associated with body-worn biosensors. With the glutamate BMAE methodically characterized, the platform was subsequently migrated to diabetic monitoring merits. GOx was confined within the BMAE microcavities using a slight variant of the GluOx immobilization protocol.

Fig. 10.16A illustrates a chronoamperometric calibration experiment for increasing levels of glucose over the entire pathophysiological range (0 - 14 mM in 1 mM increments) in a buffer matrix. A well-defined response is observed over the entire range, leading to a linear calibration plot (displayed in the inset of Fig. 10.16A; R2 = 0.996). In addition, the calibration data exhibit high sensitivity ($s_x = 0.353\ \mu$A / mM) and low deviation (RSD = 6.44%, $n = 3$), along with an LOD of 0.1 mM (S/N = 3). Note that the GOx-functionalized BMAE exhibited a lower

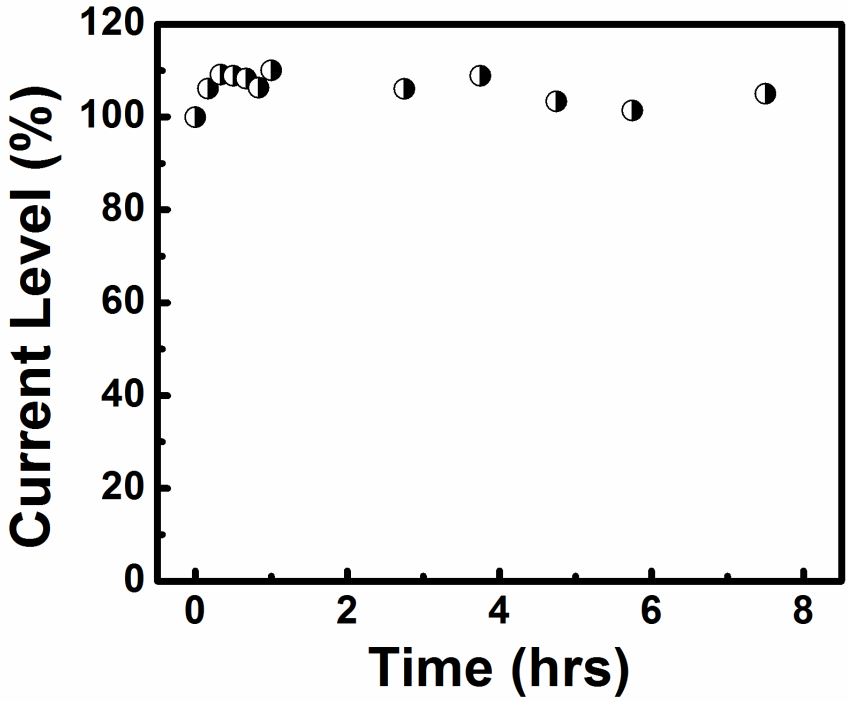

Figure 10.15: *Stability of the glutamate response over extended time periods with each data item referenced to the original current level at* t *= 0 (100%). Data was generated from chronoamperograms recorded in 0.1 M phosphate buffer (pH 7.40) with 140 μM glutamate. Conditions as in Fig. 10.13.*

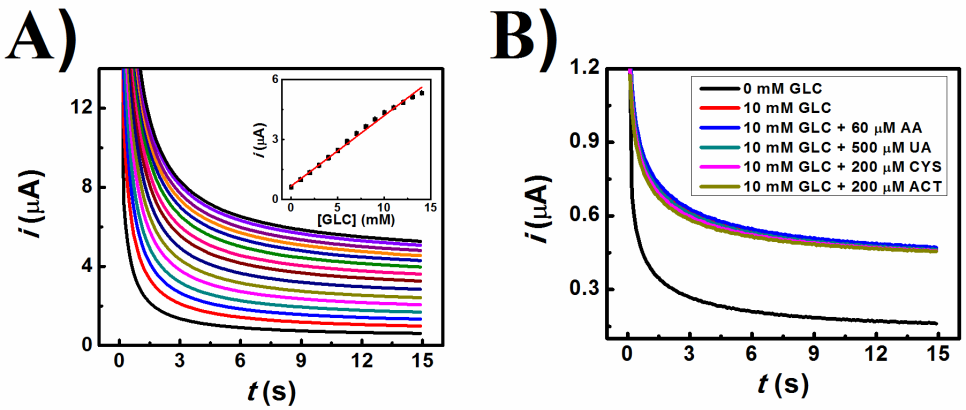

Figure 10.16: *Sensitivity (A) and selectivity (B) of the glucose microneedle biosensor. (A) Chronoamperograms for increasing concentrations of glucose from 0 mM to 14 mM in 1 mM increments. (B) Chronoamperograms recorded for the blank buffer solution, 10 mM glucose, and 10 mM glucose in the presence of the electroactive physiological interferents ascorbic acid (AA, 60 μM), uric acid (UA, 500 μM), cysteine (CYS, 200 μM), and acetaminophen (ACT, 200 μM). Conditions as in Fig. 10.13.*

sensitivity towards its substrate when compared with the GluOx-functionalized platform. This can be attributed to the dissimilar PPD growth protocol, which may affect the transport properties of the substrate and product. Accordingly, the GluOx immobilization protocol should be followed when high sensitivity is desired.

Fig. 10.16B demonstrates the high selectivity of the glucose microneedle biosensor. It illustrates the contribution imparted by the presence of potential electroactive interferents upon the current signal generated by the presence of 10 mM glucose. Physiological levels of AA, UA, CYS, and ACT resulted in negligible deviations of 1.07%, 0.88%, 1.65%, and 2.21%, respectively, from the current response for 10 mM glucose. Consequently, as with the interference study conducted with the glutamate BMAE, natural metabolic fluctuations of these compounds is not expected to interfere with the monitoring of glucose.

A stability evaluation of the GOx-functionalized BMAE was performed employing a buffer solution containing 10 mM glucose over an 8-hour period. The GOx BMAE exhibited a highly stable current response, with 97% of the original signal level extracted at the conclusion of the measurement period. Throughout

the time period under investigation, the measured current response never fell below 87% of the original level. The similar results described earlier with the GluOx-functionalized BMAE indicate that both PPD-based immobilization schemes are expected to yield a stable response over a prolonged period of continuous use.

The tandem design agglomerates the inherent advantages of solid and hollow microneedles in order to form microcavities that facilitate the electropolymeric entrapment of an enzyme, protects the enzyme layer upon epidermal penetration, and obviates the need for the extraction of biological fluids. The electrodeposition of a poly(o-phenylenediamine) thin-film for the entrapment of biorecognition elements enables the highly sensitive, selective, stable, and rapid electrochemical detection of a particular bioanalyte of interest. The high-fidelity detection of a pertinent metabolite in undiluted human serum samples over the entire pathophysiological range further substantiates the utility of the platform as a practical on-body biosensor. With further insight into the biofouling effects associated with prolonged continuous monitoring, a patch-type on-body biosensor paradigm can be realized that enables the transdermal monitoring of a number of relevant metabolites in a minimally-invasive fashion.

Portions of Chapter 10, section 1 were taken from J.R. Windmiller, N. Zhou, M.C. Chuang, G.V. Ramírez, P. Santhosh, P.R. Miller, R. Narayan, and J. Wang. Microneedle array-based carbon paste amperometric sensors and biosensors. *Analyst*, 136(9):1846–1851, 2011. The dissertation author was the primary investigator and author of this manuscript.

Portions of Chapter 10, section 2 were taken from J.R. Windmiller, G.V. Ramírez, N. Zhou, M. Zhou, P.R. Miller, C. Jin, S.M. Brozik, R. Polsky, E. Katz, R. Narayan, and J. Wang. Bicomponent microneedle array biosensor for minimally-invasive glutamate monitoring. *Electroanalysis*, 23(10):2302–2309, 2011. The dissertation author was the primary investigator and author of this manuscript.

Chapter 11

Drug delivery actuators

What you do speaks so loudly that
I cannot hear what you say.

—Ralph Waldo Emerson

Although substantial research effort has been invested in the development and optimization of the enzyme logic sensing modality, it must be realized that these systems only satisfy one of the core requirements (i.e. sensing) for an integrated feedback loop device. Granted that novel chemical and physical principles can be leveraged using the electrochemical sensing methodology to achieve particularly attractive figures of merit (i.e. sensitivity, selectivity, speed, stability, and cost), the pairing of biosensors discussed in previous chapters with drug delivery actuators would enable the autonomous treatment of a wide variety of physiological ailments. Accordingly, this synergistic combination is imperative to further development in advanced biosensor and lab-on-a-chip systems. In this manner, an integrated 'Sense-Act-Treat' feedback loop can be realized to continuously monitor the fluctuations in key biomarkers and, should a pathological state be encountered, immediately counteract the affliction in an autonomous fashion through the delivery of a targeted treatment of multiple therapeutic agents, thereby obviating the need for human intervention. Advancements in such stimuli-responsive drug delivery systems would dramatically alter the way in which disease [10] and injury [145] are currently treated.

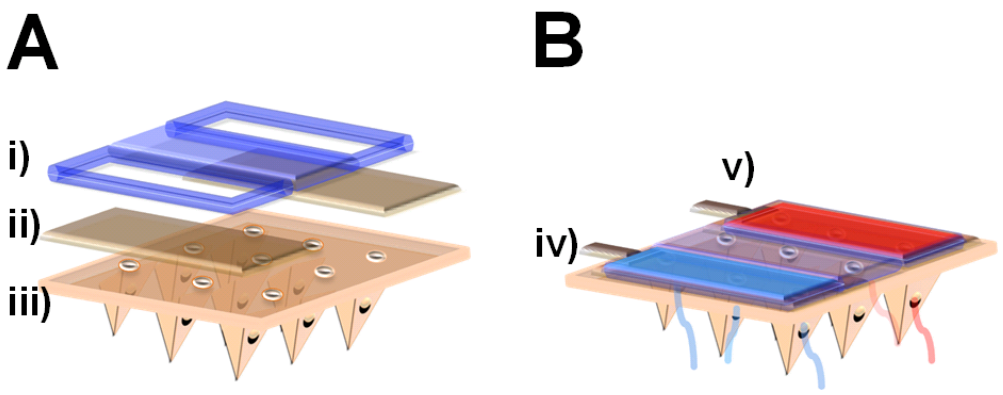

Figure 11.1: *(A) Schematic illustration of the microneedle-based multiplexed drug delivery actuator detailing the (i) hollow microneedle array, (ii) gold-sputtered polycarbonate membrane functionalized with dodecylbenzenesulfonate-doped polypyrrole (PC/Au/PPy/DBS), and (iii) polydimethylsiloxane (PDMS) reservoir. (B) Schematic illustration of the assembled dual-channel drug delivery system outlining the reservoirs for (iv) drug 1 and (v) drug 2.*

Conducting polymers such as polypyrrole (PPy), polyaniline (PANI), and poly(3,4-ethylenedioxythiophene) (PEDOT) have been identified as extremely attractive synthetic materials for utilization in controlled release systems [324, 325, 326, 327] and drug delivery actuators [328, 329, 330]. The unique properties of these materials, and PPy in particular, include their reversible mechanical behavior as "artificial muscles" [38, 331, 332], variable porosity, and ability undergo volumetric modulations in response to applied electrochemical stimuli [333, 334]. The amalgamation of these actuators with a means to deliver targeted medications in an effective and minimally invasive manner would establish the groundwork for practical body-worn devices intended for the amelioration of disease or injury in the acute phase.

Along the lines of the realization of a drug delivery contingent integrated within the biocomputing-based biosensor architecture discussed in previous chapters, a minimally invasive, electrochemically-switchable nanoactuator microneedle platform capable of delivering multiple therapeutic agents has been developed, as diagrammatically presented in Fig. 11.1. Microneedle arrays have enjoyed recent success in the transdermal biosensing [306, 335, 336] and minimally invasive drug

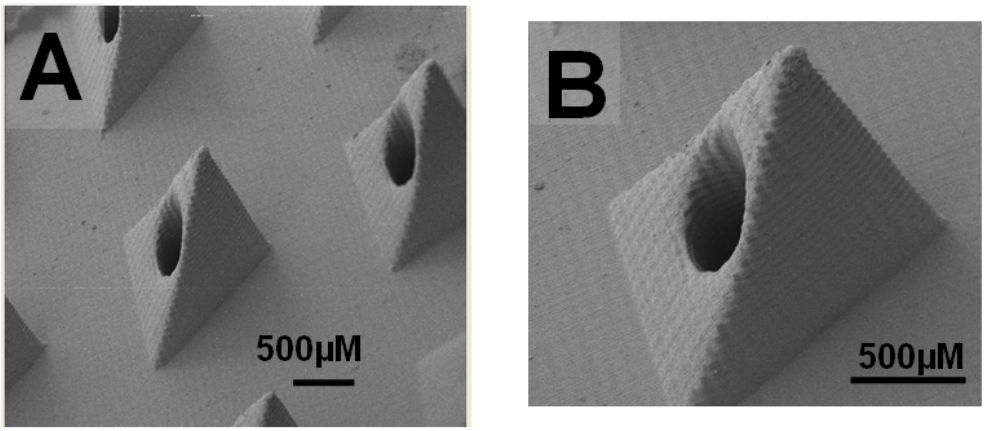

Figure 11.2: *(A) Scanning electron micrograph detailing the surface morphology of the hollow microneedle array. (B) Single needle exhibiting a well-defined cylindrical lumen.*

delivery [292, 293, 337] domains. Advantageously, these versatile microneedle platforms can be designed and fabricated to the precise specifications demanded by the application at hand [338, 339] and can assume nearly any geometry to fulfill these requirements [337, 340]. Most crucially, these devices lend themselves to body-worn patch-type embodiments that are amenable to extended durations of pain-free wear.

Whereas prior microneedle delivery devices were limited in their ability to deliver more than a single therapy [341], the new approach enables the controlled release of multiple therapeutic agents. The alternating release of model agents (various dyes) from different microneedles is clearly observed from the same miniaturized array platform; the switching accuracy and repeatability of the microneedle volumetric flow rate is also demonstrated. These experimental results are correlated with an analytical model that assesses the fluid flow characteristics through a single microneedle and subsequently can be used to assist in the design and development of future multi-section microneedle arrays for practical body-worn devices that can multiplex the delivery of various therapeutic agents on demand.

Owing to the scalability of the arrayed microneedle platform, a unique drug therapy can be released at each microneedle constituent of the array, thereby en-

abling personalized therapies. In direct contrast to conventional drug delivery microsystems, this active solid-state device does not require moving components or integrated microelectromechanical systems [342]. Thus, this simplifies device design and eliminates the need for sophisticated microfluidic-based components, which serve to complicate system architecture and increases both size and cost. Provided further insight into the biofouling effects associated with implantable devices, this minimally invasive microneedle multiplexed drug delivery paradigm is well-positioned to serve as the core component in an autonomous wearable nanopharmacy in connection to the multiplexed microneedle sensor arrays discussed in the previous chapter.

A nine-element hollow microneedle array platform was leveraged in the development of the controlled release actuator. Details regarding the fabrication of these microneedle arrays have been described in the previous chapter. Polydimethylsiloxane (PDMS) was homogenized in a 10 : 1 polymer : fixing agent ratio. The suspension was then poured into a custom mold and degassed in a vacuum desiccator. Subsequently, the PDMS suspension was cured at 110° C for 15 min. The resultant structures were exposed to UVO ozone at a gas flow rate of 3 sccm for 5 min.

The technique for the creation of the electrically-actuatable nanoporous membrane was adapted from the experimental protocol presented in [333]. Briefly, gold-sputtered PC membranes (PC/Au, pore diameter ∼600 nm, porosity ∼0.2) were attached at the periphery to a copper wire using silver conductive epoxy. A solution of 0.1 M NaDBS was purged with nitrogen for 40 min after which the pyrrole monomer was added to achieve a final concentration of 0.25 M. Subsequently, the PC/Au membrane was immersed in the solution and served as the working electrode in an electrochemical cell while 0.6 V *vs* Ag/AgCl was applied for 10 min. The application of this potential for the given amount of time resulted in optimal deposition of the polypyrrole/ dodecylbenzenesulfonate (PPy/DBS) on the PC/Au membrane, thereby minimizing the leaching of the solution through the membrane under the 'closed' state while enabling the solution to flow at appreciable rates under the 'open' state. Following electropolymerization of PPy/DBS,

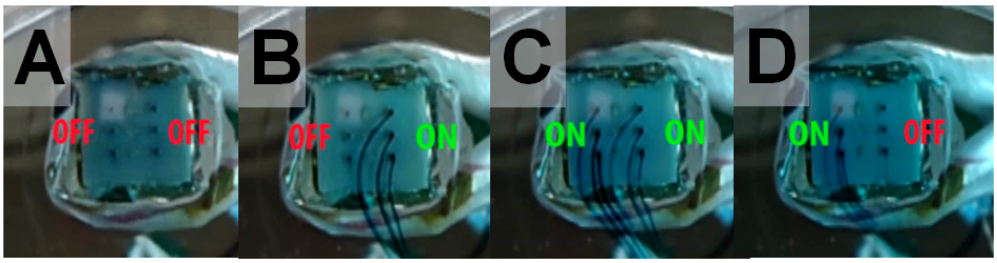

Figure 11.3: *Instigated release of methylene green (MG) from the individually addressable reservoirs: (A) reservoirs **R1** and **R2** 'OFF', (B) reservoir **R1** 'OFF', reservoir **R2** 'ON', (C) reservoirs **R1** and **R2** 'ON', (D) reservoir **R1** 'ON', reservoir **R2** 'OFF'.*

the PC/Au/PPy/DBS membranes were rinsed with deionized water and stabilized by cycling between -1.1 V and 0.5 V *vs* Ag/AgCl for ten iterations in the buffer solution. This fabrication process enabled the membrane to swell in the reduced state (-1.1 V) and contract in the oxidized state (0.5 V) in a reversible manner, the switching are similar to those established by Jeon et al. [333]. When not in use, the membranes were stored in a buffer solution at room temperature.

The PC/Au/PPy/DBS membranes were cut into slivers possessing dimensions of approximately 12 mm $\times$ 4 mm. These slivers were subsequently affixed to the reverse side of the 3 $\times$ 3 microneedle array using adhesive epoxy such that one sliver completely covered a column of three microneedles. The center column of the array was obstructed using modeling clay, enabling the formation of two individually-addressable electrically-actuatable channels. A component-level view is illustrated in Fig. 11.1A. Electrical leads were attached using silver epoxy to each of the two PC/Au/PPy/DBS membranes to facilitate ohmic contact with each actuator. The PDMS dual-channel reservoir was subsequently aligned over the membranes and affixed using adhesive epoxy. As shown in Fig. 11.1B, the reservoirs were finally loaded with $\sim$20 μL of the model chemical agent(s).

Initial experimental efforts were aimed at validating and visualizing the switching capability of the PC/Au/PPy/DBS membrane and the dual-channel operation. Both reservoirs in the assembled multiplexed drug delivery actuator, reservoir 1 (**R1**) and reservoir 2 (**R2**), were initially loaded with 12 mM of methy-

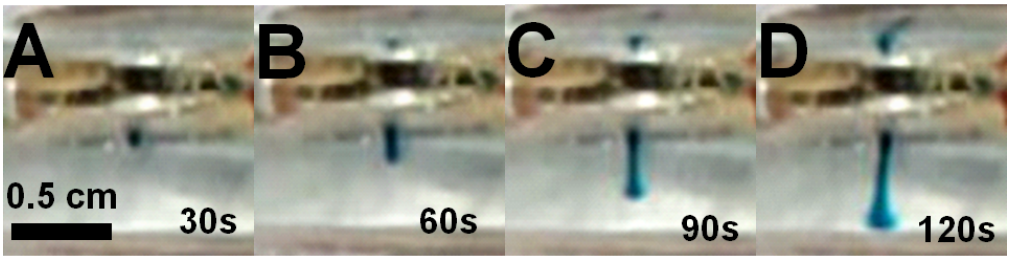

Figure 11.4: *Time-lapse still frame images of the release of methylene green (MG) from a single microneedle at distinct time intervals of (A) 30 s, (B) 60 s, (C) 90 s, and (D) 120 s.*

lene green (MG) dye and immersed in a buffer solution along with the counter and reference electrodes. Continuous agitation at a constant speed (140 rpm) was applied with a magnetic stirring bar. The DBS-doped PPy membrane entered the reduced state and engorged upon biasing with -1.1 V *vs* Ag/AgCl, thereby obstructing the flow of the solution through the porous material. Ejection of MG at either channel was not observed at this potential (represented as being in the 'OFF' state), as shown in Fig. 11.3A. Subsequently, the **R2** membrane nanoactuator was maintained at the reduced state (-1.1 V vs Ag/AgCl, 'OFF') and the membrane at **R1** was switched to the oxidized state ('ON') by applying a potential of 0.5 V *vs* Ag/AgCl. This 'ON' state caused the DBS-doped PPy membrane to become oxidized and contract, thereby facilitating the flow of the solution through the nanoporous membrane and subsequently through the microneedles. As can be observed from Fig. 11.3B, the emission of MG from **R1** is visible whereas **R2** remained closed and did not permit the release of the dye. Following this operation, **R1** was maintained at the oxidized state (0.5 V *vs* Ag/AgCl, 'ON') while **R2** was switched to the oxidized state (0.5 V *vs* Ag/AgCl, 'ON'), thus releasing MG from both reservoirs (Fig. 11.3C). Subsequently, **R1** was switched to the reduced state 'OFF' and **R2** was maintained at the oxidized state 'ON', as shown in Fig. 11.3D. This controlled and alternating release of MG from the individual reservoirs by various permutations of the applied potentials on the nanoporous membranes is clearly observed in the figure.

The execution of repeated 'ON-OFF' cycles demonstrates that the mi-

croneedle array-based actuator maintains the ability to open and close in a cyclic fashion, even following 10 iterations. Furthermore, the temporal duration (∼30 s) required to observe the release of MG at the tenth cycle was identical to that of the first cycle. The time required for complete flow shutoff was approximately 35 s following the application of the OFF potential. Based on the above results, **R1** was loaded with cresol red (CR) and **R2** was loaded with MG and all four ON/OFF permutations were applied. The controlled ejection of dye from alternating microneedle array reservoirs was clearly observed upon the application of the appropriate potential at each nanoporous membrane.

Image analysis and UV-VIS spectrophotometry techniques were utilized to analyze the drug delivery performance of the microneedle array by experimentally quantifying the flow rate of the MG dye from a single microneedle channel. Fig. 11.4 illustrates the release of MG from a single microneedle element into a quiescent buffer solution at fixed time intervals of 30 s. A potential of 0.5 V (*vs* Ag/AgCl) was applied to open the nanoporous membrane and release the dye during the experiments. Following the application of this potential for 30 s, the dye began to emerge from the microneedle aperture; a small column of dye was clearly observed at 60 s. A well-defined column of dye possessing a height of approximately 0.5 cm was observed after 120 s. Afterwards, the estimated experimental flow rate of the released dye was calculated via measurement of the column height with image processing software (i.e., ImageJ) in conjunction with the flow rate equation:

$$Q = \frac{\pi d^2 h}{4\,(t - t_0)} \tag{11.1}$$

where d is the microneedle channel diameter and h is the column height associated with a particular point at time t. Accordingly, the experimental flow rate of the dye released from the microneedle aperture was determined to be 6.3 ± 0.4 μL/h (n = 10) through analysis of multiple time-lapse still-frame images (Fig. 11.4).

In an effort to validate the flow rate obtained via image analysis, UV-VIS spectrophotometry was employed to quantify the amount of dye released and subse-

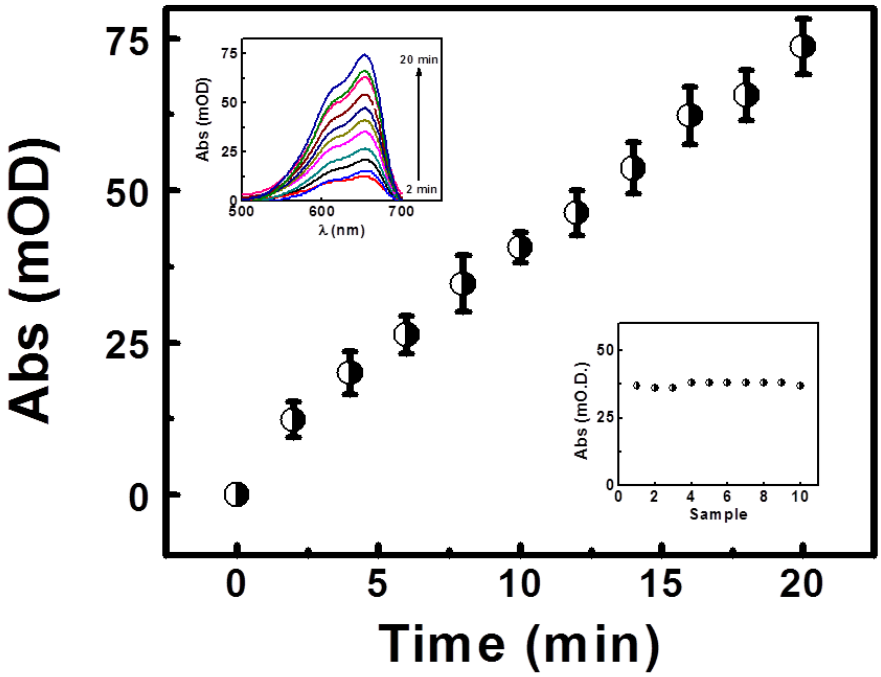

Figure 11.5: *UV-VIS spectrum illustrating the absorbance profile generated by the release of methylene green (MG) from a single microneedle at a 2 min release interval over a 20 min duration. The upper inset displays the corresponding UV-VIS spectra and the lower inset displays the absorbance of 10 distinct experiments at a single release time.*

quently assess the microneedle flow rate and repeatability. The absorbance spectra for the MG released from a single microneedle element was recorded sequentially, every 2 min, as shown in Fig. 11.5. The inset in Fig. 11.5 (bottom right) substantiates the reproducibility of the MG release from the drug-delivery nanoactuator over the same release time. The maximum deviation among these ten repetitions was 5.5 % from the original absorbance, which was measured at the maximum wavelength. Linear regression analysis was performed on the absorbance vs time plot, yielding a slope of 3.5 mO.D.$\cdot$min^{-1} with a high coefficient of determination ($R^2 = 0.993$) and low relative standard deviation (RSD = 2.74 %, $n = 3$); this result indicated a constant release of dye from the microneedle. From these experiments, the fluid flow rate was calculated to be 5.5 $\pm$ 0.2 μL/h, which is in good agreement with the image analysis data collected from the time-lapse video still-frames. The fabricated membranes were highly reproducible; interpolated flow rates deviated by less than 10 % under identical electropolymerization conditions.

Following the optical characterization of the microneedle array-based actuator, the platform was migrated to an automated system capable of generating arbitrary release profiles at the two reservoirs. As illustrated in Fig. 11.6, a PC loaded with MATLAB (MathWorks, Inc., Natick, MA) was implemented to control the instrumentation via a National Instruments (Austin, TX) USB DAQ-to-GPIB interface. Three Agilent (Santa Rosa, CA) E3645A DC power supplies were employed in the evaluation; two power supplies controlled the discharge of the model electroactive agents (one power supply per reservoir) while one power supply was dedicated to driving a variable-speed electric motor implemented to agitate the solution following the release of the electroactive agent(s). A conventional 3-electrode electrochemical contingent (glassy carbon working electrode, platinum counter electrode, and Ag/AgCl reference electrode) was employed in conjunction with a PC-interfaceable Metrohm (Herisau, CH) Autolab M101 potentiostat to monitor the release profile of the electroactive agent(s). Images of the setup are displayed in Fig. 11.7A and B.

Electrochemical characterization of the microneedle actuator commenced with the creation of user-defined waveforms (via MATLAB), which were employed

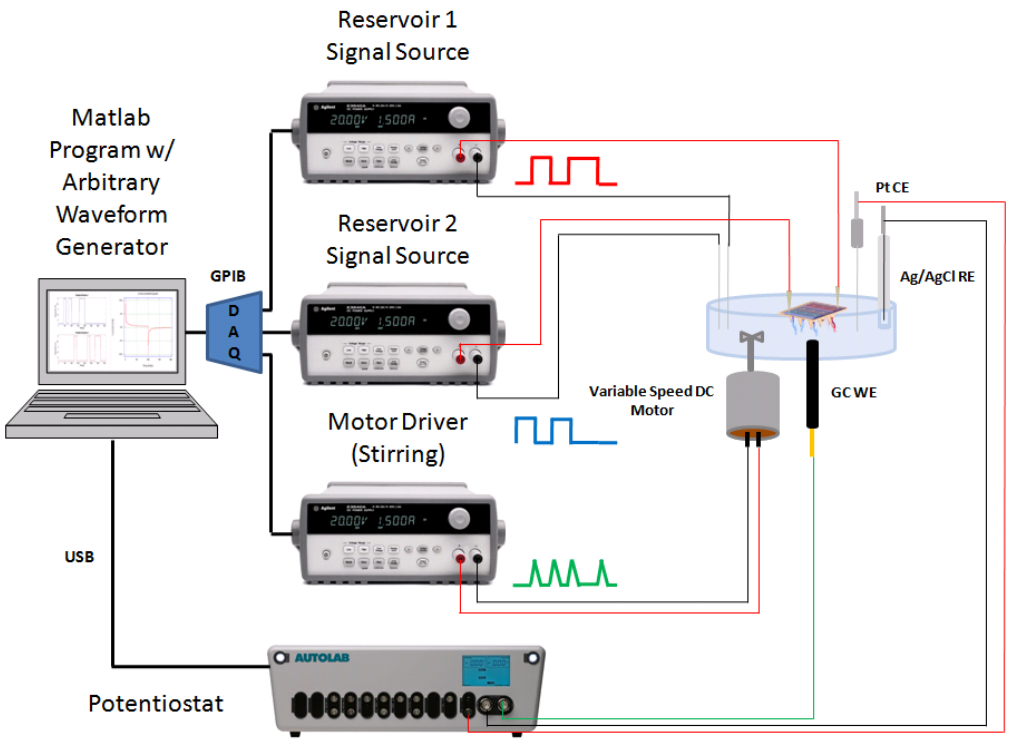

Figure 11.6: *Schematic diagram delineating the process flow associated with the electrochemical evaluation of the multiplexed microneedle array actuator. User-defined arbitrary waveforms are transferred to the power supplies via a GPIB DAQ to control the release of the model electroactive compounds from the reservoirs in addition to actuating the agitator. A potentiostat is used in conjunction with a 3-electrode electrochemical contingent to monitor the release of the electroactive agent(s).*

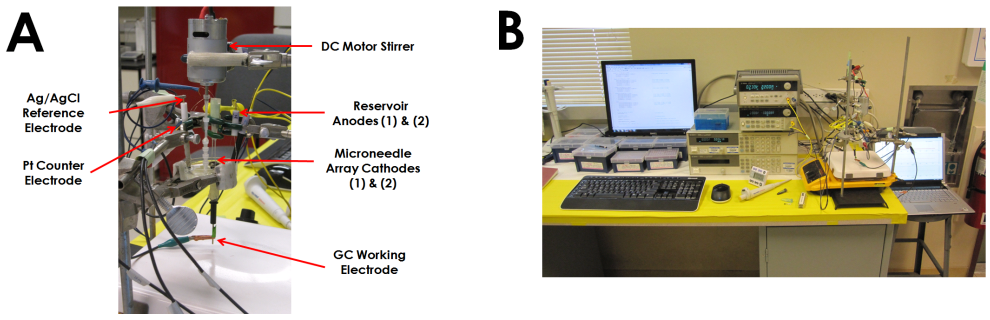

Figure 11.7: *(A) Close-up image of the setup employed to conduct the electrochemical evaluation of the microneedle array actuator with core components labeled. (B) Image of the setup workbench illustrating the extent of the test and measurement equipment involved.*

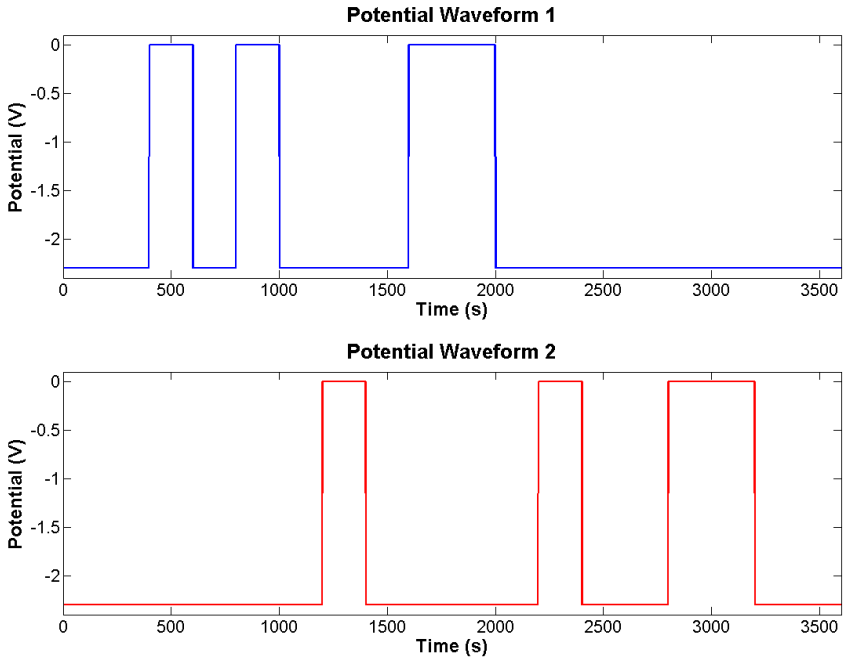

Figure 11.8: *User-defined waveforms employed to control the temporal release profile of the electroactive species present in two distinct reservoirs within the microneedle array actuator. Waveforms are employed to cycle between the 'OFF' and 'ON' states of the actuator via the application of the corresponding redox potentials.*

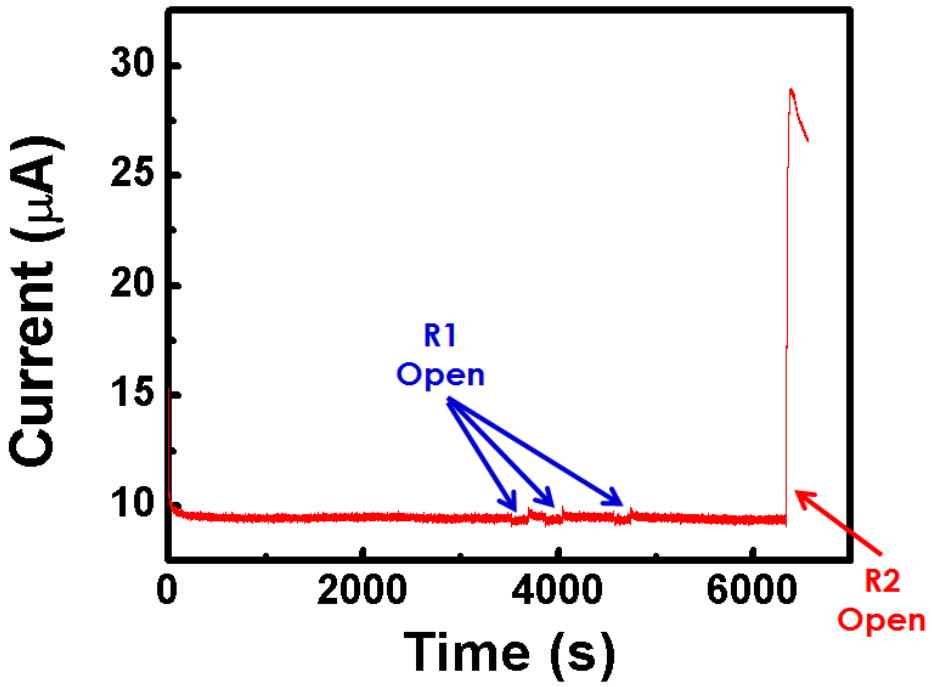

Figure 11.9: *Electrochemical response generated by the microneedle array actuator to a user-defined waveform.* ***R1*** *is loaded with a 0.1 M potassium phosphate buffer solution, whereas* ***R2*** *contains 1.0 M ascorbic acid dissolved in the buffer solution* (E_{APP} *= 0.6 V* vs *Ag/AgCl).*

to establish the output redox potential generated by the power supplies, thus regulating the temporal release profile of the electroactive species present in two distinct reservoirs within the microneedle array actuator. Exemplary waveforms are illustrated in Fig. 11.8. Agitation was employed for 5 s following each release routine to simulate batch injection and the corresponding electrochemical response was continously monitored with a potentiostat. The electrochemical oxidation profile recorded in response to a user-defined waveform is displayed in Fig. 11.9 (E_{APP} = 0.6 V *vs* Ag/AgCl). As is evident from the figure, a solution devoid of electroactive species is housed in **R1** (potassium phosphate buffer), whereas **R2** contains an oxidizable agent (1.0 M ascorbic acid).

The understanding of the fluid flow characteristics of the microneedle array

is crucial for delivering the precise amount of drug to subcutaneous tissue during transdermal drug delivery. To augment this understanding and to analytically estimate the drug delivery capability, the fluid flow characteristics of a single microneedle was modeled beginning from first principles. Given that the first law of thermodynamics is proxied by the following expression of the conservation of energy:

$$\dot{Q} - \dot{W} = \frac{\mathrm{d}E}{\mathrm{d}t} \mid_{System} \tag{11.2}$$

where $\dot{Q}$ represents the external force applied to the system, $\dot{W}$ represents the work performed by the system, and E represents the time-dependent energy state of the system, the external force applied to a fluidic system can accordingly be evaluated,

$$\dot{Q} = \oint \left(u + Pv + \frac{V^2}{2} + gz \right) \rho \vec{V} \cdot d\vec{A}. \tag{11.3}$$

The above relation assumes incompressible flow (i.e. the solution density, ρ, is constant), a fixed control volume v, uniform internal energy (E) and pressure (P) across all sections, and that mechanical energy is not released. In the relation, u represents the potential energy stored in the system, V represents the flow velocity, g is the acceleration due to gravity, z is the microchannel length, and A is the cross-sectional microchannel area. Further assuming that the internal energy remains constant in the system and a uniform fluid flow rate across all sections, Eq. (11.3) can be recast into the modified *Bernoulli equation*,

$$\frac{P_1}{\rho g} + \frac{V_1^2}{2g} + z_1 = \left(\frac{P_2}{\rho g} + \frac{V_2^2}{2g} + z_2 \right) + \frac{V_2^2}{2g} \left(\sum_{i=1}^{n} f \frac{L}{D} + \sum_{j=1}^{m} K \right) \tag{11.4}$$

where where P_1 and P_2 are the atmospheric and microneedle outlet pressures, respectively, V_1 and V_2 represent the average fluid velocities within the reservoir and microchannel, respectively, z_1 and z_2 represent the spatial extents of the reservoir and microneedle outlet, respectively, f is the friction factor, L is the channel or pore length, and D is the hydraulic diameter [343, 344], as diagrammatically represented in Fig. 11.10A and B. The second term in Eq. (11.4) refers

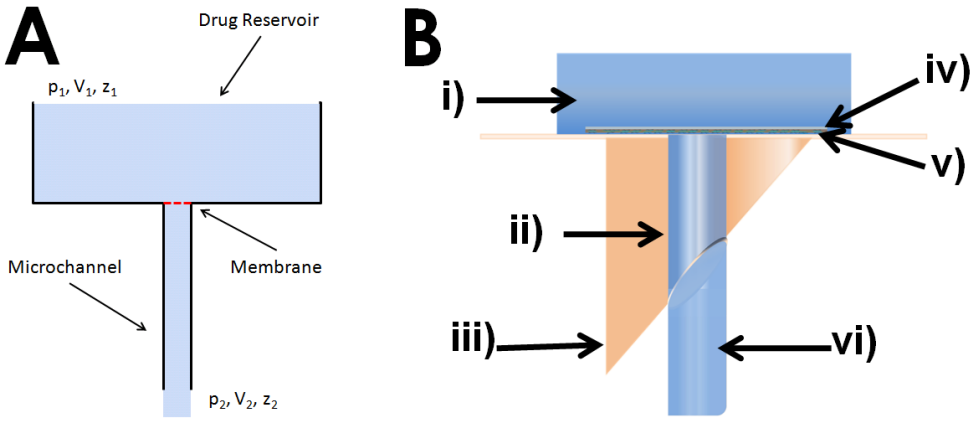

Figure 11.10: *(A) Schematic representation of a single microneedle element for modeling considerations. (B) Schematic of a single microneedle during drug delivery. Microneedle components include the following: (i) reservoir, (ii) lumen, (iii) hollow microneedle, (iv) Au/PPy/DBS nanoporous membrane, (v) PC membrane, and (vi) the released agent.*

to the friction losses through the actuating nanopores, polycarbonate membrane, and microneedle channel as shown in expanded form,

$$\sum_{i=1}^{n} f\frac{L}{D} = f_{pores}\frac{L_{pores}}{D}\frac{\tau_{pores}}{\varepsilon_{pores}} + f_{membrane}\frac{L_{membrane}}{D}\frac{\tau_{membrane}}{\varepsilon_{membrane}} + f_{microneedle}\frac{L_{microneedle}}{D} \tag{11.5}$$

where τ and ε represent the tortuosity and porosity of the nanopores and polycarbonate membranes, respectively [333] and D is the diameter of a single microchannel (342 μm). The porosity of the PC membrane is 0.2 (see previous discussion) and the porosity of the actuating nanopores is 0.4 due to the pore narrowing created by the Au/PPy/DBS functionalization. An approximate tortuosity value of 1.5 was assigned to the PC membrane and the actuating nanopores to account for the increased channel curvature created by the nanopores. The respective friction factors were calculated according to Stokes flow theory for water flow in microchannels [345, 346, 347], where the product of the friction factor and Reynolds number ($f\mathrm{Re} = 64$) utilized for macroscale laminar flow in circular channels is employed [348]. The friction factors for each flow section can be obtained by the Reynolds numbers obtained for fluid flow in each of the 3 flow sections of

Table 11.1: *Dimensions and flow characteristics of a single microneedle channel.*

Flow section	Length (μm)	Total cross-sectional area	Re
Microneedle channel	1366	A_c	6E-3
Polycarbonate membrane	7	$0.2A_c$	5E-5
Nanoporous membrane	0.75	$0.4A_c$	9E-5

the microneedle channel Tab. 11.1.

The values presented in Tab. 11.1 are calculated according to the following considerations. A_c is the cross sectional area of the microneedle $[\pi(D_{microneedle})^2/4]$. The Reynolds number ($Re = \rho VD/\mu$) was calculated using the density ($\rho = 1000$ kg/m^3) and viscosity ($\mu = 1.000$ N·s/m^2) of water at room temperature [349]. The velocity used to estimate the Reynolds number for fluid exiting the microneedle channel was determined *a priori* by averaging the experimental velocities obtained by image analysis and UV-VIS spectrophotometry. Furthermore, the *a priori* velocities within the polycarbonate membrane and the nanoporous membrane were obtained by utilizing the conservation of mass principle for incompressible fluids ($V_1A_1 = V_2A_2$) in conjunction with the average experimental velocity to calculate the corresponding Reynolds number, while the theoretical model velocity was multiplied by a factor of 0.7 to account for a 30 % widening of the fluid flow stream after exiting the microneedle, thus matching the flow stream characteristics used in the image analysis experiment (refer to Fig. 11.4).

The last term (ΣK) in Eq. (11.4) represents the sum of minor losses due to the inlet, exit, and hydrodynamic development length, which is shown in expanded form below:

$$\sum_{j=1}^{m} K = K_{inlet} + K_{outlet} \tag{11.6}$$

where K_{inlet} and K_{outlet} are loss coefficient factors for a square edge inlet (0.5) and for an exit (1) typically associated with hollow microneedles [343, 344].

Finally, an expression for the theoretical flow rate of the fluid exiting the microneedle channel can be formed by assuming quiescent flow at the top of the reservoirs ($V_1 = 0$), and negligible pressure gradients throughout the flow network

Table 11.2: *Comparison of the theoretical and empirical microneedle actuator flow rates.*

	Flow rate (Q_2) (μL/h)
Theoretical model	6.4
Image analysis	6.3 ± 0.4
UV-VIS spectrophotometry	5.5 ± 0.2

($\Delta P = P_1$ - $P_2 = 0$).

$$Q_2 = A_c \sqrt{\frac{2g\,(z_1 - z_2)}{\sum_{i=1}^{n} f\frac{L}{D} + \sum_{j=1}^{m} K}} \tag{11.7}$$

The theoretical flow rate calculated by Eq. (11.7) and the experimental flow rates obtained through image analysis and UV-VIS spectrophotometry are in good agreement, validating the veracity of the microneedle fluid flow model presented herein (Tab. 11.2).

The ability to transdermally release multiple therapeutic agents is of profound importance for the autonomous treatment of a metabolic syndrome (a combination of hypertriglyceridemia, hypertension, and insulin-dependent diabetes mellitus), human immunodeficiency virus, or other chronic medical conditions. In this study, a self-contained multiplexed drug delivery system has been presented that utilizes arrays of microneedles coupled with conducting polymer nanoactuators for the controlled release of fluidic agents. The ability of PPy/DBS to undergo volumetric changes with applied electrical potentials permits the release of fluid in a controlled and switchable fashion without the need for moving parts or integrated microelectromechanical systems. These nanopore-actuated microneedle arrays are well suited for integration into wearable drug delivery devices, in which cost and power constraints must be minimized.

In an effort to elucidate the drug delivery capacity of the microneedle array, the fluid flow characteristics were analyzed both experimentally and analytically. Image analysis software and UV-VIS spectrophotometry were used to empirically determine the flow rate of the fluid exiting the microneedle channel while the modified Bernoulli equation was employed to analytically determine the flow rate. The resultant flow rates obtained through image analysis (6.3 ± 0.4 μL/h), UV-VIS

spectrophotometry (5.5 ± 0.2 μL/h), and analytical modeling (6.4 μL/h) were in good agreement, hence validating the accuracy of the model. Furthermore, the low standard deviation obtained from the experimental flow rate measurements is indicative of the high repeatability of the volumetric flow rate exiting the microneedle channel. The juxtaposition of theoretical modeling and empirical results provides much-needed insight into the transport of fluids through distinct multi-diameter flow sections of microneedle arrays. Thus, this experimentally-corroborated analytical model provides a foundational backbone for subsequent microneedle designs in which the results can be used to predict fluid flow characteristics in microneedle configurations yet to be experimentally evaluated. The detailed understanding of the fluid flow characteristics as well as the repeatable, precise release of fluid is of critical importance for applications within the drug delivery domain.

When compared with conventional drug delivery systems, the presented methodology obviates the need for sophisticated microfluidic and/or microelectromechanical systems such as micropumps in order to actuate the delivery of the target therapeutic agent. As is evident, flow rates are somewhat lower using this 'passive' approach, however the proposed technology embodies unique advantages including minimized overall system complexity, substantially increased robustness due to its purely solid-state nature, and the ability to be sustained by a given power source for extended periods of use. Although the approach possesses these noteworthy advantages, a limitation of the approach must be considered: the relative difficulty encountered in actuating the release of highly viscous fluid formulations from the microneedle array device. Thus, in future work, the construction of this drug delivery system, including the individual microneedle diameters, should be adjusted and optimized to assure the appropriate flux rate through the membrane nanopores for fluids of varying viscosities and molecular weights.

The presented nanoporous membrane-actuated microneedle array establishes the foundation for practical body-worn devices that can deliver different therapeutic agents in an 'on-demand' manner. The microneedle array embodies the potential to deliver multiple drugs with higher precision and temporal resolution than conventional macroneedle delivery techniques offer while reducing the

pain, patient anxiety, and risk of infection commonly associated with conventional drug delivery platforms. Moreover, the new multiple-drug delivery microsystem can be integrated with a microneedle sensor array, hence coupling multiplexed analyte detection with a means to deliver a concomitant therapeutic intervention. Such a closed-loop sensing / drug delivery microneedle paradigm is well-positioned to precisely deliver multiple therapeutic agents in an on-demand basis. The manifestation of autonomous 'Sense-Act-Treat' systems may not only provide an avenue for the rapid response to biomarker fluctuations with a targeted therapy, but may also herald the development of self-regulating drug delivery microdevices that are able to modulate dosage based on the severity of the injury or extent of the illness / disease. The development of such responsive multiplexed drug-delivery systems is expected to dramatically transform outpatient, home-based civilian medical treatments as well as military medical care.

Portions of Chapter 11 were taken from G.V. Ramírez*, J.R. Windmiller*, J.C. Claussen*, A.G. Martinez, F. Kuralay, M. Zhou, P.R. Miller, N. Zhou, R. Polsky, R. Narayan, and J. Wang. Multiplexed and switchable release of distinct fluids from microneedle platforms via conducting polymer nanoactuators for potential drug delivery. *Sensors and Actuators B*, 161(1):1018–1024, 2012. The dissertation author was the co-primary investigator and author of this manuscript.

Chapter 12

Closed-loop systems

Insanity: doing the same thing over and over again and expecting different results.

—Albert Einstein

The integration of the logic-based biosensing paradigm with novel drug delivery devices for the development of reactive systems capable of autonomous therapeutic intervention would be of substantial utility in scenarios where immediate access to a caregiver is not feasible. Advanced incarnations of both components have been demonstrated throughout the course of this research program and described in detail in this thesis. However, the realization of a closed-loop 'Sense-Act-Treat' system remains the proverbial 'holy grail' in the medical devices community. Along these lines, efforts have been directed towards the integration of these two concepts (biosensing and drug delivery) in an autonomous platform and are delineated in the following sections.

12.1 Self-powered 'Sense-Act-Treat' systems employing enzyme logic gates

Enzymatic biofuel cells (BFCs) have attracted considerable recent interest owing to their ability to provide sustainable energy from renewable fuel sources under mild conditions [350, 351]. The ability to engineer these devices to process vari-

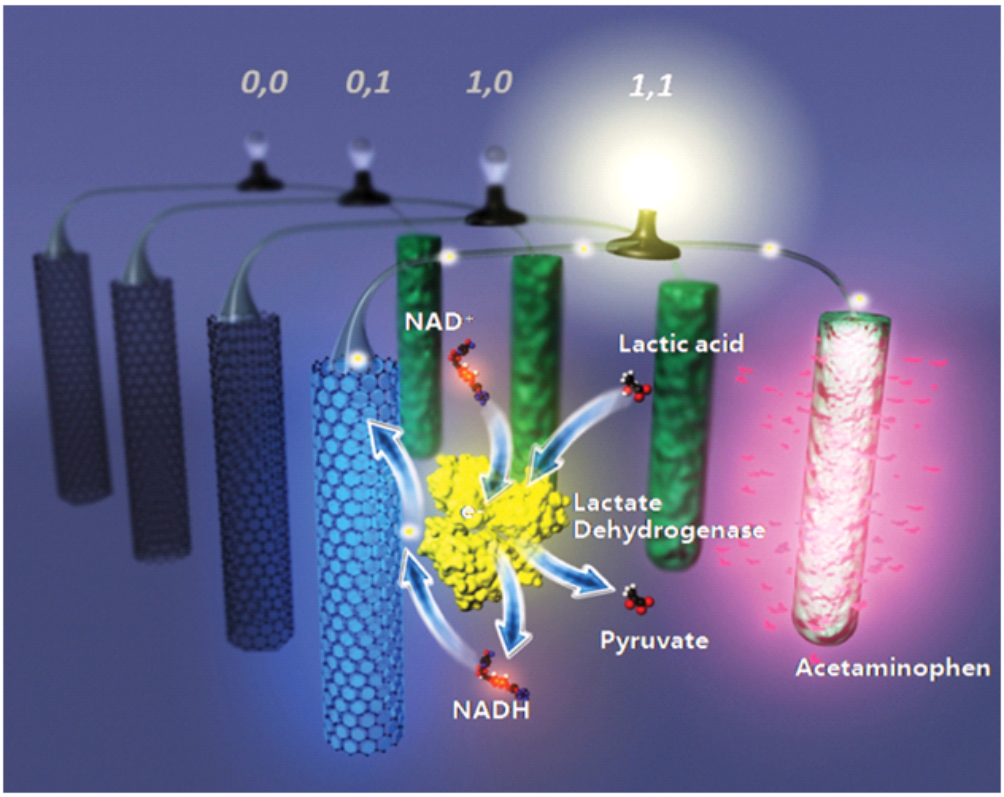

Figure 12.1: *Illustration of the self-powered, biocomputing, logic-controlled 'Sense-Act-Treat' system based on a BFC. Lactate (LAC) and lactate dehydrogenase (LDH) are used as diagnostic biomarker inputs for the* ***AND*** *logic operation in connection with the abdominal trauma (ABT) model injury. Acetaminophen (ACT) is used as the model therapeutic agent. In the presence of both inputs (*(**1**,**1**) *state), the BFC is switched* ***ON****, hence activating the release of the drug.*

ous 'renewable' biochemical species holds considerable promise for the utilization of BFCs as implantable power sources for biomedical devices [350, 351, 352, 353, 354]. In addition to major research thrusts that have focused on extended operational stability, improved power efficiency, and device miniaturization [350, 351, 352, 353, 354, 355], recent activity has been devoted to the development of BFC-based logic biosensors with potential applications in the self-powered, biocomputing diagnostics domain [356, 357, 358, 359, 360]. In accordance with the principles of Boolean logic, such self-regulating, self-powered, implantable devices could be able to extract and process analytes that reside in complex media [47, 108, 178].

A self-powered, logic-controlled, integrated 'Sense-Act-Treat' system based

on a BFC has been developed to address demands for autonomous biomedical devices. Controlled drug-release technologies leverage the ability to deliver targeted therapies on demand and thus have advantages over conventional methods, which include more rapid intervention capabilities and greater dosage efficacy [324, 361]. The BFC-based system that has been developed in this study offers simultaneous biocomputing diagnostic operation and controlled drug-release functionality without the need for external power sources. The use of a biocomputing-based detection method to trigger the release of a drug through the logic-based control of the BFC's power output has not been reported to date. In stark contrast to conventional biosensors or controlled release systems, the BFC-based biocomputing system is able to autonomously correlate the relationship between different biomedically-relevant markers according to 'programmed' Boolean logic operations, and to regulate the release of a drug to counteract the onset of abnormal physiological states. The simultaneous, self-powered diagnostic operation and the controlled release functionality are accomplished through a logic-induced change in the electrocatalytic activity at the anode, which triggers the release of a model therapeutic agent from the drug-loaded cathode. This logic-activated drug-release system could serve as the core component of an autonomous system for medical diagnoses and intelligent drug delivery that circumvents the need for any external power sources, control electronics, or microelectromechanical actuators.

Fig. 12.1 shows the configuration of the 'Sense-Act-Treat' system. The system consists of an enzyme-based logic-controlled anode and a drug-containing cathode that is functionalized with a conducting polymer (CP). Under 'normal' scenarios, the BFC is **OFF** and the drug remains embedded (doped) within the CP-modified cathode. Conversely, in the 'abnormal' state, the Boolean logic anode will switch the BFC to the **ON** state, which results in the release (undoping) of the therapeutic agent from the cathode, in conjunction with a substantial increase in the power output (as well as the corresponding open-circuit potential, OCP). In this manner, the digitally-processed information yields a final **ON** / **OFF** output, thereby enabling the direct coupling of the logic detection method with the drug-release contingent and completes the integrated 'Sense-Act-Treat' system.

To demonstrate the concept of self-powered, logic-activated therapeutic intervention, the following were assembled: An enzyme-based, logic-controlled anode (glassy carbon electrode modified with carbon nanotubes / Meldola's blue (CNT-MB/GC electrode)) and a drug-loaded, CP-modified cathode ((poly(3,4-ethylenedioxythiophene)-acetaminophen (PEDOT-ACT) functionalized gold electrode) operated in a potassium phosphate buffer solution (PBS; 0.1 M, pH 7.4) containing nicotinamide adenine dinucleotide (NAD^+) as a cofactor (20 mM).

In order to prepare the anode, a CNT-dimethylformamide (DMF) suspension was prepared by agitating 10 mg of CNTs in 1 mL DMF. The mixture was subsequently sonicated for 30 min. Subsequently, 1 μL of the CNT-DMF suspension was cast on the GC electrode and the solvent was allowed to evaporate for 15 min at 35° C. The CNT/GC electrode was then immersed in a 0.5 mg mL^{-1} MB solution for 30 min. As a final preparatory step, the CNT-MB/GC electrode was rinsed with deionized water, desiccated with a nitrogen stream, and employed as the anode component of the BFC.

For the electropolymerization routine, an Au working electrode was immersed in a solution containing 0.1 M 3,4-ethylenedioxythiophene (EDOT), 2.5 mg mL^{-1} ACT, and 0.1 M $LiClO_4$. The electropolymerization of EDOT was performed at a constant potential of 1.2 V *vs* Ag/AgCl for 900 s, thereby leading to the formation of PEDOT films incorporating ACT on the electrode surface. Following a 120 min immersion of the electrode in PBS (pH 7.4), the PEDOT-ACT/Au electrode was gently rinsed with deionized water and desiccated with nitrogen, thereby forming the cathode element of the BFC. For comparison, a PEDOT/Au electrode was also prepared. The Au electrode was firstly immersed in an aqueous solution containing 0.1 M EDOT and 0.1 M $LiClO_4$. Following this routine, the electropolymerization of EDOT was executed at a constant potential of 1.2 V *vs* Ag/AgCl for 900 s, forming a PEDOT film on the electrode surface. Following a 120 min immersion of the electrode in PBS (pH 7.4) and subsequent rinsing, the PEDOT/Au electrode was desiccated with a nitrogen stream.

Abdominal trauma (ABT) was selected as the model injury, along with the corresponding lactate (LAC) and lactate dehydrogenase (LDH, E.C. 1.1.1.27)

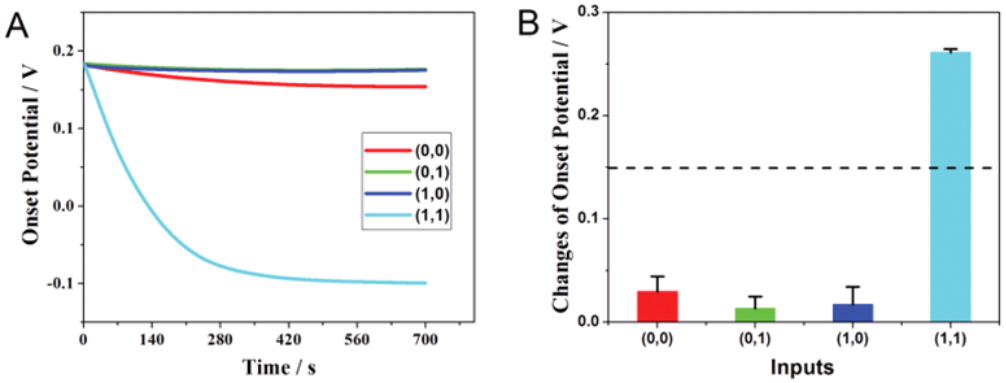

Figure 12.2: *(A) Temporal response of the open-circuit potential (OCP) at the anode after the application of different input signals: a = (**0**,**0**), b = (**0**,**1**), c = (**1**,**0**), and d = (**1**,**1**). (B) Bar diagrams comparing the OCP measured at the anode for the different combinations of the input signals, derived from A. The dashed line is established at the threshold (0.15 V). Input A, LAC (20 mM); input B, LDH (10 U mL^{-1}). The respective combinations of the inputs LAC and LDH, as well as the NAD^{+} cofactor (20 mM), were agitated and the reaction transpired for 30 min before measurements were recorded.*

biomarker inputs, as well as the **AND** logic implementation [128, 129]. The **AND** logic is represented by the situation where the gate output is activated only when both biomarker inputs are present [362]. The absence of LAC (input A) and LDH (input B) is considered as the logic input **0**, whereas LAC (20 mM) and LDH (10 U mL^{-1}) are defined as logic input **1**. Thus, these inputs provide a logic-based diagnosis of ABT. ACT, which is frequently used to control pain in abdominal injury, was selected as the model therapeutic agent [363].

The input combinations ((LAC,LDH) = (**0**,**0**), (**0**,**1**), (**1**,**0**), and (**1**,**1**)) were first mixed in the base electrolyte solution (0.1 M PBS, pH 7.4 containing 20 mM NAD^{+}) for 30 min at 37° C under quiescent conditions. Subsequently, the bioanode and CP-functionalized cathode were immersed in 1 mL of the above mixture and the galvanic reaction was allowed to ensue for 60 min. Following this procedure, the mixture (now containing the products of the biocatalytic and galvanic reactions) was transferred to a separate electrochemical cell in order to quantify the amount of ACT released.

Fig. 12.2A exhibits the temporal response of the OCP at the anode after

the application of different combinations of the biomarker inputs. In the absence of either or both of the inputs ((LAC,LDH) = (**0**,**0**), (**0**,**1**), and (**1**,**0**)), that is, 'normal' or otherwise anomalous states, the enzymatic reaction did not ensue and reduced nicotinamide adenine dinucleotide, NADH, was not produced. As a result, no appreciable alteration in the NADH oxidation OCP was detected, that is, the BFC remained in the **OFF** state. However, in 'abnormal' scenarios in which LAC and LDH were both present (input (**1**,**1**)), the LDH-catalyzed enzymatic reaction of NAD^+ and LAC proceeded, which resulted in the formation of NADH and pyruvate; accordingly, the OCP for the oxidation of NADH substantially decreased from 0.18 V to -0.10 V (input (**1**,**1**) in Fig. 12.2, **ON** state). As illustrated below, the large swing in the OCP leads to the concomitant release of the drug from the cathode upon assembling the complete BFC. The corresponding bar diagrams (Fig. 12.2B) illustrate that only the (**1**,**1**) input combination resulted in the **ON** output state upon the application of the four logic combinations. Therefore, the features of the anode correspond to the equivalent functional operation of an **AND** logic gate that is able to perform the Boolean logic operation of A•B [362]. Owing to the high dynamic range that is associated with the **AND** logic gate, such operation thus facilitates the straightforward discrimination between the **OFF** and **ON** output signals, as the OCP threshold of 0.15 V provides a clear discriminator to separate 'normal' and 'abnormal' conditions.

Subsequently, the self-powered, logic-based diagnostic paradigm was paired with a logic-activated drug-release system comprised of a cathode modified with PEDOT-ACT. CPs have been widely used in controlled drug-release devices because of their unique redox, doping / undoping, and meso- / nano-porous properties [324, 361]. The release of drug dopants that are entrapped within polymer hosts has been widely reported; the process is instigated by the application of a negative potential that serves to reduce, and thereby undope, the CP matrix host [324, 361]. Data from control experiments suggest that only the application of a suitable redox potential of 0.0 V causes the PEDOT-ACT electrode to release the model drug. Furthermore, the OCP at the PEDOT-ACT cathode, which corresponds to the reduction of PEDOT (for all input combinations) is higher than that at the

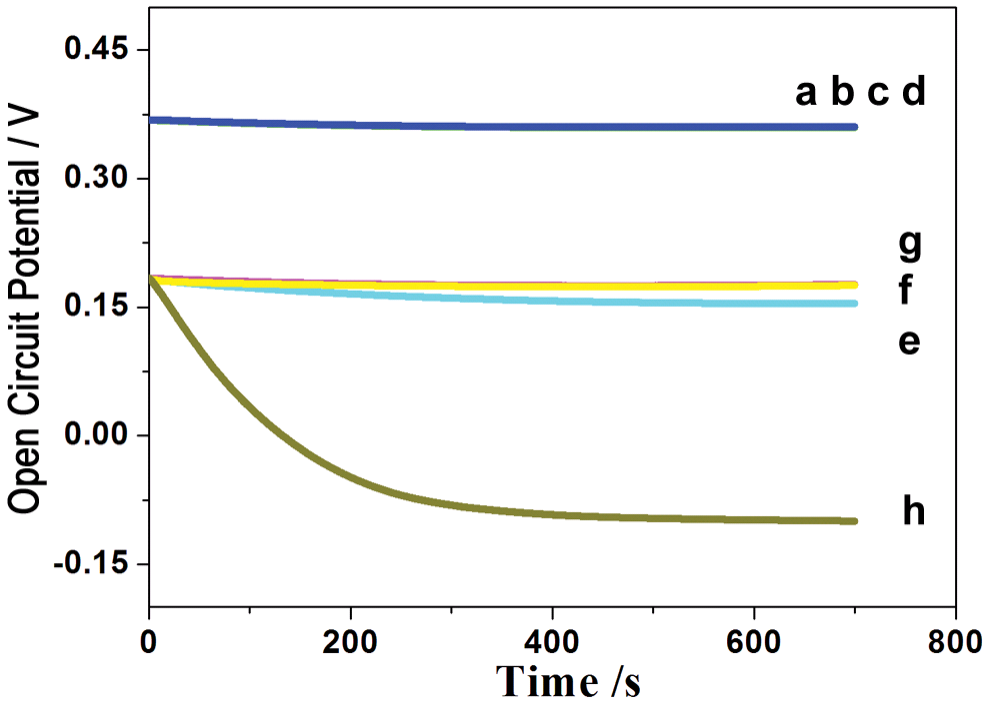

Figure 12.3: *Temporal dependence of the cathode OCP upon application of different input signals* (***0***,***0***) (a), (***0***,***1***) (b), (***1***,***0***) (c), and (***1***,***1***) (d). *Also shown is the temporal dependence of the OCP at the anode following application of the input signals* (***0***,***0***) (e), (***0***,***1***) (f), (***1***,***0***) (g), and (***1***,***1***) (h).

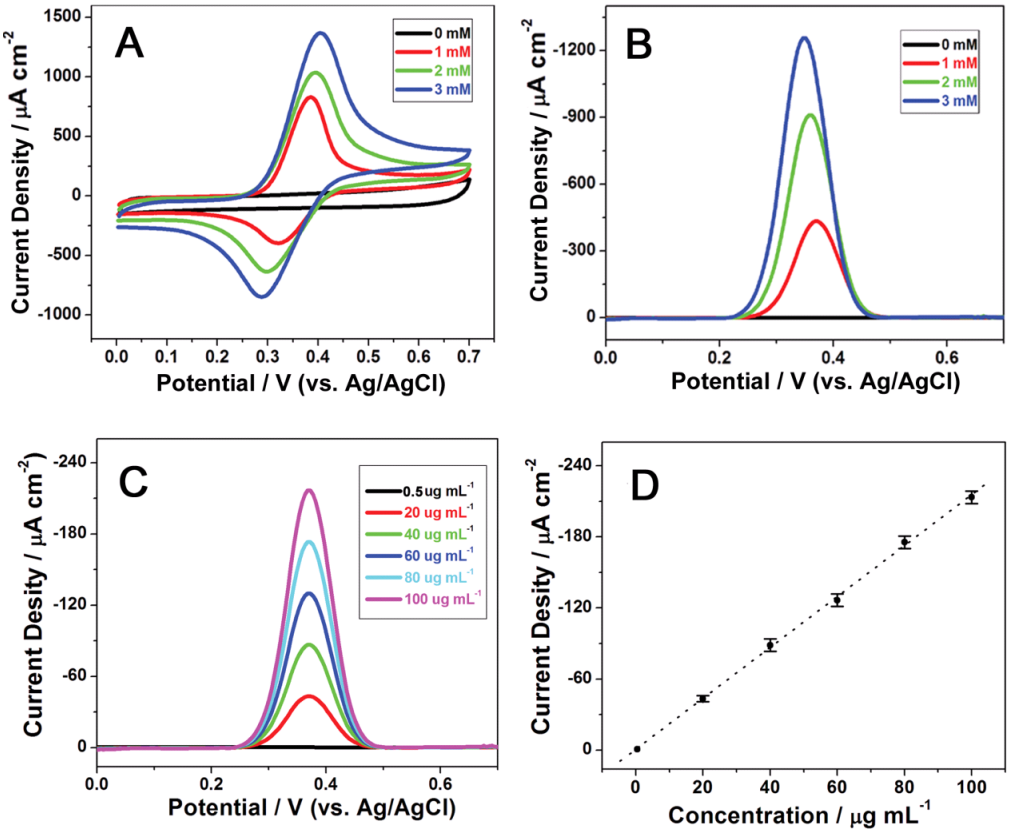

Figure 12.4: *(A) Cyclic voltammograms (CVs) at a carbon nanotube-functionalized glassy carbon (CNT/GC) electrode for 0, 1, 2, and 3 mM ACT. Scan rate: 0.1 V* s^{-1}*. (B) Differential pulse voltammograms (DPVs) at the CNT/GC electrode for 0, 1, 2, and 3 mM ACT. (C) DPVs at the CNT/GC electrode for 0.5, 20, 40, 60, 80, and 100* μg mL^{-1} *ACT. Initial potential: 0.7 V* vs *Ag/AgCl; final potential: 0 V* vs *Ag/AgCl; scan rate: 0.1 V* s^{-1}*. (D) Calibration plot for ACT at CNT/GC electrode, derived from C. Solution: 0.1 M pH 7.4 potassium phosphate buffer.*

anode (Fig. 12.3). Different combinations of the input signals, (**0**,**0**), (**0**,**1**), (**1**,**0**), and (**1**,**1**), are not observed to alter the OCP of the cathode (Fig. 12.3). Thus, the PEDOT-ACT-modified electrode is suitable to serve as the cathode within the self-powered, controlled release BFC.

In order to realize the self-powered controlled release functionality, the controlled release operation was performed initially using the PEDOT-ACT/Au electrode (in a conventional electrochemical cell) with an applied potential of 0.0 V *vs* Ag/AgCl. Differential pulse voltammetry (DPV) was employed to examine the release profile of ACT from the various functionalized electrodes (Fig. 12.4). As shown in Figs. 12.5A and D(a), the ACT peak oxidation current increases with extended release durations. At 30 min, the peak current approaches a steady-state value, implying that no further ACT is released from the single cathode after 30 min. According to the linear equation derived from Fig. 12.4, 50 μg mL^{-1} ACT was released from the single cathode after 30 min. Control experiments using an electrode devoid of the ACT doped in the polymer matrix or without the application of a potential (shown in Figs. 12.5B and C, respectively) indicate that no obvious DPV ACT peaks were observed even after 120 min transpired.

Accordingly, the complete, compartment-free BFC was assembled from the logic-controlled anode and the drug-doped cathode. The corresponding power curves were obtained for all combinations of the inputs (Fig. 12.6A). Under the 'abnormal' scenario when LAC and LDH were both present (input (**1**,**1**)), the BFC switched **ON** and yielded a maximum power output of approximately 33.8 μW cm^{-2} (at approximately 0.40 V, output = **1**, line d, Fig. 12.6A). In contrast, when the (**0**,**0**), (**0**,**1**), and (**1**,**0**) input combinations were applied, that is, a 'normal' state, only negligible alterations in the NADH oxidation OCP occurred, thereby switching the BFC **OFF** (output = **0**, lines a, b, and c, Fig. 12.6A). Fig. 12.6B shows the corresponding bar diagrams for the power output for the same four input combinations. The selected threshold value of 20μW cm^{-2} conveniently separates the **OFF** and **ON** logic states of the output power signal, whereby only the presentation of the input combination (**1**,**1**) switches the output of the system to the **ON** state.

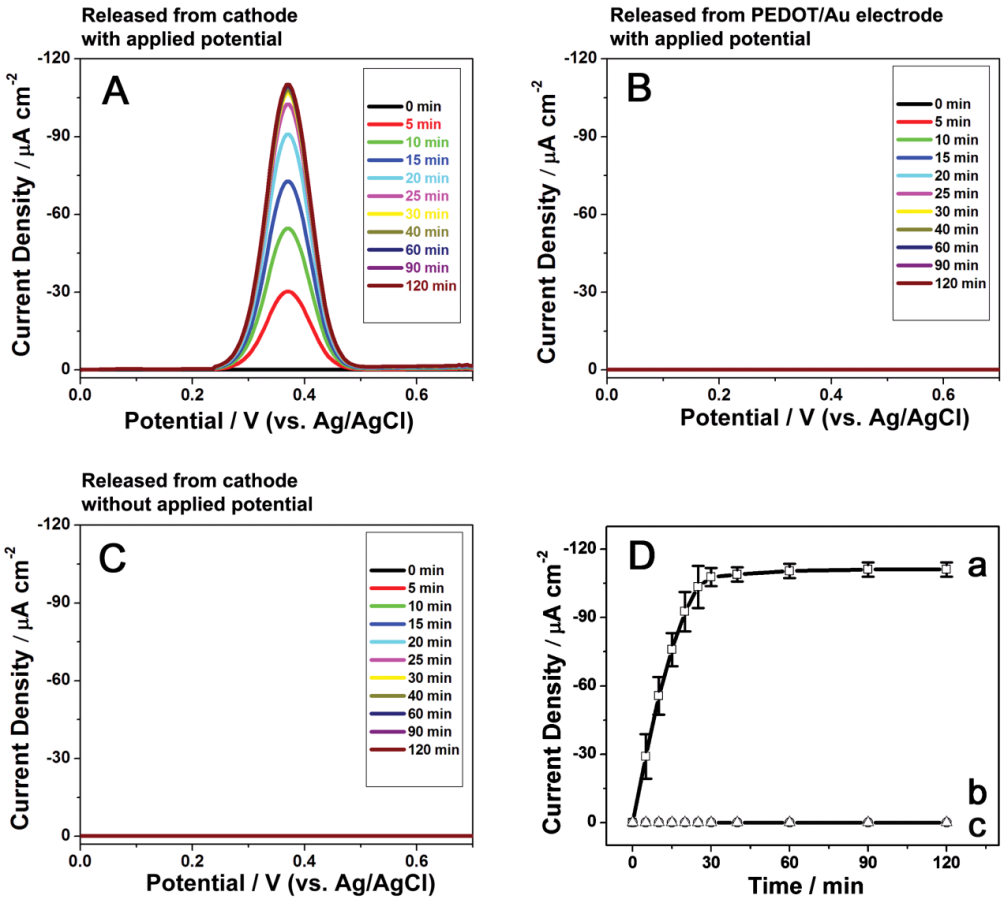

Figure 12.5: *(A) DPVs at a carbon nanotube-functionalized glassy carbon (CNT/GC) electrode corresponding to the oxidation of the ACT released from the single cathode (i.e., PEDOT-ACT/Au electrode) with an applied potential of 0.0 V* vs *Ag/AgCl at increasing temporal durations. (B) DPVs at the CNT/GC electrode corresponding to the oxidation of the ACT released from the PEDOT/Au electrode with an applied potential of 0.0 V* vs *Ag/AgCl at increasing temporal durations. (C) DPVs at the CNT/GC electrode corresponding to the oxidation of the ACT released from the single cathode (i.e., PEDOT-ACT/Au electrode) without an applied potential at increasing temporal durations. (D) Temporal dependence of the peak current corresponding to the oxidation of the ACT released from the PEDOT-ACT/Au electrode in the base solution (a, derived from A), PEDOT/Au electrode (b, derived from B), and PEDOT-ACT/GC electrode (c, derived from C). Initial potential: 0.7 V* vs *Ag/AgCl; final potential: 0.0 V* vs *Ag/AgCl; scan rate: 0.1 V* s^{-1}.

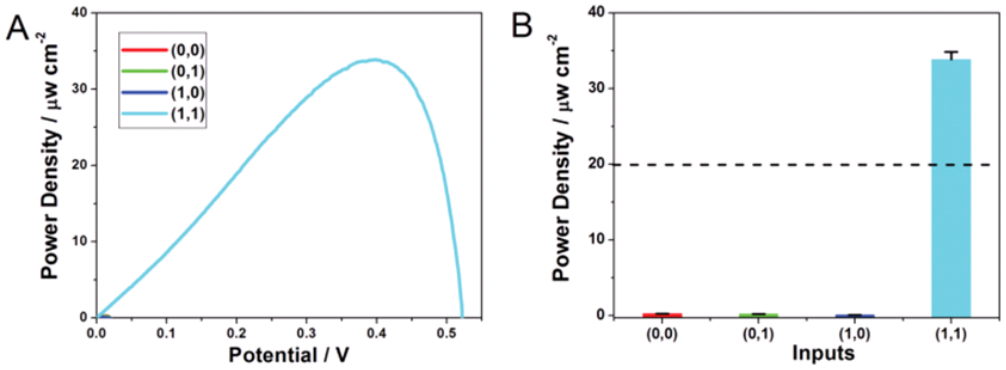

Figure 12.6: *(A) Dependence of the power density on the BFC voltage for different combinations of the input signals: a = (**0**,**0**), b = (**0**,**1**), c = (**1**,**0**), and d = (**1**,**1**). (B) Bar diagrams diagrammatically representing the power density of the BFC for all combinations of the input signals, derived from A. The dashed line is established at the threshold (20 μW cm^{-2}). Input concentrations and reaction duration, as in Fig. 12.2.*

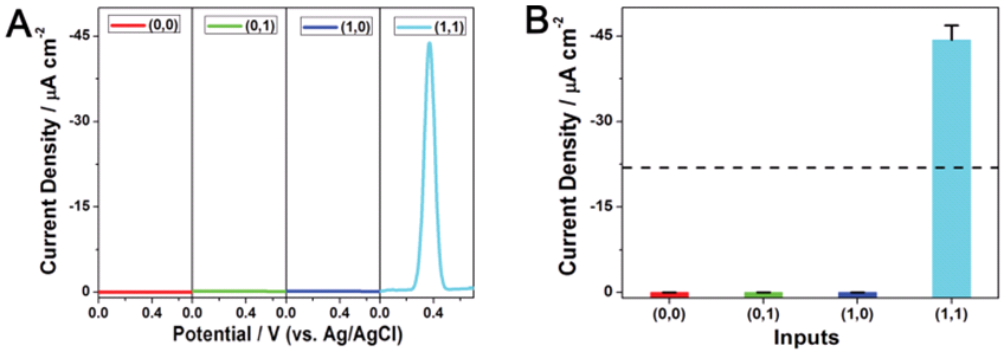

Figure 12.7: *Experimental results corroborating the logic-actived release of the therapeutic agent. (A) DPVs at the CNT/GC electrode corresponding to the oxidation of the ACT released from the 'Sense-Act-Treat' integrated system using all combinations of the input signals (**0**,**0**), (**0**,**1**), (**1**,**0**), and (**1**,**1**). Initial potential: 0.7 V* vs *Ag/AgCl; final potential: 0.0 V* vs *Ag/AgCl; scan rate: 0.1 V* s^{-1}. *(B) Bar diagrams comparing the current density response generated by the release of ACT for the different combinations of the input signals, derived from A. The dashed line is established at the threshold (-22 μA cm^{-2}). Input A, LAC (20 mM); Input B, LDH (10 U* mL^{-1}). *Input reaction duration, as in Fig. 12.2. Data were extracted following 60 min of unperturbed galvanic operation.*

Consequently, the amount of the therapeutic agent released by the complete BFC in response to different input combinations was examined by voltammetric measurements of the released ACT. Fig. 12.7 shows a comparison of the current response that was obtained from DPVs at a CNT/GC electrode corresponding to the oxidation of the ACT released under the four logic scenarios. Only the (**1**,**1**) 'abnormal' state resulted in an appreciable current response, hence, these results demonstrate that the 'Sense-Act-Treat' system releases significant quantities of ACT to counteract the onset of the abnormal state (Fig. 12.8). The substantial catalytic reactions at the anode are associated with the (**1**,**1**) logic level and dramatically increase the OCP, thus initiating the undoping and concomitant release of the therapeutic agent from the cathode. In contrast, ACT signals were not detected in the presence of the (**0**,**0**), (**0**,**1**), and (**1**,**0**) input combinations. No perceivable undoping of the CP-modified cathode occurred in this 'normal' / 'anomalous' (**OFF**) state, which is reflective of the negligible OCP and power output (Fig. 12.6). Overall, the data presented in Fig. 12.7 clearly delineate that drug release is instigated to counteract the onset of 'abnormal' physiological states manifested by elevated levels of the target biomarkers, LAC and LDH. Furthermore, the data from control experiments over a prolonged period of 120 min (after the 30 min input reaction between LAC, LDH, and NAD^+) indicated that no detectable DPV signals were generated by the oxidation of ACT (that is, drug release) upon the application of the inputs (**0**,**0**), (**0**,**1**), (**1**,**0**), or when the circuit was broken (Figs. 12.8B - E). The results of the control experiments also suggest that therapeutic release from the system is terminated when the targets are absent (Figs. 12.8G and H).

The interaction of potential electroactive interferents upon the controlled release operation was examined in further detail. No apparent ACT release was detected in the presence of physiological levels of uric acid (UA), dopamine (DA), and epinephrine (EP). However, very minor release of ACT, which corresponds to approximately 6 % and approximately 3 % of the (**1**,**1**) level, was detected in the presence of physiological levels ascorbic acid (AA) and cysteine (CySH), respectively (Fig. 12.9). Practical biomedical applications would require that careful

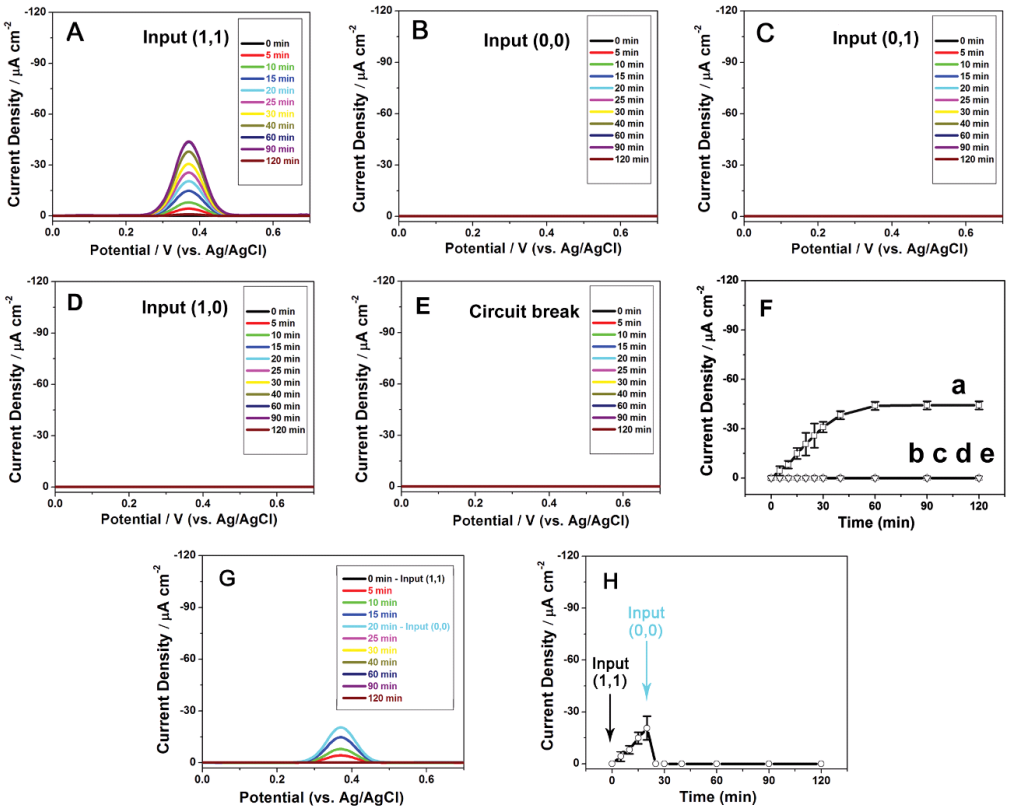

Figure 12.8: *DPVs at the CNT/GC electrode corresponding to the oxidation of ACT released from the self-powered integrated 'Sense-Act-Treat' system upon (A) input (**1**,**1**), (B) input (**0**,**0**), (C) input (**0**,**1**), (D) input (**1**,**0**), and (E) circuit break. (F) Temporal dependence of the peak currents generated by the oxidation of ACT released from the system upon input (**1**,**1**) (a, derived from A), input (**0**,**0**) (b, derived from B), input (**0**,**1**) (c, derived from C), input (**1**,**0**) (d, derived from D), and circuit break (e, derived from E). (G) DPVs at the CNT/GC electrode corresponding to the release of ACT from the system upon the application of input (**1**,**1**) at 0 min and input (**0**,**0**) at 20 min. (H) Temporal dependence of the peak currents for the continuous release of ACT from the system upon application of input (**1**,**1**) at 0 min and input (**0**,**0**) at 20 min (derived from G). Initial potential: 0.7 V* vs *Ag/AgCl; final potential: 0.0 V* vs *Ag/AgCl; scan rate: 0.1 V* s^{-1}.

attention be paid to these potential interferents, possibly by the incorporation of the appropriate permselective coatings [364].

The investigation presented embodies the first example of a biocomputing, logic-based detection methodology mated with a controlled release drug delivery actuator that is based on a closed-loop, self-powered BFC system. By harnessing built-in Boolean **AND** logic at the anode integrating physiologically-relevant biomarker inputs, the proof of concept 'Sense-Act-Treat' system instigates a therapeutic intervention upon the detection of 'abnormal' conditions through the logic-based control of the power output generated by the BFC. The concept of logic-activated therapeutic intervention could serve as the core component of an autonomous medical diagnostic and intelligent drug-delivery system that circumvents the need for external power sources, control electronics, or microelectromechanical actuators. The utilization of logic-activated delivery of a therapeutic intervention to counteract an abnormal state could thus be adapted to a plethora of diverse healthcare applications and may lead to major improvements in patient care. However, significant progress is necessary before practical biomedical applications of this concept can be implemented, which include advances in the diagnostic capabilities of enzymatic logic gates, minimization of potential interferences, and the mitigation of biofouling effects. Moreover, in order to extend the concept to practical *in vivo* applications, future devices will require further improvement, such as the covalent immobilization of the NAD^+ cofactor and the optimization of the BFC parameters, to meet relevant 'Sense-Act-Treat' scenarios. Furthermore, the implementation of biochemical filters [365] is expected to improve the **ON** / **OFF** dynamic range and response time of the device and thus enable truly binary release of the model therapeutic agent under diverse pathophysiological scenarios.

12.2 Self-powered biosensors controlled by logic gates based on DNAzymes

Biofuel cells (BFCs) represent a specific variety of novel power sources which employ enzymes or microbes as a bioprocessing contingent to oxidize a biofuel,

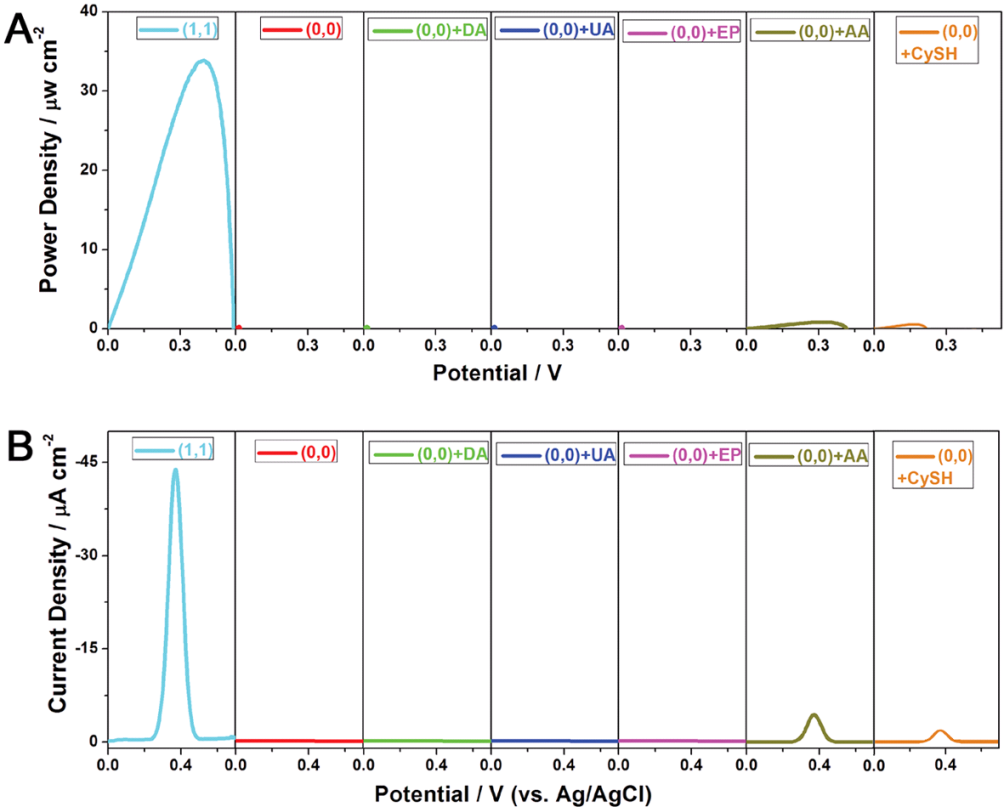

Figure 12.9: *(A) Dependence of the power density on the BFC voltage upon the application of the input signals (**1**,**1**), (**0**,**0**), (**0**,**0**) + DA, (**0**,**0**) + UA, (**0**,**0**) + EP, (**0**,**0**) + AA, and (**0**,**0**) + CySH. (B) DPVs obtained at the CNT/GC electrode for the ACT released from the integrated 'Sense-Act-Treat' system upon implementation of the input signals (**1**,**1**), (**0**,**0**), (**0**,**0**) + DA, (**0**,**0**) + UA, (**0**,**0**) + EP, (**0**,**0**) + AA, and (**0**,**0**) + CySH. Physiological levels of DA (10 nM), UA (200 μM), EP (10 nM), AA (60 μM), and CySH (100 μM) were employed in this investigation. Initial potential: 0.7 V* vs *Ag/AgCl; final potential: 0.0 V* vs *Ag/AgCl; scan rate: 0.1 V* s^{-1}.

rather than relying on traditional practices of employing precious metal catalysts for this process [350, 351]. In light of their relatively inexpensive components, ability to process renewable biofuel sources, as well as their potential application as power sources for bionic implants and bioelectronics, BFCs have been widely investigated over the past decade [350, 351, 352, 353, 354]. Besides the engineering challenges that endeavor at achieving extended operational stability, improved power output, and a higher degree of miniaturization [350, 351, 352, 353, 354, 355, 366, 367], several interesting and attractive studies have recently been reported that target the creation of logic-based biosensing systems that harness BFCs for potential self-powered medical diagnostics and therapeutics [356, 358, 359, 368, 369, 370]. Compared with traditional biosensors, one of the most significant advantages of logic-based biosensing systems integrated within BFCs resides in their ability to correlate the relationship between multiple target analytes in complex samples according to the principles of Boolean logic without the need for external power sources or control electronics [47, 108, 178, 179, 371].

Research efforts aimed at the advancement of the self-powered biosensor concept has resulted in the development of a system that harnesses deoxyribozyme (DNAzyme)-based biochemical signals processed according to Boolean logic operations in order to control the power output generated by a BFC. DNAzymes, selected by a systematic evolution of ligands by an exponential enrichment process (SELEX), are biocatalytic nucleic acids with a promising capacity to selectively identify charged organic and inorganic species at ultra-trace levels [372, 373, 374]. Owing to their unique characteristics, DNAzymes exhibit many intrinsic advantages over conventional enzymes, including high chemical stability, cost-effective reproducible synthesis, and facile chemical modification [372, 373, 374, 375]. While catalytic nucleic acid systems and DNAzymes have been widely employed for biosensing, nanomachine, logic gate applications [373, 374, 375, 376, 377, 378], as well as for the cathode component within BFCs [367], the as-developed biosensing paradigm represents the first example of a DNAzyme logic-controlled BFC for implementation as a self-powered biosensor.

Harnessing a built-in **INH** logic gate, a DNAzyme-controlled BFC has been

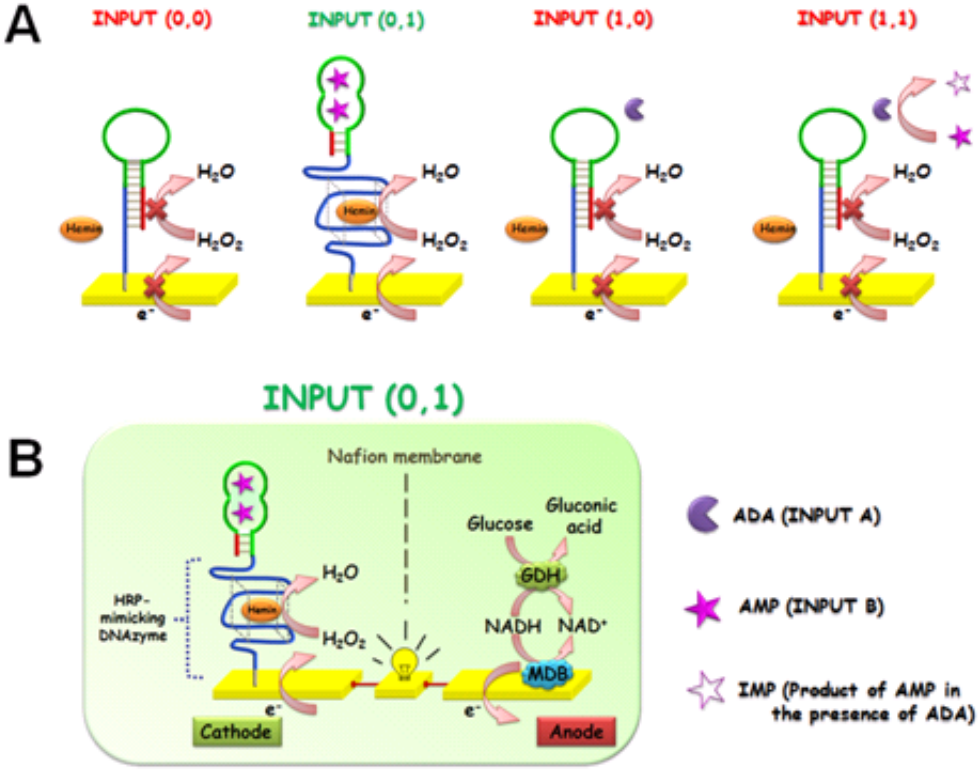

Figure 12.10: *(A) Schematic illustration of the logic-controlled cathode by different DNAzyme-based input signals. (B) Schematic illustration of the logic-controlled BFC under application of the DNAzyme-based input signal (**0**,**1**). Input A, adenosine deaminase (ADA); Input B, adenosine monophosphate (AMP).*

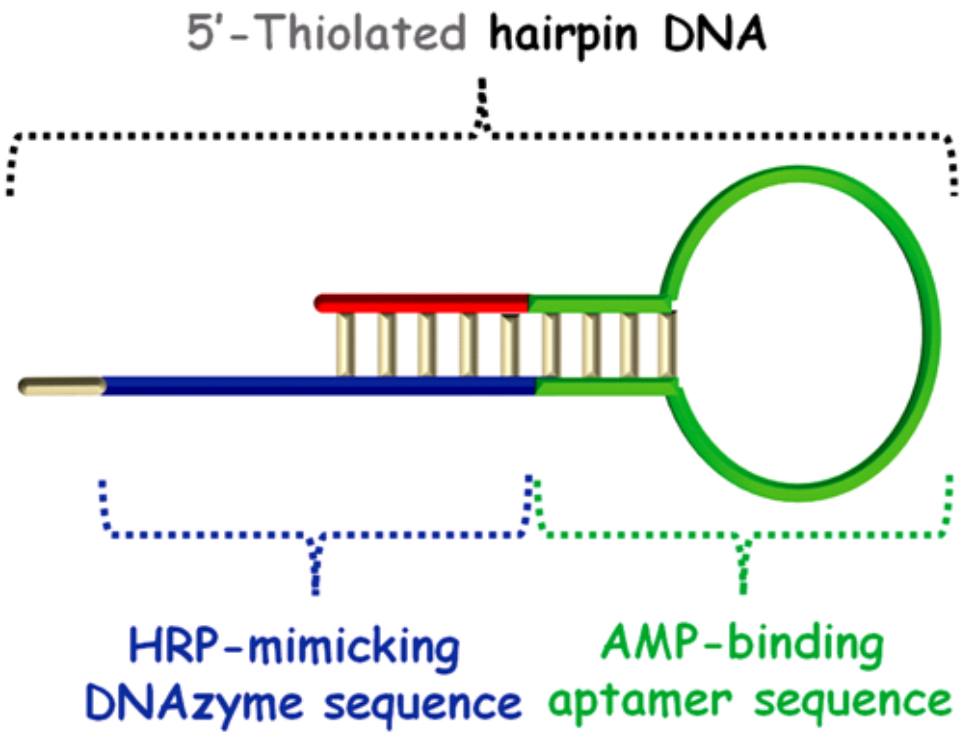

Figure 12.11: *Components of the hairpin DNA employed in the study delineating the DNAzyme and aptamer sequences.*

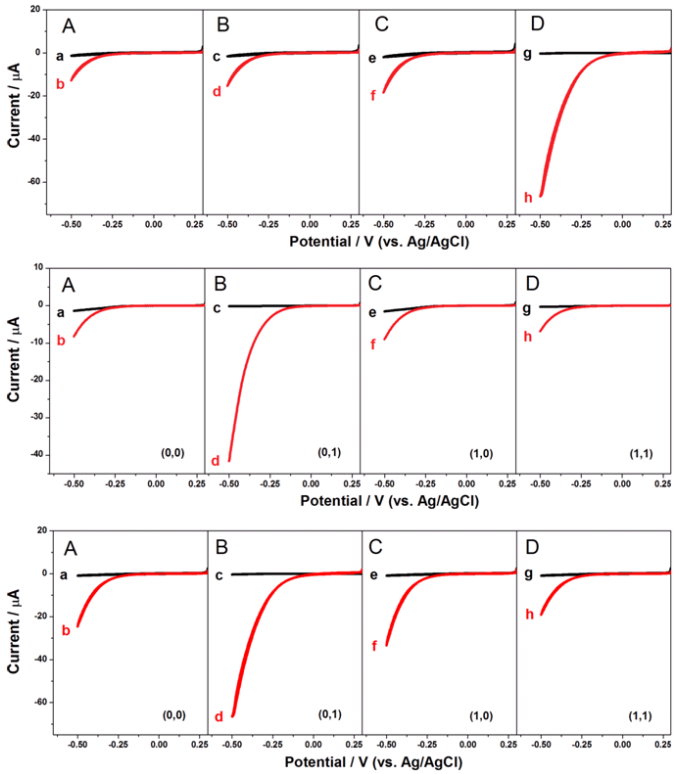

Figure 12.12: *Top: (A) Cyclic voltammograms (CVs) at the cathode for 0 (a) and 1 mM H_2O_2 (b). (B) CVs at the cathode in the presence of 1 μM hemin for 0 (c) and 1 mM H_2O_2 (d). (C) CVs at the cathode in the presence of 50 μM AMP for 0 (e) and 1 mM H_2O_2 (f). (D) CVs at the cathode in the presence of 1 μM hemin and 50 μM AMP for 0 (g) and 1 mM H_2O_2 (h). Electrolyte: N_2-saturated 10 mM 4-(2-hydroxyethyl)-1-piperazineethanesulfonic acid (HEPES) buffer (pH 7.2) containing 50 mM KCl and 100 mM NaCl. Scan rate: 20 mV s^{-1}. Middle: Linear sweep voltammograms (LSVs) at the cathode for 0 (a, c, e, and g) and 1 mM H_2O_2 (b, d, f, and h) upon application of all combinations of the input signals (A) (**0**,**0**), (B) (**0**,**1**), (C) (**1**,**0**), and (D) (**1**,**1**). Input A, 10 U mL^{-1} ADA; Input B, 50 μM AMP. Cathode electrolyte: N_2-saturated 10 mM HEPES buffer (pH 7.2) containing 50 mM KCl, 100 mM NaCl, and 1 μM hemin. Scan rate: 2 mV s^{-1}. Bottom: CVs at the cathode for 0 (a, c, e, and g) and 1 mM H_2O_2 (b, d, f, and h) upon the application of various input signals (A) (**0**,**0**), (B) (**0**,**1**), (C) (**1**,**0**), and (D) (**1**,**1**). Input A, 10 U mL^{-1} ADA; Input B, 50 μM AMP. Cathode electrolyte: N_2-saturated 10 mM HEPES buffer (pH 7.2) containing 50 mM KCl, 100 mM NaCl, and 1 μM hemin. Scan rate: 20 mV s^{-1}.*

contructed in order to lead towards the development of a self-powered DNAzyme logic biosensor. The **INH** gate implementation is leveraged in order to determine the presence of one specific target in the absence of another in a single test. The **INH** logic gate integrates the functional properties of an **AND** and **NOT** gate, where the output signal is activated by a specific combination of the inputs in accordance with a pre-defined truth table [379]. The development of a logic-controlled BFC activated by various DNAzyme-based input signals encompasses promise for the construction of potential intelligent self-powered biosensors or related bioelectronic diagnostic devices. As illustrated in Fig. 12.10, the DNAzyme-BFC system is comprised of a hairpin DNA-modified cathode and a glucose dehydrogenase (GDH)-modified anode. At the cathode, a horseradish peroxidase (HRP)-emulating DNAzyme sequence and an adenosine monophosphate (AMP)-binding aptamer sequence are both blocked in the stem region of a hairpin DNA sequence (Figs. 12.10 and 12.11). Upon exposure of the cathode to AMP in the presence of hemin, the AMP-binding aptamer-AMP complex forms, resulting in the opening of the hairpin stem and hence the self-assembly of the hemin/G-quadruplex HRP-emulating DNAzyme which serves to electrocatalyze the reduction of H_2O_2 (Figs. 12.10 and 12.11). Control experiments reveal that only the treatment of both hemin and AMP on the cathode result in notably elevated H_2O_2 reduction currents compared with the absence of hemin or AMP (Fig. 12.12, top and middle). This entails that the HRP-emulating DNAzyme formation based on hemin and AMP on the electrode interface can be employed as the cathode of a BFC operating in an N_2-saturated 10 mM 4-(2-hydroxyethyl)-1-piperazineethanesulfonic acid (HEPES) buffer (pH 7.2, containing 50 mM KCl, 100 mM NaCl, and 1 μM hemin) with H_2O_2 (1 mM) as the oxidizer. Employing an anode modified with a GDH (E.C. 1.1.1.47, 256 U mg^{-1})-carbon nanotube (CNT)-Meldola's blue (MB) composite, a glucose biofuel (24 mM) is oxidized in the presence of NAD^+ in an N_2-saturated 0.1 M pH 7.2 phosphate buffer solution (PBS) (Fig. 12.12, bottom). MB was employed as an electroatctive mediator to aid in the electron transfer from the active site of GDH to the anode and the cathode and anode were separated with a Nafion membrane (Nafion® 117, thickness 175

μm). The schematic of the BFC, represented in Fig. 12.10, clearly identifies the components required for the construction of a self-powered logic-based DNAzyme biosensor.

In order to construct the anode, a CNT-DMF suspension was prepared by agitating 10 mg CNT in 1 mL DMF and ultrasonicating the mixture for 30 min. Subsequently, 1 μL of the CNT-DMF suspension was cast on a GC electrode. Following evaporation of the solvent at 35° C for 15 min, the CNT/GC electrode was obtained. Immediately following this routine, the CNT/GC electrode was immersed in a 0.5 mg mL^{-1} MB solution for 30 min. Subsequently, the as-obtained CNT-MB/GC electrode was rinsed with deionized water and desiccated with a nitrogen stream. A bovine serum albumin (BSA) solution (1 % w/w in 0.1 M PBS, pH 7.2) was mixed with a GDH solution (6 U μL^{-1} in 0.1 M PBS, pH 7.2) with a volume ratio of 1:2 to yield a GDH-BSA mixture. After drop-casting 1.5 μL of the resulting mixture onto the surface of the CNT-MB/GC electrode, 2 μL of glutaraldehyde aqueous solution (40 mM) was cast onto the electrode surface in order to cross-link the GDH onto the CNT-MB/GC electrode. Following a 12 h incubation at 4° C, the as-prepared electrode was rinsed with distilled water, desiccated with a nitrogen stream, and utilized as the anode (i.e., GDH/CNT-MB/GC electrode) in the BFC system.

The cathode was realized as follows: 6 μL of a 1 μM thiolated DNA solution (prepared in 10 mM HEPES buffer, pH 7.2) was cast on the Au electrode for 2 h to produce a thiolated hairpin DNA self-assembled monolayer (SAM) on the electrode surface. After rinsing with the buffer solution and desiccating with a nitrogen stream, the as-prepared electrode was employed as the cathode. As shown in Fig. 12.11, the hairpin DNA on the cathode contains a horseradish peroxidase (HRP)-emulating DNAzyme sequence and an AMP-binding aptamer sequence, which are both blocked in the stem region of the hairpin.

In order to demonstrate proper DNAzyme logic operation, adenosine deaminase (ADA) (which can transform the AMP substrate into inosine monophosphate (IMP)) and AMP were applied as the model inputs (inputs A and B, respectively). The absence of ADA or AMP is considered as logic input **0**, while their optimized

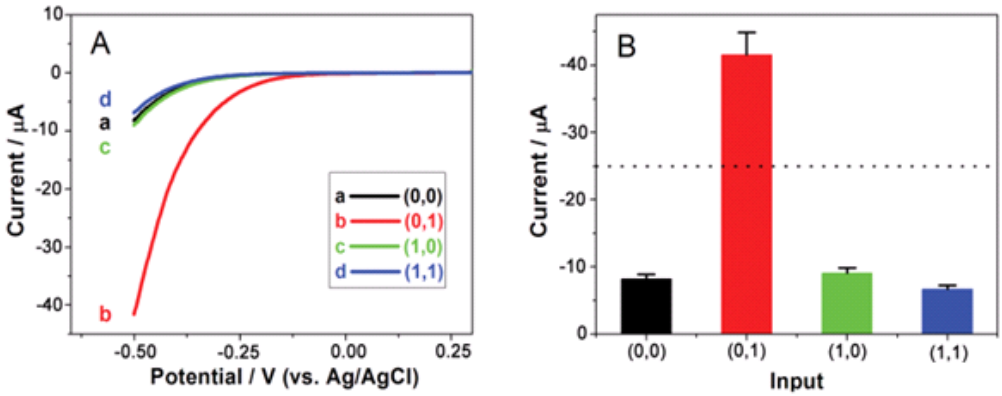

C

Input A (ADA)	Input B (AMP)	Output INH gate
0	0	0
0	1	1
1	0	0
1	1	0

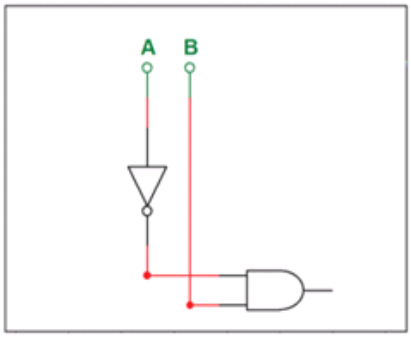

Figure 12.13: *(A) LSVs at the cathode for 1 mM H_2O_2 upon the application of the various combinations of input signals (**0**,**0**) (a), (**0**,**1**) (b), (**1**,**0**) (c), and (**1**,**1**) (d). Scan rate: 2 mV s^{-1}. (B) Bar diagrams, illustrating the current response at -0.5 V* vs *Ag/AgCl generated by all permutations of the input signals. The dashed line indicates the threshold (-25 μA). (C) Truth table for the **INH** logic gate. (D) The equivalent logic system for the **INH** logic gate. Input A, 10 U mL^{-1} ADA; Input B, 50 μM AMP. Cathode electrolyte: N_2-saturated 10 mM HEPES buffer (pH 7.2) containing 50 mM KCl, 100 mM NaCl, and 1 μM hemin.*

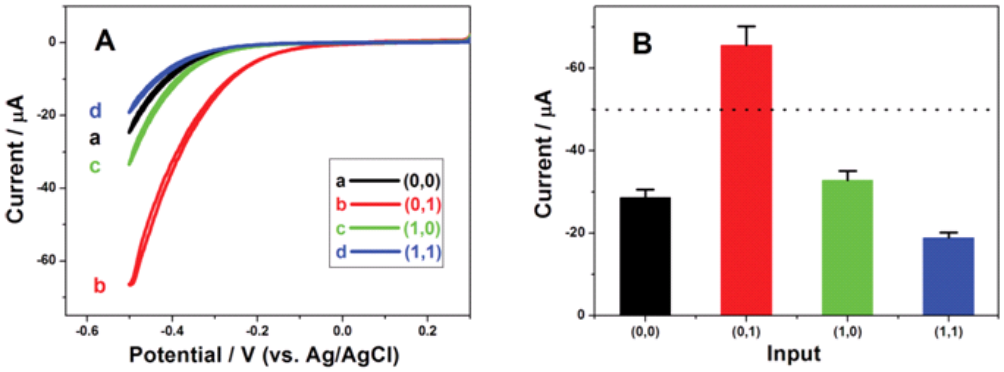

Figure 12.14: *(A) CVs at the cathode for 1 mM H_2O_2 upon the application of the various combinations of input signals (**0**,**0**) (a), (**0**,**1**) (b), (**1**,**0**) (c), and (**1**,**1**) (d). Scan rate: 20 mV s^{-1}. (B) Bar diagrams, illustrating the current response at -0.5 V* vs *Ag/AgCl generated by all permutations of the input signals, derived from A. The dashed line indicates the threshold (-50 µA). Input A, 10 U mL^{-1} ADA; Input B, 50 µM AMP. Cathode electrolyte: N_2-saturated 10 mM HEPES buffer (pH 7.2) containing 50 mM KCl, 100 mM NaCl, and 1 µM hemin.*

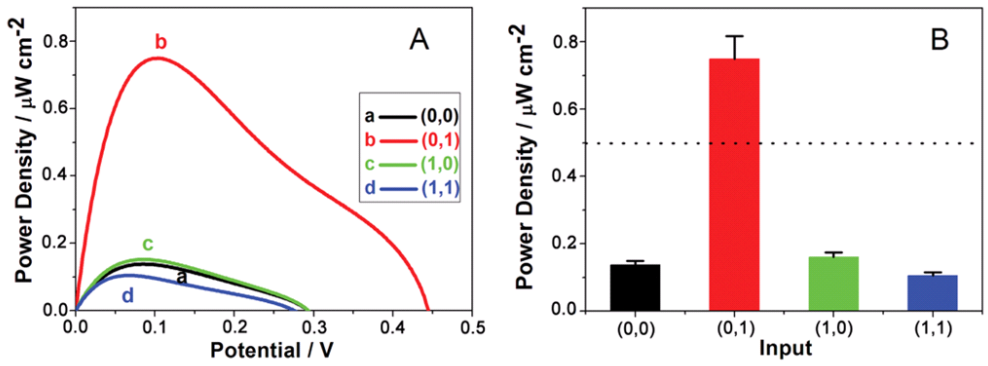

Figure 12.15: *(A) Open-circuit potential (OCP) versus the power density generated by the BFC. Anode biofuel, 24 mM glucose; cathode oxidizer, 1 mM H_2O_2; input signals are shown: (**0**,**0**) (a), (**0**,**1**) (b), (**1**,**0**) (c), and (**1**,**1**) (d). (B) Bar diagrams, illustrating the maximum power density for the different combinations of the input signals, derived from A. The dashed line is established at the threshold (0.5 µW cm^{-2}). Anode electrolyte: N_2-saturated 0.1 M PBS (pH 7.2) containing 20 mM NAD^+. Cathode electrolyte: N_2-saturated 10 mM HEPES buffer (pH 7.2) containing 50 mM KCl, 100 mM NaCl, and 1 µM hemin.*

concentrations at 10 U mL^{-1} (ADA) and 50 μM (AMP) are defined as logic input **1**. The input signals were applied in all four combinations ((**0**,**0**), (**0**,**1**), (**1**,**0**) and (**1**,**1**), where the first bit corresponds to signal A and the second bit to signal B). When ADA and AMP are both absent (input (**0**,**0**) in Fig. 12.13A), the current for the H_2O_2 reduction at the cathode was -8.62 μA (at -0.5 V *vs* Ag/AgCl). Following the addition of AMP, a significantly higher current was observed (-40.60 μA) due to the formation of the hemin/G-quadruplex HRP-emulating DNAzyme at the cathode (input (**0**,**1**) in Fig. 12.10A and Figs. 12.13A and B). Under scenarios where only ADA was present (input (**1**,**0**) in Fig. 12.10A and Figs. 12.13A and B), the DNAzyme did not form on the cathode, thereby leading to an output of **0**. When ADA and AMP were both present (input (**1**,**1**) in Fig. 12.10A, Figs. 12.13A and B, Fig. 12.12 (bottom), and 12.14), the binding aptamer-AMP complex generated on the cathode transformed into IMP, which resulted in an output of **0**. Therefore, the features of the system correspond to the equivalent behavior of an **INH** logic gate that performs the Boolean logic operation of A'B (Fig. 12.13C and D, Fig. 12.12 (bottom), and 12.14). Specific patterns of the ADA and AMP BFC inputs thus generate an output in compliance with a truth table for an **INH** gate.

The logic-controlled H_2O_2-reducing cathode was subsequently mated with a glucose-oxidizing anode to yield a complete BFC system. The application of the (**0**,**0**) input signal did not alter the power output of the BFC (input (**0**,**0**) in Figs. 12.15A and B and Fig. 12.16). When the (**0**,**1**) input signal was applied, the hemin/G-quadruplex HRP-emulating DNAzyme formed at the cathode interface; accordingly, the power output increased, thus resulting in the **ON** state of the BFC (input (**0**,**1**) in Figs. 12.15A and B as well as Fig. 12.16). When the (**1**,**0**) and (**1**,**1**) input signals were applied, the power output of the BFC did not change appreciably; accordingly, the BFC remained in the **OFF** state (inputs (**1**,**0**) and (**1**,**1**) in Figs. 12.15A and B and Fig. 12.16).

Inline with the operational functionality of an **INH** logic gate, in circumstances when only AMP is present in the sample (input (**0**,**1**)), a significantly elevated power output is observed (output **1**) and the gate switches **ON** (input (**0**,**1**) in Fig. 12.15). If AMP is not present or AMP and ADA are both in the

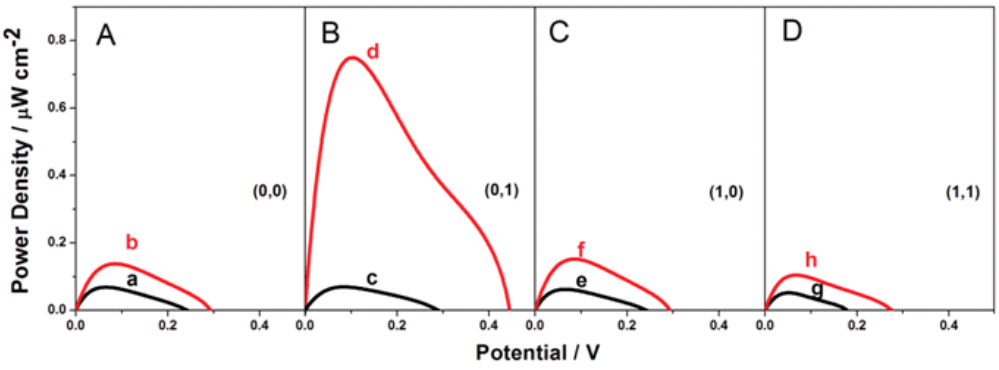

Figure 12.16: *OCP versus the power density generated by the BFC utilizing 24 mM glucose as the biofuel at the anode and 0 (a, c, e, and g) or 1 mM H_2O_2 (b, d, f, and h) as the oxidizer for the cathode upon the application of the various combinations of the input signals (A) (**0**,**0**), (B) (**0**,**1**), (C) (**1**,**0**), and (D) (**1**,**1**). Input A, 10 U mL^{-1} ADA; Input B, 50 mM AMP. Cathode electrolyte: N_2-saturated 10 mM HEPES buffer (pH 7.2) containing 50 mM KCl, 100 mM NaCl, and 1 μM hemin. Anode electrolyte: N_2-saturated 10 mM phosphate buffer (pH 7.2) containing 20 mM NAD^+.*

sample (inputs (**0**,**0**), (**1**,**0**) and (**1**,**1**)), the power output is 'disabled' (output **0**); consequently, the **INH** gate switches the BFC to the **OFF** state (inputs (**0**,**0**), (**1**,**0**) and (**1**,**1**) in Fig. 12.15). Therefore, the **INH** logic gate presented here queries only the presence of a specific target in the absence of another related input in a single test. Additionally, the present DNAzyme **INH** logic-based device is able to operate in the absence of an external power source, hence underscoring the inherent self-powered characteristics of this bioelectronic device.

The presented developments represent the first example of a DNAzyme logic system integrated within a BFC in order to provide for controlled power generation intended for 'intelligent' logic-based biosensing applications. This approach employs a pattern of ADA and AMP as inputs to a BFC, which generates an output in compliance with a truth table for an **INH** gate, based on modulating the HRP-like activity of a DNAzyme. The concept also demonstrates the feasibility of harnessing self-powered medical diagnostics that employ biologically-inspired logic gate-based designs. If pathologically-relevant targets are applied to the DNAzyme logic-controlled BFC, self-powered diagnostic operation may be realized, which

would enable the direct screening of various medical conditions. In view of the tremendous interest in DNAzyme-based bioanalytical systems [372, 373, 374, 375], the eventual integration of DNAzymes with self-powered biocomputing devices holds considerable potential for diverse applications.

It should also be noted that DNAzymes exhibit many advantages over conventional enzymes [373, 374], which could make DNAzymes versatile for various logic sensing applications. While the preliminary concept of logic-based activation of DNAzyme activity has been illustrated using AMP and ADA as model compounds, it can be expanded to the determination of metal ions (e.g., Ag^{+}, K^{+}, Hg^{2+}, Pb^{2+}, and Cu^{2+}), the amplified detection of small molecules (e.g., adenosine, cocaine, and AMP), and the identification of proteins such as lysozyme and thrombin [372, 380].

Portions of Chapter 12, section 1 were taken from M. Zhou, N. Zhou, F. Kuralay, J.R. Windmiller, S. Parkhomovsky, G.V. Ramírez, E. Katz, and J. Wang. A self-powered 'Sense-Act-Treat' system that is based on a biofuel cell and controlled by Boolean logic. *Angewandte Chemie International Edition*, 124(11):2686–2689, 2012. The dissertation author was a co-author of the manuscript and had substantial original contributions to this work.

Portions of Chapter 12, section 2 were taken from M. Zhou, F. Kuralay, J.R. Windmiller, and J. Wang. DNAzyme logic-controlled biofuel cell for self-powered biosensors. *Chemical Communications*, 48(32):3815–3817, 2012. The dissertation author was a co-author of the manuscript and had substantial original contributions to this work.

Chapter 13

Conclusions and future directions

The future belongs to those who believe
in the beauty of their dreams.

—Eleanor Roosevelt

Molecular [177, 178, 179, 180, 181, 381, 382] and biomolecular [108, 182, 183] logic gates able to process chemical input signals in a manner analogous to conventional electronic-based computing systems have received substantial attention and have witnessed rapid research and development efforts over the past decade. As a sub-domain of unconventional computing [185, 186], bio-/molecular logic gates possess the innate ability to process chemical information and emulate Boolean logic operations utilizing binary definitions **0/1**; **NO/YES**) to represent the concentrations of the chemical species partaking in the reaction. Leveraging this approach, chemical reactions can be reformulated as information processing steps with 'programmed' logic operations [142, 383, 384], hence yielding networks that perform utilitarian logic operations. Despite the fact that chemical systems, based on organic molecules [187, 188, 190, 191, 192, 193, 385, 386, 387, 388, 389, 390, 391, 392, 393, 394] or biomolecules [182, 194, 395, 396, 397, 398, 399, 400, 401, 402, 403], achieved significant success in the implementation of singular logic operations and simple cascades emulating biochemical pathways [195, 223], there still remains fundamental challenges that inhibit their potential applications. The present complexity of the chemical information processing systems is far below that of electronic

computers and the temporal duration of their computation operations (minutes-to-hours) is far too long to be competitive with electronics. There is optimism that complex combinatorial problems could be solved by biomolecular (e.g. DNA-based) systems at an exponentially faster rate than by regular computers due to the massive parallelism of information processing in chemical systems [404, 405, 406]. However, the biochemical computing field has not been developed to a sufficient extent in the direction of molecular computers. Therefore, on the one hand, future development of chemical systems in the direction of molecular computers able to compete with the current electronic infrastructure represents a formidable challenge, at least at the present state of the technology. On the other hand, one can recognize from observation that living systems, in general, and the cerebrum, in particular, are based on biomolecular systems able to process information in a substantially more efficient manner than electronic computers, albeit this method is profoundly less understood. Thus, even if a technological paradigm does not exist at the moment to emulate living systems in an artificial manner, an example manifested by nature still remains, which at least demonstrates a perspective for future developments in chemical information processing systems. An obvious advantage of biocomputing systems over their electronic counterparts is their compatibility with biochemical systems and their ability to operate in a biochemical environment [407]. A more idealistic view on the potential applications of biocomputing systems could even predict biocomputers capable of intracellular operation [408, 409, 410, 411, 412] as a component of a novel nanomedicine concept [413].

Indeed, the synthesis and integration of the components required for the construction of advanced functional biosensors have been delineated in this thesis. Future work will endeavor to apply the tools, devices, and systems that have been introduced in this treatise to relevant scenarios in the generalized healthcare, fitness, security, and environmental monitoring domains. Nonetheless, further insight into the physical considerations that are intrinsic to the operational functionality of such devices is warranted and include the development of clever techniques to mitigate the poor dynamic range and noise margins exhibited by the enzyme logic incarnations presented in this study. Paramount to such efforts

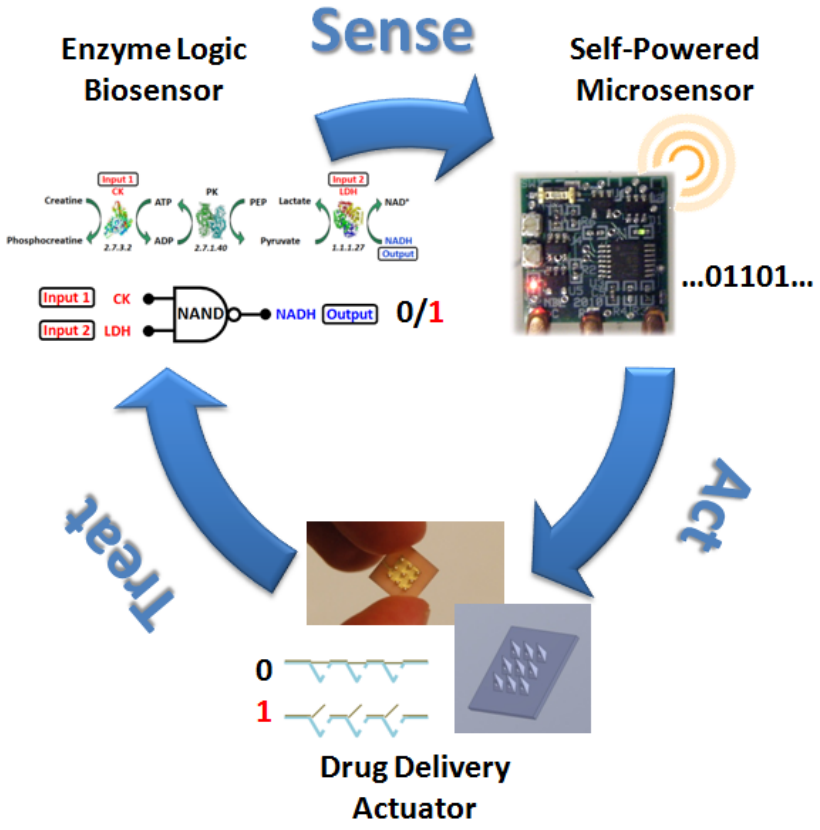

Figure 13.1: *Autonomous 'Sense-Act-Treat' feedback loop for the rapid identification and treatment of injury / trauma / disease.*

resides in non-linearizing the input-output transfer characteristics exemplified by enzyme logic gates from convex in nature to sigmoidal. Furthermore, to satisfy most bio-monitoring embodiments, the implementation of preventative measures designed to inhibit bifouling is crucial to extending the lifetime for practical use of this paradigm in the biosensing arena. Advantageously, the concept lends itself to integration with ultra-low power wireless electronics due to the binary nature of the outputs generated by the logic gates. The ubiquitous wireless infrastructure can thus be leveraged to alert first responders to the scene of injury.

A more pragmatic perspective of the utility of enzyme-based logic systems concerns their implementation as advanced diagnostic devices. Although this new approach facilitates the integration of multiple inputs to yield a single binary output, hence increasing reliability, troubles arise when cascading complex aggregates of enzyme logic gates owing to noise and cross-talk impairments. Indeed, chemical-based information processing systems simply cannot compete with their CMOS counterparts at their current stage of development or in the foreseeable future nor can such 'artificial' organic systems be engineered that even begin to emulate the simple computing units that are found at the heart of today's micro-/nanoelectronic infrastructure. This can be attributed to the stochastic nature of mass transfer via diffusion (vs. the well-defined nature of electronic drift) as well as the substantially slower rate of enzyme-mediated catalysis and chemical kinetics (vs. electron mobility in a semiconductor crystal lattice). However, the enzyme logic paradigm represents a substantial improvement over the state-of-the-art when compared in the vein of conventional chemical and biological sensors. Harnessing the innate merits of this unique approach, one is able to construct high-fidelity biosensors and 'Sense-Act-Treat' systems that dramatically extend the capabilities and robustness demonstrated by the current state-of-the-art in the diagnostics and controlled-release domains. This concept can, in turn, be directed at the demonstration of self-powered autonomous systems that completely obviate the need for user intervention and are able to deliver an immediate therapeutic response to amerliorate injury / trauma / disease.

Bearing in mind that the current physical limits of CMOS technology are

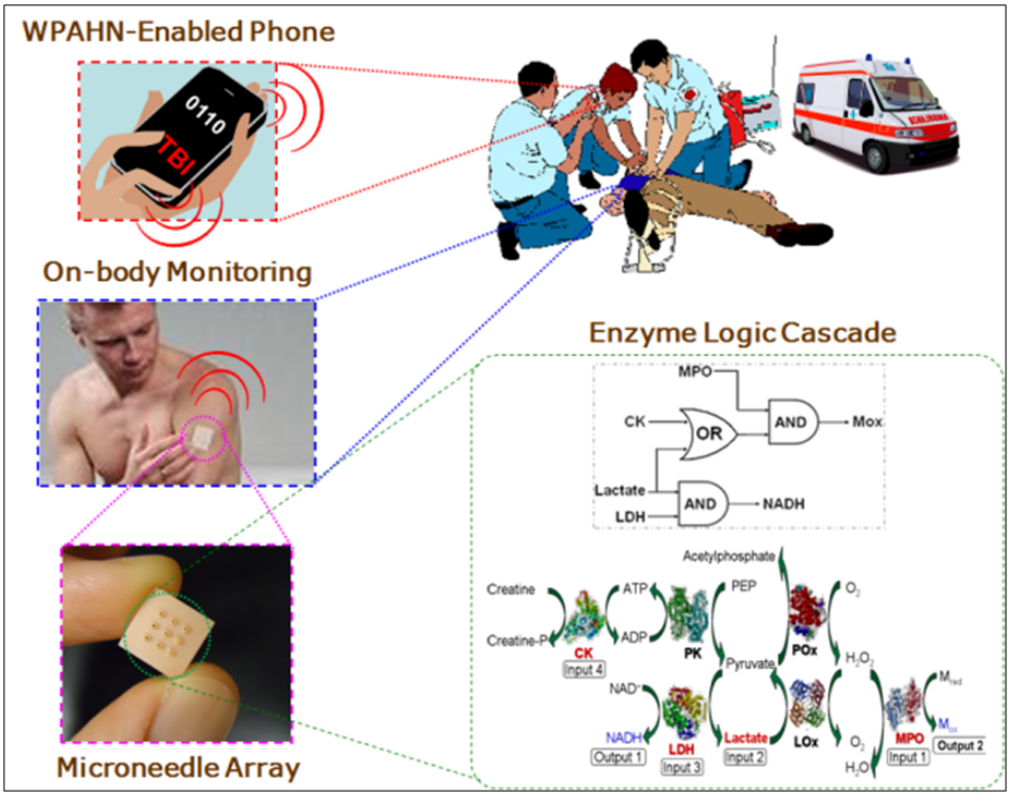

Figure 13.2: *Extension of the 'Sense-Act-Treat' concept to the mitigation of acute cardiac conditions in scenarios whereby the individual is incapacitated. An on-body, minimally invasive transdermal patch (containing an embedded enzyme logic cascade - 'Cardio-Logic') continuously monitors the interstitial fluid and alerts the dispatch of paramedics should a pathological state be identified.*

rapidly being approached, a departure from the conventional CMOS-like wisdom that has perpetuated advancements in computing for the past forty years is necessary. Above all else, the proposed enzyme logic methodology represents a truly molecular-scale avenue towards the implementation of simple, yet utilitarian biocomputing operations. From this perspective, this exercise substantiates that such devices can be mated with biological / chemical systems, thereby serving as the critical juncture between the 'analog' bio-/chemical information that underpins the operation of every living system and the robust digital signals that are requisite for high-fidelity information processing.

Appendix A

Prediction of diffusion coefficients

Diffusion of spherical particles in fluids characterized by low Reynolds numbers is given by the *Einstein-Stokes equation*,

$$D = \frac{k_B T}{6\pi\eta r}, \tag{A.1}$$

where η represents the viscosity of the solvent and r represents the radius of the spherical particle. Although this is sufficient for describing diffusion where the solute and solvent molecules possess comparable sizes [414], it has been found to be inappropriate for systems where the solute is substantially larger in spatial extent than the solvent and/or conforms to a specific macromolecular geometry. In this case, the diffusion of these macromolecules is influenced by the presence of their smaller neighbors [415] arising from electrostatic interactions and solvation effects [416] and therefore the rigid-sphere model presented in Eq. (A.1) cannot be applied to such systems.

Tyn and colleagues [414] have adapted the Einstein-Stokes relation to a model for the equivalent hydrodynamic sphere. The group has performed multiple regression analysis with nearly 200 experimental data points for nearly 100 unique protein entities. The following correlation was obtained:

$$D_M = \frac{1.69 \times 10^{-9}}{R_g}, \tag{A.2}$$

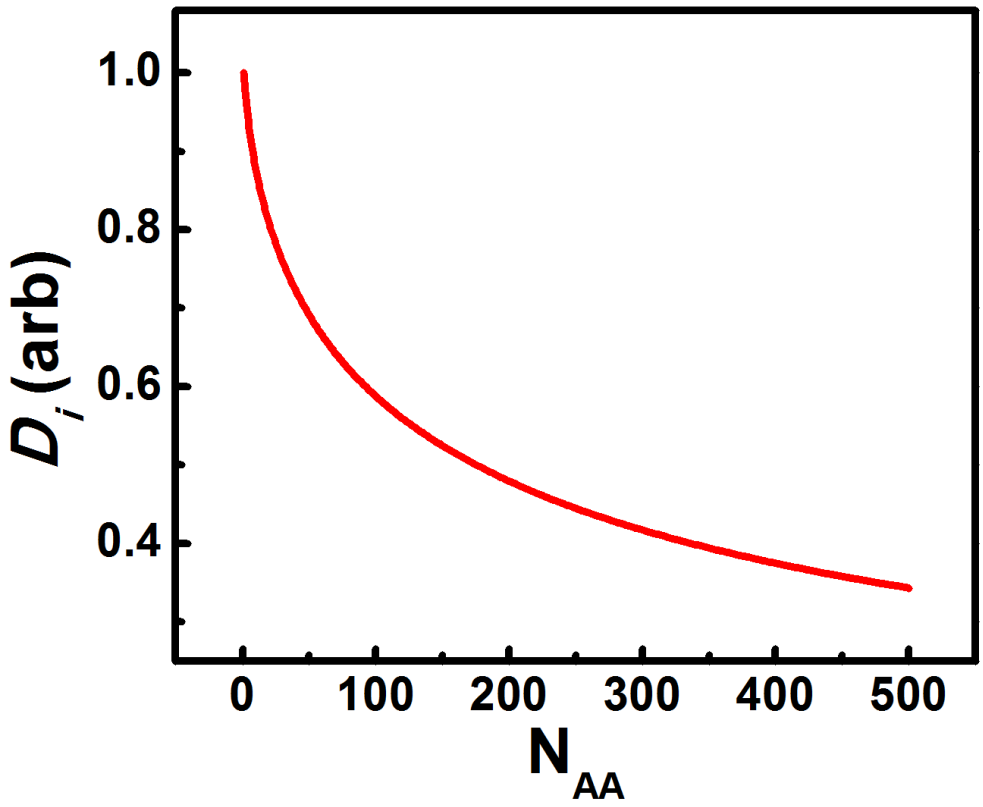

Figure A.1: *Dependence of the diffusion coefficient of a protein upon the number of amino acid residues that its structure contains according to the model of Tyn* et al.

$$0.359N_{AA}^{3/5} + 7.257, \tag{A.3}$$

where R_g is the radius of gyration ($\mathring{A}$) and N_{AA} is the number of amino acid residues. This correlative formalism remains the most accurate mathematical model for the prediction of diffusion coefficients of proteins at standard conditions whereby the spatial extent and geometrical factors of these macromolecules are accounted for.

Appendix B

Modeling the effect of pH on enzyme activity

The protonation and hydroxylation of an enzyme can be represented by the following mechanisms [417, 418]:

$$EH^+ \overset{K_1}{\leftrightarrow} E_{ACT} + H^+ \tag{B.1}$$

$$E_{ACT} \overset{K_2}{\leftrightarrow} E^- + H^+ \tag{B.2}$$

where K_1 and K_2 represent the equilibrium constants of the reactions such that:

$$K_1 = \frac{[E_{ACT}]\,[H^+]}{[EH^+]} \tag{B.3}$$

$$K_2 = \frac{[E^-]\,[H^+]}{[E_{ACT}]}. \tag{B.4}$$

Recognizing that,

$$\left[H^+\right] = 10^{-pH}, \tag{B.5}$$

we have:

$$K_1 = \frac{[E_{ACT}]\,10^{-pH}}{[EH^+]} \tag{B.6}$$

$$K_2 = \frac{[E^-]\,10^{-pH}}{[E_{ACT}]}. \tag{B.7}$$

The total amount of enzyme in any configuration must be conserved such that,

$$[E] = \left[EH^+\right] + \left[E^-\right] + [E_{ACT}]\,. \tag{B.8}$$

Synthesizing Eqs. (B.6) - (B.8), we can solve for the active enzyme concentration at any pH:

$$[E_{ACT}] = \frac{[E]}{1 + 10^{pK_1 - pH} + 10^{pH - pK_2}} \tag{B.9}$$

and

$$K_a = 10^{-pK_a}. \tag{B.10}$$

As can be inferred, it is best to operate an enzyme at its optimal pH activity range, as determined empirically.

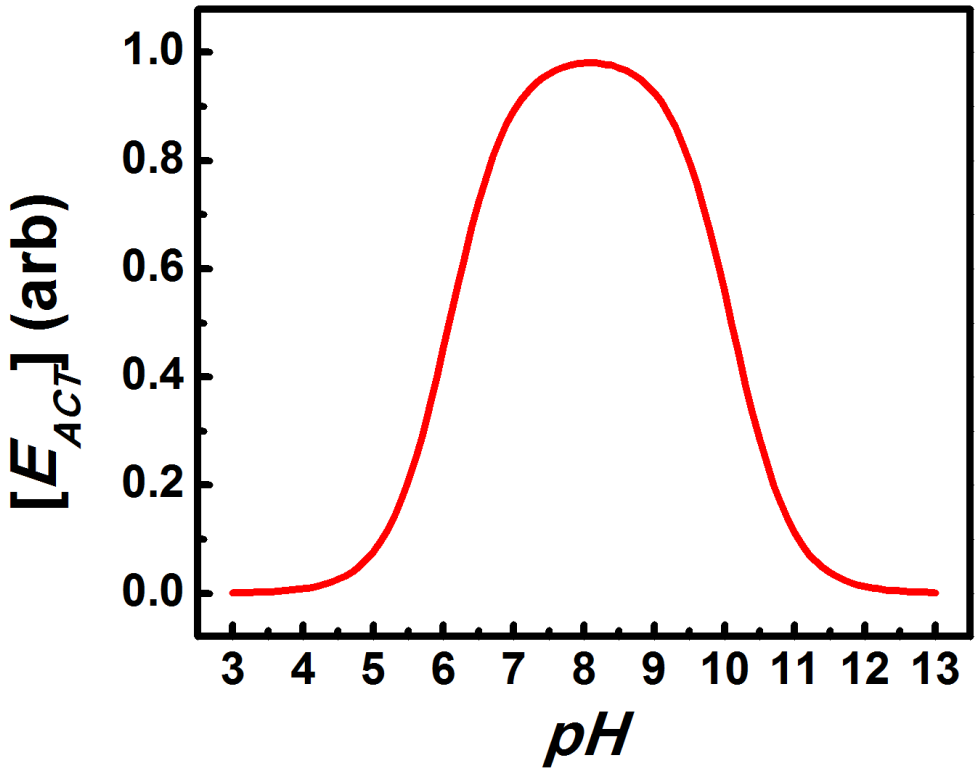

Figure B.1: *pH dependence of the activity of a hypothetical enzyme containing hystidine* ($\mathrm{pK}_1 = 6.08$) *and tyrosinase* ($\mathrm{pK}_2 = 10.10$) *side chains.*

Appendix C

Modeling the effect of temperature on enzyme activity

Modulation in the temperature can affect both the rate constants associated with the conversion of one chemical species to another as well as the activity of the enzyme. It is generally understood by the simple *Arrhenius law* that the conversion rate of one chemical species to another will increase concomitantly with a rise in temperature. Namely,

$$k = Ae^{\frac{-E_A}{RT}}, \tag{C.1}$$

where A is an arbitrary pre-exponential factor and E_A represents the activation energy required to initiate the reaction. We can express this temperature dependence in terms of a reference rate constant k_{REF} at a reference temperature T_{REF} [418],

$$k = k_{REF}\left[\frac{E_A}{R}\left(\frac{1}{T_{REF}} - \frac{1}{T}\right)\right]. \tag{C.2}$$

It is typically the case that k is obtained empirically due to the challenges associated with determining A and E_A. However, the Arrhenius law provided in Eq.(C.1) predicts that the conversion rate will increase without bounds as temperature is increased. We know that an enzyme will begin to denature at elevated temperatures and thus will lose its catalytic activity / turnover. We can express

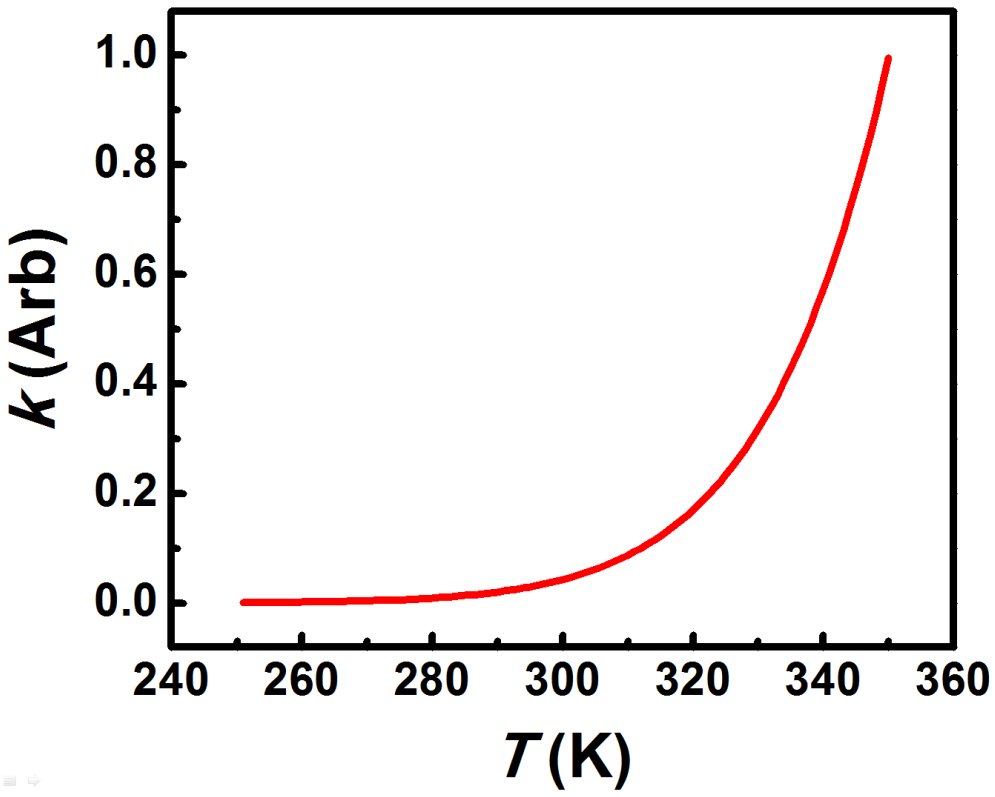

Figure C.1: *Temperature dependence of the rate constant over a standard temperature range.*

the denaturation of an enzyme according to the simple differential equation:

$$E_{ACT} \xrightarrow{k_d} E_{DEN} \tag{C.3}$$

$$\frac{\mathrm{d}\left[E_{DEN}\right]}{\mathrm{d}t} = k_d \left[E_{ACT}\right], \tag{C.4}$$

where k_d represents the rate constant associated with the denaturation of the active enzyme E_{ACT} into the denatured enzyme E_{DEN}. The solution to Eq.(C.4) is given by

$$E_{DEN} = E_{ACT} e^{\frac{-(T-T_{OPT})^2}{2\sigma^2}}, \tag{C.5}$$

where T refers to the operating temperature, T_{OPT} is the optimal temperature for maximum enzyme activity, and σ is the operating temperature range. As is evident from an inspection of Fig. C.2, maximal enzyme activity is attained at the optimal operating temperature of the enzyme (typically in the vicinity of physiological temperature) with a normal Gaussian distribution around this central value. Accordingly, a model seeking to predict the rate of biocatalysis must consider the interplay between the increase in reaction velocity provided under the Arrhenius law and the thermal considerations associated with enzyme denaturation at elevated temperatures.

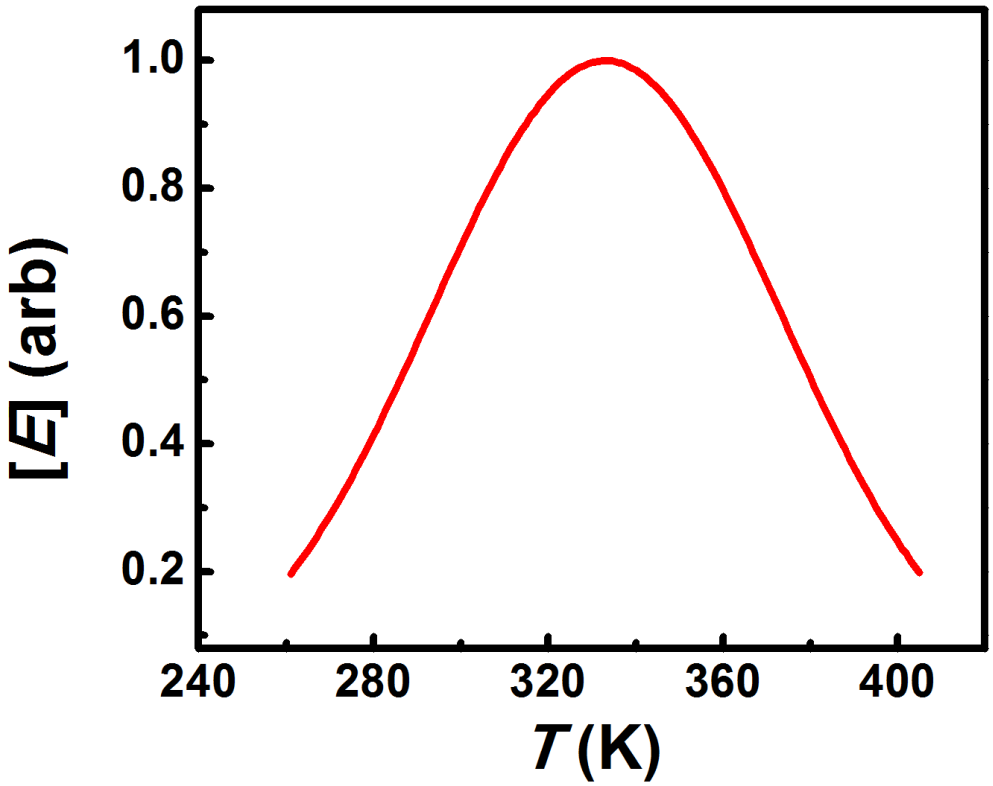

Figure C.2: *Temperature dependence of the activity of a hypothetical enzyme over a standard temperature range.*

Appendix D

Modeling the effect of ionic strength on enzyme activity

Ionic strength is defined as:

$$I = \frac{1}{2}\sum_{i=1}^{n} C_i z_i, \tag{D.1}$$

where C_i and z_i are the concentration and charge on ion i, respectively.

Beginning with *Debye-Hückel theory* [419, 420], we can express the activity coefficient γ of a charged species i as:

$$log_{10}\left(\gamma_i\right) = \frac{-z_i^2 A\sqrt{I}}{1 + B\sqrt{I}}, \tag{D.2}$$

where A and B are coefficients with values equal to 0.5 $(\mathrm{L/mol})^{1/2}$ and 1.0 $(\mathrm{L/mol})^{1/2}$, respectively, for water at 298.15 K. The activity of any charged species i is thus given by,

$$a_i = \gamma_i C_i = C_i 10^{\frac{-0.5 z_i^2 \sqrt{I}}{1+\sqrt{I}}}. \tag{D.3}$$

Considering a single-step pseudo-first-order chemical reaction:

$$A + B \xrightarrow{k_0} AB. \tag{D.4}$$

We can now express the relation using stoichiometric principles,

$$\gamma_a A + \gamma_b B \xrightarrow{k_0} \gamma AB. \tag{D.5}$$

The rate equation can hence be derived in a straightforward manner,

$$\frac{\mathrm{d}\left[\gamma AB\right]}{\mathrm{d}t} = k_0 \left[\gamma_A A\right] \left[\gamma_B B\right]. \tag{D.6}$$

Since γ is not time-varying, it can be factored from the above relation, which can be recast into the expression,

$$\frac{\mathrm{d}\left[AB\right]}{\mathrm{d}t} = k_0 \left(\frac{\gamma_A \gamma_B}{\gamma}\right) \left[A\right] \left[B\right], \tag{D.7}$$

where the new catalytic constant can be expressed as:

$$k = k_0 \left(\frac{\gamma_A \gamma_B}{\gamma}\right), \tag{D.8}$$

or,

$$log_{10}\left(k\right) = log_{10}\left(k_0\right) - log_{10}\left(\gamma\right) + log_{10}\left(\gamma_A\right) + log_{10}\left(\gamma_B\right). \tag{D.9}$$

Substituting Eq. (D.2) into (D.9) we have:

$$log_{10}\left(k\right) = log_{10}\left(k_0\right) - \frac{0.5\sqrt{I}}{1+\sqrt{I}}\left[z_A^2 + z_B^2 - \left(z_A - z_B\right)^2\right] = log_{10}\left(k_0\right) + \frac{z_A z_B \sqrt{I}}{1+\sqrt{I}} \tag{D.10}$$

and

$$k = k_0 10^{\frac{z_A z_B \sqrt{I}}{1+\sqrt{I}}}. \tag{D.11}$$

When performing electrochemical studies it is advisable to employ a buffer solution / supporting electrolyte at a concentration of at least two orders of magnitude greater than the ions that comprise the chemical system under investigation.

Index

Bibliography

[1] R. Graves. *The greek myths*, volume 1. Penguin, 1990.

[2] J.C. Lilly. *Programming and metaprogramming in the human biocomputer: theory and experiments*. The Julian Press, 1968.

[3] M.L. Simpson, G.S. Sayler, J.T. Fleming, and B. Applegate. Whole-cell biocomputing. *Trends in Biotechnology*, 19(8):317–323, 2001.

[4] M. Trupp, T. Altman, C.A. Fulcher, R. Caspi, M. Krummenacker, S. Paley, and P.D. Karp. Beyond the genome (btg) is a (pgdb) pathway genome database: Humancyc. *Genome Biology*, 11:1–1, 2010.

[5] A. Faller, M. Schünke, and G. Schünke. *The human body: an introduction to structure and function*. Thieme, 2004.

[6] A.J. Bard and L.R. Faulkner. *Electrochemical methods: fundamentals and applications, 2nd Ed*. John Wiley and Sons, 2001.

[7] J. Wang. *Analytical electrochemistry, 3rd Ed*. Wiley VCH, 2006.

[8] J. Wang. Portable electrochemical systems. *Trends in Analytical Chemistry*, 21(4):226–232, 2002.

[9] M. Pohanka and P. Skladal. Electrochemical biosensors–principles and applications. *Journal of Applied Biomedicine*, 6(2):57–64, 2008.

[10] J. Wang. Electrochemical glucose biosensors. *Chemical Reviews*, 108(2):814, 2008.

[11] G.G. Guilbault and G.J. Lubrano. An enzyme electrode for the amperometric determination of glucose. *Analytica Chimica Acta*, 64(3):439–455, 1973.

[12] I. Willner, E. Katz, A. Riklin, and R. Kasher. Mediated electron transfer in gluthathione reductase organized in self-assembled monolayers on gold electrodes. *Journal of the American Chemical Society*, 114(27):10965–10966, 1992.

[13] Y. Degani and A. Heller. Direct electrical communication between chemically modified enzymes and metal electrodes. i. electron transfer from glucose oxidase to metal electrodes via electron relays, bound covalently to the enzyme. *Journal of Physical Chemistry*, 91(6):1285–1289, 1987.

[14] G.S.F. Ling, K. Day, P. Rhee, and J.M. Ecklund. In search of technological solutions to battlefield management of combat casualties. In *Proceedings of SPIE*, volume 3712, page 1, 1999.

[15] R.J. Winterborn and T.A. Cook. The pathophysiology of severe trauma. *Surgery (Oxford)*, 21(9):240a–240e, 2003.

[16] S.G. Scott, H.G. Belanger, R.D. Vanderploeg, J. Massengale, and J. Scholten. Mechanism-of-injury approach to evaluating patients with blast-related polytrauma. *Journal of the American Osteopathic Association*, 106(5):265–270, 2006.

[17] M. Keel and O. Trentz. Pathophysiology of polytrauma. *Injury*, 36(6):691–709, 2005.

[18] PV Giannoudis. Surgical priorities in damage control in polytrauma. *Journal of Bone and Joint Surgery-British Volume*, 85(4):478–483, 2003.

[19] I. Moser, G. Jobst, and G.A. Urban. Biosensor arrays for simultaneous measurement of glucose, lactate, glutamate, and glutamine. *Biosensors and Bioelectronics*, 17(4):297–302, 2002.

[20] A. Ettinger, A.B. Laumark, R.M. Ostroff, J. Brundell, W.A. Baumgartner, and A.Y. Razumovsky. A new optical immunoassay for detection of s-100b protein in whole blood. *The Annals of Thoracic Surgery*, 68(6):2196–2201, 1999.

[21] G. Bourner, J. Dhaliwal, and J. Sumner. Performance evaluation of the latest fully automated hematology analyzers in a large, commercial laboratory setting: a 4-way, side-by-side study. *Laboratory Hematology*, 11(4):285–297, 2005.

[22] J. Wang and Q. Chen. Enzyme microelectrode array strips for glucose and lactate. *Analytical Chemistry*, 66(7):1007–1011, 1994.

[23] F.S. Ligler, K.E. Sapsford, J.P. Golden, L.C. Shriver-Lake, C.R. Taitt, M.A. Dyer, S. Barone, and C.J. Myatt. The array biosensor: portable, automated systems. *Analytical Sciences*, 23(1):5–10, 2007.

[24] R. Bashir. Biomems: state-of-the-art in detection, opportunities and prospects. *Advanced Drug Delivery Reviews*, 56(11):1565–1586, 2004.

[25] C.H. Ahn, J.W. Choi, G. Beaucage, J.H. Nevin, J.B. Lee, and A. Puntambekar. Disposable smart lab on a chip for point-of-care clinical diagnostics. *Proceedings of the IEEE*, 92(1):154–173, 2004.

[26] D.R. Thevenot, K. Toth, R.A. Durst, and G.S. Wilson. Electrochemical biosensors: recommended definitions and classification. *Analytical Letters*, 34(5):635–659, 2001.

[27] G. Strack, M. Pita, M. Ornatska, and E. Katz. Boolean logic gates that use enzymes as input signals. *ChemBioChem*, 9(8):1260–1266, 2008.

[28] J. Zhou, M.A. Arugula, J. Halámek, M. Pita, and E. Katz. Enzyme-based nand and nor logic gates with modular design. *The Journal of Physical Chemistry B*, 113(49):16065–16070, 2009.

[29] V. Privman, V. Pedrosa, D. Melnikov, M. Pita, A. Simonian, and E. Katz. Enzymatic and-gate based on electrode-immobilized glucose-6-phosphate dehydrogenase: towards digital biosensors and biochemical logic systems with low noise. *Biosensors and Bioelectronics*, 25(4):695–701, 2009.

[30] D. Melnikov, G. Strack, M. Pita, V. Privman, and E. Katz. Analog noise reduction in enzymatic logic gates. *The Journal of Physical Chemistry B*, 113(30):10472–10479, 2009.

[31] V. Privman, G. Strack, D. Solenov, M. Pita, and E. Katz. Optimization of enzymatic biochemical logic for noise reduction and scalability: how many biocomputing gates can be interconnected in a circuit? *The Journal of Physical Chemistry B*, 112(37):11777–11784, 2008.

[32] Y. Benenson, B. Gil, U. Ben-Dor, R. Adar, and E. Shapiro. An autonomous molecular computer for logical control of gene expression. *Nature*, 429(6990):423–429, 2004.

[33] J.M. Seminario and J.M. Tour. Ab initio methods for the study of molecular systems for nanometer technology: toward the first-principles design of molecular computers. *Annals of the New York Academy of Sciences*, 852(1):68–94, 1998.

[34] Y.J. Munoz and L.N. de Castro. Self-organisation and emergence in artificial life: concepts and illustrations. *Journal of Experimental & Theoretical Artificial Intelligence*, 21(4):273–292, 2009.

[35] K.J. Kim and S.B. Cho. A comprehensive overview of the applications of artificial life. *Artificial Life*, 12(1):153–182, 2006.

[36] D. Margulies and A.D. Hamilton. Digital analysis of protein properties by an ensemble of dna quadruplexes. *Journal of the American Chemical Society*, 131(26):9142–9143, 2009.

[37] E.E. May, P.L. Dolan, P.S. Crozier, S. Brozik, and M. Manginell. Towards de novo design of deoxyribozyme biosensors for gmo detection. *Sensors Journal, IEEE*, 8(6):1011–1019, 2008.

[38] G. Strack, V. Bocharova, M.A. Arugula, M. Pita, J. Halámek, and E. Katz. Artificial muscle reversibly controlled by enzyme reactions. *The Journal of Physical Chemistry Letters*, 1(5):839–843, 2010.

[39] I. Tokarev, V. Gopishetty, J. Zhou, M. Pita, M. Motornov, E. Katz, and S. Minko. Stimuli-responsive hydrogel membranes coupled with biocatalytic processes. *ACS Applied Materials & Interfaces*, 1(3):532–536, 2009.

[40] F.C. Simmel. Towards biomedical applications for nucleic acid nanodevices. *Nanomedicine*, 2(6):817–830, 2007.

[41] G. von Maltzahn, T.J. Harris, J.H. Park, D.H. Min, A.J. Schmidt, M.J. Sailor, and S.N. Bhatia. Nanoparticle self-assembly gated by logical proteolytic triggers. *Journal of the American Chemical Society*, 129(19):6064–6065, 2007.

[42] K.M. Manesh, J. Halámek, M. Pita, J. Zhou, T.K. Tam, P. Santhosh, M.C. Chuang, J.R. Windmiller, D. Abidin, E. Katz, and J. Wang. Enzyme logic gates for the digital analysis of physiological level upon injury. *Biosensors and Bioelectronics*, 24(12):3569–3574, 2009.

[43] M. Pita, J. Zhou, K.M. Manesh, J. Halámek, E. Katz, and J. Wang. Enzyme logic gates for assessing physiological conditions during an injury: Towards digital sensors and actuators. *Sensors and Actuators B: Chemical*, 139(2):631–636, 2009.

[44] M. Staiano, P. Bazzicalupo, and S. D'Auria. Glucose biosensors as models for the development of advanced protein-based biosensors. *Molecular BioSystems*, 1(5-6):354–362, 2005.

[45] J. Wang. Glucose biosensors: 40 years of advances and challenges. *Electroanalysis*, 13(12):983, 2001.

[46] P. Ciosek and W. Wróblewski. Sensor arrays for liquid sensing–electronic tongue systems. *Analyst*, 132(10):963–978, 2007.

[47] J. Wang and E. Katz. Digital biosensors with built-in logic for biomedical applicationsbiosensors based on a biocomputing concept. *Analytical and Bioanalytical Chemistry*, 398(4):1591–1603, 2010.

[48] A.L. Lehninger, D.L. Nelson, and M.M. Cox. *Lehninger principles of biochemistry*, volume 1. WH Freeman & Co, 2005.

[49] K.J. Laidler and P.S. Bunting. *The chemical kinetics of enzyme action*. Clarendon Press Oxford, 1973.

[50] A. Warshel, P.K. Sharma, M. Kato, Y. Xiang, H. Liu, and M.H.M. Olsson. Electrostatic basis for enzyme catalysis. *Chemical Reviews*, 106(8):3210–3235, 2006.

[51] Y. Cha, C.J. Murray, and J.P. Klinman. Hydrogen tunneling in enzyme reactions. *Science*, 243(4896):1325–1330, 1989.

[52] L.H. Chen, G.L. Kenyon, F. Curtin, S. Harayama, M.E. Bembenek, G. Hajipour, and C.P. Whitman. 4-oxalocrotonate tautomerase, an enzyme composed of 62 amino acid residues per monomer. *Journal of Biological Chemistry*, 267(25):17716–17721, 1992.

[53] S. Smith. The animal fatty acid synthase: one gene, one polypeptide, seven enzymes. *The FASEB Journal*, 8(15):1248–1259, 1994.

[54] C.T. Porter, G.J. Bartlett, and J.M. Thornton. The catalytic site atlas: a resource of catalytic sites and residues identified in enzymes using structural data. *Nucleic acids research*, 32(suppl 1):D129–D133, 2004.

[55] A. Radzicka and R. Wolfenden. A proficient enzyme. *Science*, 267(5194):90–93, 1995.

[56] E.C. Webb et al. *Enzyme nomenclature 1992. Recommendations of the Nomenclature Committee of the International Union of Biochemistry and Molecular Biology on the nomenclature and classification of enzymes, 6th Ed.* Academic Press, 1992.

[57] L. Menten and M.I. Michaelis. Die kinetik der invertinwirkung. *Biochemische Zeitschrift*, 49:333–369, 1913.

[58] E.L. King and C. Altman. A schematic method of deriving the rate laws for enzyme-catalyzed reactions. *The Journal of Physical Chemistry*, 60(10):1375–1378, 1956.

[59] G. Carpini, F. Lucarelli, G. Marrazza, and M. Mascini. Oligonucleotide-modified screen-printed gold electrodes for enzyme-amplified sensing of nucleic acids. *Biosensors and Bioelectronics*, 20(2):167–175, 2004.

[60] S. Centi, AI Stoica, S. Laschi, and M. Mascini. Development of an electrochemical immunoassay based on the use of an eight-electrodes screen-printed array coupled with magnetic beads for the detection of antimicrobial sulfonamides in honey. *Electroanalysis*, 22(16):1881–1888, 2010.

[61] J. Wang, J. Lu, B. Tian, and C. Yarnitzky. Screen-printed ultramicroelectrode arrays for on-site stripping measurements of trace metals. *Journal of Electroanalytical Chemistry*, 361(1-2):77–83, 1993.

[62] O. Zaouak, L. Authier, C. Cugnet, A. Castetbon, and M. Potin-Gautier. Electroanalytical device for cadmium speciation in waters. part 1: Development and characterization of a reliable screen-printed sensor. *Electroanalysis*, 22(11):1151–1158, 2010.

[63] J. Wang and B. Tian. Mercury-free disposable lead sensors based on potentiometric stripping analysis of gold-coated screen-printed electrodes. *Analytical Chemistry*, 65(11):1529–1532, 1993.

[64] O.D. Renedo, MA Alonso-Lomillo, and MJ Martinez. Recent developments in the field of screen-printed electrodes and their related applications. *Talanta*, 73(2):202–219, 2007.

[65] MA Alonso-Lomillo, O. Domínguez-Renedo, and MJ Arcos-Martínez. Screen-printed biosensors in microbiology; a review. *Talanta*, 82(5):1629–1636, 2010.

[66] J. Wang. Electrochemical sensing of explosives. *Electroanalysis*, 19(4):415–423, 2007.

[67] F. Ricci, A. Amine, G. Palleschi, and D. Moscone. Prussian blue based screen printed biosensors with improved characteristics of long-term lifetime and ph stability. *Biosensors and Bioelectronics*, 18(2):165–174, 2003.

[68] J. Wang, Q. Chen, M. Pedrero, and J.M. Pingarrón. Screen-printed amperometric biosensors for glucose and alcohols based on ruthenium-dispersed carbon inks. *Analytica Chimica Acta*, 300(1):111–116, 1995.

[69] X.M. Zhao, Y. Xia, and G.M. Whitesides. Soft lithographic methods for nano-fabrication. *Journal of Materials Chemistry*, 7(7):1069–1074, 1997.

[70] J.A. Rogers and R.G. Nuzzo. Recent progress in soft lithography. *Materials Today*, 8(2):50–56, 2005.

[71] H. Schmid and B. Michel. Siloxane polymers for high-resolution, high-accuracy soft lithography. *Macromolecules*, 33(8):3042–3049, 2000.

[72] K. Malzahn, J.R. Windmiller, G. Valdés-Ramírez, M.J. Schöning, and J. Wang. Wearable electrochemical sensors for in situ analysis in marine environments. *Analyst*, 136(14):2912–2917, 2011.

[73] J.R. Windmiller, P. Santhosh, E. Katz, and J. Wang. Bioelectronic system for the control and readout of enzyme logic gates. *Sensors and Actuators B: Chemical*, 155(1):206–213, 2011.

[74] F. Gottrup, R. Firmin, N. Chang, W.H. Goodson, and T.K. Hunt. Continuous direct tissue oxygen tension measurement by a new method using an implantable silastic tonometer and oxygen polarography. *The American Journal of Surgery*, 146(3):399–403, 1983.

[75] K.W. Johnson, J.J. Mastrototaro, D.C. Howey, R.L. Brunelle, P.L. Burden-Brady, N.A. Bryan, C.C. Andrew, H.M. Rowe, D.J. Allen, B.W. Noffke, W.C. McMahan, R.J. Morff, D. Lipson, and R.S. Nevin. In vivo evaluation of an electroenzymatic glucose sensor implanted in subcutaneous tissue. *Biosensors and Bioelectronics*, 7(10):709–714, 1992.

[76] D.N. O'Connell and B. Tursky. Silver-silver chloride sponge electrodes for skin potential recording. *The American Journal of Psychology*, 73(2):302–304, 1960.

[77] J. Wang, B. Tian, V.B. Nascimento, and L. Angnes. Performance of screen-printed carbon electrodes fabricated from different carbon inks. *Electrochimica Acta*, 43(23):3459–3465, 1998.

[78] J. Wang, M. Pedrero, H. Sakslund, O. Hammerich, and J. Pingarron. Electrochemical activation of screen-printed carbon strips. *Analyst*, 121(3):345–350, 1996.

[79] L. Garofano, M. Capra, F. Ferrari, GP Bizzaro, D. Di Tullio, M. DellOlio, and A. Ghitti. Gunshot residue: further studies on particles of environmental and occupational origin. *Forensic Science International*, 103(1):1–21, 1999.

[80] K. Schiff, D. Diehl, and A. Valkirs. Copper emissions from antifouling paint on recreational vessels. *Marine Pollution Bulletin*, 48(3):371–377, 2004.

[81] G.M. Wolten, R.S. Nesbitt, and A.R. Calloway. Particle analysis for the detection of gunshot residue. ii: Occupational and environmental. *Journal of Forensic Sciences*, 24(2):423–430, 1979.

[82] J. Wang, S.B. Hocevar, and B. Ogorevc. Carbon nanotube-modified glassy carbon electrode for adsorptive stripping voltammetric detection of ultra-trace levels of 2, 4, 6-trinitrotoluene. *Electrochemistry Communications*, 6(2):176–179, 2004.

[83] K.A. Joshi, J. Tang, R. Haddon, J. Wang, W. Chen, and A. Mulchandani. A disposable biosensor for organophosphorus nerve agents based on carbon nanotubes modified thick film strip electrode. *Electroanalysis*, 17(1):54–58, 2005.

[84] H.K. Choi, S. Liu, and G. Curhan. Intake of purine-rich foods, protein, and dairy products and relationship to serum levels of uric acid: The third

national health and nutrition examination survey. *Arthritis & Rheumatism*, 52(1):283–289, 2005.

[85] E. Barsoukov and J.R. Macdonald. *Impedance spectroscopy: theory, experiment, and applications, 2nd Ed.* John Wiley and Sons, 2005.

[86] A.H.B. Wu, F.S. Apple, W.B. Gibler, R.L. Jesse, M.M. Warshaw, and R. Valdes Jr. National academy of clinical biochemistry standards of laboratory practice: recommendations for the use of cardiac markers in coronary artery diseases. *Clinical Chemistry*, 45(7):1104–1121, 1999.

[87] G.X. Brogan Jr and J.L. Bock. Cardiac marker point-of-care testing in the emergency department and cardiac care unit. *Clinical Chemistry*, 44(8):1865–1869, 1998.

[88] P.J. Zimetbaum and M.E. Josephson. Use of the electrocardiogram in acute myocardial infarction. *New England Journal of Medicine*, 348(10):933–940, 2003.

[89] C.W. Hamm, B.U. Goldmann, C. Heeschen, G. Kreymann, J. Berger, and T. Meinertz. Emergency room triage of patients with acute chest pain by means of rapid testing for cardiac troponin t or troponin i. *New England Journal of Medicine*, 337(23):1648–1653, 1997.

[90] D.A. Morrow. Appraisal of myeloperoxidase for evaluation of patients with suspected acute coronary syndromes. *Journal of the American College of Cardiology*, 49(20):2001, 2007.

[91] M.L. Brennan, M.S. Penn, F. Van Lente, V. Nambi, M.H. Shishehbor, R.J. Aviles, M. Goormastic, M.L. Pepoy, E.S. McErlean, E.J. Topol, S.E. Nissen, and S.L. Hazen. Prognostic value of myeloperoxidase in patients with chest pain. *New England Journal of Medicine*, 349(17):1595–1604, 2003.

[92] S. Baldus, C. Heeschen, T. Meinertz, A.M. Zeiher, J.P. Eiserich, T. Münzel, M.L. Simoons, and C.W. Hamm. Myeloperoxidase serum levels predict risk in patients with acute coronary syndromes. *Circulation*, 108(12):1440–1445, 2003.

[93] T.J. Mocatta, A.P. Pilbrow, V.A. Cameron, R. Senthilmohan, C.M. Frampton, A.M. Richards, and C.C. Winterbourn. Plasma concentrations of myeloperoxidase predict mortality after myocardial infarction. *Journal of the American College of Cardiology*, 49(20):1993–2000, 2007.

[94] K. Suzuki, H. Ota, S. Sasagawa, T. Sakatani, and T. Fujikura. Assay method for myeloperoxidase in human polymorphonuclear leukocytes. *Analytical biochemistry*, 132(2):345–352, 1983.

[95] G. Graff, D.A. Gamache, M.T. Brady, J.M. Spellman, and J.M. Yanni. Improved myeloperoxidase assay for quantitation of neutrophil influx in a rat model of endotoxin-induced uveitis. *Journal of Pharmacological and Toxicological Methods*, 39(3):169–178, 1998.

[96] S. Babu, S. Mohapatra, L. Zubkov, S. Murthy, and E. Papazoglou. A pmma microcapillary quantum dot linked immunosorbent assay (qlisa). *Biosensors and Bioelectronics*, 24(12):3467–3474, 2009.

[97] K.C. Lin, V. Kunduru, M. Bothara, K. Rege, S. Prasad, and B.L. Ramakrishna. Biogenic nanoporous silica-based sensor for enhanced electrochemical detection of cardiovascular biomarkers proteins. *Biosensors and Bioelectronics*, 25(10):2336–2342, 2010.

[98] J. Anzai, H. Takeshita, Y. Kobayashi, T. Osa, and T. Hoshi. Layer-by-layer construction of enzyme multilayers on an electrode for the preparation of glucose and lactate sensors: elimination of ascorbate interference by means of an ascorbate oxidase multilayer. *Analytical Chemistry*, 70(4):811–817, 1998.

[99] F. Passardi, G. Theiler, M. Zamocky, C. Cosio, N. Rouhier, F. Teixera, M. Margis-Pinheiro, V. Ioannidis, C. Penel, L. Falquet, and C. Dunand. Peroxibase: the peroxidase database. *Phytochemistry*, 68(12):1605–1611, 2007.

[100] L. Guemouri, Y. Artur, B. Herbeth, C. Jeandel, G. Cuny, and G. Siest. Biological variability of superoxide dismutase, glutathione peroxidase, and catalase in blood. *Clinical Chemistry*, 37(11):1932–1937, 1991.

[101] J. Sedlak and R.H. Lindsay. Estimation of total, protein-bound, and nonprotein sulfhydryl groups in tissue with ellman's reagent. *Analytical Biochemistry*, 25(1):192, 1968.

[102] F.S. Apple and M. Rhodes. Enzymatic estimation of skeletal muscle damage by analysis of changes in serum creatine kinase. *Journal of Applied Physiology*, 65(6):2598–2600, 1988.

[103] J.E. Olerud, L.D. Homer, and H.W. Carroll. Incidence of acute exertional rhabdomyolysis: serum myoglobin and enzyme levels as indicators of muscle injury. *Archives of Internal Medicine*, 136(6):692, 1976.

[104] A. Kratz, M. Ferraro, P.M. Sluss, and K.B. Lewandrowski. Laboratory reference values. *New England Journal of Medicine*, 351:1548–1564, 2004.

[105] I. Hara, Y. Nakano, H. Okada, S. Arakawa, and S. Kamidono. Treatment of crush syndrome patients following the great hanshin earthquake. *International Journal of Urology*, 4(2):202–204, 1997.

[106] M. Kaste, J. Hernesniemi, H. Somer, M. Hillbom, and A. Konttinen. Creatine kinase isoenzymes in acute brain injury. *Journal of Neurosurgery*, 55(4):511–515, 1981.

[107] A.J. Pesce and L.A. Kaplan. *Methods in clinical chemistry*. Mosby, 1987.

[108] E. Katz and V. Privman. Enzyme-based logic systems for information processing. *Chemical Society Reviews*, 39(5):1835–1857, 2010.

[109] A.L. Babson and S.R. Babson. Kinetic colorimetric measurement of serum lactate dehydrogenase activity. *Clinical Chemistry*, 19(7):766–769, 1973.

[110] G. Szasz, W. Gruber, and E. Bernt. Creatine kinase in serum: 1. determination of optimum reaction conditions. *Clinical Chemistry*, 22(5):650–656, 1976.

[111] R.J. Gay, R.B. McComb, and G.N. Bowers Jr. Optimum reaction conditions for human lactate dehydrogenase isoenzymes as they affect total lactate dehydrogenase activity. *Clinical Chemistry*, 14(8):740–753, 1968.

[112] M.L. Tanzer and C. Gilvarg. Creatine and creatine kinase measurement. *Journal of Biological Chemistry*, 234(12):3201–3204, 1959.

[113] T. Sammour, A. Kahokehr, S. Caldwell, and A.G. Hill. Venous glucose and arterial lactate as biochemical predictors of mortality in clinically severely injured trauma patients–a comparison with iss and triss. *Injury*, 40(1):104–108, 2009.

[114] M. Faul, L. Xu, M.M. Wald, and V.G. Coronado. Traumatic brain injury in the united states: emergency department visits, hospitalizations, and deaths. atlanta (ga): Centers for disease control and prevention. *National Center for Injury Prevention and Control*, 2010.

[115] S.T. DeKosky, M.D. Ikonomovic, and S. Gandy. Traumatic brain injury–football, warfare, and long-term effects. *New England Journal of Medicine*, 363(14):1293–1296, 2010.

[116] B.S. Meldrum et al. Glutamate as a neurotransmitter in the brain: review of physiology and pathology. *The Journal of Nutrition*, 130(4S Suppl):1007S–1015S, 2000.

[117] D.W. Choi. Methods for antagonizing glutamate neurotoxicity. *Cerebrovascular and Brain Metabolism Reviews*, 2(2):105–147, 1990.

[118] T. Opitz and K.G. Reymann. Metabotropic glutamate receptors are involved in hypoxic/hypoglycemic injury of hippocampal ca1 neurons in vitro. *Neuropsychopharmacology*, 11(4):278–278, 1994.

[119] T. Griffiths, M.C. Evans, and B.S. Meldrum. Status epilepticus: the reversibility of calcium loading and acute neuronal pathological changes in the rat hippocampus. *Neuroscience*, 12(2):557–567, 1984.

[120] J.T. Greenamyre and A.B. Young. Excitatory amino acids and alzheimer's disease. *Neurobiology Aging*, 10(5):593–602, 1989.

[121] A.J. Baker, R.J. Moulton, V.H. MacMillan, and P.M. Shedden. Excitatory amino acids in cerebrospinal fluid following traumatic brain injury in humans. *Journal of Neurosurgery*, 79(3):369–372, 1993.

[122] A.M. Palmer, D.W. Marion, M.L. Botscheller, P.E. Swedlow, S.D. Styren, and S.T. DeKosky. Traumatic brain injury-induced excitotoxicity assessed in a controlled cortical impact model. *Journal of Neurochemistry*, 61(6):2015–2024, 1993.

[123] J.I.M. Brown, A.J. Baker, S.J. Konasiewicz, and R.J. Moulton. Clinical significance of csf glutamate concentrations following severe traumatic brain injury in humans. *Journal of Neurotrauma*, 15(4):253–263, 1998.

[124] M. Suzuki, A. Kudo, A. Sugawara, K. Yoshida, Y. Kubo, T. Suzuki, K. Ogasawara, M. Doi, and A. Ogawa. Amino acid concentrations in the blood of the jugular vein and peripheral artery after traumatic brain injury: decreased release of glutamate into the jugular vein in the early phase. *Journal of Neurotrauma*, 19(2):285–292, 2002.

[125] T. Ingebrigtsen and B. Romner. Biochemical serum markers of traumatic brain injury. *The Journal of Trauma*, 52(4):798–808, 2002.

[126] R.C. Cabot, N.L. Harris, J.A.O. Shepard, S.H. Ebeling, S.M. Ellender, C.C. Peters, A. Kratz, M. Ferraro, P.M. Sluss, and K.B. Lewandrowski. Normal reference laboratory values. *New England Journal of Medicine*, 351(15):1548–1563, 2004.

[127] R.A.E. Bakay and A.A. Ward Jr. Enzymatic changes in serum and cerebrospinal fluid in neurological injury. *Journal of Neurosurgery*, 58(1):27–37, 1983.

[128] J. Halámek, J.R. Windmiller, J. Zhou, M.C. Chuang, P. Santhosh, G. Strack, M.A. Arugula, S. Chinnapareddy, V. Bocharova, J. Wang, and E. Katz. Multiplexing of injury codes for the parallel operation of enzyme logic gates. *Analyst*, 135(9):2249–2259, 2010.

[129] D. Melnikov, G. Strack, J. Zhou, J.R. Windmiller, J. Halámek, V. Bocharova, M.C. Chuang, P. Santhosh, V. Privman, J. Wang, and E. Katz. Enzymatic and logic gates operated under conditions characteristic of biomedical applications. *The Journal of Physical Chemistry B*, 114(37):12166–12174, 2010.

[130] J. Halámek, V. Bocharova, S. Chinnapareddy, J.R. Windmiller, G. Strack, M.C. Chuang, J. Zhou, P. Santhosh, G.V. Ramirez, M.A. Arugula, J. Wang, and E. Katz. Multi-enzyme logic network architectures for assessing injuries: digital processing of biomarkers. *Molecular BioSystems*, 6(12):2554–2560, 2010.

[131] J. Zhou, J. Halámek, V. Bocharova, J. Wang, and E. Katz. Bio-logic analysis of injury biomarker patterns in human serum samples. *Talanta*, 83(3):955–959, 2011.

[132] H.U. Bergmeyer, P. Scheibe, and A.W. Wahlefeld. Optimization of methods for aspartate aminotransferase and alanine aminotransferase. *Clinical Chemistry*, 24(1):58–73, 1978.

[133] T. Yao, N. Kobayashi, and T. Wasa. Flow-injection analysis for l-glutamate using immobilized l-glutamate oxidase: comparison of an enzyme reactor and enzyme electrode. *Analytica Chimica Acta*, 231:121–124, 1990.

[134] J.R. Windmiller, G. Strack, M.C. Chuang, J. Halámek, P. Santhosh, V. Bocharova, J. Zhou, E. Katz, and J. Wang. Boolean-format biocatalytic processing of enzyme biomarkers for the diagnosis of soft tissue injury. *Sensors and Actuators B: Chemical*, 150(1):285–290, 2010.

[135] A. Liu, Q. Zhao, and X. Guan. Stochastic nanopore sensors for the detection of terrorist agents: Current status and challenges. *Analytica Chimica Acta*, 675(2):106–115, 2010.

[136] J. Yinon. Field detection and monitoring of explosives. *TrAC Trends in Analytical Chemistry*, 21(4):292–301, 2002.

[137] J.L. Staymates and G. Gillen. Fabrication and characterization of gelatin-based test materials for verification of trace contraband vapor detectors. *Analyst*, 135(10):2573–2578, 2010.

[138] A.P. de Silva. Molecular computing: A layer of logic. *Nature*, 454(7203):417–418, 2008.

[139] R. Baron, O. Lioubashevski, E. Katz, T. Niazov, and I. Willner. Elementary arithmetic operations by enzymes: A model for metabolic pathway based computing. *Angewandte Chemie International Edition*, 45(10):1572–1576, 2006.

[140] T. Konry and D.R. Walt. Intelligent medical diagnostics via molecular logic. *Journal of the American Chemical Society*, 131(37):13232–13233, 2009.

[141] A.A. Karyakin, E.A. Puganova, I.A. Budashov, I.N. Kurochkin, E.E. Karyakina, V.A. Levchenko, V.N. Matveyenko, and S.D. Varfolomeyev. Prussian blue based nanoelectrode arrays for h_2o_2 detection. *Analytical Chemistry*, 76(2):474–478, 2004.

[142] M.A. Arugula, J. Halámek, E. Katz, D. Melnikov, M. Pita, V. Privman, and G. Strack. Optimization of enzymatic logic gates and networks for noise reduction and stability. In *Advances in Circuits, Electronics and Microelectronics, 2009. CENICS'09. Second International Conference on*, pages 1–7. IEEE, 2009.

[143] T.K. Tam, M. Pita, and E. Katz. Enzyme logic network analyzing combinations of biochemical inputs and producing fluorescent output signals: Towards multi-signal digital biosensors. *Sensors and Actuators B: Chemical*, 140(1):1–4, 2009.

[144] V. Privman, M.A. Arugula, J. Halámek, M. Pita, and E. Katz. Network analysis of biochemical logic for noise reduction and stability: a system of three coupled enzymatic and gates. *The Journal of Physical Chemistry B*, 113(15):5301–5310, 2009.

[145] M. Privman, T.K. Tam, M. Pita, and E. Katz. Switchable electrode controlled by enzyme logic network system: Approaching physiologically regulated bioelectronics. *Journal of the American Chemical Society*, 131(3):1314–1321, 2008.

[146] E. Katz, V. Privman, and J. Wang. Towards biosensing strategies based on biochemical logic systems. In *Quantum, Nano and Micro Technologies, 2010. ICQNM'10. Fourth International Conference on*, pages 1–9. IEEE, 2010.

[147] D. Michaeli. Medicine on the battlefield: a review. *Journal of the Royal Society of Medicine*, 72(5):370–373, 1979.

[148] M. Wilson, D.P. Davis, and R. Coimbra. Diagnosis and monitoring of hemorrhagic shock during the initial resuscitation of multiple trauma patients: a review. *Journal of Emergency Medicine*, 24(4):413–422, 2003.

[149] H.R. Champion, R.F. Bellamy, C.P. Roberts, and A. Leppaniemi. A profile of combat injury. *The Journal of Trauma*, 54(5):S13–S19, 2003.

[150] M.E. Clark, M.J. Bair, C.C. Buckenmaier, R.J. Gironda, and RL Walker. Pain and combat injuries in soldiers returning from operations enduring freedom and iraqi freedom: implications for research and practice. *Journal of Rehabilitation Research and Development*, 44(2):179–194, 2007.

[151] B.J. Zink, C.H. Schultz, X. Wang, M. Mertz, S.A. Stern, and A.L. Betz. Effects of ethanol on brain lactate in experimental traumatic brain injury with hemorrhagic shock. *Brain Research*, 837(1-2):1–7, 1999.

[152] J.C. Rosenberg, R.C. Lillehei, J. Longerbeam, and B. Zimmermann. Studies on hemorrhagic and endotoxin shock in relation to vasomotor changes and endogenous circulating epinephrine, norepinephrine and serotonin. *Annals of Surgery*, 154(4):611–627, 1961.

[153] M.R. Prasad, C. Ramaiah, T.K. McIntosh, R.J. Dempsey, S. Hipkens, and D. Yurek. Regional levels of lactate and norepinephrine after experimental brain injury. *Journal of Neurochemistry*, 63(3):1086–1094, 1994.

[154] K.K. Tan, S.L. Bang, A. Vijayan, and M.T. Chiu. Hepatic enzymes have a role in the diagnosis of hepatic injury after blunt abdominal trauma. *Injury*, 40(9):978–983, 2009.

[155] J.A. Kline, P.C. Maiorano, J.D. Schroeder, R.M. Grattan, T.C. Vary, and J.A. Watts. Activation of pyruvate dehydrogenase improves heart function and metabolism after hemorrhagic shock. *Journal of Molecular and Cellular Cardiology*, 29(9):2465–2474, 1997.

[156] T. Weinstein, A. Chagnac, A. Korzets, M. Boaz, Y. Ori, M. Herman, T. Malachi, and U. Gafter. Haemolysis in haemodialysis patients: evidence for impaired defence mechanisms against oxidative stress. *Nephrology Dialysis Transplantation*, 15(6):883–887, 2000.

[157] R. Rossi, A. Milzani, I. Dalle-Donne, D. Giustarini, L. Lusini, R. Colombo, and P. Di Simplicio. Blood glutathione disulfide: in vivo factor or in vitro artifact? *Clinical Chemistry*, 48(5):742–753, 2002.

[158] A. Bhasale. The wrong diagnosis: identifying causes of potentially adverse events in general practice using incident monitoring. *Family Practice*, 15(4):308–318, 1998.

[159] J.A. Pineda, K.K.W. Wang, and R.L. Hayes. Biomarkers of proteolytic damage following traumatic brain injury. *Brain Pathology*, 14(2):202–209, 2004.

[160] L. Papa, G. Robinson, M. Oli, J. Pineda, J. Demery, G. Brophy, S.A. Robicsek, A. Gabrielli, C.S. Robertson, K.K. Wang, and R.L. Hayes. Use of biomarkers for diagnosis and management of traumatic brain injury patients. *Expert Opinion on Medical Diagnostics*, 2(8):937–945, 2008.

[161] I. Moser, G. Jobst, P. Svasek, M. Varahram, and G. Urban. Rapid liver enzyme assay with miniaturized liquid handling system comprising thin film biosensor array. *Sensors and Actuators B: Chemical*, 44(1-3):377–380, 1997.

[162] A.P. Wheeler and G.R. Bernard. Treating patients with severe sepsis. *New England Journal of Medicine*, 340(3):207–214, 1999.

[163] N.D. Maynard, R.C. Mason, D.J. Bihari, R.N. Dalton, R. Beale, and M.N. Smithies. Liver function and splanchnic ischemia in critically iii patients. *Chest*, 111(1):180–187, 1997.

[164] K.A. Kudsk, M.A. Croce, T.C. Fabian, G. Minard, E.A. Tolley, H.A. Poret, M.R. Kuhl, and R.O. Brown. Enteral versus parenteral feeding. effects on septic morbidity after blunt and penetrating abdominal trauma. *Annals of Surgery*, 215(5):503–513, 1992.

[165] D.P. Rignault. Abdominal trauma in war. *World Journal of Surgery*, 16(5):940–946, 1992.

[166] S.D. Sprules, J.P. Hart, S.A. Wring, and R. Pittson. A reagentless, disposable biosensor for lactic acid based on a screen-printed carbon electrode containing meldola's blue and coated with lactate dehydrogenase, nad+ and cellulose acetate. *Analytica Chimica Acta*, 304(1):17–24, 1995.

[167] I. Wedmore, J.G. McManus, A.E. Pusateri, and J.B. Holcomb. A special report on the chitosan-based hemostatic dressing: experience in current combat operations. *The Journal of Trauma*, 60(3):655–658, 2006.

[168] D. Lakstein, A. Blumenfeld, T. Sokolov, G. Lin, R. Bssorai, M. Lynn, and R.B. Abraham. Tourniquets for hemorrhage control on the battlefield: a 4-year accumulated experience. *The Journal of Trauma*, 54(5):S221–S225, 2003.

[169] G. Lanzino, N.F. Kassell, T. Germanson, L. Truskowski, and W. Alves. Plasma glucose levels and outcome after aneurysmal subarachnoid hemorrhage. *Journal of Neurosurgery*, 79(6):885–891, 1993.

[170] W.M. Manger, J.L. Bollman, F.T. Maher, and J. Berkson. Plasma concentration of epinephrine and norepinephrine in hemorrhagic and anaphylactic shock. *American Journal of Physiology–Legacy Content*, 190(2):310–316, 1957.

[171] H. Sies. Oxidative stress: oxidants and antioxidants. *Experimental Physiology*, 82(2):291–295, 1997.

[172] K. Taber, D. Warden, and R. Hurley. Blast-related traumatic brain injury: what is known? *The Journal of Neuropsychiatry and Clinical Neurosciences*, 18(2):141–145, 2006.

[173] P. Eyer and D. Podhradskỳ. Evaluation of the micromethod for determination of glutathione using enzymatic cycling and ellman's reagent. *Analytical Biochemistry*, 153(1):57–66, 1986.

[174] P.D. Josephy, T. Eling, and R.P. Mason. The horseradish peroxidase-catalyzed oxidation of 3, 5, 3', 5'-tetramethylbenzidine. free radical and charge-transfer complex intermediates. *Journal of Biological Chemistry*, 257(7):3669–3675, 1982.

[175] H.U. Bergmeyer and K. Gawehn. *Methods of enzymatic analysis: edited by Hans Ulrich Bergmeyer in collaboration with Karlfried Gawehn.* Academic Press, 1974.

[176] R.P. Berger, K. Hymel, and W.M. Gao. The use of biomarkers after inflicted traumatic brain injury: Insight into etiology, pathophysiology, and biochemistry. *Clinical Pediatric Emergency Medicine*, 7(3):186–193, 2006.

[177] A.P. de Silva, S. Uchiyama, T.P. Vance, and B. Wannalerse. A supramolecular chemistry basis for molecular logic and computation. *Coordination Chemistry Reviews*, 251(13-14):1623–1632, 2007.

[178] A.P. de Silva and S. Uchiyama. Molecular logic and computing. *Nature Nanotechnology*, 2(7):399–410, 2007.

[179] K. Szaciłowski. Digital information processing in molecular systems. *Chemical Reviews*, 108(9):3481–3548, 2008.

[180] A. Credi. Molecules that make decisions. *Angewandte Chemie International Edition*, 46(29):5472–5475, 2007.

[181] U. Pischel. Chemical approaches to molecular logic elements for addition and subtraction. *Angewandte Chemie International Edition*, 46(22):4026–4040, 2007.

[182] A. Saghatelian, N.H. Völcker, K.M. Guckian, S.Y.L. Victor, and M.R. Ghadiri. Dna-based photonic logic gates: And, nand, and inhibit. *Journal of the American Chemical Society*, 125(2):346–347, 2003.

[183] G. Ashkenasy and M.R. Ghadiri. Boolean logic functions of a synthetic peptide network. *Journal of the American Chemical Society*, 126(36):11140–11141, 2004.

[184] I. Willner. *Bioelectronics: from theory to applications.* Wiley-VCH, 2006.

[185] A. Adamatzky, L. Bull, and B.D.L. Costello. *Unconventional computing 2007.* Luniver Press, 2007.

[186] C.S. Calude, J.F.G. da Costa, and N. Dershowitz. *Unconventional Computation: 8th International Conference, UC 2009, Ponta Delgada, Portugal, September 7-11, 2009, Proceedings*, volume 5715. Springer-Verlag New York Inc, 2009.

[187] P.A. de Silva, N.H.Q. Gunaratne, and C.P. McCoy. A molecular photoionic and gate based on fluorescent signalling. *Nature*, 364(6432):42–44, 1993.

[188] A.P. de Silva, H.Q.N. Gunaratne, and C.P. McCoy. Molecular photoionic and logic gates with bright fluorescence and off-on digital action. *Journal of the American Chemical Society*, 119(33):7891–7892, 1997.

[189] A. Credi, V. Balzani, S.J. Langford, and J.F. Stoddart. Logic operations at the molecular level. an xor gate based on a molecular machine. *Journal of the American Chemical Society*, 119(11):2679–2681, 1997.

[190] A.P. de Silva and N.D. McClenaghan. Simultaneously multiply-configurable or superposed molecular logic systems composed of ict (internal charge transfer) chromophores and fluorophores integrated with one-or two-ion receptors. *Chemistry-A European Journal*, 8(21):4935–4945, 2002.

[191] S.D. Straight, P.A. Liddell, Y. Terazono, T.A. Moore, A.L. Moore, and D. Gust. All-photonic molecular xor and nor logic gates based on photochemical control of fluorescence in a fulgimide–porphyrin–dithienylethene triad. *Advanced Functional Materials*, 17(5):777–785, 2007.

[192] T. Gunnlaugsson, D.A. Mac Dónaill, and D. Parker. Lanthanide macrocyclic quinolyl conjugates as luminescent molecular-level devices. *Journal of the American Chemical Society*, 123(51):12866–12876, 2001.

[193] M. de Sousa, B. de Castro, S. Abad, M.A. Miranda, and U. Pischel. A molecular tool kit for the variable design of logic operations (nor, inh, ennor). *Chemical Communications*, (19):2051–2053, 2006.

[194] R. Baron, O. Lioubashevski, E. Katz, T. Niazov, and I. Willner. Logic gates and elementary computing by enzymes. *The Journal of Physical Chemistry A*, 110(27):8548–8553, 2006.

[195] N. Wagner and G. Ashkenasy. Systems chemistry: logic gates, arithmetic units, and network motifs in small networks. *Chemistry-A European Journal*, 15(7):1765–1775, 2009.

[196] G. Strack, S. Chinnapareddy, D. Volkov, J. Halámek, M. Pita, I. Sokolov, and E. Katz. Logic networks based on immunorecognition processes. *The Journal of Physical Chemistry B*, 113(35):12154–12159, 2009.

[197] T. Niazov, R. Baron, E. Katz, O. Lioubashevski, and I. Willner. Concatenated logic gates using four coupled biocatalysts operating in series. *Proceedings of the National Academy of Sciences*, 103(46):17160, 2006.

[198] M.N. Chatterjee, E.R. Kay, and D.A. Leigh. Beyond switches: ratcheting a particle energetically uphill with a compartmentalized molecular machine. *Journal of the American Chemical Society*, 128(12):4058–4073, 2006.

[199] R. Baron, A. Onopriyenko, E. Katz, O. Lioubashevski, I. Willner, S. Wang, and H. Tian. An electrochemical/photochemical information processing system using a monolayer-functionalized electrode. *Chemical Communications*, (20):2147–2149, 2006.

[200] E. Katz and I. Willner. A quinone-functionalized electrode in conjunction with hydrophobic magnetic nanoparticles acts as a write–read–erase information storage system. *Chemical Communications*, (45):5641–5643, 2005.

[201] F. Galindo, J.C. Lima, S.V. Luis, A.J. Parola, and F. Pina. Write–read–erase molecular-switching system trapped in a polymer hydrogel matrix. *Advanced Functional Materials*, 15(4):541–545, 2005.

[202] A. Bandyopadhyay and A.J. Pal. Memory-switching phenomenon in acceptor-rich organic molecules: Impedance spectroscopic studies. *The Journal of Physical Chemistry B*, 109(13):6084–6088, 2005.

[203] M. Pita, G. Strack, K. MacVittie, J. Zhou, and E. Katz. Set- reset flip-flop memory based on enzyme reactions: toward memory systems controlled by biochemical pathways. *The Journal of Physical Chemistry B*, 113(49):16071–16076, 2009.

[204] U. Pischel and B. Heller. Molecular logic devices (half-subtractor, comparator, complementary output circuit) by controlling photoinduced charge transfer processes. *New Journal of Chemistry*, 32(3):395–400, 2008.

[205] J. Andréasson, D. Stephen, S. Bandyopadhyay, R.H. Mitchell, T.A. Moore, A.L. Moore, and D. Gust. A molecule-based 1: 2 digital demultiplexer. *The Journal of Physical Chemistry C*, 111(38):14274–14278, 2007.

[206] M. Amelia, M. Baroncini, and A. Credi. A simple unimolecular multiplexer/demultiplexer. *Angewandte Chemie International Edition*, 120(33):6336–6339, 2008.

[207] E. Perez-Inestrosa, J.M. Montenegro, D. Collado, and R. Suau. A molecular 1:2 demultiplexer. *Chemical Communications*, (9):1085–1087, 2008.

[208] M.A. Arugula, V. Bocharova, J. Halámek, M. Pita, and E. Katz. Enzyme-based multiplexer and demultiplexer. *The Journal of Physical Chemistry B*, 114(15):5222–5226, 2010.

[209] J. Andréasson, S.D. Straight, T.A. Moore, A.L. Moore, and D. Gust. Molecular all-photonic encoder-decoder. *Journal of the American Chemical Society*, 130(33):11122–11128, 2008.

[210] D.H. Qu, Q.C. Wang, and H. Tian. A half adder based on a photochemically driven [2] rotaxane. *Angewandte Chemie International Edition*, 44(33):5296–5299, 2005.

[211] J. Andréasson, D. Stephen, G. Kodis, Choong-Do Park, M. Hambourger, M. Gervaldo, B. Albinsson, T.A. Moore, A.L. Moore, and D. Gust. All-photonic molecular half-adder. *Journal of the American Chemical Society*, 128(50):16259–16265, 2006.

[212] J. Andréasson, G. Kodis, Y. Terazono, P.A. Liddell, S. Bandyopadhyay, R.H. Mitchell, T.A. Moore, A.L. Moore, and D. Gust. Molecule-based photonically switched half-adder. *Journal of the American Chemical Society*, 126(49):15926–15927, 2004.

[213] M.V. López, M.E. Vázquez, C. Gómez-Reino, R. Pedrido, and M.R. Bermejo. A metallo-supramolecular approach to a half-subtractor. *New Journal of Chemistry*, 32(9):1473–1477, 2008.

[214] D. Margulies, G. Melman, and A. Shanzer. A molecular full-adder and full-subtractor, an additional step toward a moleculator. *Journal of the American Chemical Society*, 128(14):4865–4871, 2006.

[215] O. Kuznetz, H. Salman, N. Shakkour, Y. Eichen, and S. Speiser. A novel all optical molecular scale full adder. *Chemical Physics Letters*, 451(1-3):63–67, 2008.

[216] D. Margulies, C.E. Felder, G. Melman, and A. Shanzer. A molecular keypad lock: A photochemical device capable of authorizing password entries. *Journal of the American Chemical Society*, 129(2):347–354, 2007.

[217] M. Suresh, A. Ghosh, and A. Das. A simple chemosensor for hg2+ and cu2+ that works as a molecular keypad lock. *Chemical Communications*, (33):3906–3908, 2008.

[218] M. Kumar, R. Kumar, and V. Bhalla. A reversible fluorescent hg2+/k+ switch that works as keypad lock in the presence of f- ion. *Chemical Communications*, (47):7384–7386, 2009.

[219] Z. Guo, W. Zhu, L. Shen, and H. Tian. A fluorophore capable of crossword puzzles and logic memory. *Angewandte Chemie International Edition*, 119(29):5645–5649, 2007.

[220] G. Strack, M. Ornatska, M. Pita, and E. Katz. Biocomputing security system: concatenated enzyme-based logic gates operating as a biomolecular keypad lock. *Journal of the American Chemical Society*, 130(13):4234–4235, 2008.

[221] J. Halámek, T.K. Tam, S. Chinnapareddy, V. Bocharova, and E. Katz. Keypad lock security system based on immune-affinity recognition integrated with a switchable biofuel cell. *The Journal of Physical Chemistry Letters*, 1(6):973–977, 2010.

[222] J. Halámek, T.K. Tam, G. Strack, V. Bocharova, M. Pita, and E. Katz. Self-powered biomolecular keypad lock security system based on a biofuel cell. *Chemical Communications*, 46(14):2405–2407, 2010.

[223] M.N. Stojanovic, D. Stefanovic, et al. A deoxyribozyme-based molecular automaton. *Nature Biotechnology*, 21(9):1069–1074, 2003.

[224] J. Macdonald, Y. Li, M. Sutovic, H. Lederman, K. Pendri, W. Lu, B.L. Andrews, D. Stefanovic, and M.N. Stojanovic. Medium scale integration of molecular logic gates in an automaton. *Nano letters*, 6(11):2598–2603, 2006.

[225] V. Privman. Error-control and digitalization concepts for chemical and biomolecular information processing systems. *Journal of Computational and Theoretical Nanoscience*, 8(3):490–502, 2011.

[226] V. Zewe and H.J. Fromm. Kinetic studies of rabbit muscle lactate dehydrogenase. ii. mechanism of the reaction*. *Biochemistry*, 4(4):782–792, 1965.

[227] C.O. Hewitt, C.M. Eszes, R.B. Sessions, K.M. Moreton, T.R. Dafforn, J. Takei, C.E. Dempsey, A.R. Clarke, and J.J. Holbrook. A general method for relieving substrate inhibition in lactate dehydrogenases. *Protein Engineering*, 12(6):491–496, 1999.

[228] M.J. Boland and H. Gutfreund. Pig heart lactate dehydrogenase. binding of pyruvate and the interconversion of pyruvate-containing ternary complexes. *Biochemical Journal*, 151(3):715, 1975.

[229] EF Pai and G.E. Schulz. The catalytic mechanism of glutathione reductase as derived from x-ray diffraction analyses of reaction intermediates. *Journal of Biological Chemistry*, 258(3):1752–1757, 1983.

[230] M.A. Vanoni, K.K. Wong, D.P. Ballou, and J.S. Blanchard. Glutathione reductase: comparison of steady-state and rapid reaction primary kinetic isotope effects exhibited by the yeast, spinach, and escherichia coli enzymes. *Biochemistry*, 29(24):5790–5796, 1990.

[231] B. Tandoğan and N.N. Ulusu. Kinetic mechanism and molecular properties of glutathione reductase. *FABAD J. Pharm. Sci*, 31(4):230–237, 2006.

[232] F.J. Nöhring. *Fachwörterbuch kompakt Medizin Englisch*. Elsevier, Urban&FischerVerlag, 2004.

[233] W. Heil, R. Koberstein, and B. Zawta. *Pre-Analytical Considerations*.

[234] S.A. Wring, J.P. Hart, and B.J. Birch. Development of an improved carbon electrode chemically modified with cobalt phthalocyanine as a re-usable sensor for glutathione. *Analyst*, 114(12):1563–1570, 1989.

[235] N. Sehlotho, S. Griveau, N. Ruillé, M. Boujtita, T. Nyokong, and F. Bedioui. Electro-catalyzed oxidation of reduced glutathione and 2-mercaptoethanol by cobalt phthalocyanine-containing screen printed graphite electrodes. *Materials Science and Engineering: C*, 28(5-6):606–612, 2008.

[236] J.A. Smith. Exercise, training and red blood cell turnover. *New Zealand Journal of Sports Medicine*, 19(1):9, 1995.

[237] W. Laureyn and L. Lagae. Microelectronics-based biosensors for the detection of proteins and nucleic acids. *Sensors for Environment, Health and Security*, pages 319–332, 2009.

[238] J.J. Davis, I. Cohn Jr, and F.C. Nance. Diagnosis and management of blunt abdominal trauma. *Annals of Surgery*, 183(6):672, 1976.

[239] A.K. Malhotra, R. Latifi, T.C. Fabian, R.R. Ivatury, S. Dhage, T.K. Bee, P.R. Miller, M.A. Croce, and J.A. Yelon. Multiplicity of solid organ injury: influence on management and outcomes after blunt abdominal trauma. *The Journal of Trauma*, 54(5):925, 2003.

[240] JE Randles. Kinetics of rapid electrode reactions. *Discussions of the Faraday Society*, 1(1):11–19, 1947.

[241] B. Ershler. Investigation of electrode reactions by the method of charging-curves and with the aid of alternating currents. *Discussions of the Faraday Society*, 1(0):269–277, 1947.

[242] A.J. Bard and L.R. Faulkner. *Electrochemical methods: fundamentals and applications*. A1bazaar, 2006.

[243] D. Diamond, S. Coyle, S. Scarmagnani, and J. Hayes. Wireless sensor networks and chemo-/biosensing. *Chemical Reviews*, 108(2):652–679, 2008.

[244] S. Coyle, K.T. Lau, N. Moyna, D. O'Gorman, D. Diamond, F. Di Francesco, D. Costanzo, P. Salvo, M.G. Trivella, D.E. De Rossi, et al. Biotexbiosensing textiles for personalised healthcare management. *IEEE Transactions on Information Technology in Biomedicine*, 14(2):364–370, 2010.

[245] J. Berzowska. Electronic textiles: Wearable computers, reactive fashion, and soft computation. *Textile: The Journal of Cloth and Culture*, 3(1):58–75, 2005.

[246] S. Coyle, Y. Wu, K.T. Lau, D. De Rossi, G. Wallace, and D. Diamond. Smart nanotextiles: A review of materials and applications. *MRS Bulletin*, 32(05):434–442, 2007.

[247] Y.L. Yang, M.C. Chuang, S.L. Lou, and J. Wang. Thick-film textile-based amperometric sensors and biosensors. *Analyst*, 135(6):1230–1234, 2010.

[248] S. Brady, L.E. Dunne, A. Lynch, B. Smyth, and D. Diamond. Wearable sensors? what is there to sense? *Studies in Health Technology and Informatics*, 117:80–88, 2005.

[249] C.M. Harris. The science of detecting terror. *Analytical Chemistry*, 74(5):126–133, 2002.

[250] W.L. Waugh. Terrorism as disaster. *Handbook of Disaster Research*, pages 388–404, 2007.

[251] J. Almog, G. Burda, Y. Shloosh, S. Abramovich-Bar, E. Wolf, and T. Tamiri. Recovery and detection of urea nitrate in traces. *Journal of Forensic Sciences*, 52(6):1284–1290, 2007.

[252] A. Cagan, D. Lu, K. Cizek, J. La Belle, and J. Wang. Reliable, rapid and simple voltammetric detection ofurea nitrate explosive. *Analyst*, 133(5):585–587, 2008.

[253] J.C. Oxley, J.L. Smith, E. Rogers, and M. Yu. Ammonium nitrate: thermal stability and explosivity modifiers. *Thermochimica Acta*, 384(1-2):23–45, 2002.

[254] E. Capua, R. Cao, C.N. Sukenik, and R. Naaman. Detection of triacetone triperoxide (tatp) with an array of sensors based on non-specific interactions. *Sensors and Actuators B: Chemical*, 140(1):122–127, 2009.

[255] D. Lu, A. Cagan, R.A.A. Munoz, T. Tangkuaram, and J. Wang. Highly sensitive electrochemical detection of trace liquid peroxide explosives at a prussian-blue artificial-peroxidasemodified electrode. *Analyst*, 131(12):1279–1281, 2006.

[256] J.M. Sylvia, J.A. Janni, JD Klein, and K.M. Spencer. Surface-enhanced raman detection of 2, 4-dinitrotoluene impurity vapor as a marker to locate landmines. *Analytical Chemistry*, 72(23):5834–5840, 2000.

[257] Z. Naal, J.H. Park, S. Bernhard, JP Shapleigh, CA Batt, and HD Abruna. Amperometric tnt biosensor based on the oriented immobilization of a nitroreductase maltose binding protein fusion. *Analytical Chemistry*, 74(1):140–148, 2002.

[258] J. Wang, R.K. Bhada, J. Lu, and D. MacDonald. Remote electrochemical sensor for monitoring tnt in natural waters. *Analytica Chimica Acta*, 361(1-2):85–91, 1998.

[259] I.B. Bakaltcheva, F.S. Ligler, C.H. Patterson, and L.C. Shriver-Lake. Multi-analyte explosive detection using a fiber optic biosensor. *Analytica Chimica Acta*, 399(1-2):13–20, 1999.

[260] P.T. Charles, P.R. Gauger, C.H. Patterson Jr, and A.W. Kusterbeck. On-site immunoanalysis of nitrate and nitroaromatic compounds in groundwater. *Environmental Science & Technology*, 34(21):4641–4650, 2000.

[261] J.P. Agrawal and R.D. Hodgson. *Organic chemistry of explosives*. Wiley Online Library, 2007.

[262] K.S. Ro, A. Venugopal, D.D. Adrian, D. Constant, K. Qaisi, K.T. Valsaraj, L.J. Thibodeaux, and D. Roy. Solubility of 2, 4, 6-trinitrotoluene (tnt) in water. *Journal of Chemical & Engineering Data*, 41(4):758–761, 1996.

[263] J. Wang. Microchip devices for detecting terrorist weapons. *Analytica Chimica Acta*, 507(1):3–10, 2004.

[264] R.W. Gore and S.B. Allen Jr. Waterproof laminate, March 18 1980. US Patent 4,194,041.

[265] J. Wang, F. Lu, D. MacDonald, J. Lu, M.E.S. Ozsoz, and K.R. Rogers. Screen-printed voltammetric sensor for tnt. *Talanta*, 46(6):1405–1412, 1998.

[266] R.G. Bozic, A.C. West, and R. Levicky. Square wave voltammetric detection of 2, 4, 6-trinitrotoluene and 2, 4-dinitrotoluene on a gold electrode modified with self-assembled monolayers. *Sensors and Actuators B: Chemical*, 133(2):509–515, 2008.

[267] H.B. Glasgow, J.A.M. Burkholder, R.E. Reed, A.J. Lewitus, and J.E. Kleinman. Real-time remote monitoring of water quality: a review of current applications, and advancements in sensor, telemetry, and computing technologies. *Journal of Experimental Marine Biology and Ecology*, 300(1-2):409–448, 2004.

[268] B. Mizaikoff. Mid-infrared evanescent wave sensors-a novel approach for subsea monitoring. *Measurement Science and Technology*, 10:1185, 1999.

[269] S.E. Bufflap and H.E. Allen. Sediment pore water collection methods for trace metal analysis: a review. *Water Research*, 29(1):165–177, 1995.

[270] GE Batley and D. Gardner. Sampling and storage of natural waters for trace metal analysis. *Water Research*, 11(9):745–756, 1977.

[271] X. Fu, R.F. Benson, J. Wang, and D. Fries. Remote underwater electrochemical sensing system for detecting explosive residues in the field. *Sensors and Actuators B: Chemical*, 106(1):296–301, 2005.

[272] J. Wang and S. Thongngamdee. On-line electrochemical monitoring of (tnt) 2, 4, 6-trinitrotoluene in natural waters. *Analytica Chimica Acta*, 485(2):139–144, 2003.

[273] M. Taillefert, G.W. Luther III, and D.B. Nuzzio. The application of electrochemical tools for in situ measurements in aquatic systems. *Electroanalysis*, 12(6):401–412, 2000.

[274] A. Zirino, S.H. Lieberman, and C. Clavell. Measurement of copper and zinc in san diego bay by automated anodic stripping voltammetry. *Environmental Science & Technology*, 12(1):73–79, 1978.

[275] J. Wang, D. Larson, N. Foster, S. Armalis, J. Lu, X. Rongrong, K. Olsen, and A. Zirino. Remote electrochemical sensor for trace metal contaminants. *Analytical Chemistry*, 67(8):1481–1485, 1995.

[276] J.W. Lloyd, P. Decoufle, and R.M. Moore Jr. Background information on chloroprene. *Journal of Occupational and Environmental Medicine*, 17(4):263, 1975.

[277] E. Bardy, J. Mollendorf, and D. Pendergast. A comparison of the thermal resistance of a foam neoprene wetsuit to a wetsuit fabricated from aerogel-syntactic foam hybrid insulation. *Journal of Physics D: Applied Physics*, 39:4068, 2006.

[278] P.R. Stang and E.L. Wiener. Diver performance in cold water. *Human Factors: The Journal of the Human Factors and Ergonomics Society*, 12(4):391–399, 1970.

[279] M.C. Chuang, J.R. Windmiller, P. Santhosh, G.V. Ramírez, M. Galik, T.Y. Chou, and J. Wang. Textile-based electrochemical sensing: effect of fabric substrate and detection of nitroaromatic explosives. *Electroanalysis*, 22(21):2511–2518, 2010.

[280] R.J. Schmidt. Industrial catalytic processes–phenol production. *Applied Catalysis A: General*, 280(1):89–103, 2005.

[281] R.S. Freire, S. Thongngamdee, N. Durán, J. Wang, and L.T. Kubota. Mixed enzyme (laccase/tyrosinase)-based remote electrochemical biosensor for monitoring phenolic compounds. *Analyst*, 127(2):258–261, 2002.

[282] C. Kokkinos, I. Raptis, A. Economou, and T. Speliotis. Determination of trace tl (i) by anodic stripping voltammetry on novel disposable microfabricated bismuth-film sensors. *Electroanalysis*, 22(20):2359–2365, 2010.

[283] B.C. Nindl, A.P. Tuckow, J.A. Alemany, E.A. Harman, K.R. Rarick, J.S. Staab, M.L. Faupel, and MJ Khosravi. Minimally invasive sampling of transdermal body fluid for the purpose of measuring insulin-like growth factor-i during exercise training. *Diabetes Technology & Therapeutics*, 8(2):244–252, 2006.

[284] C. Henry. Getting under the skin: implantable glucose sensors. *Analytical Chemistry*, 70(17):594A, 1998.

[285] B.C. Nindl. Insulin-like growth factor-i as a candidate metabolic biomarker: military relevance and future directions for measurement. *Journal of Diabetes Science and Technology*, 3(2):371, 2009.

[286] G.S. Wilson and Y. Hu. Enzyme-based biosensors for in vivo measurements. *Chemical Reviews*, 100(7):2693–2704, 2000.

[287] ES Wilkins. Towards implantable glucose sensors: a review. *Journal of Biomedical Engineering*, 11(5):354–361, 1989.

[288] MM Rhemrev-Boom, J. Korf, K. Venema, G. Urban, and P. Vadgama. A versatile biosensor device for continuous biomedical monitoring. *Biosensors and Bioelectronics*, 16(9-12):839–847, 2001.

[289] A.P. Raphael, T.W. Prow, M.L. Crichton, X. Chen, G.J.P. Fernando, and M.A.F. Kendall. Targeted, needle-free vaccinations in skin using multilayered, densely-packed dissolving microprojection arrays. *Small*, 6(16):1785–1793, 2010.

[290] W. Martanto, S.P. Davis, N.R. Holiday, J. Wang, H.S. Gill, and M.R. Prausnitz. Transdermal delivery of insulin using microneedles in vivo. *Pharmaceutical Research*, 21(6):947–952, 2004.

[291] M. Cormier, B. Johnson, M. Ameri, K. Nyam, L. Libiran, D.D. Zhang, and P. Daddona. Transdermal delivery of desmopressin using a coated microneedle array patch system. *Journal of Controlled Release*, 97(3):503–511, 2004.

[292] M.R. Prausnitz and R. Langer. Transdermal drug delivery. *Nature Biotechnology*, 26(11):1261–1268, 2008.

[293] S. Henry, D.V. McAllister, M.G. Allen, and M.R. Prausnitz. Microfabricated microneedles: a novel approach to transdermal drug delivery. *Journal of Pharmaceutical Sciences*, 87(8):922–925, 1998.

[294] EV Mukerjee, SD Collins, RR Isseroff, and RL Smith. Microneedle array for transdermal biological fluid extraction and in situ analysis. *Sensors and Actuators A: Physical*, 114(2-3):267–275, 2004.

[295] K. Tsuchiya, N. Nakanishi, Y. Uetsuji, and E. Nakamachi. Development of blood extraction system for health monitoring system. *Biomedical Microdevices*, 7(4):347–353, 2005.

[296] I. Švancara, K. Vytřas, K. Kalcher, A. Walcarius, and J. Wang. Carbon paste electrodes in facts, numbers, and notes: A review on the occasion of the 50-years jubilee of carbon paste in electrochemistry and electroanalysis. *Electroanalysis*, 21(1):7–28, 2009.

[297] J. Wang, N. Naser, L. Angnes, H. Wu, and L. Chen. Metal-dispersed carbon paste electrodes. *Analytical Chemistry*, 64(11):1285–1288, 1992.

[298] J. Wang, J. Liu, L. Chen, and F. Lu. Highly selective membrane-free, mediator-free glucose biosensor. *Analytical Chemistry*, 66(21):3600–3603, 1994.

[299] J. Wang, Q. Chen, and M. Pedrero. Highly selective biosensing of lactate at lactate oxidase containing rhodium-dispersed carbon paste electrodes. *Analytica Chimica Acta*, 304(1):41–46, 1995.

[300] J. Wang, F. Lu, L. Angnes, J. Liu, H. Sakslund, Q. Chen, M. Pedrero, L. Chen, and O. Hammerich. Remarkably selective metallized-carbon amperometric biosensors. *Analytica Chimica Acta*, 305(1-3):3–7, 1995.

[301] S.D. Gittard, R. Narayan, J. Lusk, P. Morel, F. Stockmans, M. Ramsey, C. Laverde, J. Phillips, N.A. Monteiro-Riviere, A. Ovsianikov, et al. Rapid prototyping of scaphoid and lunate bones. *Biotechnology Journal*, 4(1):129–134, 2009.

[302] X. Cai, K. Kalcher, G. Kölbl, C. Neuhold, W. Diewald, and B. Ogorevc. Electrocatalytic reduction of hydrogen peroxide on a palladium-modified carbon paste electrode. *Electroanalysis*, 7(4):340–345, 1995.

[303] K. Schachl, H. Alemu, K. Kalcher, J. Ježkova, I. Švancara, and K. Vytřas. Amperometric determination of hydrogen peroxide with a manganese dioxide-modified carbon paste electrode using flow injection analysis. *Analyst*, 122(9):985–989, 1997.

[304] U. Spohn, D. Narasaiah, L. Gorton, and D. Pfeiffer. A bienzyme modified carbon paste electrode for the amperometric detection of l-lactate at low potentials. *Analytica Chimica Acta*, 319(1-2):79–90, 1996.

[305] R. Garjonyte, Y. Yigzaw, R. Meskys, A. Malinauskas, and L. Gorton. Prussian blue-and lactate oxidase-based amperometric biosensor for lactic acid. *Sensors and Actuators B: Chemical*, 79(1):33–38, 2001.

[306] J.R. Windmiller, N. Zhou, M.C. Chuang, G. Valdés-Ramírez, P. Santhosh, P.R. Miller, R. Narayan, and J. Wang. Microneedle array-based carbon paste amperometric sensors and biosensors. *Analyst*, 136(9):1846–1851, 2011.

[307] C. Malitesta, F. Palmisano, L. Torsi, and P.G. Zambonin. Glucose fast-response amperometric sensor based on glucose oxidase immobilized in an electropolymerized poly (o-phenylenediamine) film. *Analytical Chemistry*, 62(24):2735–2740, 1990.

[308] J.P. Lowry, K. McAteer, S.S. El Atrash, A. Duff, and R.D. O'Neill. Characterization of glucose oxidase-modified poly (phenylenediamine)-coated electrodes in vitro and in vivo: homogeneous interference by ascorbic acid in hydrogen peroxide detection. *Analytical Chemistry*, 66(10):1754–1761, 1994.

[309] GE De Benedetto, F. Palmisano, and PG Zambonin. One-step fabrication of a bienzyme glucose sensor based on glucose oxidase and peroxidase immobilized onto a poly (pyrrole) modified glassy carbon electrode. *Biosensors and Bioelectronics*, 11(10):1001–1008, 1996.

[310] J.P. Lowry and R.D. O'Neill. Partial characterization in vitro of glucose oxidase-modified poly (phenylenediamine)-coated electrodes for neurochemical analysis in vivo. *Electroanalysis*, 6(5-6):369–379, 1994.

[311] E. Dempsey, J. Wang, and M.R. Smyth. Electropolymerised o-phenylenediamine film as means of immobilising lactate oxidase for a l-lactate biosensor. *Talanta*, 40(3):445–451, 1993.

[312] F. Palmisano, D. Centonze, and PG Zambonin. An in situ electrosynthesized amperometric biosensor based on lactate oxidase immobilized in a poly-o-phenylenediamine film: determination of lactate in serum by flow injection analysis. *Biosensors and Bioelectronics*, 9(7):471–479, 1994.

[313] Q. Yang, P. Atanasov, and E. Wilkins. Needle-type lactate biosensor. *Biosensors and Bioelectronics*, 14(2):203–210, 1999.

[314] M.O.M. Berners, M.G. Boutelle, and M. Fillenz. Online measurement of brain glutamate with an enzyme/polymer-coated tubular electrode. *Analytical Chemistry*, 66(13):2017–2021, 1994.

[315] M.R. Ryan, J.P. Lowry, and R.D. ONeill. Biosensor for neurotransmitter l-glutamic acid designed for efficient use of l-glutamate oxidase and effective rejection of interference. *Analyst*, 122(11):1419–1424, 1997.

[316] C.P. McMahon, G. Rocchitta, P.A. Serra, S.M. Kirwan, J.P. Lowry, and R.D. O'Neill. Control of the oxygen dependence of an implantable polymer/enzyme composite biosensor for glutamate. *Analytical Chemistry*, 78(7):2352–2359, 2006.

[317] K. McAteer and R.D. O'Neill. Strategies for decreasing ascorbate interference at glucose oxidase-modified poly (o-phenylenediamine)-coated electrodes. *Analyst*, 121(6):773–777, 1996.

[318] S. Cosnier. Biosensors based on electropolymerized films: new trends. *Analytical and Bioanalytical Chemistry*, 377(3):507–520, 2003.

[319] M.S. Swain, M. Bergeron, R. Audet, A.T. Bleiz, and R.F. Butterworth. Monitoring of neurotransmitter amino acids by means of an indwelling cisterna magna catheter: a comparison of two rodent models of fulminant liver failure. *Hepatology*, 16(4):1028–1035, 1992.

[320] E. Zilkha, TP Obrenovitch, A. Koshy, H. Kusakabe, and HP Bennetto. Extracellular glutamate: on-line monitoring using microdialysis coupled to enzyme-amperometric analysis. *Journal of Neuroscience Methods*, 60(1-2):1–9, 1995.

[321] T. Iijima, C. Shimase, Y. Iwao, and H. Sankawa. Relationships between glutamate release, blood flow and spreading depression: real-time monitoring using an electroenzymatic dialysis electrode. *Neuroscience Research*, 32(3):201–207, 1998.

[322] E. Valencia, A. Marin, and G. Hardy. Impact of oral l-glutamine on glutathione, glutamine, and glutamate blood levels in volunteers. *Nutrition*, 18(5):367–370, 2002.

[323] AC Carter, W. Chang, SB Qadri, JS Horwitz, R. Leuchtner, and DB Chrisey. Micron thick epitaxial (100) ag film growth on mgo. *Journal of materials research*, 13(06):1418–1421, 1998.

[324] D. Svirskis, J. Travas-Sejdic, A. Rodgers, and S. Garg. Electrochemically controlled drug delivery based on intrinsically conducting polymers. *Journal of Controlled Release*, 146(1):6–15, 2010.

[325] M.R. Abidian, D.H. Kim, and D.C. Martin. Conducting-polymer nanotubes for controlled drug release. *Advanced Materials*, 18(4):405–409, 2006.

[326] R. Wadhwa, C.F. Lagenaur, and X.T. Cui. Electrochemically controlled release of dexamethasone from conducting polymer polypyrrole coated electrode. *Journal of Controlled Release*, 110(3):531–541, 2006.

[327] H.D. Tran, D. Li, and R.B. Kaner. One-dimensional conducting polymer nanostructures: Bulk synthesis and applications. *Advanced Materials*, 21(14-15):1487–1499, 2009.

[328] S. Geetha, C.R.K. Rao, M. Vijayan, and DC Trivedi. Biosensing and drug delivery by polypyrrole. *Analytica Chimica Acta*, 568(1-2):119–125, 2006.

[329] L.M. Low, S. Seetharaman, K.Q. He, and M.J. Madou. Microactuators toward microvalves for responsive controlled drug delivery. *Sensors and Actuators B: Chemical*, 67(1-2):149–160, 2000.

[330] J.M. Pernaut and J.R. Reynolds. Use of conducting electroactive polymers for drug delivery and sensing of bioactive molecules. a redox chemistry approach. *The Journal of Physical Chemistry B*, 104(17):4080–4090, 2000.

[331] V.A. Pedrosa, X. Luo, J. Burdick, and J. Wang. "nanofingers" based on binary gold–polypyrrole nanowires. *Small*, 4(6):738–741, 2008.

[332] H. Xu, C. Wang, C. Wang, J. Zoval, and M. Madou. Polymer actuator valves toward controlled drug delivery application. *Biosensors and Bioelectronics*, 21(11):2094–2099, 2006.

[333] G. Jeon, S.Y. Yang, J. Byun, and J.K. Kim. Electrically actuatable smart nanoporous membrane for pulsatile drug release. *Nano Letters*, 2011.

[334] E. Smela and N. Gadegaard. Volume change in polypyrrole studied by atomic force microscopy. *The Journal of Physical Chemistry B*, 105(39):9395–9405, 2001.

[335] P.R. Miller, S.D. Gittard, T.L. Edwards, D.A.M. Lopez, X. Xiao, D.R. Wheeler, N.A. Monteiro-Riviere, S.M. Brozik, R. Polsky, and R.J. Narayan. Integrated carbon fiber electrodes within hollow polymer microneedles for transdermal electrochemical sensing. *Biomicrofluidics*, 5:013415, 2011.

[336] J.R. Windmiller, G. Valdés-Ramírez, N. Zhou, M. Zhou, P.R. Miller, C. Jin, S.M. Brozik, R. Polsky, E. Katz, R. Narayan, et al. Bicomponent microneedle array biosensor for minimally-invasive glutamate monitoring. *Electroanalysis*, 23(10):2302–2309, 2011.

[337] M.R. Prausnitz. Microneedles for transdermal drug delivery. *Advanced Drug Delivery Reviews*, 56(5):581–587, 2004.

[338] A. Ovsianikov, B. Chichkov, P. Mente, NA Monteiro-Riviere, A. Doraiswamy, and RJ Narayan. Two photon polymerization of polymer–ceramic hybrid materials for transdermal drug delivery. *International Journal of Applied Ceramic Technology*, 4(1):22–29, 2007.

[339] S.D. Gittard, A. Ovsianikov, N.A. Monteiro-Riviere, J. Lusk, P. Morel, P. Minghetti, C. Lenardi, B.N. Chichkov, and R.J. Narayan. Fabrication of polymer microneedles using a two-photon polymerization and micromolding process. *Journal of Diabetes Science and Technology*, 3(2):304, 2009.

[340] D.V. McAllister, P.M. Wang, S.P. Davis, J.H. Park, P.J. Canatella, M.G. Allen, and M.R. Prausnitz. Microfabricated needles for transdermal delivery of macromolecules and nanoparticles: fabrication methods and transport studies. *Proceedings of the National Academy of Sciences*, 100(24):13755, 2003.

[341] L. Nordquist, N. Roxhed, P. Griss, and G. Stemme. Novel microneedle patches for active insulin delivery are efficient in maintaining glycaemic control: an initial comparison with subcutaneous administration. *Pharmaceutical Research*, 24(7):1381–1388, 2007.

[342] J.D. Goud, P.M. Raj, J. Liu, R. Narayan, M. Iyer, and R. Tummala. Electrochemical biosensors and microfluidics in organic system-on-package technology. In *Electronic Components and Technology Conference, 2007. ECTC'07. Proceedings. 57th*, pages 1550–1555. IEEE, 2007.

[343] D.W. Bodhale, A. Nisar, and N. Afzulpurkar. Structural and microfluidic analysis of hollow side-open polymeric microneedles for transdermal drug delivery applications. *Microfluidics and Nanofluidics*, 8(3):373–392, 2010.

[344] B. Stoeber and D. Liepmann. Arrays of hollow out-of-plane microneedles for drug delivery. *Journal of Microelectromechanical Systems*, 14(3):472–479, 2005.

[345] J. Judy, D. Maynes, and BW Webb. Characterization of frictional pressure drop for liquid flows through microchannels. *International Journal of Heat and Mass Transfer*, 45(17):3477–3489, 2002.

[346] M. Mala, D. Li, et al. Flow characteristics of water in microtubes. *International Journal of Heat and Fluid Flow*, 20(2):142–148, 1999.

[347] W. Qu and I. Mudawar. Experimental and numerical study of pressure drop and heat transfer in a single-phase micro-channel heat sink. *International Journal of Heat and Mass Transfer*, 45(12):2549–2565, 2002.

[348] W.S. Janna. *Design of fluid thermal systems*. Thomson Engineering, 2010.

[349] R.C. Weast, M.J. Astle, and W.H. Beyer. *CRC handbook of chemistry and physics*, volume 69. CRC press Boca Raton, FL, 1988.

[350] M.J. Moehlenbrock and S.D. Minteer. Extended lifetime biofuel cells. *Chemical Society Reviews*, 37(6):1188–1196, 2008.

[351] J.A. Cracknell, K.A. Vincent, and F.A. Armstrong. Enzymes as working or inspirational electrocatalysts for fuel cells and electrolysis. *Chemical Reviews*, 108(7):2439–2461, 2008.

[352] S.C. Barton, J. Gallaway, and P. Atanassov. Enzymatic biofuel cells for implantable and microscale devices. *Chemical Reviews*, 104(10):4867–4886, 2004.

[353] W. Gellett, M. Kesmez, J. Schumacher, N. Akers, and S.D. Minteer. Biofuel cells for portable power. *Electroanalysis*, 22(7-8):727–731, 2010.

[354] F. Davis and S.P.J. Higson. Biofuel cells–recent advances and applications. *Biosensors and Bioelectronics*, 22(7):1224–1235, 2007.

[355] P. Cinquin, C. Gondran, F. Giroud, S. Mazabrard, A. Pellissier, F. Boucher, J.P. Alcaraz, K. Gorgy, F. Lenouvel, S. Mathé, et al. A glucose biofuel cell implanted in rats. *PloS One*, 5(5):e10476, 2010.

[356] Z. Li, M.A. Rosenbaum, A. Venkataraman, T.K. Tam, E. Katz, and L.T. Angenent. Bacteria-based and logic gate: a decision-making and self-powered biosensor. *Chemical Communications*, 47(11):3060–3062, 2011.

[357] E. Katz. Biofuel cells with switchable power output. *Electroanalysis*, 22(7-8):744–756, 2010.

[358] M. Zhou, Y. Du, C. Chen, B. Li, D. Wen, S. Dong, and E. Wang. Aptamer-controlled biofuel cells in logic systems and used as self-powered and intelligent logic aptasensors. *Journal of the American Chemical Society*, 132(7):2172–2174, 2010.

[359] M. Zhou and S. Dong. Bioelectrochemical interface engineering: toward the fabrication of electrochemical biosensors, biofuel cells, and self-powered logic biosensors. *Accounts of Chemical Research*, 44(11):1232–1243, 2011.

[360] M. Zhou and J. Wang. Biofuel cells for self-powered electrochemical biosensing and logic biosensing: a review. *Electroanalysis*, 24(2):197–209, 2012.

[361] J.T. Santini Jr, A.C. Richards, R. Scheidt, M.J. Cima, and R. Langer. Microchips as controlled drug-delivery devices. *Angewandte Chemie International Edition*, 39(14):2396–2407, 2000.

[362] M. Ben-Ari. *Mathematical logic for computer science*. Springer Verlag, 2001.

[363] M.E. Lieberman and M.A. Levitt. Spontaneous rupture of the spleen: a case report and literature review. *The American Journal of Emergency Medicine*, 7(1):28–31, 1989.

[364] J. Wang, M. Musameh, and Y. Lin. Solubilization of carbon nanotubes by nafion toward the preparation of amperometric biosensors. *Journal of the American Chemical Society*, 125(9):2408–2409, 2003.

[365] J. Halámek, J. Zhou, L. Halámková, V. Bocharova, V. Privman, J. Wang, and E. Katz. Biomolecular filters for improved separation of output signals in enzyme logic systems applied to biomedical analysis. *Analytical Chemistry*, 83(22):8383–8386, 2011.

[366] A. Zebda, C. Gondran, A. Le Goff, M. Holzinger, P. Cinquin, and S. Cosnier. Mediatorless high-power glucose biofuel cells based on compressed carbon nanotube-enzyme electrodes. *Nature Communications*, 2:370, 2011.

[367] M. Zhang, S. Xu, S.D. Minteer, and D.A. Baum. Investigation of a deoxyribozyme as a biofuel cell catalyst. *Journal of the American Chemical Society*, 133(40):15890–15893, 2011.

[368] M. Zhou and J. Wang. Biofuel cells for self-powered electrochemical biosensing and logic biosensing: a review. *Electroanalysis*, 24(2):197–209, 2012.

[369] M. Zhou, N. Zhou, F. Kuralay, J.R. Windmiller, S. Parkhomovsky, G. Valdés-Ramírez, E. Katz, and J. Wang. A self-powered "sense-act-treat" system that is based on a biofuel cell and controlled by boolean logic. *Angewandte Chemie International Edition*, 51(11):2686–2689, 2012.

[370] M. Zhou, F. Wang, and S. Dong. Boolean logic gates based on oxygen-controlled biofuel cell in "one pot". *Electrochimica Acta*, 56(11):4112–4118, 2011.

[371] A.P. de Silva. Analytical chemistry: sense and versatility. *Nature*, 445(7129):718–719, 2007.

[372] J.C. Achenbach, W. Chiuman, R.P.G. Cruz, and Y. Li. Dnazymes: from creation in vitro to application in vivo. *Current Pharmaceutical Biotechnology*, 5(4):321–336, 2004.

[373] J. Liu, Z. Cao, and Y. Lu. Functional nucleic acid sensors. *Chemical Reviews*, 109(5):1948–1998, 2009.

[374] B. Li, S. Dong, and E. Wang. Homogeneous analysis: label-free and substrate-free aptasensors. *Chemistry–An Asian Journal*, 5(6):1262–1272, 2010.

[375] R. Vannela and P. Adriaens. Dnazymes in environmental sensing. *Critical Reviews in Environmental Science and Technology*, 36(5):375–403, 2006.

[376] T. Li, S. Dong, and E. Wang. Label-free colorimetric detection of aqueous mercury ion (hg2+) using hg2+-modulated g-quadruplex-based dnazymes. *Analytical Chemistry*, 81(6):2144–2149, 2009.

[377] T. Li, S. Dong, and E. Wang. A lead (ii)-driven dna molecular device for turn-on fluorescence detection of lead (ii) ion with high selectivity and sensitivity. *Journal of the American Chemical Society*, 132(38):13156–13157, 2010.

[378] T. Li, E. Wang, and S. Dong. Potassium- lead-switched g-quadruplexes: A new class of dna logic gates. *Journal of the American Chemical Society*, 131(42):15082–15083, 2009.

[379] L. Martin. *All you really need to know to interpret arterial blood gases*. Lippincott Williams & Wilkins, 1999.

[380] M. Lin Tan, P.F.M. Choong, and C.R. Dass. Dnazyme delivery systems: getting past first base. *Expert Opinion on Drug Delivery*, 6(2):127–138, 2009.

[381] U. Pischel. Digital operations with molecules–advances, challenges, and perspectives. *Australian Journal of Chemistry*, 63(2):148–164, 2010.

[382] J. Andréasson and U. Pischel. Smart molecules at workmimicking advanced logic operations. *Chemical Society Reviews*, 39(1):174–188, 2009.

[383] D. van Noort. A programmable molecular computer in microreactors. *DNA Computing*, pages 365–374, 2005.

[384] J.H. Reif and S. Sahu. Autonomous programmable dna nanorobotic devices using dnazymes. *Theoretical Computer Science*, 410(15):1428–1439, 2009.

[385] A.P. de Silva, H.Q.N. Gunaratne, and G.E.M. Maguire. off–onfluorescent sensors for physiological levels of magnesium ions based on photoinduced electron transfer (pet), which also behave as photoionic or logic gates. *Journal of the Chemical Society, Chemical Communications*, (10):1213–1214, 1994.

[386] A.P. de Silva, I.M. Dixon, H.Q.N. Gunaratne, T. Gunnlaugsson, P.R.S. Maxwell, and T.E. Rice. Integration of logic functions and sequential operation of gates at the molecular-scale. *Journal of the American Chemical Society*, 121(6):1393–1394, 1999.

[387] B. Turfan and E.U. Akkaya. Modulation of boradiazaindacene emission by cation-mediated oxidative pet. *Organic Letters*, 4(17):2857–2859, 2002.

[388] Z. Wang, G. Zheng, and P. Lu. 9-(cycloheptatrienylidene)-fluorene derivative: remarkable ratiometric ph sensor and computing switch with nor logic gate. *Organic Letters*, 7(17):3669–3672, 2005.

[389] H.T. Baytekin and E.U. Akkaya. A molecular nand gate based on watson-crick base pairing. *Organic Letters*, 2(12):1725–1727, 2000.

[390] G. Zong, L. Xian, and G. Lu. l-arginine bearing an anthrylmethyl group: fluorescent molecular nand logic gate with h+ and atp as inputs. *Tetrahedron Letters*, 48(22):3891–3894, 2007.

[391] T. Gunnlaugsson, D.A. Mac Dónail, and D. Parker. Luminescent molecular logic gates: the two-input inhibit (inh) function. *Chemical Communications*, (1):93–94, 2000.

[392] L. Li, M.X. Yu, F.Y. Li, T. Yi, and C.H. Huang. Inhibit logic gate based on spiropyran sensitized semiconductor electrode. *Colloids and Surfaces A: Physicochemical and Engineering Aspects*, 304(1-3):49–53, 2007.

[393] V. Luxami and S. Kumar. Molecular half-subtractor based on 3, 3-bis (1h-benzimidazolyl-2-yl)[1, 1] binaphthalenyl-2, 2-diol. *New Journal of Chemistry*, 32(12):2074–2079, 2008.

[394] J. Qian, X. Qian, Y. Xu, and S. Zhang. Multiple molecular logic functions and molecular calculations facilitated by surfactants versatility. *Chemical Communications*, (35):4141–4143, 2008.

[395] S. Sivan and N. Lotan. A biochemical logic gate using an enzyme and its inhibitor. 1. the inhibitor as switching element. *Biotechnology Progress*, 15(6):964–970, 1999.

[396] S. Sivan, S. Tuchman, and N. Lotan. A biochemical logic gate using an enzyme and its inhibitor. part ii: The logic gate. *Biosystems*, 70(1):21–33, 2003.

[397] A.S. Deonarine, S.M. Clark, and L. Konermann. Implementation of a multifunctional logic gate based on folding/unfolding transitions of a protein. *Future Generation Computer Systems*, 19(1):87–97, 2003.

[398] G. Ashkenazi, DR Ripoll, N. Lotan, and HA Scheraga. A molecular switch for biochemical logic gates: conformational studies. *Biosensors and Bioelectronics*, 12(2):85–95, 1997.

[399] R. Unger and J. Moult. Towards computing with proteins. *Proteins: Structure, Function, and Bioinformatics*, 63(1):53–64, 2006.

[400] M.N. Win and C.D. Smolke. Higher-order cellular information processing with synthetic rna devices. *Science*, 322(5900):456, 2008.

[401] A. Ogawa and M. Maeda. Easy design of logic gates based on aptazymes and noncrosslinking gold nanoparticle aggregation. *Chemical Communications*, (31):4666–4668, 2009.

[402] M.N. Stojanovic, T.E. Mitchell, and D. Stefanovic. Deoxyribozyme-based logic gates. *Journal of the American Chemical Society*, 124(14):3555–3561, 2002.

[403] M. Pita and E. Katz. Multiple logic gates based on electrically wired surface-reconstituted enzymes. *Journal of the American Chemical Society*, 130(1):36–37, 2008.

[404] Z. Ezziane. Dna computing: applications and challenges. *Nanotechnology*, 17:R27, 2006.

[405] M. Darehmiraki and H. Mishmast Nehi. Molecular solution to the 0-1 knapsack problem based on dna computing. *Applied Mathematics and Computation*, 187(2):1033–1037, 2007.

[406] J.Y. Lee, H.W. Lim, S.I. Yoo, B.T. Zhang, and T.H. Park. Efficient initial pool generation for weighted graph problems using parallel overlap assembly. *DNA Computing*, 3384:215–223, 2005.

[407] M. Kahan, B. Gil, R. Adar, and E. Shapiro. Towards molecular computers that operate in a biological environment. *Physica D: Nonlinear Phenomena*, 237(9):1165–1172, 2008.

[408] Y. Benenson. Rna-based computation in live cells. *Current Opinion in Biotechnology*, 20(4):471–478, 2009.

[409] Y. Benenson. Biocomputers: from test tubes to live cells. *Molecular Biosystems*, 5(7):675–685, 2009.

[410] K. Rinaudo, L. Bleris, R. Maddamsetti, S. Subramanian, R. Weiss, and Y. Benenson. A universal rnai-based logic evaluator that operates in mammalian cells. *Nature Biotechnology*, 25(7):795–801, 2007.

[411] S. Ji. The cell as the smallest dna-based molecular computer. *BioSystems*, 52(1-3):123–133, 1999.

[412] E.A. Liberman and S.V. Minina. Cell molecular computers and biological information as the foundation of nature's laws. *BioSystems*, 38(2-3):173–177, 1996.

[413] V. Maojo, F. Martin-Sanchez, C. Kulikowski, A. Rodriguez-Paton, and M. Fritts. Nanoinformatics and dna-based computing: catalyzing nanomedicine. *Pediatric Research*, 67(5):481, 2010.

[414] M.T. Tyn and T.W. Gusek. Prediction of diffusion coefficients of proteins. *Biotechnology and Bioengineering*, 35(4):327–338, 1990.

[415] R. Gutiérrez, E.M.M. del Valle, and M.A. Galán. Theoretical model to predict the diffusion coefficients of enzymes on adsorption processes based on hard-core two-yukawa potential. *Industrial & Engineering Chemistry Research*, 46(23):7410–7416, 2007.

[416] C. Tanford. Physical chemistry of macromolecules. 1961.

[417] E. Jurado, F. Camacho, G. Luzón, and JM Vicaria. Kinetic models of activity for β-galactosidases: influence of ph, ionic concentration and temperature. *Enzyme and Microbial Technology*, 34(1):33–40, 2004.

[418] L.M.M. Tijskens, R. Greiner, E.S.A. Biekman, and U. Konietzny. Modeling the effect of temperature and ph on activity of enzymes: the case of phytases. *Biotechnology and Bioengineering*, 72(3):323–330, 2001.

[419] K. Buchholz, V. Kasche, and U.T. Bornscheuer. *Biocatalysts and enzyme technology*. Wiley-VCH, 2005.

[420] A. Illanes. *Enzyme biocatalysis: principles and applications*. Springer Verlag, 2008.